**Sapienza University of Rome**

Department of Physics
PhD in Accelerator Physics

THESIS FOR THE DEGREE OF DOCTOR OF PHYSICS

# Simulations and Experimental Activities on Electron Diagnostics for EuPRAXIA@SPARC_LAB

Relatori
**Anna Giribono**
**Enrica Chiadroni**

Candidate
**Francesco Demurtas**
**2064330**

**Academic Year MMXXII–MMXXV (XXXVIII cycle)**

## Abstract

The development of advanced beam diagnostics is essential in next-generation high-brightness accelerator facilities, including free-electron lasers and plasma-based accelerators.
The EuPRAXIA@SPARC_LAB facility, currently under construction at INFN-LNF, will demonstrate a high-brightness plasma-driven accelerator capable of delivering beams suitable for a free-electron laser. In this context, this thesis presents dedicated beam dynamics studies aimed at characterizing and determining the resolution limits of the diagnostic systems foreseen for EuPRAXIA@SPARC_LAB. The work evaluates the performance of diagnostics at three representative energies — low (118 MeV), medium (400 MeV), and high (1 GeV) — through dedicated beam dynamics simulations. Particular attention is devoted to the PolariX Transverse Deflection Structure (PolariX TDS), an X-band cavity with variable polarization developed by PSI, CERN, and DESY. Its capability to continuously rotate the streaking field in the transverse plane allows the same device to perform longitudinal diagnostics in orthogonal planes. This unique flexibility also enables tomographic reconstruction of the longitudinal and transverse phase-space distributions. The work presents theoretical activities, including RF studies and beam dynamics simulations of the PolariX TDS, such as the validation of 3D field maps and the RF design of the 50-cell structure for the low-energy section. In addition, dedicated simulations were performed to evaluate the measurement resolution for emittance, energy, and bunch length across the EuPRAXIA diagnostic sections. Finally, experimental results from the SwissFEL Athos beamline demonstrate the feasibility of 3D and 5D beam tomography using the PolariX TDS, performed on realistic high-brightness beams and intended for future implementation at both SwissFEL and EuPRAXIA. The outcomes of this research establish the achievable resolution of the EuPRAXIA diagnostic systems and validate the integration of the PolariX TDS concept as a key enabling technology for next-generation compact FEL facilities.



Keywords: EuPRAXIA@SPARC_LAB, Beam dynamics, Diagnostics, PolariX TDS, Transverse Deflection Structure, Phase Space tomography

# Contents

# List of Figures

# List of Tables

# Chapter 1

# Introduction

Particle accelerators play a central role in both fundamental research and technological applications. Facilities for high-energy physics, synchrotron light sources, and free-electron lasers (FELs) have been demonstrated to be fundamental to a wide range of applications, including medicine, materials science, and industry. Despite their enormous impact, conventional radio-frequency accelerators are often limited by their size and cost, which scale unfavorably with the accelerating gradient. For this reason, there has been an increasing effort to develop novel acceleration techniques, aiming to produce compact, cost-effective accelerators while maintaining, or even improving, beam quality. Among the most promising approaches, plasma-based acceleration techniques can sustain accelerating gradients of tens of GeV/m, which are more than two orders of magnitude higher than those achievable with conventional RF technology. This opens the way for a new generation of compact FELs and high-brightness electron-beam facilities. However, to fully exploit the potential of these novel accelerators, the development of advanced beam diagnostics is equally essential. Indeed, precise control and characterization of electron beam parameters such as emittance, energy spread, and longitudinal profile are mandatory to meet the stringent requirements of next-generation FELs [1, 2]. In this context, the EuPRAXIA@SPARC_LAB facility, under construction at INFN-LNF, will serve as the first European research infrastructure based on a plasma accelerator designed not only to demonstrate the generation of high-brightness electron beams suitable for a free-electron laser, but also to operate as a user facility for multidisciplinary applications. The machine design combines a high-brightness S-band photoinjector with X-band linac modules for intermediate acceleration, while a final plasma acceleration stage provides the ultimate energy boost [3–5].

The research activity presented in this thesis is primarily devoted to the study and characterization of the diagnostic systems foreseen for EuPRAXIA@SPARC_LAB. The goal is to assess, through extensive beam dynamics simulations, the resolution limits of measurements of bunch parameters at the diagnostics stations distributed along the accelerator. Each station is studied to measure, with high precision, the fundamental beam parameters: transverse emittance, beam energy, and longitudinal profile. The simulations were carried out by reproducing the full diagnostic process, including the effects of optics matching, measurement errors, and finite instrumental resolution, to determine not only the measurable quantities but also the accuracy with which they can be obtained.

At the heart of the diagnostic system stands the PolariX Transverse Deflection Structure (TDS), a novel X-band device specifically designed within a collaboration of PSI, CERN, and DESY [6]. Unlike conventional TDSs, the PolariX can operate with a variable polarization of the input electromagnetic wave. This unique feature allows the streaking force to be rotated in the transverse plane, enabling the beam to be deflected along any desired transverse axis. Such flexibility opens the way to multidimensional characterization techniques that go well beyond the standard measurement of bunch length. In particular, PolariX plays a central role in the implementation of so-called 5D tomography, which exploits streaking-angle scans combined with quadrupole scans in both transverse planes. By interpreting these scans as projections along different axes in phase space, it is possible to reconstruct higher-dimensional beam distributions, moving from one-dimensional to multi-dimensional characterizations [7, 8].

The thesis is organized as follows. Chapter 2 provides an overview of the beam dynamics theory that underpins the studies presented in this work. It also describes the various diagnostic techniques foreseen for implementation in the facility, together with the corresponding beamline elements required for their realization. Finally, it introduces the numerical tracking codes used to model the beam diagnostics, which are employed to simulate the various measurements and determine the achievable resolution. Chapter 3 focuses on the design aspects of the Polarix TDS and optimization of Field maps. Detailed simulations were conducted to verify the electromagnetic fields in multi-cell structures and to validate the design of the 50-cell deflector required at low energies. The accuracy of these field maps is crucial for predicting the integrated kick experienced by the beam and, therefore, for ensuring the reliability of the diagnostic process. Chapter 4 is devoted to the evaluation of the achievable resolution for emittance, energy, and bunch length measurements at low, medium, and high energies along the EuPRAXIA beamline, respectively at a nominal energy of 118 MeV, 400 MeV, and 1 GeV. The methodology is based on beam dynamics simulations performed with tracking codes to model the beamline and determine the intrinsic resolution of the measurements, taking into account contributions from the screen resolution, the camera pixel size, and the statistical uncertainties of the beam distribution. Finally, chapter 5 discusses the application of PolariX to advanced diagnostic techniques, particularly the use of 5D tomography at the SwissFEL facility. Here, the reconstruction of the multi-dimensional phase-space distributions of the beam is explored, highlighting the characterization of realistic beams employed at the 3-GeV Athos beamline at SwissFEL. This approach, based on tomographic methods, and first developed and demonstrated at DESY, provides information that is generally not characterized in standard diagnostics and represents a powerful tool for characterizing beams in plasma-based accelerators [9, 10].

In summary, the work reported in this thesis contributes to the design and validation of the diagnostic system for EuPRAXIA@SPARC_LAB, with a specific emphasis on the resolution limits of conventional measurements and on the novel opportunities enabled by the PolariX TDS. By combining beam dynamics simulations, electromagnetic field studies, and innovative reconstruction methods, this research aims to ensure that the diagnostic system can match the unprecedented performance of plasma-based acceleration. This represents a necessary step towards the realization of compact, reliable, and user-oriented FEL facilities based on novel acceleration techniques.

## 1.1 Overview of longitudinal beam diagnostic techniques

The characterization of longitudinal beam properties is a critical aspect in modern high-brightness electron linacs for FEL facilities. The generation of high-peak-current beams, combined with stringent requirements for preserving beam quality, demands diagnostic techniques capable of resolving femtosecond temporal structures. Several approaches have been developed to address these challenges, each providing complementary information and exhibiting specific advantages and limitations. RF transverse deflection structures are the most widely adopted and direct diagnostic technique for longitudinal beam characterization in FEL linacs. By exploiting the time-dependent transverse momentum imparted by the RF fields, a TDS maps the bunch longitudinal coordinate onto a transverse spatial dimension on a downstream screen. This principle enables multi-shot measurements of the bunch length and, when combined with dispersive sections, provides access to the longitudinal phase space and slice beam parameters. Owing to their direct and model-independent nature, TDSs have become a standard diagnostic tool at many FEL facilities. Their main limitations are associated with RF power availability and with the energy spread induced by the RF fields, which becomes particularly relevant at low beam energies; nevertheless, they remain the reference technique for high-resolution longitudinal diagnostics [11–13]. Electro-Optical Sampling (EOS) techniques offer a complementary, single-shot, non-intercepting approach to longitudinal diagnostics and are particularly relevant for high-brightness FEL linacs. By probing the transient electric field of an electron bunch with an ultrafast laser pulse, EOS enables measurements of arrival time, timing jitter, and relative synchronization between different bunches, such as the driver and witness beams in advanced acceleration schemes. EOS diagnostics are therefore primarily used for stability and synchronization studies, which are crucial for reliable FEL operation. However, the temporal resolution achievable with EOS is limited by the properties of the electro-optic crystal and the laser system, and the technique typically provides indirect information on the longitudinal charge distribution rather than a direct measurement of the phase space [14–16]. Additional longitudinal diagnostics are based on the detection of coherent radiation emitted by the electron bunch, such as coherent transition radiation, coherent synchrotron radiation, or THz radiation. These methods exploit the frequency-domain signature of ultrashort bunches and can achieve high sensitivity for strongly compressed beams. Nevertheless, reconstructing the temporal profile from spectral measurements generally relies on model-dependent assumptions, and the interpretation can be complicated by collective effects, microbunching instabilities, and radiation transport [17–19]. More recently, machine-learning-based approaches have been proposed to assist longitudinal beam diagnostics. In this context, data-driven models have been explored as fast surrogate tools to infer longitudinal beam properties or to reduce the number of measurements required for complex diagnostics, including phase-space reconstruction. While these methods are still under active development and typically rely on training datasets or supporting physical models, they represent a complementary approach to established diagnostic techniques, particularly for high-repetition-rate FEL facilities [20]. Within this broader landscape of longitudinal beam diagnostics, advanced implementations of RF deflecting structures are of particular interest. In particular, concepts enabling additional degrees of freedom in the streaking configuration naturally extend conventional TDS diagnostics toward multidimensional phase-space reconstruction, addressing the requirements of next-generation high-brightness FEL and plasma-based accelerator facilities.

# Chapter 2

# Beam dynamics theory for diagnostics studies

Precise knowledge of the beam properties is essential for the operation and optimization of particle accelerators, especially in advanced applications such as Free-Electron Lasers (FELs), plasma accelerators, and high-energy linacs. In this chapter, the theoretical groundwork for understanding and modeling the diagnostic tools used throughout this thesis to characterize electron beams is presented. The approach is based on linear beam optics and phase space formalism to describe the dynamics of relativistic particle beams under the influence of magnetic elements.

Section 2.1 describes the particle beam in terms of statistical moments and phase space variables. Section 2.2 focuses on the transverse beam dynamics, introducing the concepts of emittance and Twiss parameters, and the beam evolution along the accelerator. The second part of the chapter is devoted to the theoretical models behind specific diagnostic techniques, detailing the principles of quadrupole scans in section 2.3, transverse deflection structures (TDS) in section 2.4, and energy spectrometers in section 2.5, and presenting widely used methods for measuring transverse and longitudinal bunch parameters. Finally, in section 2.6, the simulation codes used throughout the thesis are briefly introduced and described.

## 2.1 Particle beam description

Each particle is identified by a set of six coordinates describing horizontal and vertical position $x$ and $y$, divergence in the transverse plane $x' = \frac{p_x}{p_z}$ and $y' = \frac{p_y}{p_z}$, the longitudinal position of the particle along the beam, which can be expressed in time "$t$" or spatial units "$z$", and its energy $E$, commonly indicated as the energy deviation from the reference particle energy $\delta = \frac{E_0 - E}{E_0}$. The conjugate variables $(x, x')$ and $(y, y')$ define the transverse plane, while $(z, \delta)$ are referred to as the longitudinal plane.
When extending these variables to an electron beam instead of a single particle, a statistical description is given by defining the average values of the beam parameters over the number of particles in the bunch. The quantities $\langle x \rangle$, $\langle x^2 \rangle$, $\langle x'^2 \rangle$, and $\langle xx' \rangle$ represent, respectively, the mean position, the beam size squared, the angular divergence squared, and the correlation term between position and angle.

$$\langle x \rangle = \bar{x} = \frac{1}{N}\sum_{i}^{N} x_i \tag{2.1}$$

$$\langle x^2 \rangle = \sigma_x^2 = \frac{1}{N}\sum_{i}^{N} x_i^2 \tag{2.2}$$

$$\langle x'^2 \rangle = \sigma_x^2 = \frac{1}{N}\sum_{i}^{N} x_i'^2 \tag{2.3}$$

$$\langle xx' \rangle = \sigma_{xx'} = \frac{1}{N}\sum_{i}^{N} x_i x_i' \tag{2.4}$$

These quantities can be defined to allow for describing the beam in the related transverse space by defining the corresponding beam matrix:

$$\Sigma = \begin{pmatrix} \Sigma_{11} & \Sigma_{12} \\ \Sigma_{21} & \Sigma_{22} \end{pmatrix} = \begin{pmatrix} \langle x^2 \rangle & \langle xx' \rangle \\ \langle xx' \rangle & \langle x'^2 \rangle \end{pmatrix} \tag{2.5}$$

The same formalism and definitions can be extended to the other conjugate pairs of variables, $(y, y')$ and $(z, \delta)$, depending on the specific plane under investigation.
The complete 6D covariance matrix, which describes all the correlations in the beam, is then given by:

$$\Sigma_{6D} = \begin{pmatrix} \langle x^2 \rangle & \langle xx' \rangle & \langle xy \rangle & \langle xy' \rangle & \langle xz \rangle & \langle x\delta \rangle \\ \langle x'x \rangle & \langle x'^2 \rangle & \langle x'y \rangle & \langle x'y' \rangle & \langle x'z \rangle & \langle x'\delta \rangle \\ \langle yx \rangle & \langle yx' \rangle & \langle y^2 \rangle & \langle yy' \rangle & \langle yz \rangle & \langle y\delta \rangle \\ \langle y'x \rangle & \langle y'x' \rangle & \langle y'y \rangle & \langle y'^2 \rangle & \langle y'z \rangle & \langle y'\delta \rangle \\ \langle zx \rangle & \langle zx' \rangle & \langle zy \rangle & \langle zy' \rangle & \langle z^2 \rangle & \langle z\delta \rangle \\ \langle \delta x \rangle & \langle \delta x' \rangle & \langle \delta y \rangle & \langle \delta y' \rangle & \langle \delta z \rangle & \langle \delta^2 \rangle \end{pmatrix} \tag{2.6}$$

## 2.2 Transverse beam dynamics

To study the evolution of a particle beam through the accelerator, the particle dynamics in the phase space $(x, p_x, y, p_y, z, E)$ is considered, where $p_x \approx p_z x'$ and $p_y \approx p_z y'$, and $p_z$ is the reference particle momentum. These variables are dependent on the longitudinal position $s$, and at fixed $s$, each particle is represented by a point in the phase space. When working on the beam dynamics, it is convenient to use the trajectory slopes $x'$, $y'$ in place of the respective momentum, representing the particle in what is called the trace space. In this case, the coupling between the planes is not considered, so that it is possible to split the six-dimensional phase space into three three-dimensional spaces that can be treated separately [21].

### 2.2.1 Emittance

The area $A$ occupied by the beam ensemble in the trace space is a convenient figure of merit to describe the quality of the beam. This allows to define the geometric emittance $\varepsilon$ as:

$$A = \pi\, \varepsilon \tag{2.7}$$

The emittance quantifies the beam quality by characterizing how tightly the particles are packed in phase space. For a given beam energy, lower emittance implies better focusability and higher brightness. In transverse phase space, the occupied area remains constant, assuming the system is subject only to conservative forces. This is a direct consequence of Liouville's Theorem, which states that the phase space volume is conserved in a Hamiltonian system [22]. When considering a monochromatic beam with constant energy, the theorem also applies to the trace space area, implying that the geometrical emittance is an invariant of the particle motion. During acceleration, only the phase space area is conserved according to Liouville's Theorem:

$$\int p_x \, dx = constant\,. \tag{2.8}$$

By considering :

$$x' = \frac{dx}{ds} = \frac{dx}{dt}\frac{dt}{ds} = \frac{\beta_x}{\beta_s} \tag{2.9}$$

Eq. 2.8 can be rewritten as:

$$\int \, p_x \, dx = m_e c \gamma \beta \int x' \, dx = const.\,, \tag{2.10}$$

in which $\gamma$ is the relativistic Lorentz factor, $\beta$ is the is the normalized particle velocity, and $\int x' \, dx$ corresponds to the geometric emittance. The term $\varepsilon_n = \gamma\beta\varepsilon_x$ is conserved under acceleration in case of a monochromatic beam and it is called normalized emittance. As a consequence of this definition, as $\beta\gamma$ is proportional to the particle momentum, during acceleration the geometrical emittance shrinks as $\varepsilon_x \propto \frac{1}{p}$, a process known as adiabatic damping.

A more general definition of the normalized emittance has to take into account the contribution arising from the energy spread of the bunch so that the normalized emittance can be generalized as:

$$\varepsilon_n^2 = <\gamma>^2 \, (\sigma_E^2 <\gamma>^2 \sigma_{x'}^2 + \varepsilon_0^2)\,, \tag{2.11}$$

where $<\gamma>$ is the average Lorentz factor, $\sigma_x$ and $\sigma_{x'}$ are the rms beam size and divergence, and $\varepsilon_0$ is the initial geometric emittance [23]. The relative energy spread $\sigma_E$ is defined as:

$$\sigma_E^2 = \frac{<\beta^2\gamma^2> - <\beta\gamma>^2}{<\gamma>^2}\,. \tag{2.12}$$

Different emittance definitions, such as RMS, projected, and slice emittance, together with the conventions adopted in this work, are summarized in Appendix A.1.

### 2.2.2 Twiss parameters

The evolution of the transverse beam envelope and its correlation in phase space are conveniently described using the Twiss parameters $\alpha$, $\beta$, and $\gamma$. These functions characterize the shape and orientation of the beam ellipse in the $(x, x')$ trace space and are directly related to the statistical moments of the particle distribution. The parameter $\beta$ defines the beam envelope, $\gamma$ represents the beam divergence per unit emittance, and $\alpha$ quantifies the correlation between position and angle, being proportional to the derivative of the $\beta$ function.
The Twiss parameters provide a compact formalism to describe the beam transport along the accelerator and are extensively used in this work to express both measured and simulated beam properties. A detailed description of their definitions, interrelations, and transformation through linear optics is reported in Appendix A.2.

### 2.2.3 Space Charge Effects

Space charge forces arise directly from the charge distribution within the bunch, due to the Coulomb interaction between particles. These forces influence both the transverse and longitudinal beam dynamics and can lead to a deterioration in beam quality as the bunch propagates through the accelerator. To analyze these effects, one can consider an idealized model consisting of a uniform, infinitely long cylindrical beam of radius $R_b$ that propagates along the $z$-axis with an average current $I$. The resulting longitudinal and radial electric fields are given by:

$$E_z(\xi) = \frac{IL}{2\pi\varepsilon_0 R_b^2 \beta c} h(\xi)\,, \tag{2.13}$$

$$E_z(r_b, \xi) = \frac{I r_b}{2\pi\varepsilon_0 R_b^2 \beta c} g(\xi)\,, \tag{2.14}$$

where $h(\xi) = \sqrt{A + (1-\xi)^2} - \sqrt{A + \xi^2} + (2\xi - 1)$ and $g(\xi) = \frac{(1-\xi)}{\sqrt{A^2+(1-\xi)^2}} + \frac{\xi}{2\sqrt{A^2+\xi^2}}$ are field-dependent factors. As the beam energy increases, these functions tend toward 0 and 1, respectively. The force experienced by a generic particle inside the cylinder at a radial position $r_b$ is given by:

$$\vec{F_{sc}} = q \frac{I}{2\pi\varepsilon_0 R_b^2 \beta c \gamma^2} r_q \hat{r} \tag{2.15}$$

This simple model highlights several key features of space charge forces: they scale with the Lorentz factor as $\frac{1}{\gamma^2}$, making them significantly stronger at low beam energies; they are also directly proportional to the beam current $I$, which means they can be problematic even for very short, high-current bunches. Moreover, the behavior of the field factors indicates that direct space charge forces primarily affect the transverse beam dynamics [24].

### 2.2.4 Envelope Equation

The transverse beam dynamics and the evolution of the beam envelope, defined as $\sigma = \sqrt{\beta\varepsilon}$, are described by the envelope equation:

$$\sigma'' + \frac{\gamma'}{\gamma}\sigma' + k_{ext}^2 \sigma = \frac{K_{sc}}{\gamma^3 \sigma} + \frac{\varepsilon_{n,th}^2}{\gamma^2 \sigma^3}\,. \tag{2.16}$$

The first term accounts for the evolution of the beam slope, while the second describes envelope oscillations induced by acceleration, commonly referred to as adiabatic damping. The third term corresponds to the variation of the envelope due to external linear focusing forces. Space charge effects are included through the fourth term, which depends on $K_{sc} = \frac{\hat{I}}{2I_A}$, where $\hat{I}$ is the peak current and $I_A \sim 17\ kA$ is the Alfven current. The final term represents the envelope growth due to emittance pressure, where the thermal rms emittance is defined as $\frac{<x^2><p_x^2>}{(m_0c)^2}$ [25].
Space charge effects can induce longitudinal correlations within the bunch, causing the envelope evolution to depend on the longitudinal coordinate. These correlations may lead to emittance oscillations and are typically accounted for by slicing the beam longitudinally and applying the envelope equation to each slice individually. The resulting contribution to the emittance is defined as:

$$\varepsilon_{n,rms,corr} =< \gamma > \sqrt{< \sigma_s^2 >< \sigma_{s'}^2 > - < \sigma_s \sigma_{s'} >} \ . \tag{2.17}$$

The overall contribution is then obtained by averaging over all slices. Finally, the total normalized emittance is given by the quadrature sum of the thermal and correlated components:

$$\varepsilon_{n,rms} = \sqrt{\varepsilon_{n,th}^2 + \varepsilon_{n,rms,corr}^2} \tag{2.18}$$

### 2.2.5 Transfer matrices and linear optics

In an accelerator, it is important to describe the evolution of the particle distribution at any longitudinal point $s$ along the machine. The equations of motion in the transverse plane are defined by Hill's Equations:

$$\frac{d^2x}{ds^2} + K_x(s)x = \frac{1}{\rho}\frac{\Delta p}{p_0} \tag{2.19}$$

$$\frac{d^2y}{ds^2} + K_y(s)y = 0 \tag{2.20}$$

The parameter $K(s)$ is a parameter that depends on the magnetic elements in the beamline. In the case of only linear field changes, so assuming the presence of only dipole, for simplicity deflecting in the $x$ direction, and quadrupole optics, $K(s)$ will depend on the dipole deflection radius $\rho$ (weak focusing term) and on the quadrupole strength $k$ (weak focusing term): $K(s) = 1/\rho^2 \pm k(s)$, where the sign is chosen as the quadrupole is focusing or defocusing in the considered plane [26].
The general solution of Hill's equations can be expressed in matrix form, leading to the definition of the *transfer matrix*, which relates the transverse phase-space coordinates of a particle at an initial position $s_0$ to those at a downstream position $s$:

$$\vec{X}(s) = M(s, s_0)\,\vec{X}(s_0)\,, \tag{2.21}$$

where $\vec{X} = (x, x', y, y')^T$ and $M(s, s_0)$ is the corresponding transfer matrix. This formalism provides a compact and general method for describing the beam transport through the accelerator lattice. The analytical expressions of the transfer matrices for the most common beamline elements—drifts, quadrupoles, and dipoles—are reported in Appendix A.3, together with the derivation of the dispersion function.

## 2.3 Quadrupole Scan

The quadrupole scan is a method used to measure the beam emittance in a particle accelerator. This method involves measuring the beam size at a screen as a function of the magnetic field of an upstream quadrupole. In this way, it is possible to retrieve the beam emittance, as well as the Courant-Snyder parameters in the transverse plane where the beam size is measured.
At any point, the beam is described by its beam matrix $\Sigma_b$, which can be expressed in terms of the distribution second momentum and in terms of the Twiss parameters:

$$\Sigma_b = \begin{pmatrix} \Sigma_{11} & \Sigma_{12} \\ \Sigma_{21} & \Sigma_{22} \end{pmatrix} = \begin{pmatrix} \varepsilon\beta & -\varepsilon\alpha \\ -\varepsilon\alpha & \varepsilon\gamma \end{pmatrix} , \tag{2.22}$$

where $\varepsilon$ is the rms geometrical emittance:

$$\varepsilon = \sqrt{\Sigma_{11}\Sigma_{22} - \Sigma_{12}^2} = \sqrt{\langle x^2\rangle\langle x'^2\rangle - \langle xx'\rangle^2} \, . \tag{2.23}$$

Defining the transport matrix $M = \begin{pmatrix} R_{11} & R_{12} \\ R_{21} & R_{22} \end{pmatrix}$ from the reconstruction point to the screen, the beam matrix transforms under the relation:

$$\Sigma_{screen} = M\Sigma_0 M^T \, . \tag{2.24}$$

By expliciting the matricial product, the equation for the element $\Sigma_{11}^{screen}$ can be derived:

$$\Sigma_{11}^{screen} = \sigma_{screen}^2 = R_{11}^2\Sigma_{11} + 2R_{11}R_{12}\Sigma_{21} + R_{12}\Sigma_{22} \tag{2.25}$$

This expression indicates that the beam size at the screen is proportional to the square of the transport matrix elements $R_{11}$ and $R_{12}$, which are determined by the focusing strength of the quadrupole magnet. By measuring the beam size for different quadrupole settings, the elements of the beam matrix at the reconstruction point can be retrieved.
Considering the case depicted in Fig. 2.1 of a single quadrupole Q1 and a screen placed at a distance $d$, the transport matrix is derived by considering the quadrupole as a thin lens:

$$M_Q = \begin{pmatrix} 1 & 0 \\ Kl & 1 \end{pmatrix} , \tag{2.26}$$

where K is the quadrupole strength, related to the magnetic field $B$ and the electron momentum $p$ by the relation $K = \frac{B}{p/e}$, and $l$ is the magnetic length.

The drift of length $d$ between the quadrupole and the screen is described by the matrix:

$$M_D = \begin{pmatrix} 1 & d \\ 0 & 1 \end{pmatrix} \tag{2.27}$$

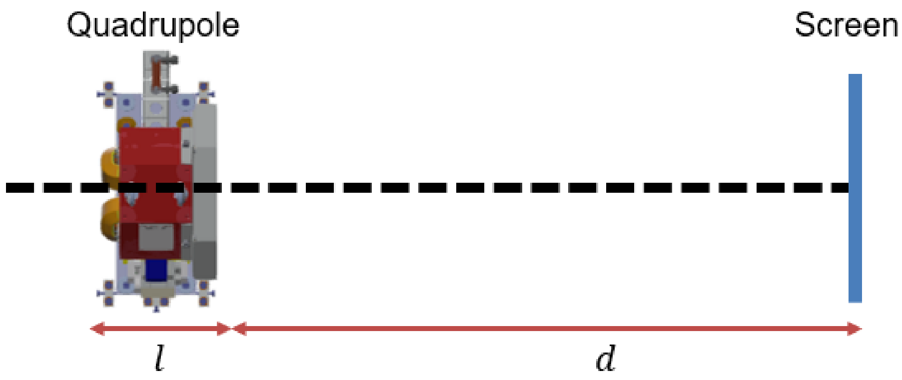


**Figure 2.1:** Basic beamline needed for the quadrupole scan, including a quadrupole of length $l$, a drift $d$ and a screen.

Therefore, the overall matrix is given by their product:

$$M = M_D M_Q = \begin{pmatrix} 1 + Kld & d \\ Kl & 1 \end{pmatrix} \tag{2.28}$$

Under the thin-lens approximation, the quadratic dependence of the beam size on the quadrupole strength can be derived from Eq. 2.25:

$$\begin{aligned} \Sigma_{11}^{\text{screen}} &= \big(1 + Kdl\big)^2 \Sigma_{11} + 2d\big(1 + Kdl\big)\Sigma_{12} + d^2\Sigma_{22} \\ &= (l^2 d^2\, \Sigma_{11})\, K^2 + \big(2ld\, \Sigma_{11} + 2ld^2\, \Sigma_{12}\big)\, K + \big(\Sigma_{11} + 2d\, \Sigma_{12} + d^2\, \Sigma_{22}\big)\,. \end{aligned} \tag{2.29}$$

By measuring $\sigma_{screen}$ with respect to the variation in quadrupole strength, the coefficients can be determined from the corresponding fit, allowing for the calculation of the emittance and Twiss parameters, according to equation 2.23 and:

$$\beta = \frac{\Sigma_{11}}{\varepsilon}, \quad \alpha = -\frac{\Sigma_{12}}{\varepsilon}, \quad \gamma = \frac{\Sigma_{22}}{\varepsilon}, \tag{2.30}$$

## 2.4 Transverse Deflection Structure

Accurate measurement of the longitudinal parameters of the electron beam is essential in accelerator physics, particularly for optimizing beam quality and performance. One of the most critical parameters is the bunch length, which can be measured using different techniques, including the Transverse Deflection Structure (TDS), a special type of radio-frequency (RF) cavity.

A TDS is an RF cavity in which the dominant component of the electromagnetic field lies in the transverse plane rather than along the beam's longitudinal (accelerating) axis. Unlike conventional accelerating cavities that impart energy to the beam, the TDS is designed to apply a transverse kick to the particles, depending on their longitudinal position within the bunch.

When an electron bunch enters the TDS at the zero-crossing phase of the RF field, the central slice of the bunch, which arrives at the phase zero point, experiences no transverse deflection. However, the head and tail of the bunch, arriving at earlier or later phases, receive transverse kicks in opposite directions due to the sinusoidal nature of the RF field. This results in the streaking of the bunch in the direction of the deflecting force, effectively converting the longitudinal (temporal) profile into a measurable transverse spatial distribution, as illustrated in Fig. 2.2.

The transverse beam size observed on a downstream screen, after passing through the TDS, depends on several factors:

- The parameters of the TDS: RF frequency, cavity length, and the integrated deflecting voltage.
- The beam properties: beam energy, emittance, and bunch length.
- The beamline optics: specifically, the transport matrix element between the TDS and the observation screen.

By accurately determining all other parameters, the bunch length can be extracted from the measured transverse beam size at the screen [27].

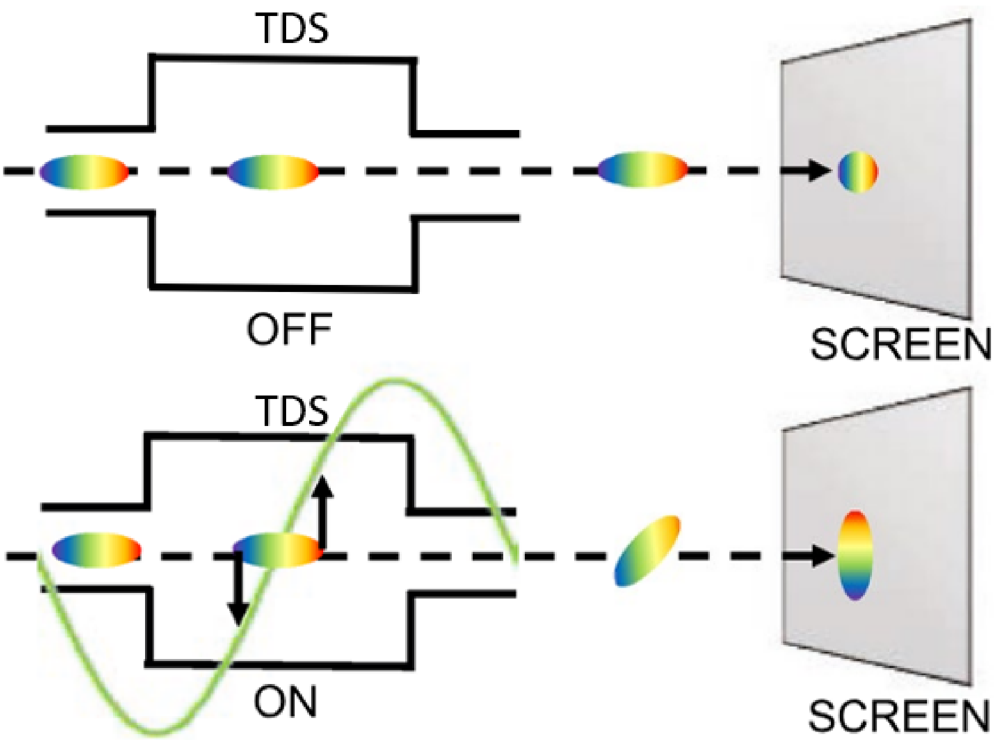


**Figure 2.2:** Transverse Deflection Structure working principle: TDS off (upward) and on (downward) [27].

From a beam dynamics perspective, the TDS can be approximated as a thin element and the transverse kick is applied at its center [13]. The electric and magnetic fields in the TDS are excited in a transverse hybrid electromagnetic mode HEM, with both transverse electric and magnetic fields [28]. In the case of vertical streaking, the Lorentz force experienced by a particle of charge $e$ is given by the components:

$$F_x = 0 \tag{2.31}$$

$$F_y = eE_0 sin(\phi_{rf} + k_{rf}\xi) \tag{2.32}$$

$$F_z = eE_0 k_{rf} y cos(\phi_{rf} + k_{rf}\xi) \tag{2.33}$$

where $E_0$ is the amplitude of an equivalent transverse deflecting field, $\phi_{rf}$ is the RF phase of the structure at the location of the beam with respect to the zero crossing, $k_{rf} = \frac{2\pi\nu_{rf}}{c}$ is the structure wave number related to the frequency $\nu_{rf}$, and $\xi = -c(t - t_0)$ is the difference between the particle position in time with respect to the reference particle position.

The deflecting voltage is given by the following equation:

$$V = V_0 sin(k_{rf}\xi + \phi_{rf}) = V_0 sin(k_{rf}\xi) cos(\phi_{rf}) + sin(\phi_{rf}) cos(k_{rf}\xi)\,, \tag{2.34}$$

where $V_0 = E_0 L$ is the integrated voltage in a structure of length $L$.
This expression can be approximated by considering that the bunch length is much smaller than the structure wavelength, leading to the condition $k_{rf}\xi << 1$. In this case, the fact that the field increases the total beam momentum by accelerating in the transverse direction is also neglected.

After the propagation in the structure, an electron of longitudinal momentum $p_0$ subject to the transverse field will acquire a momentum in the field direction, given by:

$$y' \sim y'_0 + \frac{eV_0}{p_0 c}(k_{rf}\xi \cdot cos(\phi_{rf}) + sin(\phi_{rf})) \tag{2.35}$$

At the measurement screen the particle position is related to the transfer matrix element from the center of the TDS to the screen $R_M = \sqrt{\beta\beta_0} sin\Delta\mu$, depending on the beta function at the screen $\beta$ and at the TDS $\beta_0$, and on the corresponding phase advance $\Delta\mu$.

From equation 2.35, a deflection occurs if $sin(\phi_{rf}) \neq 0$ and an angular pitch is generated along the bunch, which is linear in $\xi$ [12]. Therefore, the transverse position of a particle is given by:

$$\Delta y = \frac{eV_0 R_M}{p_0 c}(k_{RF}\xi \cdot cos(\phi_{RF}) + sin(\phi_{RF})) \tag{2.36}$$

Taking the average over all the particles, and considering the case $< \xi >= 0$, the centroid offset at the screen is:

$$\Delta y = \frac{eV_0 R_M}{p_0 c} sin(\phi_{rf})\ , \tag{2.37}$$

which can be approximated to a linear relation for small RF phase:

$$\Delta y \approx \frac{eV_0 R_M}{p_0 c} \phi_{rf}\ . \tag{2.38}$$

For an RF phase $\phi_{rf} = [0, \pi]$, there will not be a deflecting effect on the bunch centroid, but there will be a streaking effect that scales linearly with the particle longitudinal position along the bunch, characterized by the constant $K_{rfd}$:

$$K_{rfd} = \pm\frac{eV_0 k_{rf}}{p_0 c} \tag{2.39}$$

This parameter is determined by equation 2.38, performing a phase scan around the field zero crossing and measuring the consequent centroid shift with respect to the beam position when the

RF deflector is off.
The equation for the single particle position after the TDS is given by:

$$y(\xi) = y_0 + (\sqrt{\beta\beta_0} sin\Delta\mu) \cdot y_0' \pm \frac{eV_0}{p_0 c} \cdot k_{rf}\xi \cdot (\sqrt{\beta\beta_0} sin\Delta\mu)\,, \tag{2.40}$$

with the sign $\pm$ depending on the choice of the RF phase [29].

By calculating the second momentum of the distribution and considering that $< z >= 0$, $< y_0 >= 0$, $< y_0' >= 0$, the beam size at the screen can be calculated:

$$< (y- < y >)^2 >=< y_0^2 > +2R_M < y_0 y_0' > +R_M^2 < y_0'^2 > +(R_M K_{rfd})^2 < z^2 > \tag{2.41}$$

By definition, the first three terms correspond to the unstreaked beam size, while the third only depends on the effect of the TDS, so that:

$$\sigma_y^2 = \sigma_0^2 + (R_M K_{rfd})^2 \sigma_z^2 = \sigma_0^2 + (cR_M K_{rfd})^2 \sigma_t^2 \tag{2.42}$$

The shear parameter $S = R_M K_{rfd}$ is defined as the parameter which relates the measured transverse coordinate $y*$ on the screen, along the streaking direction, to the longitudinal position $t$ within the bunch $y* = S \cdot ct$ [30]. By determining $S$ from the calibration and measuring the beam size both with the deflector off and on, the equation 2.42 can be solved with respect to $\sigma_t$, allowing for the calculation of the corresponding bunch length.

To retrieve the bunch duration, the streaking effect induced by the TDS must dominate over the unstreaked term. This allows to define the longitudinal resolution of the measurement, by solving the equation for the case of equal unstreaked and streaked terms, so that:

$$R_t = \frac{\sigma_0}{Sc}\,, \tag{2.43}$$

which is the figure of merit typically used to characterize the resolution power of a TDS system.
By expressing $S$ in terms of the matrix element and measurement parameters, and by writing the unstreaked beam size in terms of the Courant-Snyder parameters, the resolution can be written as:

$$R_t = \frac{\sqrt{\varepsilon_y}}{\sqrt{\beta_{y0}}|sin\Delta\mu|} \frac{p_0}{eV_0 k_{rf}}\,, \tag{2.44}$$

where $\varepsilon_y$ is the beam geometrical emittance in the streaking plane, and $\beta_{y0}$ is the beta function at the center of the TDS. This equation simplifies in case of a simple drift between the TDS and the screen, since the matrix element becomes $R_M = \sqrt{\beta_y \beta_{y0}} |\sin\Delta\mu| = L_{drift}$, where $L_{drift}$ is the distance between the center of the TDS and the screen:

$$R_t = \frac{\sigma_0 p_0}{eV_0 k_{rf} L_{drift}}\,. \tag{2.45}$$

The main limitation to the achievable resolution comes from the transport optics after the TDS. In particular, the phase advance should ideally satisfy $|\sin\Delta\mu| \approx 1$, while the $\beta$-function at the TDS center should be as large as possible. These conditions ensure a small, unstreaked beam size at the

screen, thus providing better resolution. In the only drift case, the resolution can be improved only by decreasing the unstreaked beam size, thus limiting the obtainable resolution.
An optimal transport condition for the beam is achieved when parallel-to-point imaging conditions are fulfilled [31]. In the transverse plane $(y, y')$, this corresponds to a transfer matrix of the form:

$$\begin{pmatrix} 0 & R_{34} \\ R_{43} & R_{44} \end{pmatrix}, \tag{2.46}$$

which is equivalent to setting the phase advance to satisfy $|\sin \Delta\mu| = 1$ and the Twiss parameter in the streaking direction $\alpha_y = 0$ at the TDS entrance.

## 2.5 Energy Spectrometer

The beam energy distribution is measured by means of a spectrometer composed of quadrupoles for focusing on the screen and a magnetic dipole as in Fig. 2.4, and the beam energy is calculated by acquiring the beam position on the screen [32].

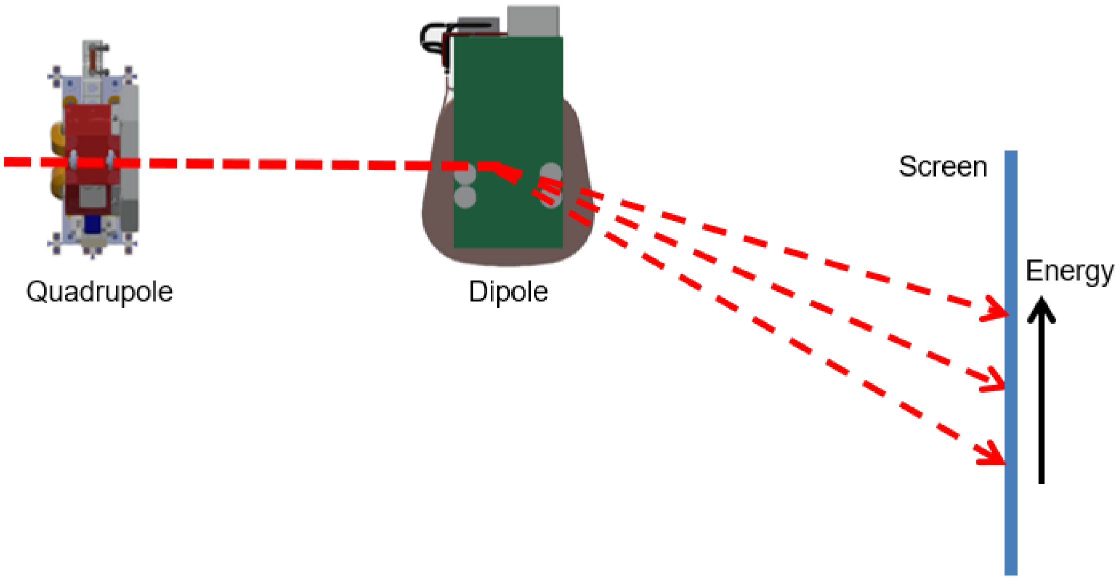


**Figure 2.3:** Layout of a simple spectrometer beamline, composed of a quadrupole to focus the beam on the screen and the dipole magnet.

The bending radius $\rho$ of a charged particle of given energy $\gamma$ in a magnetic field $B$ is given by the Larmor formula :

$$\rho = \frac{\gamma m_e \beta c}{eB} \tag{2.47}$$

With geometrical considerations, considering a curvature angle $\varphi$, the curvature radius $\rho$ can be related to the position $x_{scr}$ of the electron on the screen :

$$x_{scr} = 2Rsin^2(\frac{\varphi}{2}) + dtg(\varphi) \tag{2.48}$$

In Fig. 2.4, the geometrical scheme of the electron trajectory is reported.

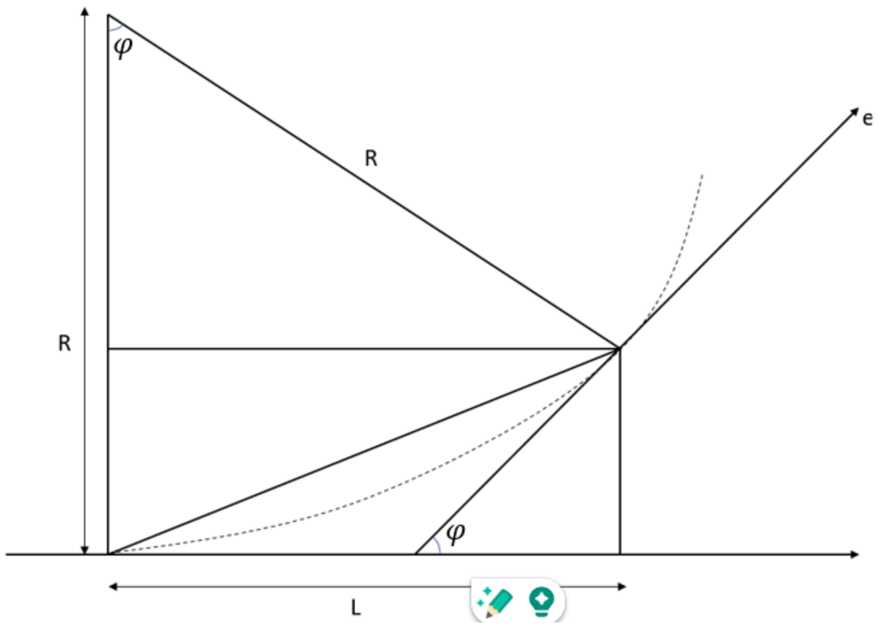


**Figure 2.4:** Electron trajectory passing through the dipole. The dotted curve represents the Larmor orbit of the electron(with radius R) in the magnetic field; the axis 'e' is the electron direction when out of the dipole.

The measured beam size at the screen will take into account different contributions, according to :

$$\sigma_M^2 = \sigma_R^2 + \frac{E_0}{E}\sigma_B^2 + \frac{D^2}{E^2}\sigma_E^2 \ , \tag{2.49}$$

where $\sigma_R$ is the screen resolution, $\sigma_B^2 = \beta_x \varepsilon_N$ is the natural beam size, $D$ is the dispersion, $E_0$ and $E$ are the reference and beam energy. In this equation, the term depending on $\beta_x \varepsilon_n$ emphasises the importance of focusing the beam onto the screen to perform the measurement, as the energy resolution improves when the dispersion contribution is larger than the natural beam size.

**Slice energy spread** Relevant in FEL operation is also the measurement of the slice energy spread, since the properties of the emitted radiation depends on the characteristics of the slices along the bunch. To measure the slice energy spread the measurement at the spectrometer is complemented with a transverse deflection cavity to longitudinally streak the beam in the non dispersive plane. Since the TDS introduces a contribution to the beam energy, as described in equation 2.49, the measured beam size becomes:

$$\sigma_M^2 = \sigma_R^2 + \frac{E_0}{E}\sigma_B^2 + \frac{D^2}{E^2}\sigma_E^2 + \frac{(DeVk)^2 E_0}{E^3}\sigma_I^2 \ , \tag{2.50}$$

where $\sigma_I^2 = \frac{\varepsilon_N(\beta_y^0 + 0.25L^2\gamma_y^0 - L\alpha_y^0)}{\gamma_0}$. $\beta_y^0$, $\alpha_y^0$ and $\gamma_y^0$ are the Twiss parameters in the deflecting plane, and $L$, $V$, $k$ are the TDS parameters (respectively TDS length, voltage, and wavenumber). The term corresponding to the contribution of the beam energy spread through the dispersion is:

$$\sigma_M \approx \frac{D}{E}\sigma_E \ . \tag{2.51}$$

Therefore, it is possible to define the resolution in the measurement as :

$$R_{\sigma_E} = \frac{E}{D}\sqrt{\sigma_R^2 + \frac{E_0}{E}\sigma_B^2 + \frac{(DeVk)^2 E_0}{E^3}\sigma_I^2} \tag{2.52}$$

Given this equation, methods to improve the accuracy of the measurements by characterizing the additional terms in the resolution have been proposed. The first method involves measuring the beam for different energies at constant deflecting voltages and vice versa, allowing for the estimation of those terms by fitting the obtained data [33]. In [34] a variant is proposed by keeping constant the shear parameters and adjusting the voltage proportionally to the beam energy $V(E) = \frac{V_0}{E_0}E$. In this case the polynomial is reduced from third to second order :

$$\sigma_M^2 = \sigma_R^2 + \frac{E_0}{E}\sigma_{BI}^2 + \frac{D^2}{E^2}\sigma_E^2 \tag{2.53}$$

where $\sigma_{BI}^2 = \sigma_B^2 + (DK_0\sigma_I)^2$. However, a limitation in this method arises from the necessity of matching the optics for every energy of the scan. Another approach to avoid this problem is to vary the dispersion rather than the beam energy. In the first step, the voltage is changed while keeping other factors constant to evaluate the quadratic relation :

$$\sigma_M^2 = A_V + B_V\ V^2\ , \tag{2.54}$$

where $A_V$ represents the contribution independent of the deflecting voltage, mainly due to the beam size and instrumental resolution, while $B_V$ accounts for the dependence on the deflecting voltage and is proportional to the squared shear parameter of the TDS. In the second step, the dispersion in the beamline is changed, so that the equation to evaluate is :

$$\sigma_M^2 = A_D + B_D\ D^2\ , \tag{2.55}$$

where $A_D$ represents the term independent of the dispersion, and $B_D$ is proportional to the squared relative energy spread of the beam. From the fit of these two relations, all the terms of equation 2.50 can be determined.

## 2.6 Simulation Codes

The diagnostics studies will be carried out by simulating the measurement employing three different simulation codes with different purposes: ELEGANT (Electron Generation and Tracking), MADX (Methodical Accelerator Design), and ASTRA (A Space Charge Tracking Algorithm).

### 2.6.1 ELEGANT

ELEGANT is a tracking code capable of tracking particles in Linac and circular accelerators, including the description and integration of all the standard elements of a beam line. The elements of the beam line are referred to a coordinate system $(x, y, s)$, where the longitudinal coordinate $s$ is defined as the total, equivalent distance travelled by the single particle. All the particles are considered to be at the same position $s$ and the equations of motion are integrated with a step

$s \to s + ds$, moving the bunch element by element. Each particle is identified by the coordinates $(x, x', y, y', t, E)$. The code capabilities include 6-D tracking using matrices up to third order, canonical integration, and numerical integration [35]. ELEGANT also implements an optimization algorithm to calculate the elements' parameters, achieving the desired parameters along the machine. This can be done with either a single particle or the entire bunch. However, the code is not suitable for considering space-charge effects, and it does not include the implementation of 3D maps describing the electromagnetic field of a beam line element. These reasons make it necessary to use a different simulation code like ASTRA.

### 2.6.2 ASTRA

ASTRA is a tracking code employed for the design of Linacs and Photo-Injector systems. It enables tracking the particles under the influence of internal and external fields, thereby considering the space charge fields of the particle distribution. The beamline elements and the particle beam are referred to a global coordinate system, and each particle is defined by the coordinates $(x, p_x, y, p_y, z, p_z)$, where the longitudinal coordinates $z, p_z$ are referred to a reference particle. The tracking is based on a non-adaptive Runge-Kutta integration of $4^{th}$ order, so that all particles are considered to be at the same time $t$, and the equations of motion are integrated in time with a step $t \to t + dt$ [36]. The main feature for the diagnostics studies is the capability of implementing 3D maps of electro-magnetic fields, as the fields in a transverse deflection cavity, to study the beam dynamics and the interaction of the beam with a map generated by a simulation code like HFSS. The field map of a travelling wave structure is inserted as a superposition of real and imaginary parts, represented by two standing waves shifted by $\pi/2$ degrees. Therefore, each map is composed of six files containing the real and imaginary components of electric and magnetic fields referred to the global reference system.

### 2.6.3 MADX

MADX is a single-particle tracking code used as a tool for charged optics design and studies in alternating-gradient accelerators and beam lines. It shares the same description of the bunch with ELEGANT. It allows for the calculation of optics parameters, the design of a lattice, and the tracking of particle positions within it. In this work, the primary application of the code has been the optimization and calculation of the magnetic strength of the optics in the beamline to achieve the desired parameters at a specified point in the machine [37].

# Chapter 3

# Polarizable X Band Transverse Deflection Structure

In this chapter, the studies performed to investigate the Polarizable X-Band Transverse Deflection Structure (PolariX TDS) design and implementation in the beam dynamics simulations reported in the thesis are presented. The PolariX TDS is a system unique in its capability to select the streaking direction by varying the polarization of the input electric field. This feature enables tomography of the beam by capturing images at different streaking angles, which can then be used to reconstruct the 3D charge distribution of the bunch. When combined with quadrupole scans and energy measurements obtained with a dipole spectrometer placed after the TDS, it enables complete 6D characterization of the beam. Moreover, the ability to adjust the streaking direction enables slice emittance measurements in various transverse planes using the same transverse deflecting structure [38]. The operation principle of a transverse deflecting structure relies on the interaction between the electron bunch and the time-varying RF electromagnetic fields. When the bunch passes through the cavity at the zero-crossing of the longitudinal electric field, the transverse components of the RF field impart a time-correlated transverse momentum kick to the electrons. This maps the longitudinal bunch profile into a transverse spatial distribution observable on a downstream screen. In conventional TDS designs, the streaking direction is fixed by the cavity geometry, limiting diagnostics to a single transverse plane unless multiple devices are installed. The PolariX TDS overcomes this limitation by utilizing a dual-feed coupler system and a carefully optimized cavity design that enables the rotation of the polarization of the input RF power. This capability enables the streaking field to be oriented along any arbitrary transverse axis, offering unprecedented flexibility in beam characterization and greatly expanding the diagnostic potential compared to standard devices. Within the framework of this thesis, particular emphasis has been placed on the electromagnetic field maps of the PolariX TDS and their implementation in beam dynamics simulations. The analysis begins with a description of the device's main components and the RF system that enables polarization control. Subsequently, a detailed investigation of the field distributions, both in amplitude and phase, is presented to validate the cavity design and assess its implications for bunch diagnostics. Numerical studies of the 3D field maps have been performed, and the results have been compared with single-particle tracking simulations to ensure consistency with theoretical expectations. Special attention has also been devoted to the role of the input and output couplers, whose influence on the effective kick and on the beam parameters has been quantified. By comparing simulations with and without couplers, the residual effects induced by these components have been identified and characterized. These studies confirm the feasibility and robustness of the PolariX TDS concept, providing a foundation for realistic simulations of bunch diagnostics based on this device. The outcomes are of particular relevance in the context of the EuPRAXIA@SPARC_LAB research program, where advanced diagnostics are essential for the development and operation of high-brightness plasma-based accelerators.

This chapter is organized as follows. Section 3.1 introduces the theoretical concepts of RF cavities that are relevant for the discussion developed throughout the chapter. Section 3.2 describes the PolariX TDS, outlining its main components and RF characteristics. Section 3.3 focuses on the field maps of the PolariX TDS, presenting both their electromagnetic features and the corresponding beam dynamics effects. Section 3.4 is dedicated to the design and beam-dynamics tests of the 50-cell deflector, which is employed in the high-energy diagnostics station of EuPRAXIA. Finally, Section 3.5 summarizes the results and compares the two TDS configurations (50-cell and 96-cell), providing a concluding overview of the chapter.

## 3.1 Fundamentals of Radio-Frequency Structures

Radio-frequency (RF) structures are fundamental components of particle accelerators. Transverse Deflecting Structures (TDS) are a special class of radio-frequency cavities used as beam diagnostic devices, exploiting a time-dependent transverse electromagnetic field to map the longitudinal bunch profile onto the transverse plane. In RF systems, the electromagnetic fields are confined within metallic resonant cavities powered by a time-varying external source. The behavior of these fields within the cavity is governed by Maxwell's equations, subject to boundary conditions determined by the cavity's geometry and material properties. In an ideal cavity—assumed to be perfectly conducting and lossless—the electromagnetic fields form standing wave modes, each characterized by a specific resonant frequency, spatial distribution, and polarization type (TE, TM, or TEM). The set of admissible solutions of Maxwell's equations describing the electromagnetic fields depends on the cavity geometry. A well-known example is the cylindrical "pill-box" cavity, which supports the fundamental $TM_{01}$ mode, commonly employed for longitudinal acceleration.
When multiple cavity cells are coupled together, they form a periodic structure in which electromagnetic modes interact, resulting in passbands of allowed propagation. These coupled modes are characterized by a specific phase advance per cell, typically denoted by $\phi$, which defines the relative phase shift of the RF field from one cell to the next. In the 0 mode, all cells oscillate in phase. In the $\pi$ mode, there is a 180° phase shift between adjacent cells, resulting in a field that reverses sign from one cell to the next. In the $\pi/2$ mode, the fields in non-adjacent cells are 180° out of phase, while the intermediate cells experience zero field. This leads to a periodic configuration in which only alternate cells are active, and the others serve as coupling cells [39].
A cavity in which the electromagnetic wave propagates along a specially designed guide such that the phase velocity of the wave matches the velocity of the particles—allowing continuous energy transfer to the beam—is referred to as a travelling wave (TW) structure. In this configuration, RF power is fed into one end of the cavity via an input coupler and propagates toward the opposite end. The wave can travel in the same direction as the beam or in the opposite direction, as

in backward-travelling wave structures. An output coupler located at the downstream end of the cavity is connected to a matched load, which absorbs the incident RF power without generating reflections. In RF structures, the electromagnetic wave propagates with a specific phase velocity $v_{ph}$, which defines the speed at which the phase of the wave—such as the crest of the electric field—travels along the structure. This quantity is given by:

$$v_{ph} = \frac{\omega}{k}\,, \tag{3.1}$$

where $\omega$ is the angular frequency of the wave, and $k$ is the wavenumber. The wave propagates as a group, formed by the superposition of multiple frequency and wavenumber components. The envelope of this wave packet moves with the so-called group velocity, which represents the speed at which energy is transported through the structure and is given by:

$$v_g = \frac{d\omega}{dk}\,. \tag{3.2}$$

In the simple case of a constant cross-section waveguide, the phase velocity is always greater than the speed of light. As a result, the electromagnetic wave cannot remain in synchronism with the particle beam. To reduce the phase velocity and enable energy transfer to the beam, the waveguide is periodically loaded with irises, creating a spatially periodic structure that modifies wave propagation. As illustrated in Fig. 3.1, the dispersion curve of a smooth circular waveguide lies entirely above the line corresponding to $v_{ph} = c$, indicating that synchronism is not possible (Fig. 3.1 (a)). The introduction of irises alters the dispersion relation, allowing certain modes to match the velocity of the particle beam and thus enabling effective acceleration (Fig. 3.1 (b)).

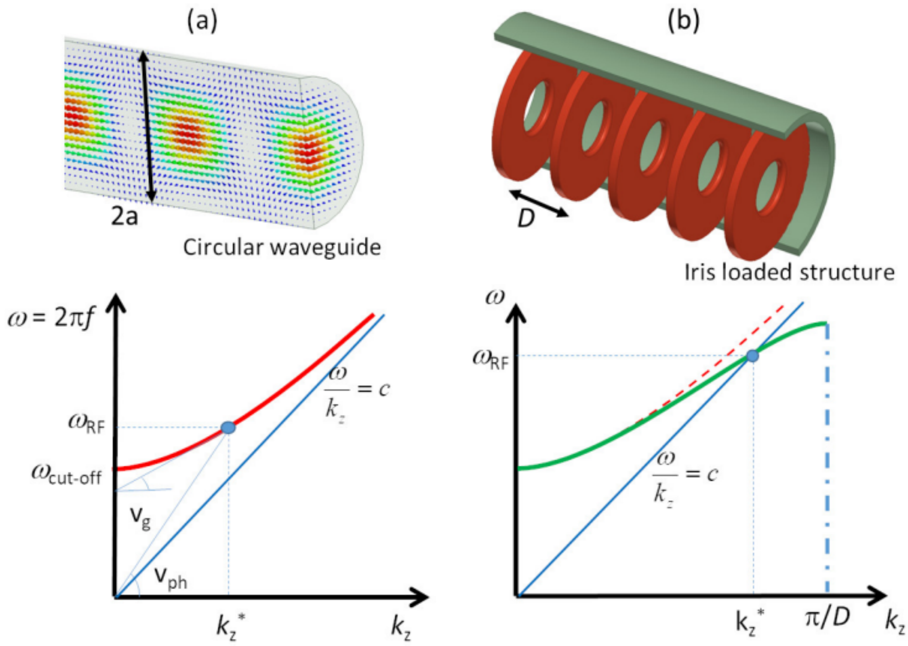


**Figure 3.1:** Comparison between a circular waveguide and an iris loaded structure, in the bottom are shown the dispersion curves in the two cavities [40].

In a purely periodic structure, composed of a sequence of identical cells, known as a "constant impedance structure", both the RF power flux and the amplitude of the accelerating field decrease

exponentially along the structure due to power dissipation. Alternatively, the iris aperture can be progressively reduced along the structure, compensating for the field attenuation by increasing the stored energy in each successive cell. This results in a gradual decrease of the group velocity and maintains a constant accelerating field throughout the structure. Such a configuration is referred to as a "constant gradient structure" [40].
To characterize an RF structure, a figure of merit is introduced, which is the Shunt impedance $R_s$, and is given by:

$$R_s = \frac{V_{acc}^2}{p_{diss}} \quad . \tag{3.3}$$

This parameter quantifies the efficiency of the cavity: the higher its value, the greater the achievable accelerating voltage $V_{acc}$ for a given level of dissipated power $p_{diss}$.

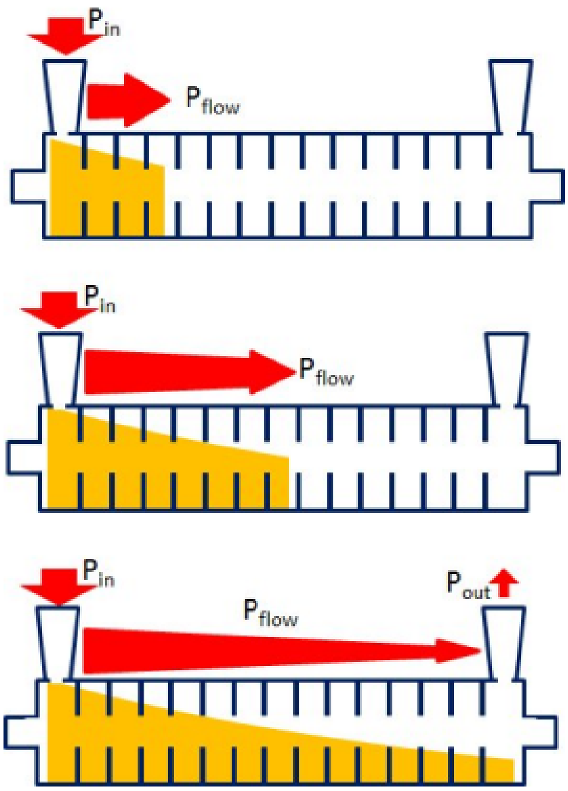


**Figure 3.2:** Power flowing in a TW structure, showing the exponential decay along the cells [40].

As shown in Fig. 3.2, power flowing in a TW structure decays exponentially inside the cavity due to RF losses in the metallic walls. This behavior is characterized by the attenuation constant $\alpha$ $[m^{-1}]$, defined as:

$$\alpha = \frac{p_{diss}}{2P_F} = -\frac{dP_F/dz}{2P_F} \,, \tag{3.4}$$

where $P_F$ is the power flowing into the structure and $p_{diss}$ is the dissipated power per unit length. The RF power takes a finite time, denoted as the filling time $\tau_F$, to propagate from the input coupler to the end of a section of length $L$. This time is given by:

$$\tau_F = \frac{L}{v_g} \quad . \tag{3.5}$$

## 3.2 PolariX Radio-Frequency System

The Radio-Frequency system is designed to generate an electromagnetic field with variable polarization inside the deflecting structure. The key components enabling this polarization control are illustrated in Fig. 3.3. The input RF pulse coming from an RF power source is injected into the system through a port connected to a 3-dB E-Hybrid component, which splits the input wave into two output signals of equal amplitude and fixed phase relationship. The fourth port of the E-Hybrid is connected to a vacuum pumping system, which maintains high-vacuum conditions inside the waveguide. A variable phase shifter is installed in one of the waveguide arms to introduce a controllable phase delay between the two RF signals. These phase-shifted signals are then recombined using a circular waveguide $TE_{11}$ mode launcher, the E-Rotator, producing an RF wave with a resultant polarization determined by the phase difference between the two waves. The mode is launched into the TDS, which supports both degenerate $TM_{110}$-like dipole modes, and thus can operate at any polarization angle. The output RF signal from the TDS is split again using another E-Rotator into two output waveguides. The two resulting waves are directed into RF loads, which absorb the residual power, preventing reflections and ensuring safe operation of the system [41]. Each component is described in more detail in the following sections.

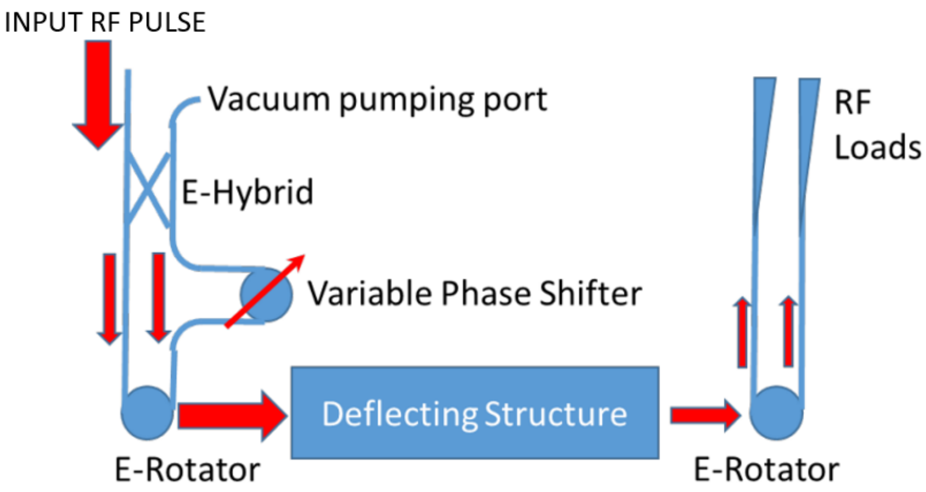


**Figure 3.3:** Layout of the RF system of the PolariX TDS [42].

### 3.2.1 E-Hybrid

The E-hybrid is a type of hybrid component used for combining and splitting RF signals. The term "hybrid" refers to the splitting of RF power in the plane tangential to the electric field.
It consists of four ports, as shown in Fig. 3.4, implemented using standard WR90 waveguides, which operate in the frequency range of 8.2 GHz to 12.2 GHz.
In this configuration, input power is applied at port 1 and is equally split between ports 3 and 4. Port 2 remains isolated (assuming no reflections return from ports 3 and 4) and is typically used for vacuum pumping [42].

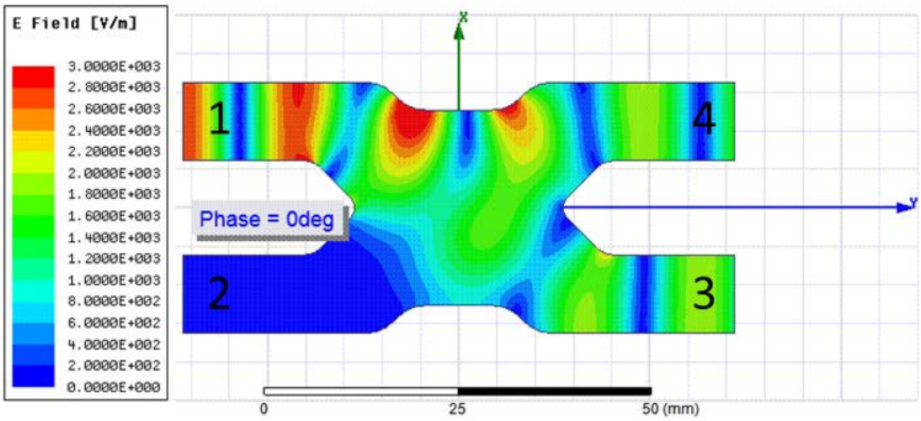


**Figure 3.4:** E-Hybrid Electric Field Distribution for 1 W input power, where the power is split between ports 3 and 4 [42].

### 3.2.2 E-Rotator

The E-Rotator is a type of hybrid component with two rectangular and one circular waveguide, designed starting from the E-Hybrid, by circuiting the forward branches 3 and 4 and attaching a circular waveguide in the middle, as shown in Fig. 3.5. When the power is injected from port 1, it results in a circularly polarized $TE_{11}$ mode at port 3, rotating in the negative direction (clockwise). Injecting power from port 2 results in a mode rotating in the positive direction (anti-clockwise). The rotating mode at port 3 is a superposition of two degenerate $TE_{11}$ circular waveguide modes with vertical and horizontal polarization and a 90-degree phase shift between the two components.

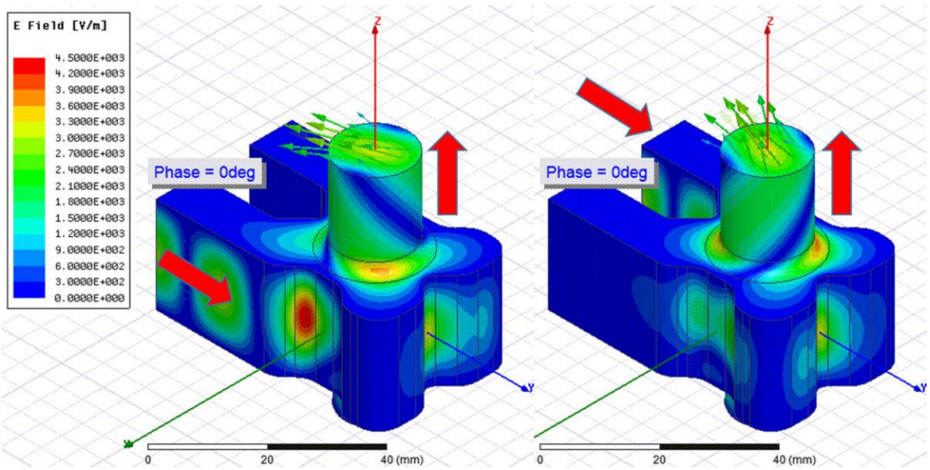


**Figure 3.5:** E-Rotator Electric Field Distribution for 1 W input power, when the input power is injected from port 1 (left) and port 2 (right), giving a circularly polarized mode at port 3 respectively rotating in negative (clockwise) and positive (anti-clockwise) direction [42].

Injecting the same amount of power from the two input ports results in a linearly polarized mode at port 3, as in Fig. 3.6. The orientation of the output mode is determined by the phase difference between the waves injected from the two ports. A 180-degree phase difference leads to a change of 90 degrees in the input wave polarization from horizontal (input at the E-Hybrid) to vertical [42].

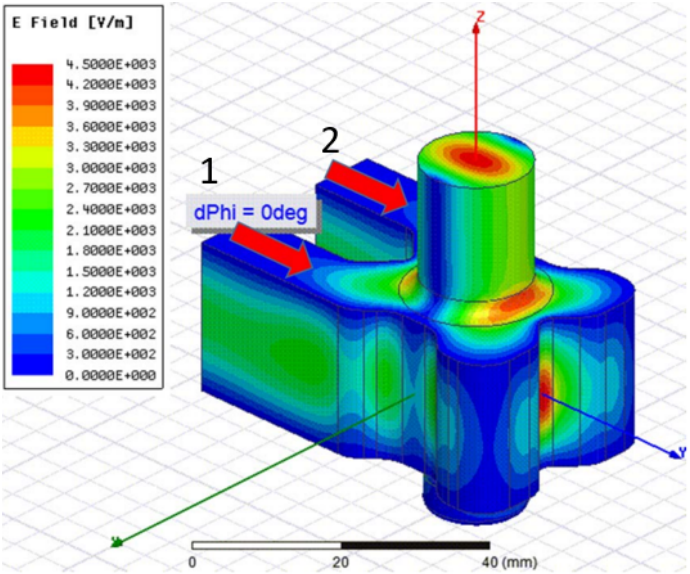


**Figure 3.6:** E-Rotator Electric Field Distribution for 1 W input power, when the input power is injected from both ports 1 and 2, giving a linearly polarized mode at port 3 [42].

### 3.2.3 Phase Shifter

To change the phase of the RF wave in one arm, a variable phase shifter is inserted. This device is obtained by combining the E-rotator with a movable short circuit attached to the circular waveguide, as shown in Fig. 3.7. Applying the input signal to port 1 of the E-rotator and terminating the circular waveguide with a short circuit will cause a full reflection of the circularly polarized wave back to the device, with a signal propagating to port 2. The phase shifter is composed of a piston that implies a phase variation of 20 degrees/mm of piston displacement, and by moving the position of the short circuit, it will change the RF-phase of the output signal without causing any reflection back to the input port. The piston of the movable circuit features a compact choke integrated at its end, which suppresses the penetration of the field into the gap between the piston and the circular waveguide wall.

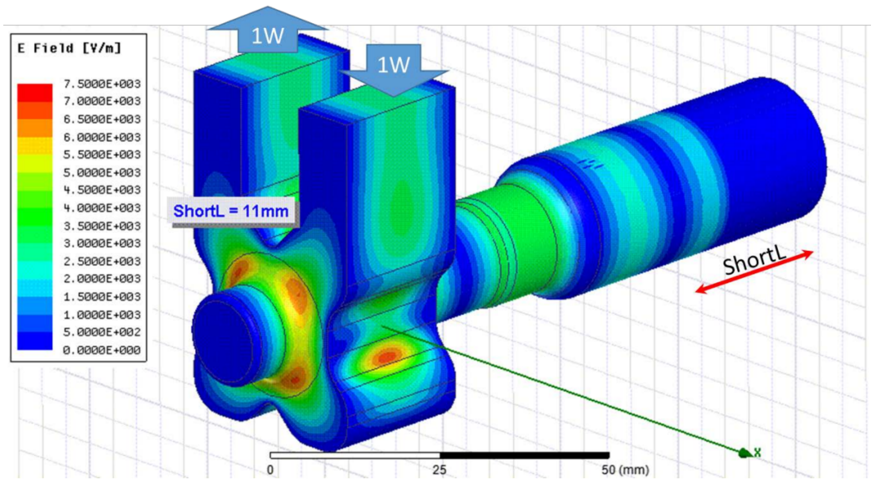


**Figure 3.7:** Variable Phase Shifter geometry and Electric Field Distribution for 1 W of input power, composed by the E-Rotator and the movable circuit [42].

### 3.2.4 Polarix TDS RF Design

The PolariX TDS is a constant impedance structure with a circular disk-loaded waveguide. It operates at $TM_{110}$-like mode in the backward traveling regime. The chosen cell design is azimuthally symmetric, allowing it to support the two input polarizations and to maintain the degeneracy of the $TM_{110}$-like modes, while the cell length is designed to have a phase advance per cell of 120 deg [38]. The input power is split into two equal parts and then combined with a 90-degree phase difference in a dual-feed coupler (E-rotator) to launch it into the corrugated waveguide. The power absorbed in the corrugations generates heat on the outer walls, which is cooled by a water system placed around the structure. The cooling water temperature can be regulated to tune the structure's resonance frequency.

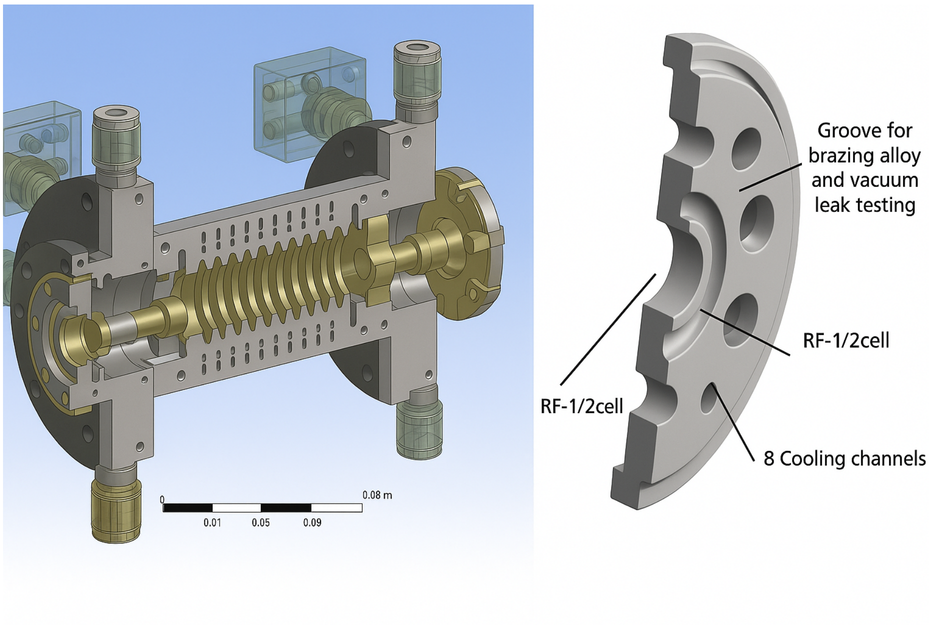


**Figure 3.8:** Mechanical drawing of a PolariX TDS structure of a few cells, with the disk composing the cell represented on the right [41].

The key parameters of the structure are reported in Table 3.1 [43].

| **TDS Design Parameters** | | |
|---|---|---|
| Nominal Frequency | 11.9952 | $GHz$ |
| Nominal Temperature | 30 | $^{\circ}C$ |
| Phase Advance per Cell | 120 | $deg$ |
| Iris Radius | 4 | $mm$ |
| Iris Thickness | 2.6 | $mm$ |
| Group Velocity | $-2.666$ | $\%c$ |
| Quality Factor | 6490 | |
| Shunt Impedance | 50 | $M\Omega$ |
| Cell Length | 8.3 | $mm$ |
| Power-to-Voltage Ratio | 6.1 | $MV/MW^{1/2}$ |

**Table 3.1:** Nominal Parameters of the PolariX TDS Structure.

## 3.3 PolariX Field Maps Studies

The PolariX TDS is central in the simulations presented in this thesis work. To simulate the beam dynamics with high accuracy, a precise representation of the electromagnetic fields within the cavity is essential. This section focuses on the implementation and use of 3D field maps, which provide a realistic model of the electromagnetic fields in the PolariX TDS, thereby surpassing the limitations of idealized analytical models and allowing for the investigation of the effects of the modular RF design on beam dynamics. In particular, the modular configuration enables adaptation to different beam energies by varying the number of cells, and the 50-cell version used at low energy required a more detailed investigation of its impact on the beam dynamics. The electromagnetic field maps used in the simulations are generated through 3D electromagnetic simulations conducted with HFSS software. Ansys HFSS (High-Frequency Structure Simulator) is a commercial finite element method (FEM) solver for electromagnetic fields. It is widely used in accelerator physics and RF engineering for the design and analysis of high-frequency components, including cavities, waveguides, and antennas. HFSS allows the computation of full 3D field distributions by solving Maxwell's equations under realistic boundary conditions [44]. The resulting data represent the electric and magnetic field components on a 3D grid spanning the entire volume of a single or multiple cells. Each point in the grid contains the real and imaginary parts of the electric $(E_x, E_y, E_z)$ and magnetic $(H_x, H_y, H_z)$ field components. The general considerations will be performed on a field map reproducing a 96-cell structure, with a total length of 96 cm, in which the total space occupied by the cells is 80 cm. The choice to study this specific structure is due to its existing use in activities at operating accelerators, which means it has been already tested and is ready for daily operations. The map has been generated for a vertical streaking configuration and an input power of 1 W, assuming a power-to-voltage ratio of 6.1 MV/MW$^{1/2}$ corresponding to the full 120-cell structure. This value is obtained by extending the field map to the complete structure length and is assumed to scale linearly with the TDS length. Figures 3.9 and 3.10 show the module and phase of respectively electric and magnetic fields contributing to the vertical streaking force, i.e., $E$ field along $y$ and $B$ field along $x$. The on-axis module grows along $z$, highlighting the backward traveling characteristics of the structure. Respectively, the phase velocity is negative, so the phase decreases along $z$.

**Field Phase** The unwrapped phase of the fields contributing to the vertical streaking, $E_y$ and $B_x$, has been analyzed along the structure axis and reported in Fig. 3.11. A linear fit of the phase evolution with respect to $z$ yields a slope of $k_\phi = -251$ rad/m, corresponding to a guiding wavelength of $\lambda_g = 2.50$ cm and a phase velocity $v_{\mathrm{ph}}/c = 1.001$. The negative slope confirms the

**Table 3.2:** A table that fits into a single column of a two-column layout. Note that REVTEX 4 adjusts the intercolumn spacing so that the table fills the entire width of the column. Table captions are numbered automatically. This table illustrates left-, center-, decimal- and right-aligned columns, along with the use of the `ruledtabular` environment which sets the Scotch (double) rules above and below the alignment, per APS style.

| Left[1] | Centered[2] | Decimal | Right |
|---|---|---|---|
| 1 | 2 | 3.001 | 4 |
| 10 | 20 | 30 | 40 |
| 100 | 200 | 300.0 | 400 |

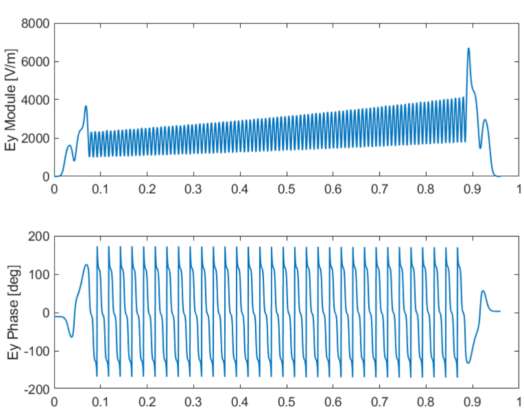


**Figure 3.9:** On-axis electric field along $y$: magnitude (upper plot) and phase (lower plot) vs longitudinal position (1 W input power).

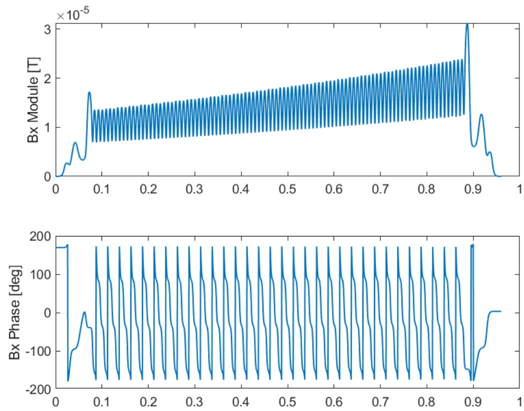


**Figure 3.10:** On-axis magnetic field along $x$: magnitude (upper plot) and phase (lower plot) vs longitudinal position (1 W input power).

backward-travelling nature of the PolariX structure, as expected from the RF design. The quality of the linear fit is very high, with $R^2 = 0.994$ and residual fluctuations below 0.26 rad, indicating that the traveling-wave behavior is well reproduced in the field map. The comparison between the unwrapped phases of $E_y$ and $B_x$ shows identical slopes, and therefore consistent values of $\lambda_g$ and $v_{ph}$, as required by Maxwell's equations. The phase difference $\Delta\phi = \phi_{E_y} - \phi_{B_x}$ remains close to 90° in the regular cells (mean value $\Delta\phi \simeq 90°$), confirming the quadrature relation between the transverse electric and magnetic fields. Deviations from this value are observed only in the input and output coupler regions, where the field composition departs from the ideal travelling-wave pattern. This demonstrates that either $E_y$ or $B_x$ can be reliably used for the determination of the phase velocity of the structure.

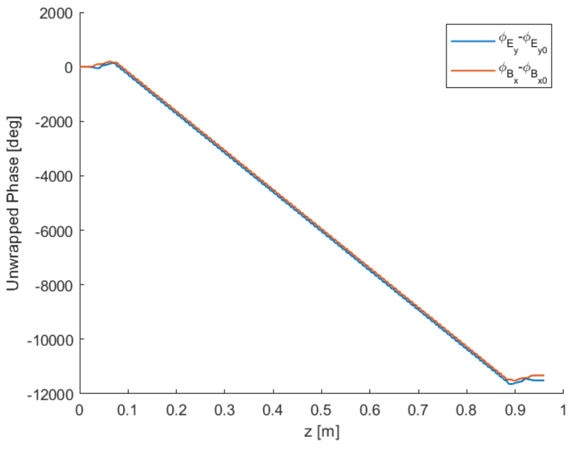


**Figure 3.11:** Unwrapped phase of the streaking fields along the PolariX TDS axis.The phases of $E_y$ and $B_x$ exhibit identical slopes, yielding consistent values of guiding wavelength and phase velocity. The negative slope confirms the backward-travelling nature of the structure. The two curves are offset by approximately 90 deg, in agreement with the expected quadrature relation between electric and magnetic fields; deviations occur only in the input and output coupler regions.

**Field Integral** The integrated transverse voltage $V_0$ of the PolariX TDS has been obtained by numerically integrating the vertical Lorentz force along the structure axis. For an input power of 1 W the result is $V_0 = 5.24$ kV, which is in agreement with the expected voltage-to-power scaling factor $D = 5.24$ MV/MW$^{1/2}$ derived from the RF design of the original 120-cell PolariX rescaled with respect to the 96-cell cavity length. This confirms the consistency of the imported field map with the analytical parameters of the cavity. To further validate the field map, a single-particle tracking simulation was performed at the RF zero-crossing, with an integrated voltage of 20 MV. Fig. 3.12 reports the transverse force $F_y$, the vertical momentum $\Delta p_y$, and the resulting vertical offset $\Delta y$ of the reference particle along the cavity axis.Although the RF phase is nominally set at the zero-crossing, the cumulative integration of the Lorentz force along the structure can result in a non-zero net transverse effect. This behavior can be attributed to residual field asymmetries and to the presence of longitudinal field components, particularly in the regions affected by the couplers.

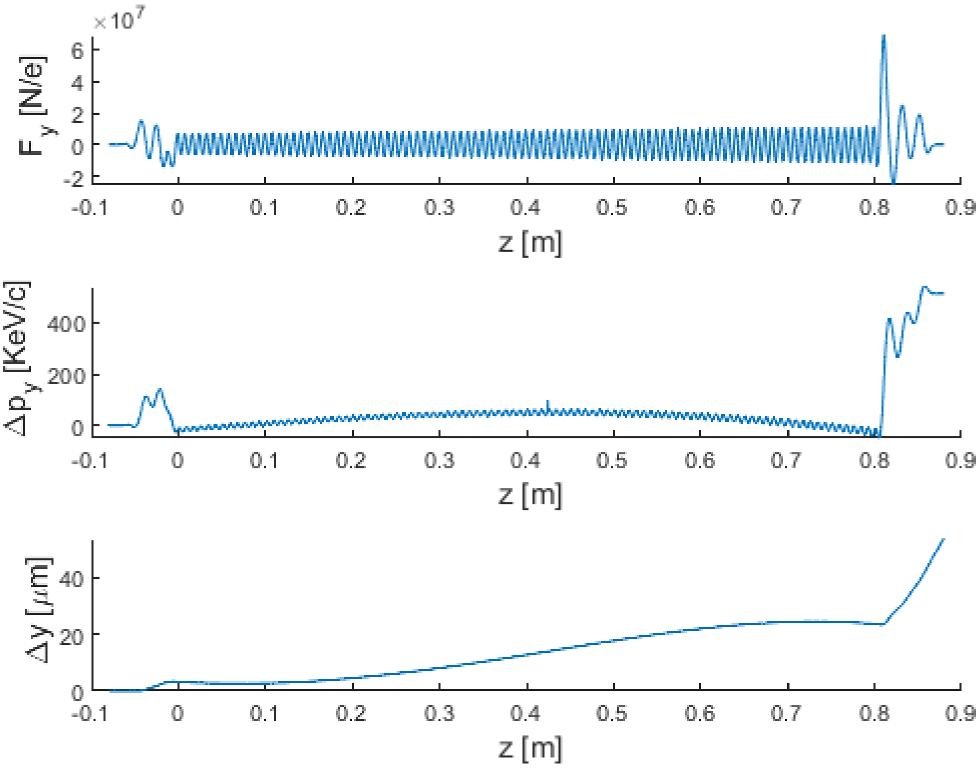


**Figure 3.12:** Tracking of a reference particle at the RF zero-crossing with 20 MV integrated voltage, in the 96-cells structure. Top: transverse Lorentz force $F_y$. Middle: vertical momentum deviation $\Delta p_y$. Bottom: vertical displacement $\Delta y$. The periodic force integrates to a net momentum gain, resulting in a steady vertical offset consistent with the streaking mechanism of the PolariX TDS.

### 3.3.1 Beam Dynamics Studies on the 96-cells PolariX TDS

To validate the imported 3D field maps of the PolariX TDS, beam dynamics studies were performed with the tracking code ASTRA. The maps obtained from HFSS were implemented in ASTRA as external electromagnetic field maps, allowing the direct tracking of particles through the realistic distribution of $E$ and $B$ fields, including the coupler regions. This approach enables a direct com-

parison between the theoretical expectations of transverse deflecting structures and the numerical results from the imported fields.
As a benchmark, an ideal Gaussian bunch with a nominal energy of 1 GeV was used. The bunch is defined with a temporal rms length of $\sigma_t = 17$ fs, a transverse rms size of $\sigma_{x,y} = 100\ \mu m$ at the beamline entrance, and normalized emittances of $\varepsilon_{n,x,y} = 1.2\ \mu m$. All the beam parameters at the beamline entrance are reported in Table 3.3.

| **Beam Parameters** | | |
|---|---|---|
| Charge | 30 | $pC$ |
| Energy | 1 | $GeV$ |
| $\delta$ Energy Spread | $\sim 10^{-4}$ | |
| $\sigma_{x,y}$ (Input) | 100 | $\mu m$ |
| $\sigma_x$ (Screen) | 50 | $\mu m$ |
| $\sigma_y$ (Screen) | 24 | $\mu m$ |
| $\sigma_t$ | 17 | $fs$ |
| $\varepsilon_{n_{x,y}}$ | 1.2 | $\mu m$ |

**Table 3.3:** Parameters of the ideal beam used in the 96-cells structure field maps studies.

The beamline considered for the test, as reported in Fig. 3.13, includes a set of matching quadrupoles, the PolariX TDS of 96 cm, and a downstream imaging screen placed after a drift of length $L_d \sim 3.3$ m. The dipole is set off in the presented simulations.

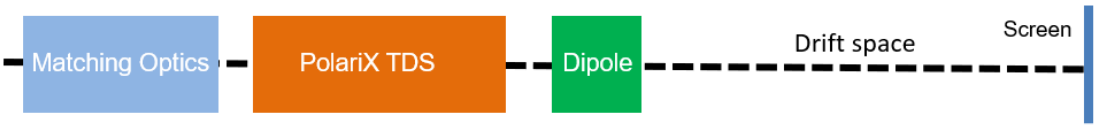


**Figure 3.13:** Schematic layout of the test beamline for the PolariX TDS studies. Quadrupoles are used to match the beam to the TDS and the screen, and a drift length of $\sim 3\ m$ allows for a relevant streaking effect to be seen in the screen.

The purpose of these simulations is twofold:

1. verify that the field maps reproduce the expected streaking behaviour and allow for the reconstruction of the temporal bunch profile according to the theoretical shear parameter;
2. assess the extent to which the non-ideal field components present in the coupler regions affect the beam dynamics, in particular the longitudinal phase space and the output energy distribution.

Collective effects such as space charge and coherent synchrotron radiation were neglected, as the goal of these studies is to isolate the impact of the electromagnetic fields of the TDS. To achieve this, three complementary sets of simulations have been performed:

1. TDS switched off (baseline, pure drift through the structure);
2. TDS switched on at the RF zero-crossing with the full 96-cell map including couplers;
3. TDS switched on at the RF zero-crossing with a modified map in which the coupler regions are removed and only the regular cells are retained.

For the simulation analysis, the system was calibrated by measuring the beam centroid shift with respect to its reference position on the screen in absence of the deflecting field. This procedure yielded a calibration factor of $5.7 \pm 0.1\ fs/\mu m$ for an input voltage of 20 MV (corresponding to 14.5 MW of input power). Fig. 3.14 shows the beam spot size that would be recorded by a screen placed at the end of the drift section, with an assumed screen resolution of 3.5 $\mu m$/pixel. The comparison highlights the effect of the TDS streaking: while the unstreaked beam maintains a nearly round distribution at the screen, the streaked beam is elongated along the vertical axis, mapping the temporal bunch length into the transverse plane.

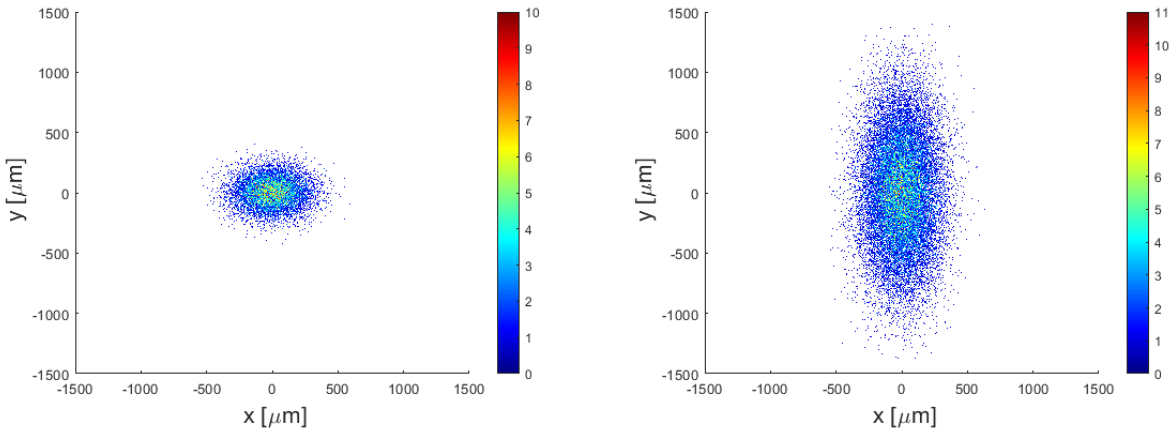


**Figure 3.14:** Simulated beam spot at the screen located downstream of the diagnostics beamline. Left: TDS switched off, showing the natural beam size. Right: TDS switched on at zero crossing, where the temporal bunch profile is mapped into a vertical streak.

Fig. 3.15 reports the reconstructed current profiles at the screen for two configurations (TDS on with and without couplers), compared with the input temporal profile obtained from the macroparticle distribution. When the TDS is operated at zero crossing, the streaking process maps the temporal coordinate into the vertical plane, allowing the bunch profile to be retrieved on the screen. The profile was obtained by applying the calibration factor, derived from the deflector calibration, to the vertical coordinate measured at the screen. The agreement between the reconstructed profile and the input one demonstrates that the field map implementation preserves the shear relation. A direct comparison between the full map and the coupler-free map shows that the coupler regions do not significantly alter the temporal mapping, as the current profiles overlap within numerical accuracy. This result is significant because it demonstrates that temporal diagnostics can be reliably performed without being affected by the local field asymmetries of the couplers.

To quantify the effect on the beam energy distribution, the rms energy spread at the screen has been evaluated for the three cases. The results indicate that the spread increases from approximately $\sim$ 100 keV to $\sim$ 420 keV when the TDS is switched on, with a negligible difference without the couplers. This confirms that the inclusion of the couplers does not significantly affect the energy spectrum, and that the broadening is an intrinsic feature of the deflecting process. From a practical perspective, this increase in energy spread does not compromise the reconstruction of the longitudinal profile: the comparison between the expected temporal distribution and the one retrieved at the screen shows excellent agreement. Therefore, while the broadening should be considered when interpreting energy-related measurements, it does not affect the reliability of the temporal diagnostics performed

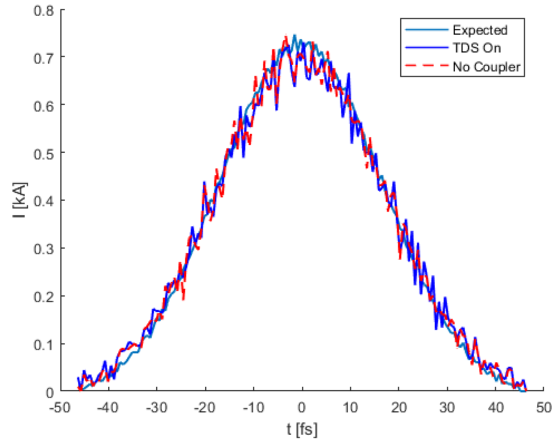


**Figure 3.15:** Simulated beam current profiles for two configurations, TDS on with and without couplers, compared with the expected temporal profile (obtained from the input distribution). The streaked case (TDS on) accurately reproduces the expected profile, demonstrating that the temporal mapping is correctly preserved. The comparison with the coupler-free case confirms that the couplers do not introduce any distortion in the reconstructed time profile.

with the PolariX TDS.

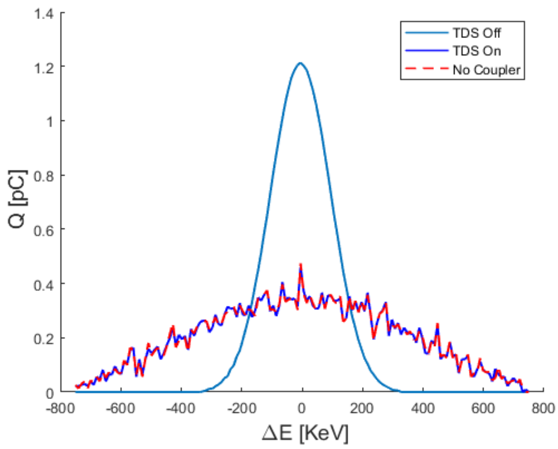


**Figure 3.16:** Simulated energy spectra at the screen for three configurations: TDS off, TDS on, and TDS on without couplers. The TDS-off case exhibits the nominal Gaussian distribution with the expected input spread. When the TDS is switched on, the spectrum broadens and the peak amplitude decreases, indicating an increase in the rms energy spread. The similarity between the full map and the coupler-free map demonstrates that the observed broadening is intrinsic to the structure cells and not induced by the couplers.

The results, which are reported in Table 3.4, demonstrate that the reconstructed bunch length is consistent with the expected value within uncertainties, confirming the reliability of the temporal measurement. The rms energy spread, on the other hand, increases when the TDS is switched on, independently on the presence of the couplers, indicating that the broadening is an intrinsic feature of the deflecting process.

| | **Expected** | **TDS On (Sim.)** | **No Coupler (Sim.)** |
|---|---|---|---|
| Calibration [$\mu m/fs$] | - | $5.7 \pm 0.1$ | $5.7 \pm 0.1$ |
| Resolution [$fs$] | - | 4.2 | 4.2 |
| $\sigma_t$ [$fs$] | 17.0 | $16.4 \pm 0.6$ | $16.5 \pm 0.6$ |
| $\Delta\sigma_t$ (rel) [%] | - | $\sim 3.8$ | $\sim 3.7$ |
| $\delta_E$ [$10^{-4}$] | 1 | $4.20 \pm 0.01$ | $4.19 \pm 0.01$ |

**Table 3.4:** Expected and reconstructed parameters for two configurations: TDS on, and TDS on without couplers. The uncertainties in the bunch length are obtained by propagating simulation parameter errors, while those in the energy spread are estimated through statistical sampling.

## 3.4 50 Cells Structure Design

The demands from the EuPRAXIA@SPARC_LAB project include the realization of a device shorter than the described 96-cell structure, to be implemented for the measurements at low energy ($E_{nominal} = 118$ MeV), at the exit of the RF Photoinjector. Thus, studies are required to determine the structure parameters and length, by taking into account the desired measurement resolution, and the space limitations in the beamline. The available space for the installation of the structure is approximately 60 cm, which must accommodate the cavity body as well as the input/output couplers and the regular cells. A 50-cell configuration results in a total length of 57.6 cm, thus fitting within the allocated space and leaving a small margin for possible adjustments. The use of a shorter structure inevitably reduces the maximum deflecting voltage achievable for a given input power, and therefore the temporal resolution. Nevertheless, this reduction is largely compensated by the fact that the device is operated at a significantly lower beam energy compared to the 1 GeV case of the long structure, resulting in a lower beam rigidity and hence sufficient streaking strength for diagnostics.

The design of the 50-cell structure was derived from the available field maps of the 96-cell configuration by truncating the number of regular cells and reproducing the relevant electromagnetic parameters. The transition from the 96-cell to the 50-cell configuration can be carried out either at the EM-model level in the HFSS simulations or by post-processing the field maps. In the latter case, cells can be truncated or generated by tiling a shorter 6-cell map, since the regular cells are identical in a constant-impedance structure. The shorter structure maintains the same operational frequency and phase advance per cell, while the overall length is reduced to approximately half of the original. The transverse voltage $V_\perp$ was recalculated to evaluate the integrated deflecting strength. At equal input power, the reduction in length results in a lower $V_\perp$ (about half of the 96-cell value), which directly translates into a smaller streaking slope. Nevertheless, the reduced energy of 118 MeV implies a lower beam rigidity, partially compensating the effect of the reduced $V_\perp$.

The analysis presented in this section includes:

- the calculation of the vertical force distribution $F_y(z)$ and the corresponding integrated transverse momentum $\Delta p_y(z)$ along the 50-cell structure,
- the multi-particle simulation to evaluate the structure impact on the beam energy spread,
- a qualitative assessment of the impact of the input/output couplers, which can be more pronounced in shorter structures due to the larger relative weight of fringe fields.

### 3.4.1 Integrated Voltage and Kick

Fig. 3.17 shows the Lorentz Force $F_y(z)$ along the streaking direction, the respective momentum deviation $\Delta p_y(z)$ calculated from the integral of the force, and the particle displacement $\Delta y(z)$ as a function of the longitudinal position in the structure, for an integrated voltage of 10 MV. The behavior is qualitatively identical to that observed in the 96-cell case, confirming the correct implementation of the field maps and the consistency of the scaling. The coupler regions indicate a residual kick similar to the structure of 96-cells, leading to an increase in particle momentum and displacement. While this effect on the measurement is negligible in the long structure, it needs to be evaluated for the short structure through multi-particle simulations to investigate its impact on the low-energy beam distribution and time profile reconstruction.

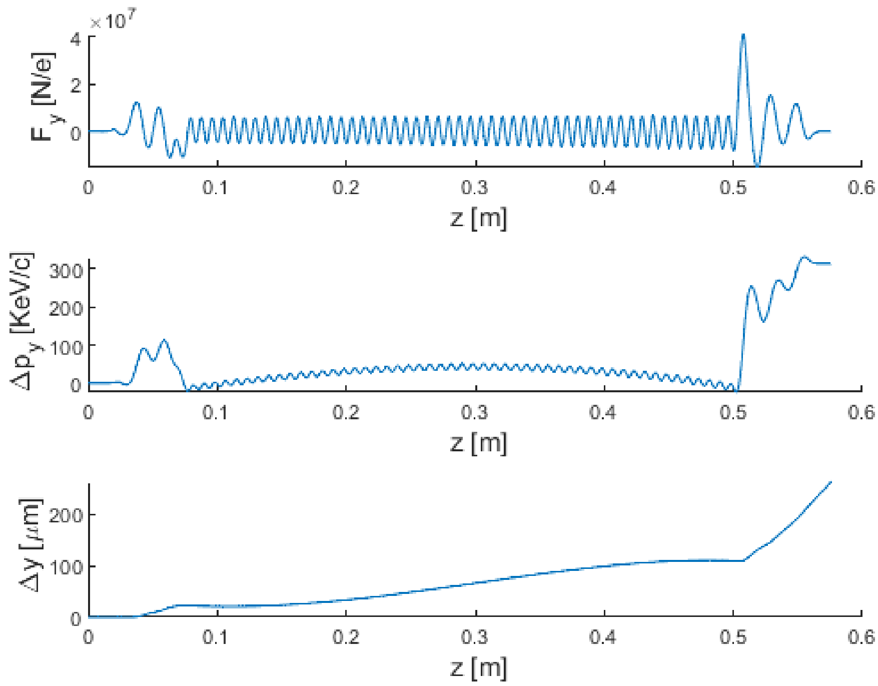


**Figure 3.17:** Tracking of a reference particle at the RF zero-crossing with 10 MV integrated voltage, in the 50-cell structure. Top: transverse Lorentz force $F_y$. Middle: vertical momentum deviation $\Delta p_y$. Bottom: vertical displacement $\Delta y$.

The integrated transverse voltage $V_\perp$ of the 50-cell structure was evaluated from the Lorentz force integral and compared with that of the long structure. At an input power of 1 W, the 96-cell TDS provides $V_\perp \approx 5.24$ kV, while the corresponding value for the 50-cell configuration is $V_\perp \approx 3.21$ kV. The reduction is consistent with the shorter length of the cavity, which contains nearly half the number of regular cells of the long structure. Although the shorter cavity delivers a lower deflecting strength for the same input power, this effect is partly compensated in practice by the lower beam energy (118 MeV) at which the device is intended to operate. The reduced beam rigidity ensures that the achievable temporal resolution remains sufficient for bunch diagnostics, even with the lower $V_\perp$ of the 50-cell structure. A distinctive feature observed in the 50-cell configuration concerns the effect of the couplers on the integrated voltage. In this case, the absence of the input and output couplers results in a small reduction in the effective deflecting strength, so that the integral result is $V_\perp \approx 3.05$ kV. For an integrated voltage of 10 MV (input power of 9.7 MW), the effective value is 5% lower when the couplers are not included.

### 3.4.2 Beam Dynamics Studies on the 50-cells PolariX TDS

In this section, the results of multi-particle tracking simulations performed with ASTRA using the 50-cell PolariX TDS are presented. These studies aim to evaluate both the modification of the energy distribution and the temporal mapping introduced by the streaking process. The simulations were carried out with the same lattice layout shown in Fig. 3.13, consisting of a 57.6 cm long TDS followed by a drift space of 3.45 m to the diagnostic screen. This configuration reproduces the experimental conditions foreseen for the installation of the short structure for the low-energy beam diagnostics. Particular attention is given to the impact of the reduced integrated voltage on the achievable streaking strength and on the associated energy spread, as well as to the possible influence of the input and output couplers. In this way, the simulations provide a quantitative benchmark for assessing the performance of the short structure in realistic operating conditions. The beam parameters used in the simulations are summarized in Table 3.5. They are chosen to be consistent with those of the ideal beam employed for the 96-cell structure simulations, except for the beam energy and emittance.

| **Beam Parameters** | | |
|---|---|---|
| Charge | 30 | $pC$ |
| Energy | 118 | $MeV$ |
| $\delta$ Energy Spread | $\sim 10^{-4}$ | |
| $\sigma_{x,y}$ (Input) | 100 | $\mu m$ |
| $\sigma_x$ (Screen) | 156 | $\mu m$ |
| $\sigma_y$ (Screen) | 110 | $\mu m$ |
| $\sigma_t$ | 17 | $fs$ |
| $\varepsilon_{n_{x,y}}$ | 0.7 | $\mu m$ |

**Table 3.5:** Parameters of the ideal beam used in the 50-cells structure field maps studies.

The observed reduction of the integrated voltage when excluding the coupler regions highlights the role of the calibration factor and its impact on the achievable resolution of the TDS. The calibration curves, obtained by scanning the RF phase around the zero crossing, show a small but measurable influence of the couplers on the effective deflecting voltage. In particular, the slope of the centroid displacement fit is slightly reduced in the case without couplers, corresponding to a lower effective calibration. Comparing the zero-crossing phase for the structure with and without couplers, the phase is respectively $\phi = -105.4$ deg (with couplers) and $\phi = -103.8$ deg (without couplers), due to the slippage effect. In the example shown in Fig. 3.18, in which the phase has been shifted to have the zero-crossing at the same phase to compare only the slope, the deflecting voltage obtained from the linear fit decreases of about 5% when the couplers are removed. At nominal operation, this results in a modest degradation of the temporal resolution, by about 5%. Although the effect is minor and does not significantly impact the measurement accuracy, it provides clear evidence of a non-zero contribution to the streaking effect from the coupler regions. This effect was not observed in the long structure, where the removal of the couplers does not affect the kick received from the beam.

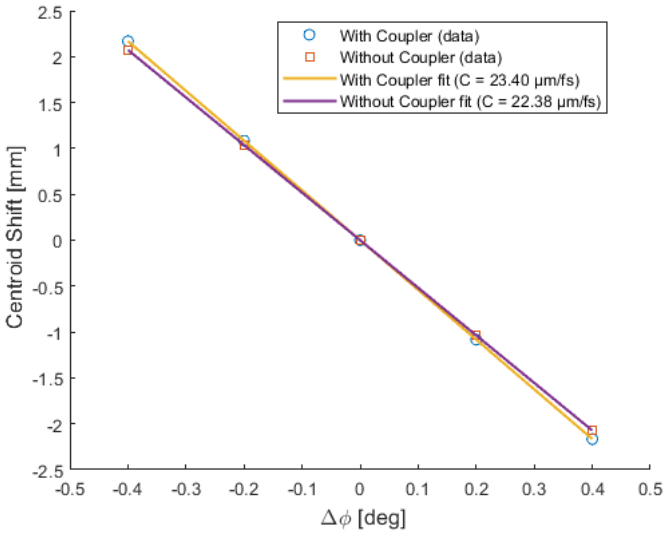


**Figure 3.18:** Calibration fit of the centroid displacement as a function of the RF phase for the configurations with and without couplers. The fit without couplers exhibits a slightly lower slope, corresponding to a reduced integrated voltage and shear parameter. This indicates a non-zero contribution from the coupler region to the streaking effect, in contrast to the behavior of the conventional structure.

In Fig. 3.19, the expected and reconstructed temporal profiles from the simulation are shown. The reconstructed current profile remains unchanged in both cases, with and without couplers, and shows excellent agreement with the input Gaussian distribution. This confirms that the temporal mapping is not affected by the coupler regions. The estimated rms bunch length from the simulation is $16.9 \pm 0.6$ fs for $16.8 \pm 0.6$ fs, respectively, in full-structure and only-cells configurations, in good agreement with the expected value of 17 fs.

When the TDS is switched on at the zero crossing, the spectrum exhibits a clear broadening compared to the case without deflection, as expected from the 96-cell structure. The rms energy spread increases from 10 keV to 275 keV in the case of the complete structure, while not including the couplers leads to a smaller energy spread 264 keV. The comparison between the simulations with and without couplers shows only a minor difference, in line with the small reduction of the integrated voltage observed in the calibration results. This confirms that the coupler regions have no significant impact on the energy profile. All the results are summarized in Table 3.6.

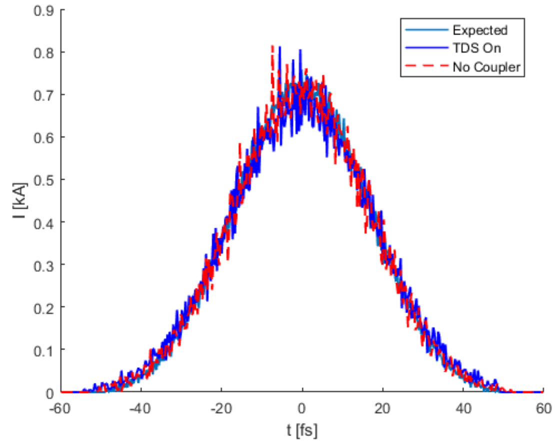


**Figure 3.19:** Simulated beam current profiles for two configurations, TDS on with and without couplers, compared with the expected temporal profile (obtained from the input distribution). The streaked case (TDS on) accurately reproduces the expected profile, demonstrating that the temporal mapping is correctly preserved. The comparison with the coupler-free case confirms that the couplers do not introduce any distortion in the reconstructed time profile.

| | **Expected** | **TDS On (Sim.)** | **No Coupler (Sim.)** |
|---|---|---|---|
| Calibration $[\mu m/fs]$ | - | $23.4 \pm 0.1$ | $22.4 \pm 0.1$ |
| Resolution $[fs]$ | - | $\sim 4.6$ | $\sim 4.8$ |
| $\sigma_t$ $[fs]$ | 17.0 | $16.8 \pm 0.6$ | $16.9 \pm 0.6$ |
| $\Delta\sigma_t$ (rel) [%] | - | $\sim 3.5$ | $\sim 3.7$ |
| $\delta_E$ $[10^{-4}]$ | 1 | $27.5 \pm 0.1$ | $26.4 \pm 0.1$ |

**Table 3.6:** Summary of the main parameters obtained from the 50-cell PolariX TDS simulations. The values are compared for the configurations with and without couplers.

### 3.4.3 Comments on couplers' effect on a short structure

A distinctive outcome of the studies performed on the 50-cell TDS concerns the role of the input and output couplers. In the long structure, the contribution of the couplers to the overall streaking process was negligible, as their relative length was small compared to the total cavity. In the short structure, however, the couplers represent a larger fraction of the total length, and their influence becomes more visible in the numerical results.

The first indication comes from the calibration analysis, where a measurable reduction of the integrated voltage is observed when the couplers are removed. Specifically, the deflecting voltage decreases by about 5%, resulting in a comparable (∼5%) increase in the estimated temporal resolution. Although this degradation is modest and does not compromise the diagnostic capability of the device, it represents a clear signature of a non-zero contribution to the streaking coming from the coupler regions. The same behavior is observed in the field integrals, confirming the consistency of the effect across different evaluation methods.

From a physical point of view, this result can be understood by considering that the coupler regions introduce non-ideal field components and partial reflections that slightly change the net deflecting strength. While in long structures these effects are diluted over a large number of regular cells, in the short structure, their relative contribution becomes more significant compared to that of the active cells.

These couplers' effects also introduce a difference in the phase shift zero-crossing that is observed in the simulations. The zero crossing was determined by scanning the RF phase and identifying the condition where the centroid displacement on the screen vanished. From this analysis, the zero-crossings are in correspondence with phase $\phi = -105.4$ deg (with couplers) and $\phi = -103.8$ deg (without couplers), leading to an overall slippage of $\Delta\phi = 1.4$ deg, which corresponds to a temporal offset of 324 fs at X-band frequencies. This shift originates from the coupler-induced slippage, as the end cells and coupler geometry modify the effective electrical length of the structure. The correction is applied in the analysis by recentering the phase to the effective zero crossing.

Importantly, the reconstructed temporal profile remains unaffected, which means that the couplers do not distort the time–transverse mapping. Their effect is limited to a small reduction in the effective voltage and a corresponding adjustment of the calibration factor. This implies that, in experimental operation, careful calibration will allow one to correct for the coupler contribution and achieve the expected resolution. Nevertheless, the observation of this contribution highlights that coupler design and optimization are particularly important in more compact structures.

## 3.5 Summary of the comparison between long and short structure

The results obtained with the 50-cell TDS can be directly compared to those of the long (96-cell) structure to assess the consistency and limitations of the two designs. The most evident difference concerns the integrated voltage: at the same input power (1 W), the short structure delivers approximately 3.21 kV, compared to 5.24 kV for the long one. Consequently, the accumulated kick and the shear parameter are reduced by nearly a factor of two. This scaling is consistent with the reduced length of the cavity and was clearly confirmed by both the field integrals and the single-particle simulations. Despite the lower streaking strength, the 50-cell structure operates at a significantly lower beam energy (118 MeV instead of 1 GeV), which implies a lower beam rigidity. As a result, the achievable temporal resolution remains sufficient for diagnostics, as confirmed by the reconstructed bunch profiles. The reduced $V_\perp$ is therefore not a limitation in practice, provided that the device is used in the low-energy section of the beamline.

Another important aspect is the effect of the couplers. In the long structure, their contribution was essentially negligible, whereas in the short device, a small but measurable impact was observed, reducing the effective voltage by approximately 5%. Although this does not compromise the diagnostic performance, it represents a relevant difference between the two cases and highlights the need for accurate calibration in the short structure.

Finally, the energy spread induced by the streaking process was found to increase in both cases, with the broadening scaling consistently with the deflecting voltage. The comparison shows that the short structure reproduces the same physical behavior as the long one, but with proportionally smaller values. This confirms the robustness of the PolariX TDS Field Maps across different lengths.

In conclusion, the 96-cell TDS remains the optimal solution for high-energy diagnostics, providing the largest kick and highest resolution. The 50-cell version, while delivering a reduced deflecting strength, is well-suited for installation at 118 MeV, where space is limited and beam rigidity is lower. The main distinction lies in the more visible effect of the couplers in the short structure, which was evaluated to verify that it does not significantly affect the TDS measurement. Overall, the comparison validates the use of both configurations within their respective operational contexts.

# Chapter 4

# EuPRAXIA@SPARC_LAB Diagnostics

This thesis work is inserted in the framework of the EuPRAXIA collaboration, for the realization of the EuPRAXIA@SPARC_LAB user facility ongoing at Laboratori Nazionali di Frascati of the INFN. The facility represents the fundamental contribution to the first European research infrastructure dedicated to plasma-based accelerators. Its main feature is the integration of a Plasma Wakefield Acceleration (PWFA) stage to produce and accelerate high-quality electron bunches up to 1 GeV, with the ultimate goal of driving two Free Electron Laser (FEL) beamlines for user experiments: one operating in the VUV spectral range (50–180 nm) and the other in the XUV–soft X-ray region (4–10 nm). The accelerator layout also includes a high-brightness S-band photoinjector, followed by an advanced X-band linac, which prepares the beam for the plasma acceleration stage [45].

Free Electron Lasers (FELs) are key instruments for a wide range of scientific applications, thanks to their distinctive properties: extremely high peak brilliance, ultrashort pulse durations in the femtosecond regime, and broad wavelength tunability. These features enable experiments with unprecedented temporal resolution and signal-to-noise ratio. However, conventional X-ray FEL facilities require large infrastructures, with tens to hundreds of meters dedicated to electron accelerators, undulators, and photon beamlines. To address this limitation, plasma-based accelerators have emerged as a promising solution to drastically reduce the accelerator footprint while maintaining the beam quality required for FEL operation. Fundamental results obtained at the SPARC_LAB test facility at INFN-LNF, have demonstrated the capability of plasma acceleration to generate electron beams suitable for FEL applications and reliable enough to be delivered to external users [46].

A key advantage of plasma acceleration lies in its ability to overcome the electrical breakdown limitations of conventional RF structures. While traditional accelerators sustain accelerating gradients of the order of tens of MV/m, plasma accelerators can reach fields that are two to three orders of magnitude higher. The principle relies on the excitation of a plasma wave, i.e., a density perturbation in the plasma, which can be driven by either a high-power laser pulse (LWFA) or a relativistic charged-particle bunch (PWFA). In the PWFA scheme, the Coulomb force of the driver bunch displaces plasma electrons, leaving a positively charged ion channel behind. This charge separation creates both longitudinal accelerating fields and transverse focusing fields. A properly timed witness bunch, injected in the correct phase of the wake, can then be simultaneously accelerated and focused, reaching GeV-scale energies over distances of only a few centimeters.

The application of plasma acceleration to FELs imposes stringent requirements on the electron beams. In particular, the accelerated bunches must exhibit high energy, ultrashort duration (tens of femtoseconds or less), and low projected and slice emittance. Meeting such demanding beam parameters requires not only innovative acceleration schemes but also a comprehensive and advanced diagnostic system capable of fully characterizing the beam phase space [47].

The diagnostic suite of EuPRAXIA@SPARC_LAB is designed to meet these challenges. Conventional methods, such as quadrupole scans combined with magnetic spectrometers, will provide measurements of emittance and energy spread. At the same time, advanced X-band transverse deflecting structures, such as the PolariX TDS, will enable the reconstruction of the longitudinal phase space and support multi-dimensional tomographic techniques. The synergy between these diagnostics is fundamental to ensure a complete understanding of the electron beam parameters, thereby guaranteeing reliable FEL operation.

The beamline foresees three main diagnostic stations, strategically located at different energies along the machine: at the photoinjector exit (∼118 MeV), after the magnetic bunch compressor (∼400 MeV), and upstream of the undulator section (∼1 GeV). Each station will host a dedicated set of instruments tailored to the beam parameters at that stage.

This chapter is organized as follows. In Section 4.1, an outline of the simulation studies reported in the chapter is presented. Section 4.2 describes the procedure adopted to determine the temporal and spatial resolution of the diagnostics, including the analysis of the simulated measurements and the characterization of the CCD camera and its corresponding screen resolution. Section 4.3 provides an overview of the EuPRAXIA@SPARC_LAB facility and of the diagnostic beamline layout, focusing on the elements reproduced in simulation and on the measurements foreseen for each section. The following three sections 4.4, 4.5, 4.6, present descriptions and simulation results for the respective diagnostic beamlines, following a common structure and including evaluations of emittance, energy, and longitudinal phase-space measurements. Section 4.7 presents the longitudinal diagnostic based on Electro-Optic Sampling (EOS), which complements the TDS-based simulations discussed in the low- and high-energy sections to provide complete characterization of the bunch longitudinal profile and acceleration stability. Finally, Section 4.9 summarizes the main results and conclusions of the performed simulations.

## 4.1 Simulation outline

All the simulations presented in this chapter were performed using a combination of the particle-tracking codes ASTRA and ELEGANT, depending on the specific aspects under investigation. Both codes have been previously introduced, and a general overview of their use and implementation within the diagnostic studies is provided here. Low-energy simulations were primarily carried out with ASTRA to account for the space-charge effects that can be significant at these energies, especially for the short, high-charge bunches considered. ASTRA was also employed for the studies involving the PolariX TDS, since it allows importing and tracking through the three-dimensional field maps developed in the previous chapter (see Section 3.3). This enabled reproducing the interaction between the bunch and the deflecting structure's realistic electromagnetic fields, as well as evaluating the resulting beam dynamics and diagnostic performance. ELEGANT, on the other hand, was mainly used for higher-energy simulations, where space-charge effects become negligible and collective phenomena such as synchrotron radiation can be modeled more efficiently. In particular, ELEGANT was adopted to simulate the energy measurements and to evaluate the impact of synchrotron radiation on the reconstructed energy profiles. In all cases, the simulations were designed to reproduce as closely as possible the conditions of an actual measurement. This includes modeling the diagnostic elements and their intrinsic limitations, such as the finite screen resolution of the imaging system, the calibration accuracy of the quadrupole magnets, and collective effects that can modify the measured beam parameters. By including these factors, the numerical results from simulations can be directly compared with realistic experimental conditions, providing a reliable estimate of the expected measurement resolution and overall diagnostic performance across different setups. In the present study, beam transport is primarily described using a linear optics formalism. Higher-order magnetic aberrations and RF curvature effects are expected to be subdominant for the considered optical settings and beam parameters, and their impact is partially included through full particle-tracking simulations.

## 4.2 Uncertainties and Resolution determination

### 4.2.1 Simulated CCD image

To reproduce the imaging system's response, a numerical CCD simulation was implemented, modeling the image formation process at the camera output level without explicitly including the physical response of the screen. An ideal scintillating screen is therefore assumed, neglecting additional broadening effects related to screen thickness, light diffusion, and optical depth-of-field. The simulation input is the distribution of macroparticles obtained from tracking. Each macroparticle is described by a set of coordinates $(x, x', y, y', t, E)$, that determines the beam profile on the screen. The simulation involves creating a two-dimensional histogram of the particle's coordinates $(x, y)$. The histogram bins represent camera pixels, with their sizes determined by the optical system's magnification factor. In this way, the macroparticles are "stacked" into the corresponding bins, and the output is a two-dimensional intensity distribution equivalent to the image recorded by a CCD camera. This approach accounts for the finite pixel size and number, both of which are directly affected by magnification, thereby providing a realistic representation of the measured beam profile and camera resolution.

The simulated acquisition system is based on a Basler ace 2 CMOS camera, which represents a typical choice for beam diagnostics. The sensor features a pixel pitch of 3.5 $\mu$m and a resolution of 1920 × 1200 pixels, resulting in an active area of approximately [6.6 × 4.0] mm$^2$ [48]. The acquisition system is modeled with a magnification factor ranging from 1:1 to 1:2, which defines the effective pixel size at the screen plane. This parameter directly determines both the spatial resolution and the field of view of the simulated images, thereby defining the instrumental error $\sigma^{(instr)}$ that is accounted for in the simulation analysis.

### 4.2.2 Bunch length measurement resolution

The bunch length is measured using a TDS, which maps the particles' longitudinal coordinates onto transverse displacements at the diagnostic screen. The vertical beam size at the screen in the streaked configuration can be expressed as

$$\sigma^2 = (C\,\sigma_t)^2 + \sigma_0^2 \ , \tag{4.1}$$

where $\sigma_t$ is the bunch length (rms), $C$ is the time-to-position calibration factor (in $\mu m/fs$), and $\sigma_0$ is the unstreaked beam size due to optics. The calibration factor $C$ is determined from beam dynamics simulations of the TDS and depends on the integrated deflecting voltage and the beam energy. The temporal resolution of the measurement is defined as the bunch length corresponding to the condition where the streaked contribution $C\sigma_t$ becomes comparable to the unstreaked beam size contribution:

$$\text{Resolution} \simeq \frac{\sigma_0}{C} \ . \tag{4.2}$$

The validity of each reconstructed bunch-length measurement is assessed using a two-fold criterion:

- the relative uncertainty of the reconstructed value is below 10%;
- the relative deviation between the reconstructed and the expected bunch length is also below 10%.

### 4.2.3 Emittance measurement resolution

The transverse emittance is measured through a quadrupole scan, in which the beam size at the diagnostic screen is recorded as a function of the strength of a quadrupole magnet. The square of the beam size on the screen can be expressed as

$$\sigma^2(s) = A\,k^2 + B\,k + C \ , \tag{4.3}$$

where $k$ is the quadrupole strength and the coefficients $A$, $B$, and $C$ are related to the initial Twiss parameters and to the emittance of the beam. A parabolic fit to the measured $\sigma^2$ versus $k$ curve allows the retrieval of the Twiss parameters and the calculation of the emittance. The accuracy of the emittance measurement is limited by the uncertainty in the determination of the beam size $\sigma$. The instrumental error on $\sigma$ is taken as the effective resolution of the imaging system, defined as the effective pixel size at the screen. Consequently, the relative error on $\sigma^2$ can be approximated as

$$\frac{\Delta\sigma^2}{\sigma^2} \simeq 2\frac{\Delta\sigma}{\sigma} \ , \tag{4.4}$$

which directly propagates into the fitted coefficients $A$, $B$, $C$ and ultimately into the retrieved emittance. The emittance resolution is therefore defined as the minimum measurable emittance for which the relative error and the difference between input and reconstructed values remain consistent with a threshold of $\approx 10\%$. In practice, the procedure is the following:

1. generate simulated beam distributions with decreasing emittance values,

2. perform a quadrupole scan and apply the reconstruction procedure,
3. compare the reconstructed emittance with the input value,
4. identify the emittance value for which the relative error or the difference between reconstructed and input value increases over $\sim 10\%$.

This value defines the resolution floor of the emittance measurement. Below this threshold, the measurement is dominated by instrumental resolution and does not reflect the true beam properties. Additional sources of uncertainty, such as jitter of the beam trajectory and fluctuations of the quadrupole strength, can be evaluated through repeated measurements or dedicated simulations. In this work, their effect is included in the quoted uncertainty, while the resolution floor is defined by the procedure described above.

### 4.2.4 Energy measurement resolution

The beam energy is measured using the diagnostic line's dispersive section. After the dipole magnet, the horizontal position at the spectrometer screen is related to the relative energy deviation $\delta = (E - E_0)/E_0$ through the horizontal dispersion function $D$:

$$x = x_0 + D\,\delta \ . \tag{4.5}$$

This relation provides a direct calibration factor between the horizontal position at the screen and the relative energy spread of the bunch. The instrumental resolution of the measurement corresponds to the minimum energy spread distinguishable at the screen and is defined as:

$$\sigma_E^{(\mathrm{res})} = E_0 \frac{\sigma_x^{(\mathrm{instr})}}{|D|} \ , \tag{4.6}$$

where $\sigma_x^{(\mathrm{instr})}$ is the effective transverse resolution of the imaging system, estimated from the camera calibration. The measured horizontal beam size on the screen can then be expressed as:

$$\sigma_x^2 = (D\,\sigma_\delta)^2 + \beta_x \varepsilon_x + \sigma_x^{(\mathrm{instr})2} \, , \tag{4.7}$$

where the first term represents the contribution from the energy spread, the second term accounts for the betatron beam size transported to the screen, and the last term is the screen resolution. The resolution limit of the energy measurement corresponds to the condition where the dispersive contribution becomes comparable to the quadrature sum of the other terms. In particular, the presence of the betatron term $\beta_x \varepsilon_x$ sets a practical limit: if the natural beam size transported to the screen dominates over the dispersive contribution, the measurement resolution increases, so that for each energy measurement, the matching is performed to minimize the horizontal beta function at the screen. The spectrometer was calibrated by tracking single particles of known energy through the dipole magnetic field, establishing a correlation between the horizontal position on the screen and the beam energy. From this calibration, the average beam energy and energy spread $\Delta E$ were extracted for each configuration. These quantities were then analyzed as a function of the screen distance and of the camera magnification, which defines the effective screen resolution on the dispersive axis.

## 4.3 EuPRAXIA Diagnostics Beamlines Layout

To fully characterize the electron beam along the EuPRAXIA@SPARC_LAB accelerator, three dedicated diagnostic stations have been designed and implemented at different energies: low (118 MeV), medium (400 MeV), and high energy (up to 1 GeV). Each station is optimized to provide a complete set of measurements of the main beam parameters, including the bunch length, the transverse emittance (both projected and slice), and the beam energy.
The diagnostic layout follows a common scheme. A set of quadrupoles is placed upstream of the measurement section to match the transverse optics and optimize the beam size on the observation screens. A TDS is employed to provide time-resolved measurements of the longitudinal profile, and it is present in both the low- and high-energy stations. Downstream, a dipole magnet disperses the beam in the horizontal plane, enabling the measurement of the energy spectrum and energy spread on a screen positioned along the dispersive axis. In contrast, an additional screen on the straight section allows for emittance and temporal profile characterization.
The combination of these elements ensures a comprehensive characterization of the electron beam at the three relevant energies, enabling multi-shot and time-resolved diagnostics. In particular, the low-energy station plays a crucial role in injector tuning and assessing the initial beam quality. The medium-energy station enables monitoring and control before beam compression and subsequent acceleration. The high-energy station serves as the final benchmark for the beam parameters required for FEL driving and user experiments.

The complete beamline of the EuPRAXIA@SPARC_LAB accelerator is depicted in Fig. 4.1, in which the diagnostics positions are highlighted.

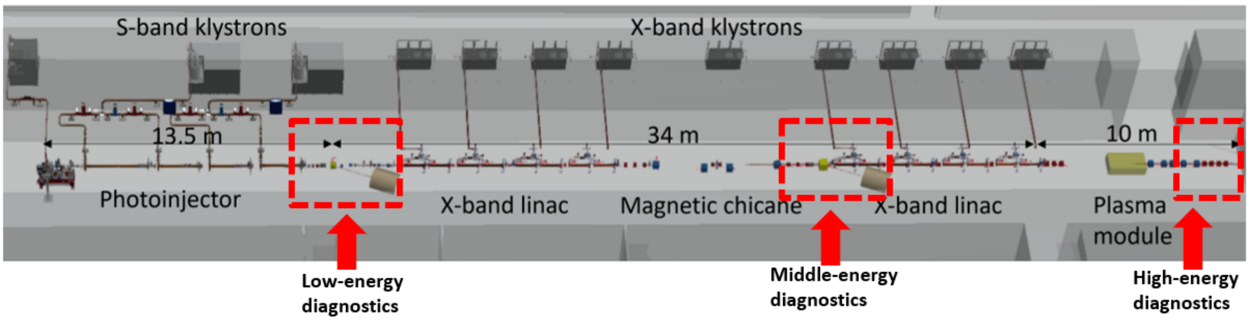


**Figure 4.1:** Layout of the EuPRAXIA@SPARC_LAB beamline, with highlighted the main components and diagnostics station along the accelerator [45].

In the following sections, the three diagnostic beamlines will be presented. For each case, the beamline layout, the beam characteristics, and the matching procedure applied at the entrance will be described. The matching was performed to provide consistent initial Twiss parameters and to ensure stable beam transport through the diagnostic section. This common starting point was then adapted to the specific constraints of the low-, medium-, and high-energy beamlines.

## 4.4 Low-Energy beamline

The low-energy diagnostics is designed to characterize the electron beams produced from the photoinjector under various configurations. The nominal working point corresponds to an energy of 118 MeV, achieved with velocity bunching compression scheme [49].

### 4.4.1 Beamline layout

Three electromagnetic quadrupoles, each with a magnetic length of 0.1 m and a magnetic field gradient limit of up to 30 T/m, are placed to focus and match the beam to the diagnostics screen, with a spacing of 0.1 m between them. The beamline relies on a 60-cm-long space allocated for the PolariX TDS system and a sector dipole of magnetic length 0.25 m (which is the first dipole of the laser-heater chicane) with a maximum field of 1.28 T, corresponding to a maximum bending angle of 22 degrees at 250 MeV. The screen on the straight section is placed at a flag 3.35 m from the TDS, before the entrance of the first X-band linac section. The dispersive screen is positioned 1.5 m after the dipole, with the beamline terminating approximately 3 m later on a beam dump. The straight section of the described layout is depicted in Fig. 4.2. The PolariX TDS fields have been designed as described in Chapter 2, and the structure will be fed by an X-band klystron that alternately feeds the deflector and X-band accelerating cavities, providing a maximum available integrated voltage of 23 MV.

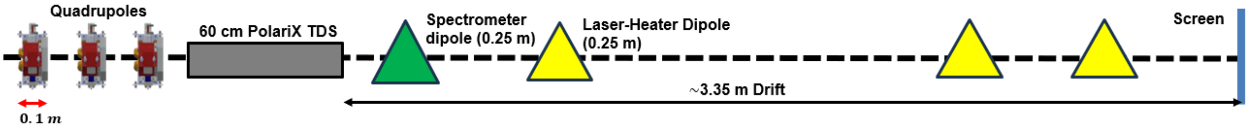


**Figure 4.2:** Layout of the low-energy diagnostic station (118 MeV). This section features quadrupoles, a 60 cm PolariX TDS, a sequence of 0.25 m dipoles in the laser-heater chicane along a 3.35 m drift, and a downstream screen.

### 4.4.2 Simulated Beam Parameters

At low energy, the working point is defined to produce the driver and the witness bunch simultaneously. The machine was operated in velocity-bunching mode, resulting in a beam with an energy of 118 MeV. This configuration is particularly useful for evaluating the intrinsic resolution of the diagnostic station, as the bunches are still relatively long and the transverse beam sizes are larger than at higher energies. In addition to the 118 MeV case, a second working point at 250 MeV, which relies on the accelerations being fully on crest in the injector cavities, was considered in determining the longitudinal resolution, as it depends critically on the beam energy. The phase space distribution of the beam was kept identical to the low-energy case, while only the beam energy was increased from 118 to 250 MeV. This allows for direct comparison of diagnostic performance at the same longitudinal and transverse beam properties, but at a higher energy, thereby isolating the effect of beam energy on the measurement system's resolution. The beam parameters for the driver and witness beam are reported in Table 4.1.

| **Parameters** | **Driver** | **Witness** |
|---|---|---|
| Charge [$pC$] | 200 | 30 |
| Mean Energy [$MeV$] | 119.70 | 118.22 |
| Energy Spread [%] | 0.65 | 0.12 |
| RMS Bunch length [$fs$] | 193 | 17 |
| RMS Bunch length [$\mu m$] | 57.9 | 5.1 |
| $\varepsilon_{n_x}$ [$\mu m$] | 1.50 | 0.66 |
| $\varepsilon_{n_y}$ [$\mu m$] | 1.50 | 0.65 |
| $\beta_x$ [$m$] | 7.65 | 3.47 |
| $\beta_y$ [$m$] | 7.64 | 3.50 |
| $\alpha_x$ | $-3.40$ | $-3.17$ |
| $\alpha_y$ | $-3.40$ | $-3.20$ |

**Table 4.1:** Beams parameters of the working point at the low-energy (118 MeV) diagnostics station.

In Fig. 4.3 are reported, respectively, the longitudinal phase space (left) and current profiles (right) of the driver and witness beams. A critical aspect is the limited separation between driver and witness bunches. In this configuration, the center-to-center distance between driver and witness is about $\sim$ 0.5 ps. At the same time, their longitudinal profiles partially overlap, making the measurement of individual bunch parameters more challenging and imposing constraints on diagnostic resolution.

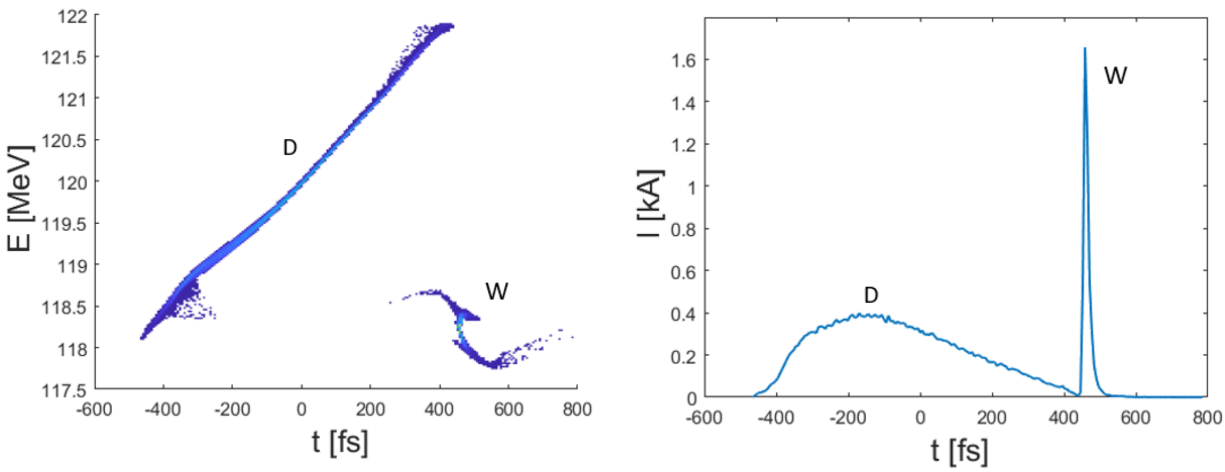


**Figure 4.3:** Longitudinal phase space (left) and corresponding current profiles (right) of the driver (D) and witness (W) beams at the low-energy (118 MeV) diagnostics beamline, as provided by the input macroparticle distribution in ASTRA.

### 4.4.3 Beamline matching

The diagnostic line must transport two beams with different properties (high-charge driver and low-charge witness). In practical emittance measurements, the screen signal is dominated by the driver, while the resolution of interest concerns the witness. Therefore, two matching conditions are evaluated: the first optimizes the driver beam, which corresponds to operational matching, and the second optimizes the witness beam for resolution-oriented studies. The reference optics presented

here are obtained by imposing symmetric beta functions at the screen and by requiring the alpha functions to be close to zero. All matching conditions used for the different measurements are derived consistently from this criterion.
The driver-optimized matching is illustrated in Fig. 4.4 and is adopted as the reference optics because it reflects the standard operating condition and ensures robust transport for the dominant beam on the screen.

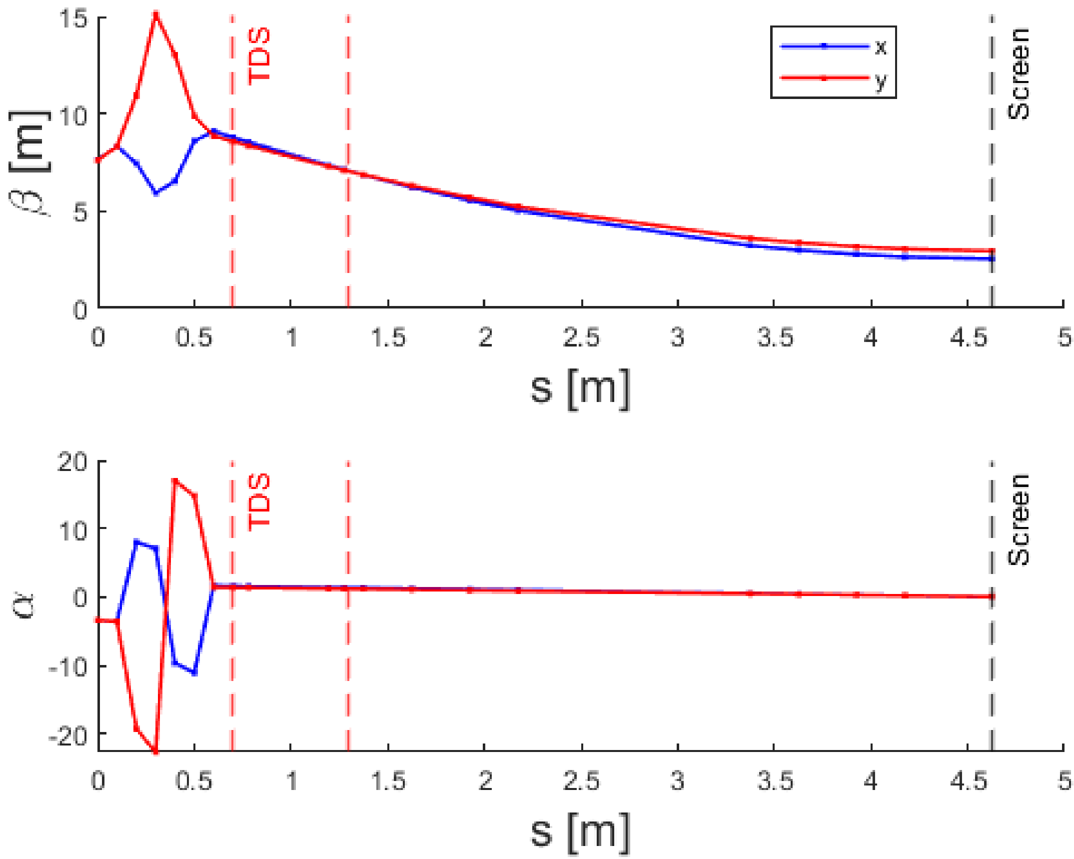


**Figure 4.4:** Twiss parameters evolution of the driver beam in the low-energy diagnostics beamline, up to the screen on the straight section, for the last quadrupole focusing in x.

To assess the diagnostic resolution on the low-charge witness, it is also considered a witness-optimized optics, shown in Fig. 4.5, obtained by performing the matching using the witness Twiss parameters as initial conditions. This reduces the witness $\beta$ (and spot) at the screen, enabling the intended resolution study, at the cost of a larger driver spot.

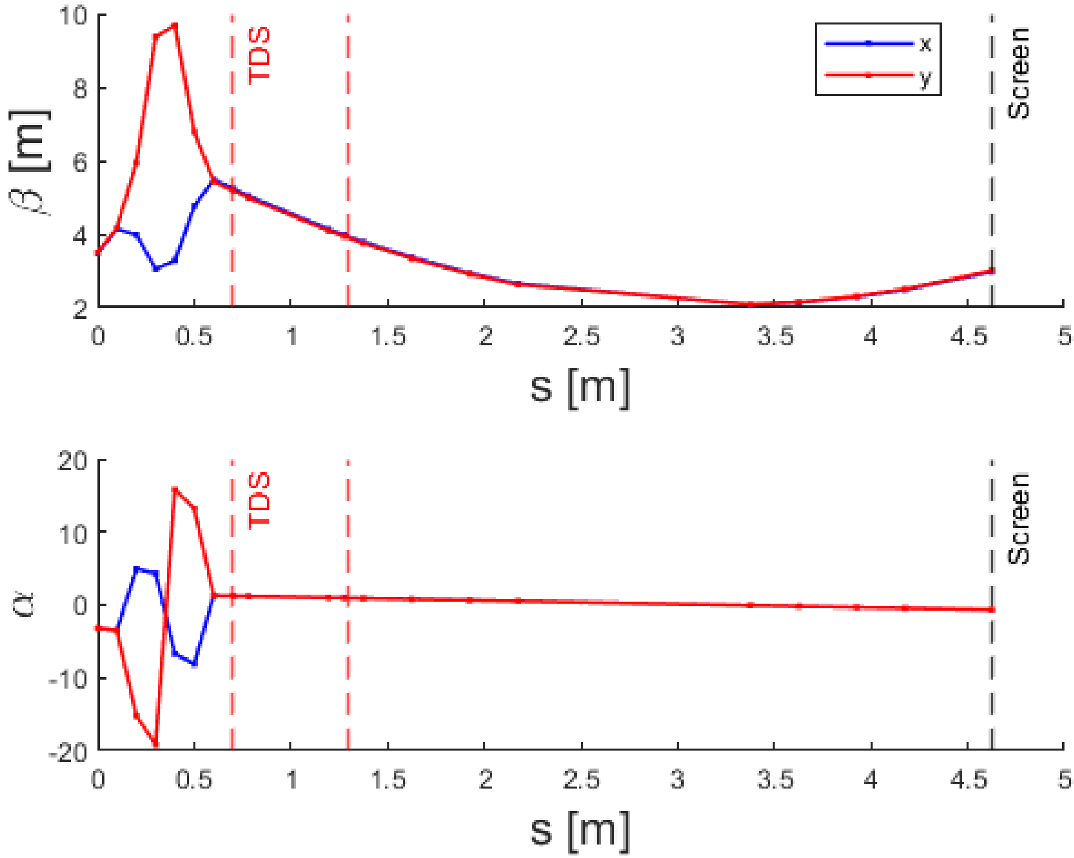


**Figure 4.5:** Twiss parameters evolution of the witness beam in the low-energy diagnostics beamline, up to the screen on the straight section.

Since the Twiss parameters at the line entrance are symmetric in $x$ and $y$, changing the sign of the quadrupole strengths yields identical transport with the roles of the two planes swapped, leading to the same parameters at the screen. In Table 4.2, the Twiss parameters at the screen for two configurations are reported.

| **Parameters** | **Driver**(1) | **Witness**(1) | **Driver**(2) | **Witness**(2) |
|---|---|---|---|---|
| $\beta_x$ $[m]$ | 2.6 | 18.2 | 17.4 | 2.3 |
| $\beta_y$ $[m]$ | 2.9 | 19.0 | 15.4 | 3.0 |
| $\alpha_x$ | 0.03 | $-1.87$ | $-6.92$ | $-0.66$ |
| $\alpha_y$ | 0.05 | $-2.22$ | $-6.30$ | $-0.67$ |

**Table 4.2:** Driver and witness Twiss parameters at the screen, for the driver-optimized(case 1) and witness-optimized (case 2) matching.

### 4.4.4 Space charge effects on beam dynamics

At low energies (118 MeV), space-charge (SC) forces can influence the beam dynamics of both the driver and the witness bunches, affecting their transverse and longitudinal phase spaces. To quantify their impact, dedicated simulations were performed with and without space-charge effects enabled. The results allow assessing whether SC plays a significant role in the measured quantities or can be safely neglected for the considered working point.
The comparison was carried out for both bunches, focusing on the main reconstructed parameters at the screen: the transverse beam sizes $\sigma_x$ and $\sigma_y$, the normalized emittances, and the temporal bunch length $\sigma_t$. For each case, the values obtained with SC OFF and SC ON were compared, and their relative variations were computed. Fig. 4.6 shows, for the witness bunch, the transverse beam sizes with (solid line) and without (dashed line) space charge, indicating minimal differences between the two cases (a few $\mu m$). In Fig. 4.7 A similar behavior is observed for the driver, with slightly larger variations, in the order of $\sim 10\ \mu m$.

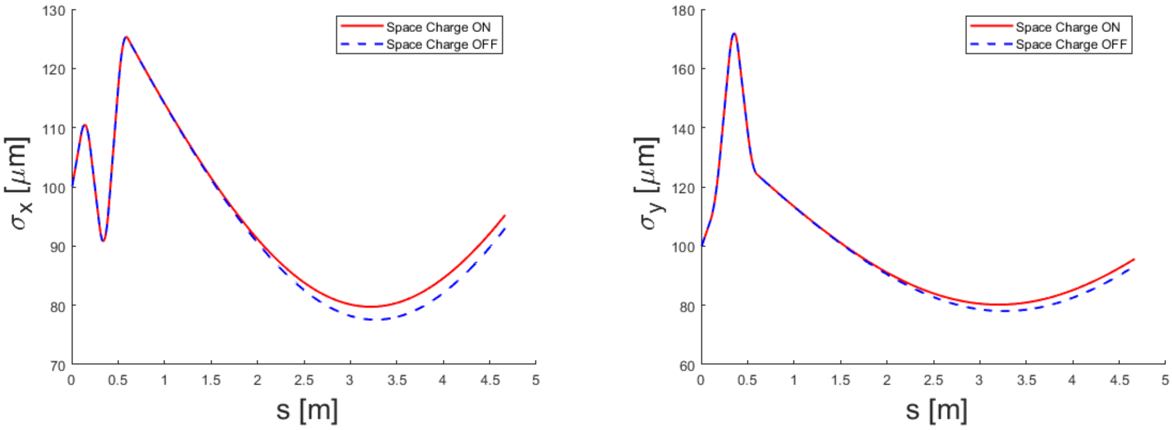


**Figure 4.6:** Transverse beam size of the witness beam along the low-energy beamline, for $x$ (left) and $y$ (right), with (solid line) and without (dashed line) space charge.

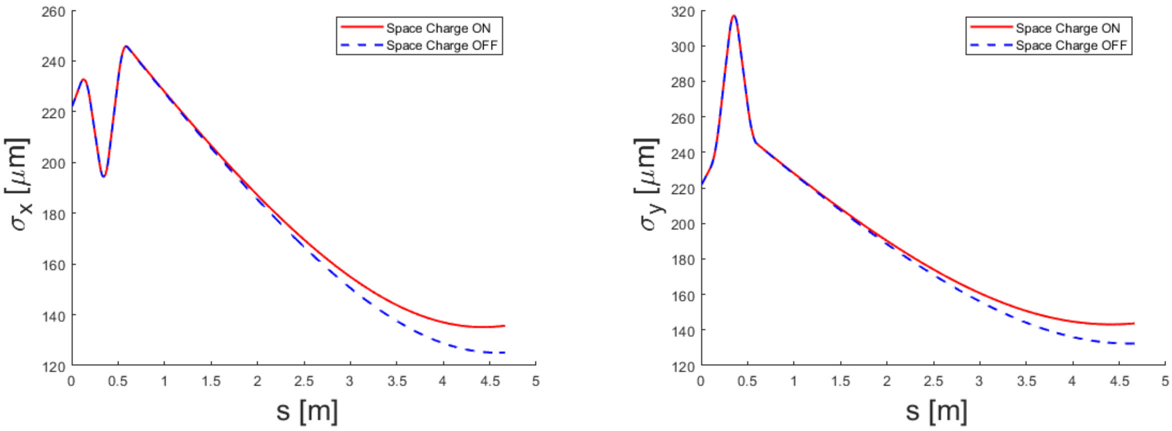


**Figure 4.7:** Transverse beam size of the driver beam along the low-energy beamline, for $x$ (left) and $y$ (right), with (solid line) and without (dashed line) space charge.

The temporal profiles of both bunches, shown in Fig. 4.8, are perfectly overlapping, confirming that the longitudinal dynamics is not affected by SC at this energy.

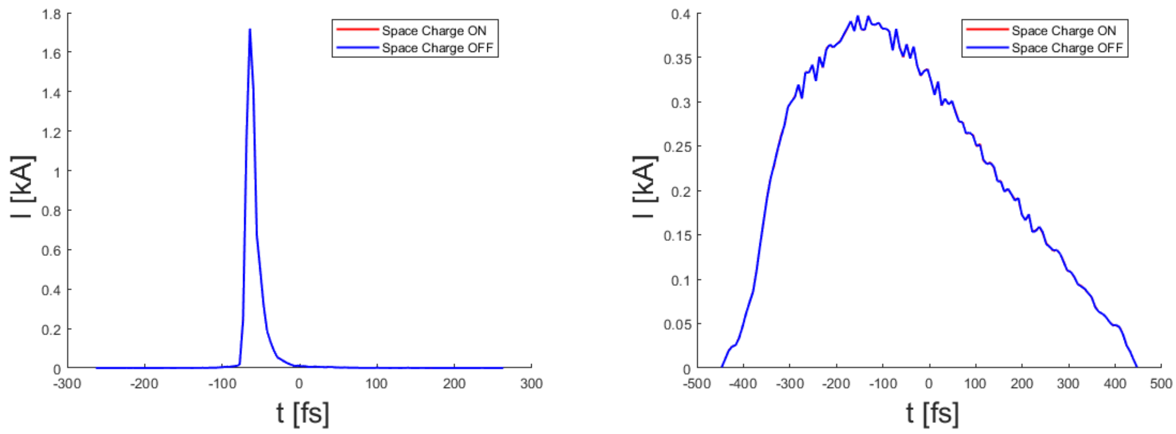


**Figure 4.8:** Temporal profile of the witness (left) and driver (right) at the end of the low-energy beamline, with (red line) and without (blue line) space charge; the profiles are completely overlapped, showing that there is no significant effect on the longitudinal profile originating from the space charge.

The quantitative results are summarized in Table 4.3, reporting for both driver and witness the transverse sizes, normalized emittances, and bunch length with and without SC, together with their relative variations. The differences are within a few percent, demonstrating that space-charge effects have a negligible influence on the beam parameters at 118 MeV for the simulated charge and optics configuration. These effects will be included in the simulations carried out at this diagnostics beamline.

| | **SC. ON** | **SC. OFF** | **Diff. [%]** |
|---|---|---|---|
| **Witness** | | | |
| $\sigma_x$ [$\mu m$] | 95 | 93 | 2.6 |
| $\sigma_y$ [$\mu m$] | 96 | 93 | 2.4 |
| $\varepsilon_{n,x}$ [$\mu m$] | 0.662 | 0.660 | 0.2 |
| $\varepsilon_{n,y}$ [$\mu m$] | 0.658 | 0.656 | 0.3 |
| $\sigma_t$ [fs] | 17.23 | 17.22 | 0.05 |
| **Driver** | | | |
| $\sigma_x$ [$\mu m$] | 136 | 125 | 8.5 |
| $\sigma_y$ [$\mu m$] | 144 | 132 | 8.6 |
| $\varepsilon_{n,x}$ [$\mu m$] | 1.58 | 1.55 | 2.4 |
| $\varepsilon_{n,y}$ [$\mu m$] | 1.62 | 1.58 | 2.6 |
| $\sigma_t$ [fs] | 191.10 | 191.07 | 0.02 |

**Table 4.3:** Comparison of main beam parameters with and without space charge at 118 MeV. Relative variations are computed as (SC. ON − SC. OFF)/SC. OFF × 100.

### 4.4.5 Emittance measurement simulation

**Nominal bunch at 118 MeV** The quadrupole scan method was applied to both the witness and driver beams at 118 $MeV$ in both transverse planes. For each transverse plane, the quadrupole strength $k$ was varied over a range of values corresponding to $\alpha$ spanning from about -2.1 to 0.45. The distance between the last quadrupole and the screen is about 4.05 m. At each setting, the transport matrix elements and the beam size at the screen are determined from the simulation. The dependence of $\sigma^2$ from the quadrupole strength was then fitted with the model described in Sec. 2.4, from which the emittance is reconstructed.
Figure 4.9 shows the fit for the nominal witness beam in both transverse planes, as a function of the quadrupole normalized strength $k$. In addition to the analytic estimate of the uncertainty on $\sigma$ obtained from the screen resolution, the error on the reconstructed beam size is also evaluated through Monte Carlo simulations, in which shot-to-shot fluctuations are generated within the instrumental resolution, giving a consistent estimate of the corresponding uncertainty. The uncertainty on $\sigma^2$ is estimated by evaluating the function at the extreme values of the measured quantity, i.e. at $\sigma \pm \delta\sigma$, and taking the largest deviation as the error bar:

$$\delta(\sigma^2) = \max\left[(\sigma + \delta\sigma)^2 - \sigma^2,\ \sigma^2 - (\sigma - \delta\sigma)^2\right].$$

The reconstructed emittances are then summarized in Table 4.4, together with the input values used in the simulation and the corresponding relative errors.

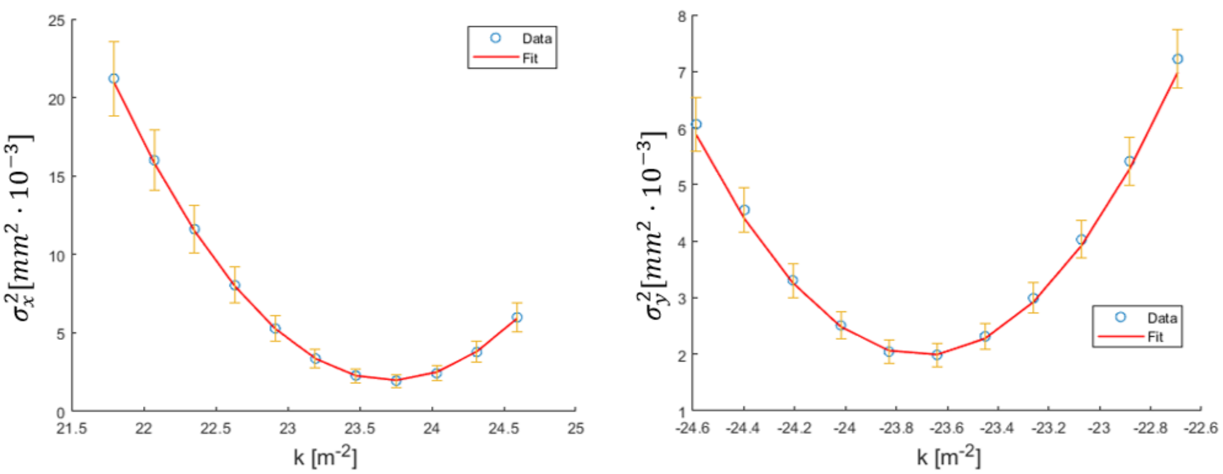


**Figure 4.9:** Virtual measurement of the transverse beam size as a function of the normalized quadrupole strength $k$ for the witness beam in the $x$-plane (left) and $y$-plane (right), at the low-energy diagnostics beamline.

**Resolution determination** The resolution of the emittance measurement was estimated through dedicated simulations with ideal Gaussian beams of progressively smaller input emittance. For each case, the quadrupole scan procedure was repeated as described above, and the reconstructed emittance was compared with the corresponding input value. The results are summarized in Table 4.5 for both the $x$ and $y$ planes. The reconstructed emittance follows the input values down to about 0.3 $\mu m$, below which the relative and differential errors increase significantly over 10%. Therefore, the effective resolution of the measurement at 118 MeV is estimated to be approximately 0.3 $\mu m$.

| **Parameters** | **Witness** | | **Driver** | |
|---|---|---|---|---|
| | $x$ | $y$ | $x$ | $y$ |
| Input $\varepsilon_n$ [$\mu m$] | 0.66 | 0.65 | 1.50 | 1.50 |
| Reconstructed $\varepsilon_n$ [$\mu m$] | 0.68 | 0.65 | 1.48 | 1.46 |
| Error [$\mu m$] | 0.05 | 0.05 | 0.08 | 0.06 |
| Rel. error [%] | 7.7 | 6.2 | 5.4 | 4.1 |

**Table 4.4:** Input and reconstructed emittances at 118 MeV for the witness and driver beams in both transverse planes.

| Plane | Input $\varepsilon_n$ [$\mu m$] | Reconstructed $\varepsilon_n$ [$\mu m$] | Error [$\mu m$] | Rel. error [%] | Difference [%] |
|---|---|---|---|---|---|
| $x$ | 0.50 | 0.52 | 0.04 | 7.6 | 4.9 |
| $x$ | 0.40 | 0.44 | 0.03 | 7.7 | 9.0 |
| $x$ | 0.30 | 0.34 | 0.03 | 8.1 | 13.1 |
| $x$ | 0.20 | 0.24 | 0.02 | 8.6 | 19.7 |
| $x$ | 0.10 | 0.13 | 0.01 | 9.6 | 33.9 |
| $y$ | 0.50 | 0.52 | 0.03 | 4.1 | 4.9 |
| $y$ | 0.40 | 0.43 | 0.02 | 5.1 | 6.5 |
| $y$ | 0.30 | 0.33 | 0.02 | 6.2 | 9.2 |
| $y$ | 0.20 | 0.23 | 0.02 | 7.4 | 15.2 |
| $y$ | 0.10 | 0.13 | 0.02 | 11.8 | 25.1 |

**Table 4.5:** Input and reconstructed emittances for the resolution study at 118 MeV, obtained with Gaussian beams of decreasing emittance.

**Screen resolution influence on emittance measurement** To assess the influence of the imaging system on the emittance measurement, a dedicated scan was performed by varying the screen resolution while keeping all other parameters fixed. The simulations were first carried out for the nominal configuration, corresponding to a screen resolution of 3.5 $\mu m$ (magnification $M = 1$), and then repeated for higher magnifications, resulting in effective resolutions of 5.25 $\mu m$ ($M = 1.5$) and 7.0 $\mu m$ ($M = 2$). For each case, the reconstructed emittance, considered here as the effective measurement resolution, was evaluated together with the relative error on its calculation and the deviation from the input value used in the simulation. Considering as a reference the measurement in the $x$-plane, since it is the plane limiting the overall resolution, the obtained results are summarized in Table 4.6, and show how the uncertainties on the emittance corresponding to the resolution limit increase, showing that the resolution limit increases up to 0.4 $\mu m$ at 7 $\mu m$ of screen resolution.

| **Parameter** | 3.5 [$\mu m$] | 5.2 [$\mu m$] | 7.0 [$\mu m$] |
|---|---|---|---|
| Reconstructed $\varepsilon_{n,x}$ [$\mu m$] | 0.3 | 0.3 | 0.4 |
| Rel. Error [%] | 8.1 | 10.6 | 9.7 |
| Deviation from input [%] | 13.1 | 11.2 | 9.1 |

**Table 4.6:** Emittance resolution scan as a function of the screen resolution at the low-energy beamline. The reconstructed emittance is taken as the effective measurement resolution; the corresponding relative error and deviation from the input value are also reported.

### 4.4.6 Spectrometer simulation

The low-energy diagnostics station includes a magnetic spectrometer designed to measure the beam energy and energy spread in the 100–250 MeV range. The system employs a 25 cm-long dipole magnet with a nominal deflection angle of 22 degrees. A dispersive screen is positioned downstream of the dipole to image the beam's energy distribution. In this section, the measurement parameters for different dipole-screen distances and different screen resolutions are evaluated. The spectrometer line extends for approximately 3 m, terminating at the beam dump. Simulations were performed by varying the screen position from 0.5 m to 2 m downstream of the dipole exit to determine the optimal configuration for energy measurements. A reference distance of 1.5 m has been adopted for most of the following analyses, as it provides a good compromise between energy resolution and screen image coverage.

Both the driver and the witness bunches were simulated, and their energy distributions were measured under identical conditions (1.5 m screen distance, 3.5 $\mu m$ of screen resolution). This allows evaluating the achievable energy separation and the measurement accuracy for each bunch individually. Figures 4.10 and 4.11 show the simulated images and energy profiles of the two bunches on the dispersive screen. The main parameters of the measurement are reported in Table 4.7.

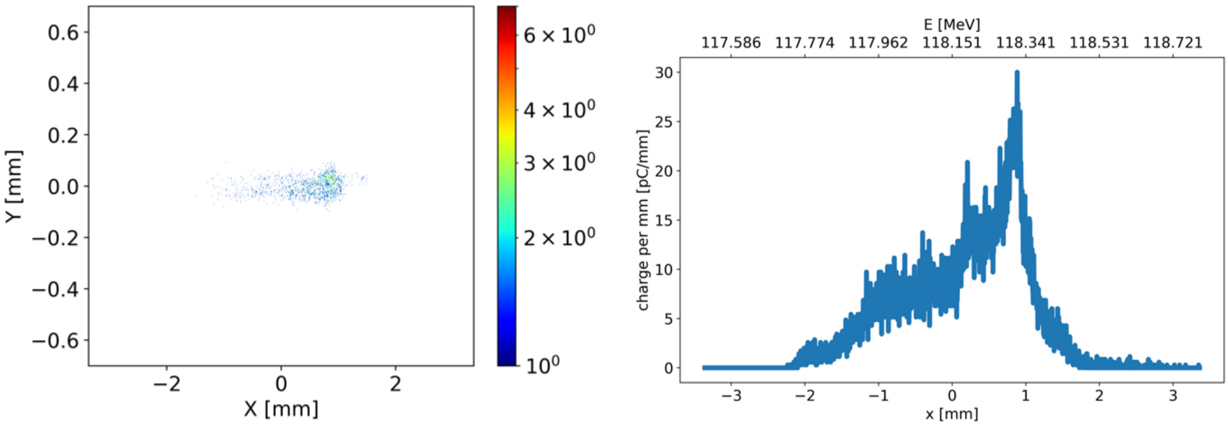


**Figure 4.10:** Witness signal acquired at the low-energy spectrometer screen (left) and the corresponding energy profile (right), taken at the reference distance of 1.5 m from the dipole, and a screen resolution of 3.5 $\mu m$.

| Parameter | Witness | Driver | Unit |
|---|---|---|---|
| $E_{\text{mean}}$ | 118.2 | 119.7 | MeV |
| $\sigma_E$ | 156.0 | 784.8 | keV |
| $E_{\text{FWHM}}$ | 714.7 | 3704.3 | keV |

**Table 4.7:** Summary of the spectrometer measurement results for the driver and witness bunches at the low-energy diagnostics station. $E_{\text{mean}}$ is the average beam energy, $\sigma_E$ the RMS energy spread, and $E_{\text{FWHM}}$ the full width at half maximum of the energy distribution.

In Fig. 4.12, the driver and witness beams are visible in the same screen acquisition. The result confirms that the spectrometer provides sufficient resolution to separate the two bunches.

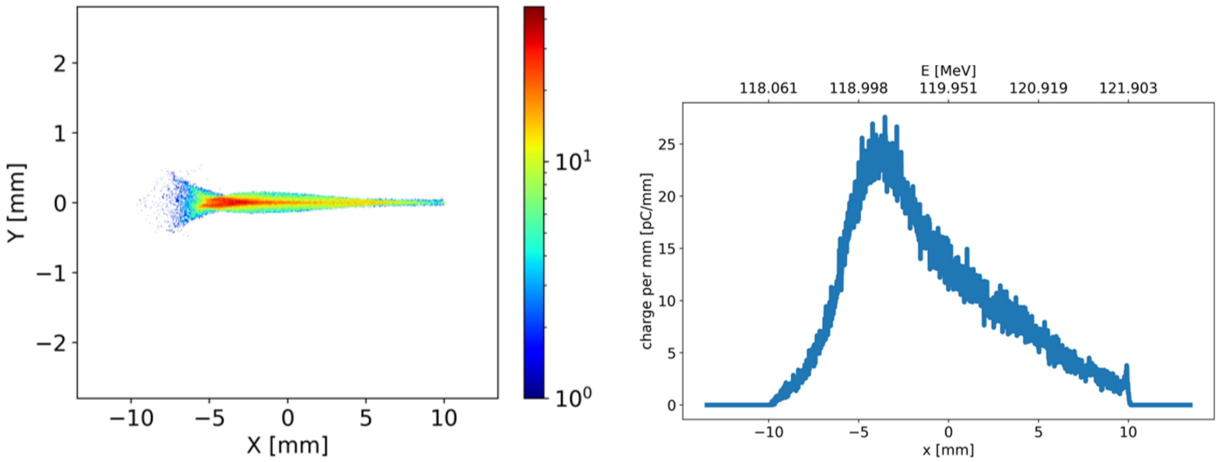


**Figure 4.11:** Driver signal acquired at the low-energy spectrometer screen (left) and the corresponding energy profile (right), taken at the reference distance of 1.5 m from the dipole, and a screen resolution of 3.5 $\mu m$.

**Effect of synchrotron radiation** In energy measurements, collective effects, such as coherent and incoherent synchrotron radiation (SR), must also be considered. These effects can alter the bunch's energy distribution as it passes through the dipole, leading to a discrepancy between the beam energy profile reconstructed at the spectrometer screen and that evaluated at the dipole entrance.

In Table 4.8 are reported the variations of the reconstructed parameters with and without SR, with the difference between the reconstructed and initial mean energies, and between the reconstructed and initial RMS energy spreads. In the presence of synchrotron radiation, the differences between the reconstructed and expected mean energy and RMS energy spread increase, showing that SR can significantly modify the measured energy profile, producing deviations of a few keV from the nominal values. Although such differences are negligible in terms of mean energy, they are non-negligible when evaluating the energy spread and should therefore be properly accounted for in the analysis.

| **Parameter** | **SR** | **NO SR** |
|---|---|---|
| $E_{\text{mean}}$ [MeV] | 118.18 | 118.22 |
| $\sigma_E$ [keV] | 156.0 | 143.1 |
| $E_{\text{FWHM}}$ [keV] | 714.7 | 705.6 |
| $(E_{\text{mean}_{\text{input}}} - E_{\text{mean}_{\text{screen}}})$ [keV] | -34.8 | 1.5 |
| $(\sigma_{E_{\text{input}}} - \sigma_{E_{\text{screen}}})$ [keV] | 15.4 | 2.4 |

**Table 4.8:** Summary of the synchtron radiation influence in the spectrometer measurement for the witness bunch at the low-energy diagnostics station (screen distance 1.5 m, screen resolution 3.5 $\mu m$).

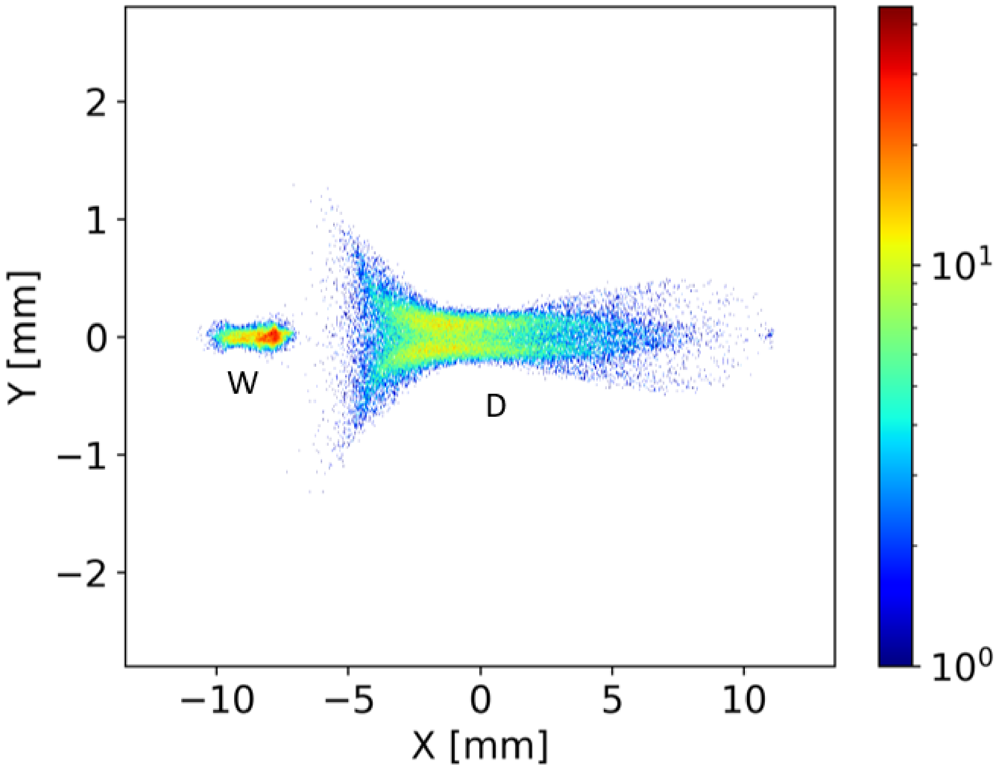


**Figure 4.12:** Low-energy driver (D) and witness (W) bunches observed in the same spectrometer screen image, demonstrating the system's capability to resolve both beams, considering a screen at 1.5 m from the dipole with a resolution of 3.5 $\mu m$.

**Screen position determination** The energy resolution was evaluated as a function of the screen position along the spectrometer line, considering the witness beam as a reference. For each configuration, the differences between the simulated parameters (average and RMS energy) before the dipole and at the screen, the minimum and maximum energy bin sizes, and the retrieved RMS energy of the bunch were computed. The results are summarized in Table 4.9.

| **Parameter** | **0.5 m** | **1 m** | **1.5 m** | **2 m** |
|---|---|---|---|---|
| $(E_{\text{mean}_\text{input}} - E_{\text{mean}_\text{screen}})$ [keV] | -33.9 | -34.5 | -34.8 | -35.4 |
| $(\sigma_{E_\text{input}} - \sigma_{E_\text{screen}})$ [keV] | 10.1 | 13.2 | 15.4 | 16.0 |
| Min $E_{bin}$ [keV] | 1.67 | 0.94 | 0.66 | 0.50 |
| Max $E_{bin}$ [keV] | 1.77 | 0.97 | 0.67 | 0.51 |
| $\sigma_E$ [keV] | 150.8 | 153.8 | 156.0 | 156.7 |

**Table 4.9:** Simulated energy measurement parameters at the low-energy spectrometer for different dipole-screen distances. All values are expressed in [keV].

The reference screen position at 1.5 m was selected as it provides a sufficient energy resolution while accurately reproducing the expected energy profile of the bunch.

**Effect of the Screen Resolution** The impact of the screen resolution was assessed by varying the effective pixel size on the dispersive axis to 3.5 $\mu m$, 5.25 $\mu m$, and 7 $\mu m$, corresponding to magnification settings of $M = \{1.0, 1.5, 2.0\}$, respectively. For each configuration, the same figures of merit used in the screen-distance scan are computed: the difference between the reconstructed values before and after the dipole, minimum and maximum bin width values along the energy axis, and the retrieved RMS energy spread of the bunch. The results are summarized in Table 4.10.

| **Parameter** | **3.5** $\mu m$ | **5.25** $\mu m$ | **7** $\mu m$ |
|---|---|---|---|
| $(E_{\text{mean}_{\text{input}}} - E_{\text{mean}_{\text{screen}}})$ [keV] | -34.8 | -34.8 | -34.8 |
| $(\sigma_{E_{\text{input}}} - \sigma_{E_{\text{screen}}})$ [keV] | 15.4 | 15.6 | 15.6 |
| Min $E_{bin}$ [keV] | 0.66 | 0.98 | 1.30 |
| Max $E_{bin}$ [keV] | 0.67 | 1.01 | 1.35 |
| $\sigma_E$ [keV] | 156.0 | 156.3 | 156.3 |

**Table 4.10:** Simulated energy measurement parameters at the low-energy spectrometer for different screen resolutions (effective pixel sizes). All values are expressed in [keV].

Within the explored range, increasing the effective pixel size (i.e., coarser screen resolution) enlarges the energy-bin width as expected, yet the reconstructed mean energy and RMS energy spread remain essentially unaffected by the screen resolution (even for the coarsest setting), accurately reproducing the expected energy profile.

### 4.4.7 Bunch length measurement simulation

**Longitudinal resolution** The bunch length measurement at the low-energy beamline was carried out using the 60 cm PolariX TDS, operated in both vertical and horizontal streaking configurations. To estimate the achievable system resolution, a maximum deflecting voltage of $V_{\text{max}} = 23$ MV was considered, in accordance with the RF limits of the structure. The unstreaked beam size at the measurement screen was $\sigma_{\text{off}} = 60$ $\mu$m in both transverse planes, with shot-to-shot fluctuations of approximately 10%, which translate into a comparable variation of the expected resolution.

Table 4.37 summarizes the main parameters used for the resolution calculation. Two beam configurations were analyzed: the nominal case at 118 MeV and the maximum-energy case at 250 MeV (all injector cavities operated on-crest). The target resolution was set to 0.5 $\mu$m in both planes for the 118 MeV case. This limit was relaxed to 1 $\mu$m for the 250 MeV beam, as the bunch is expected to be longer when operating the injector in velocity-bunching mode.

| **Parameter** | **Nominal** | **On-crest** |
|---|---|---|
| Beam energy [MeV] | 118 | 250 |
| Max Deflecting voltage [MV] | 23 | |
| TDS Length [m] | 0.60 | |
| Distance TDS-Screen [m] | 3.45 | |
| $\sigma_{off}$ [$\mu m$] | 60 | |
| Max resolution [fs] | 1.1 | 2.3 |

**Table 4.11:** Beam and TDS parameters adopted for the longitudinal resolution evaluation at the low-energy section.

Figure 4.13 shows the estimated longitudinal resolution as a function of the deflecting voltage for the given beam parameters. The dashed line represents the target resolution for each beam configuration, while the shaded upper and lower bounds correspond to a ±10% variation of the unstreaked beam size at the measurement screen.

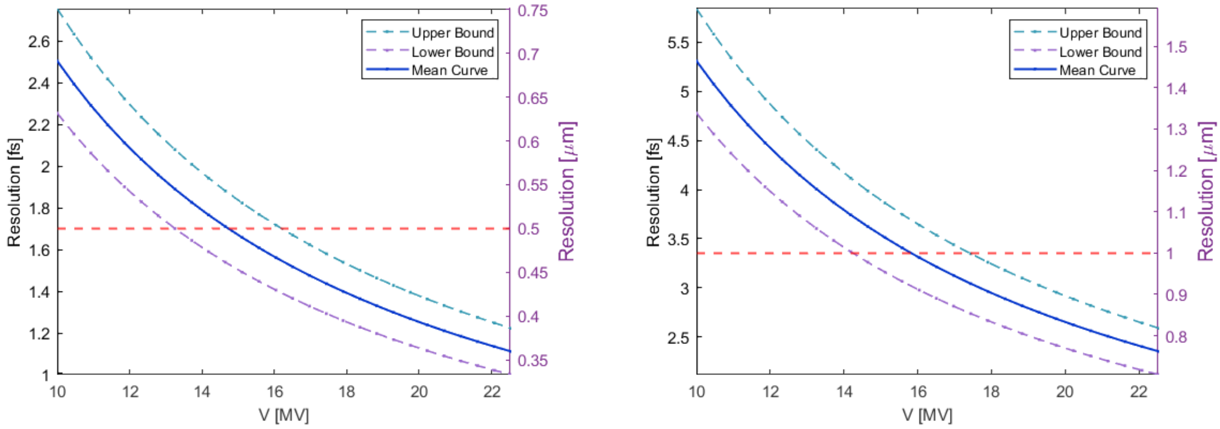


**Figure 4.13:** Estimated longitudinal resolution at the low-energy diagnostic beamline as a function of the deflecting voltage, up to the maximum achievable value of 23 MV, for nominal 118 MeV beam configuration (left), and 250 MeV case (right). The solid curve indicates the mean estimated resolution, with upper and lower boundaries obtained by considering a ±10% variation of the unstreaked beam size at the measurement screen. The dashed horizontal lines represent the target resolutions of 0.5 $\mu$m and 1 $\mu$m for the two energy configurations, respectively.

**TDS calibration** The calibration was performed by varying the RF phase of the deflecting cavity around the zero-crossing using ASTRA simulations. For each phase setting, the bunch centroid position at the screen was extracted, and the relative offset was computed with respect to the centroid position at the zero-crossing (corresponding to the unstreaked beam centroid position). The resulting calibration fit is shown in Fig. 4.14, where the centroid position is plotted as a function of the RF phase. A linear fit was performed to extract the calibration coefficient (slope) and to retrieve the integrated deflecting voltage from the data. The latter value is expected to match the nominal 20 MV used as input to the simulation, validating the accuracy of the procedure. The parameters obtained from the calibration at vertical and horizontal streaking are reported in Table 4.12.

| **Parameter** | **x Streaking** | **y Streaking** |
|---|---|---|
| $\sigma_{off}$ [$\mu m$] | $54 \pm 5$ | $54 \pm 5$ |
| V [MV] | $20.0 \pm 0.5$ | $20.0 \pm 0.6$ |
| Calibration [$\mu m$/fs] | $47 \pm 1$ | $47 \pm 2$ |
| Screen Calibration [fs/pixel] | $\sim 0.07$ | $\sim 0.07$ |
| Shear Parameter [$\mu m/\mu m$] | $156.2 \pm 0.7$ | $156.1 \pm 0.7$ |
| Resolution [fs] | $1.1 \pm 0.2$ | $1.1 \pm 0.2$ |

**Table 4.12:** TDS Calibration results for the low-energy beamline. The reported uncertainty corresponds to the propagated error from the linear fit parameters.

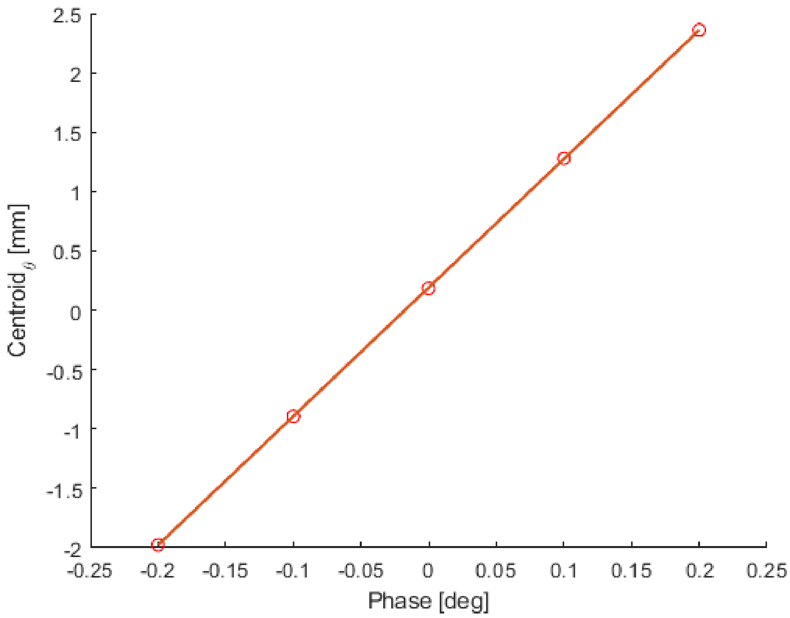


**Figure 4.14:** TDS calibration at 118 MeV: centroid position on the screen versus RF phase around the zero-crossing. The linear fit (solid line) provides the calibration factor.

**Driver-witness separation** As shown in Fig. 4.3, the separation between the driver and witness must be evaluated to confirm that it is possible to distinguish them, and thus to perform an independent measurement of the witness, which could otherwise overlap with the driver. This section aims to verify the longitudinal diagnostic system based on the TDS ability to resolve the driver and witness bunches on the observation screen. The purpose of this analysis is to assess, for different deflecting voltages, whether the witness can be clearly distinguished in the longitudinal phase space, given the imaging system's intrinsic resolution. In this study, the reference screen resolution was chosen as the worst among those considered, corresponding to a pixel size of approximately 7 $\mu m$ per pixel. A voltage scan of the TDS was then performed at this fixed resolution to evaluate the bunch-separation capability as a function of the deflecting voltage.

For each voltage setting, the TDS calibration factor and the corresponding temporal calibration on the screen (expressed in fs/pixel) were used to estimate the effective distance between the two bunches. The separation was quantified as the center-to-center distance and the head-to-tail distance, with the bunch extremities defined as the points at which the signal intensity decreased to 99% of the peak amplitude. These quantities are reported in Table 4.13.

| V [MV] | $\mu$m/fs | fs/pixel | Center–Center [fs] | Head–Tail [fs] | Separated? |
|---|---|---|---|---|---|
| 1 | 2.3 | 3.0 | - | - | No |
| 3 | 7.0 | 1.0 | 509.4 | 10.4 | Partial |
| 6 | 13.9 | 0.5 | 507.8 | 17.0 | Yes |
| 8 | 18.5 | 0.4 | 507.3 | 21.5 | Yes |
| 12 | 27.8 | 0.3 | 504.8 | 25.3 | Yes |

**Table 4.13:** Driver–witness separation scan as a function of the TDS deflecting voltage, performed at the reference screen resolution of 7 $\mu m$/pixel. For each voltage, the effective calibration in $\mu m$/fs and fs/pixel, the center-to-center and head–tail distances between the two bunches, and the visibility of the separation are reported.

The images in Fig. 4.15 show the temporal projections of the driver and witness bunches for different deflecting voltages. For low voltages (e.g., 1–3 MV), the two bunches are not clearly distinguishable on the screen, whereas a progressive separation becomes visible for voltages above 6 MV. At voltages higher than 8 MV, the two bunches are well resolved, enabling a reliable measurement of the witness charge distribution. This confirms that the TDS system provides sufficient temporal resolution to distinguish and measure the two beams independently.

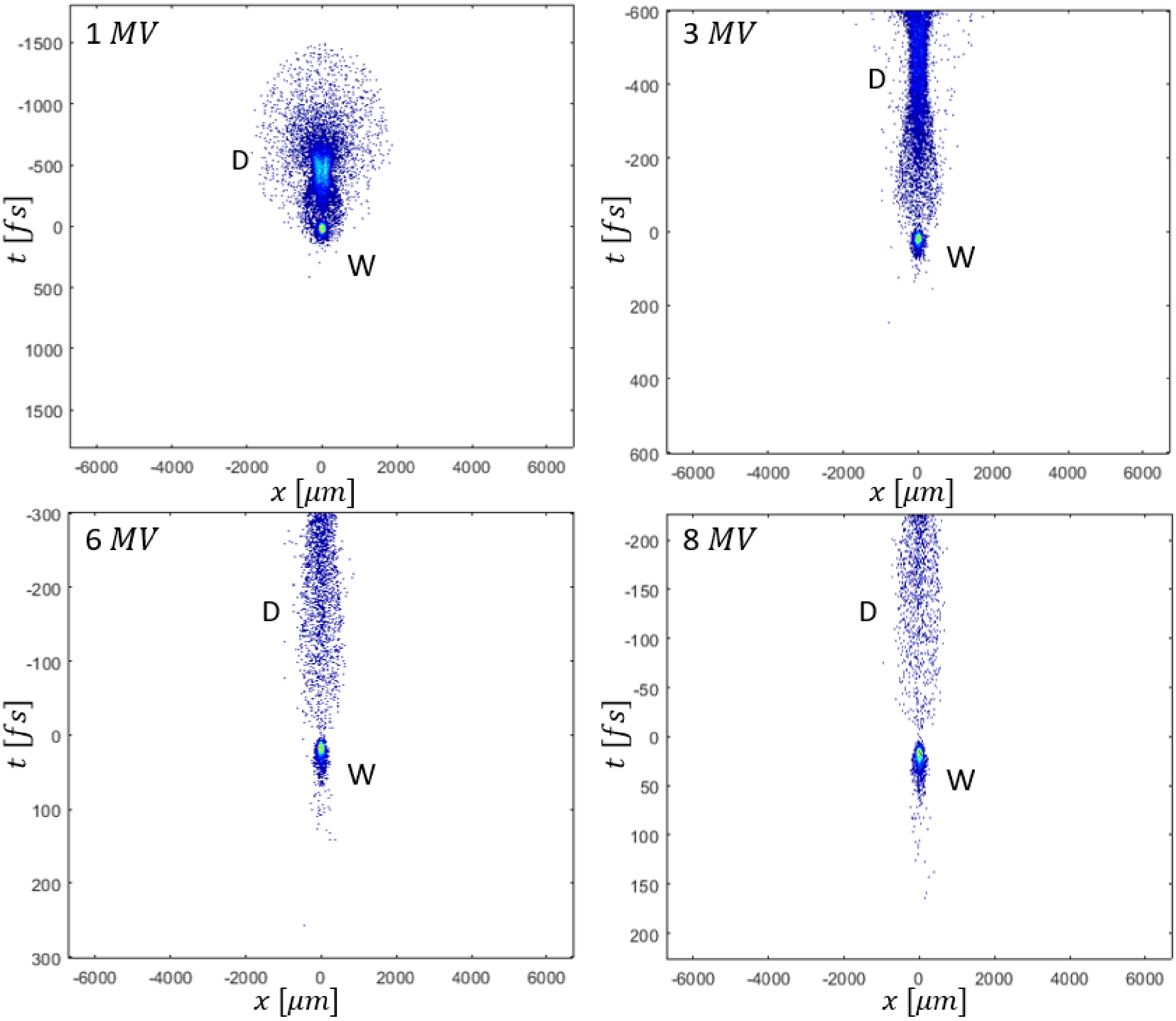


**Figure 4.15:** Screen images showing the longitudinal projections of the driver (D) and witness (W) bunches for different TDS deflecting voltages (1, 3, 6, and 8 MV). For low voltages (1–3 MV), the two bunches are not clearly distinguishable, while for voltages above 6 MV the separation becomes evident, allowing the witness to be individually identified and measured.

**Measurement results** Once the calibration was established, the bunch streaked beam size was measured for both measurements by streaking at the zero-crossing phase. Figure 4.16 shows the simulated beam images obtained at the measurement screen for the two streaking configurations. Finally, the measured temporal profile is shown in Fig. 4.17, together with the expected profile from simulations, showing that the temporal reconstruction correctly matches the input macroparticle distribution.

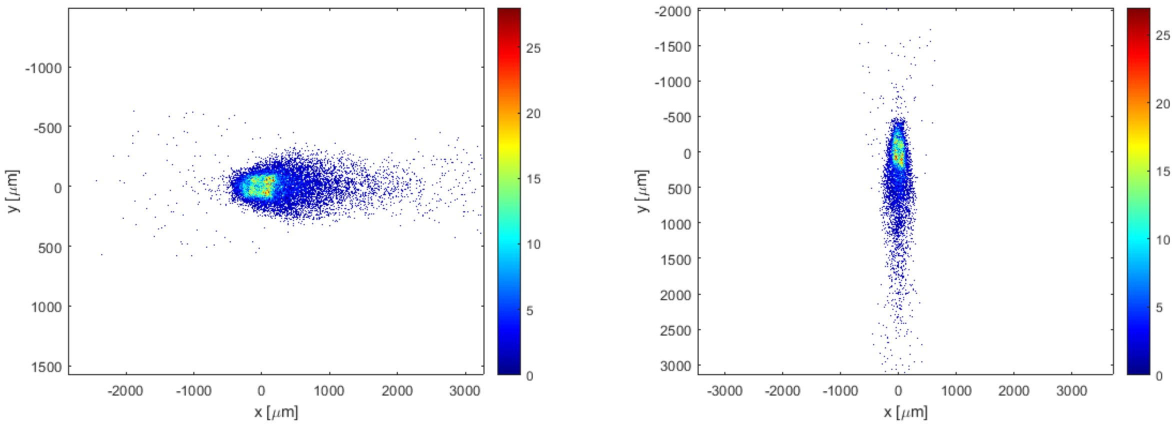


**Figure 4.16:** Simulated beam images at the measurement screen for the horizontal (left) and vertical (right) streaking configurations, obtained with the low-energy PolariX TDS at 20 MV integrated voltage.

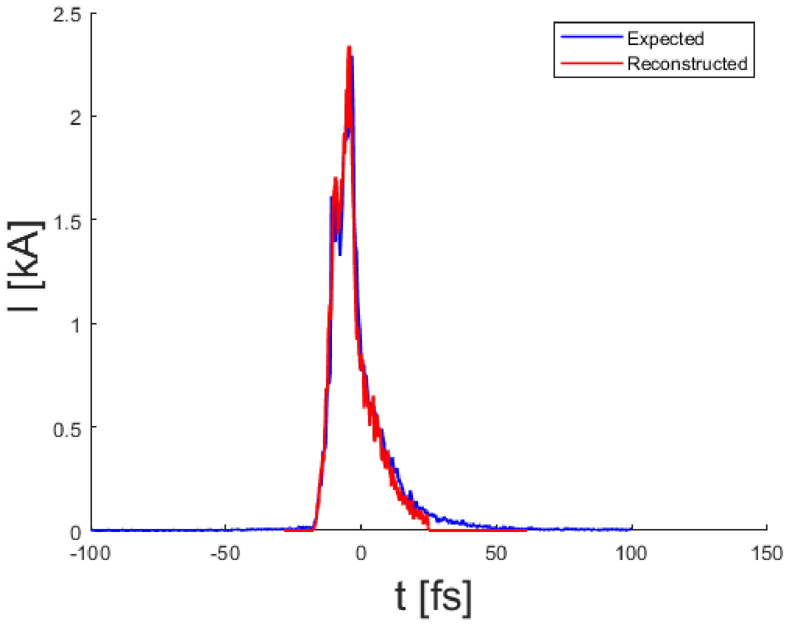


**Figure 4.17:** Reconstructed temporal profile of the witness bunch at 118 MeV compared with the expected profile from simulations. The reconstruction is obtained by vertically streaking the beam and applying the calibration factor to the streaking axis, while the expected one is obtained from the input macroparticle distribution.

Table 4.14 summarizes the comparison between measured and expected values. In summary, the reconstructed bunch length is $\sigma_t = 16 \pm 1$ fs for the witness and $\sigma_t = 188 \pm 3$ fs for the driver beam, in good agreement with the expected value computed from the macroparticle distribution, with respective relative deviation respectively of $\sim 5.9\%$ and $\sim 1.6\%$ from the input value.

**Table 4.14:** Summary of bunch length measurement at 118 MeV for both streaking directions at the low-energy beamline. The mean bunch length is obtained as the weighted average of the two measurements.

| | **Witness** | | **Driver** | |
|---|---|---|---|---|
| | **x-streaking** | **y-streaking** | **x-streaking** | **y-streaking** |
| $\sigma_{t_{\text{expected}}}$ [fs] | $\sim 17$ | | $\sim 191$ | |
| $\sigma_t$ [fs] | $16 \pm 1$ | $16 \pm 1$ | $184 \pm 4$ | $192 \pm 3$ |
| $\sigma_{t_{\text{mean}}}$ [fs] | $16 \pm 1$ | | $188 \pm 3$ | |
| Rel. Error [%] | $\sim 6.1$ | | $\sim 1.6$ | |
| $\lvert\sigma_{t_{\text{mean}}} - \sigma_{t_{\text{expected}}}\rvert$ [%] | $\sim 5.9$ | | $\sim 1.6$ | |

Table 4.15 shows how the result of the bunch length measurement varies as a function of the screen resolution, i.e., of the effective pixel size. As expected, the relative error increases for lower screen resolutions; however, it remains below 10% even for the worst resolution considered, confirming the robustness of the measurement.

| **Screen Res.** | 3.5 $\mu m$ | 5.25 $\mu m$ | 7 $\mu m$ |
|---|---|---|---|
| Pixel Calibration [fs/pixel] | 0.07 | 0.11 | 0.15 |
| $\sigma_t$ [fs] | 16.4 | 16.4 | 16.4 |
| Err. $\sigma_t$ [fs] | 1 | 1.3 | 1.6 |
| Rel. Error [%] | $\sim 6.1$ | $\sim 8.1$ | $\sim 9.8$ |
| $\lvert\sigma_{t_{\text{mean}}} - \sigma_{t_{\text{expected}}}\rvert$ [%] | $\sim 5.9$ | $\sim 5.9$ | $\sim 5.9$ |

**Table 4.15:** Summary of the bunch length measurement with respect to the screen resolution at the low-energy beamline.

## 4.5 Middle-Energy beamline

The middle-energy station is positioned after the bunch compressor, in the section before the last X-band acceleration module. At 400 MeV, the driver and witness pass through a magnetic chicane, where the bunches are longitudinally compressed.

### 4.5.1 Beamline layout

The magnets deployed in this position are three quadrupoles with a magnetic length of 0.15 m and magnetic characteristics equivalent to those of the low-energy quadrupoles. The beam energy is roughly 400 MeV. Downstream of the quadrupoles, a 0.96 m drift section is reserved to accommodate a future installation of a PolariX TDS. Although the deflector is not included in the baseline design of the beamline, the space has been intentionally preserved to allow its integration at a later stage. The measurement screen on the straight section is located at 4.11 m from the last quadrupole, respectively. Since there is no transverse deflector, the planned beamline measurements are limited to emittance measurements via a quadrupole scan and beam energy measurements. The spectrometer consists of a dipole with a magnetic length of 0.4 m and a screen placed 1.5 m in front of the dipole. The straight section of the described layout is depicted in Fig. 4.18.

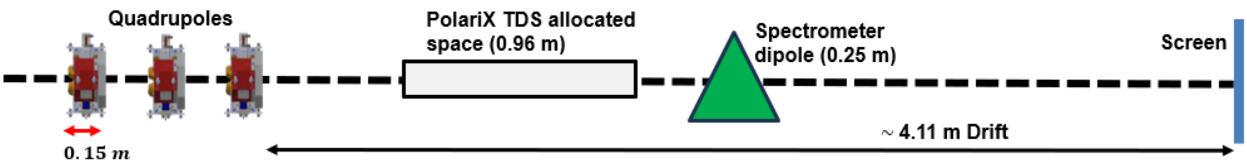


**Figure 4.18:** Layout of the middle-energy diagnostic station (400 MeV). It consists of quadrupoles, a 0.96 m allocated space for the PolariX TDS, a 0.4 m dipole spectrometer, and a screen located after a 2.55 m drift.

### 4.5.2 Simulated beam parameters

In this working point, a transverse mask is inserted in the middle of the chicane. The mask exploits the energy–time correlation of the beam: particles with different energies are transversely displaced in the dispersive region, and the mask physically separates the driver and witness, which would otherwise overlap. This technique provides two distinct bunches, at the cost of reduced charge and potential distortions in the longitudinal phase space. The driver's and witness's charges depend on their separation in the compression chicane. The longitudinal phase space and current profiles of the beams are reported in Fig. 4.19.

The different working points have been chosen to vary the parameters measured relative to the low-energy case. The beam parameters for the driver and witness beam are reported in Table 4.16. After the chicane and mask, the center-to-center distance between driver and witness is about $\sim 1$ ps.

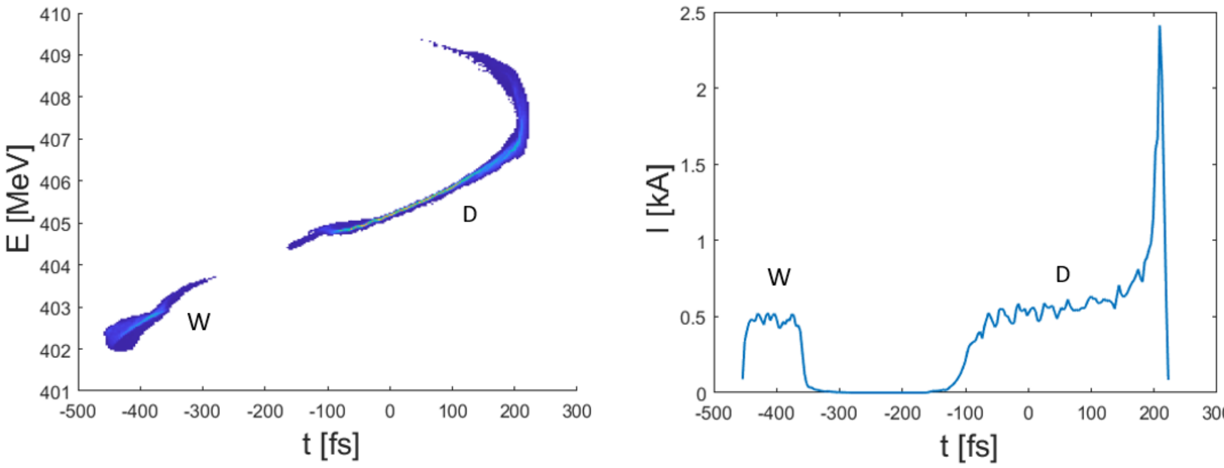


**Figure 4.19:** Longitudinal phase space (left) and corresponding current profiles (right) of the driver (D) and witness (W) beams at the mid-energy (400 MeV) diagnostics beamline, after the bunch compressor, as provided by the input macroparticle distribution in ELEGANT.

| **Parameters** | **Driver** | **Witness** |
|---|---|---|
| Charge $[pC]$ | 207 | 45 |
| Mean Energy $[MeV]$ | 405.98 | 402.62 |
| Energy Spread [%] | 0.22 | 0.06 |
| RMS Bunch length $[fs]$ | 97.23 | 28.46 |
| RMS Bunch length $[\mu m]$ | 29.15 | 8.53 |
| $\varepsilon_{n_x}$ $[\mu m]$ | 1.20 | 1.37 |
| $\varepsilon_{n_y}$ $[\mu m]$ | 0.74 | 0.68 |
| $\beta_x$ $[m]$ | 4.12 | 3.71 |
| $\beta_y$ $[m]$ | 7.64 | 2.31 |
| $\alpha_x$ | 14.96 | $-1.45$ |
| $\alpha_y$ | $-5.01$ | $-5.82$ |

**Table 4.16:** Beams parameters of the working point at the middle-energy (400 MeV) diagnostics station.

### 4.5.3 Beamline matching

The diagnostic line at medium energy must also transport both the high-charge driver and the low-charge witness beams. In analogy with the low-energy case, the screen signal is dominated by the driver, while the emittance-resolution requirement concerns the witness. Therefore, two matching conditions are considered: a driver-optimized optics, representing the operational reference, and a witness-optimized optics, tailored for resolution-oriented studies. The non-symmetric Twiss parameters at the screen impose a strict limitation on the achievable optics. When the last quadrupole is focusing in the $y$-plane, the resulting beta functions at the screen are significantly larger than in the x-focusing case. Therefore, for the emittance measurements in both planes, the x-focusing matching is adopted as the reference configuration to determine the resolution.

The driver-optimized matching is illustrated in Fig. 4.20 and is adopted as the reference optics because it reflects the standard operating condition and ensures robust transport for the dominant beam on the screen. In Table 4.17, the matched Twiss parameters of both beams at the screen are reported.

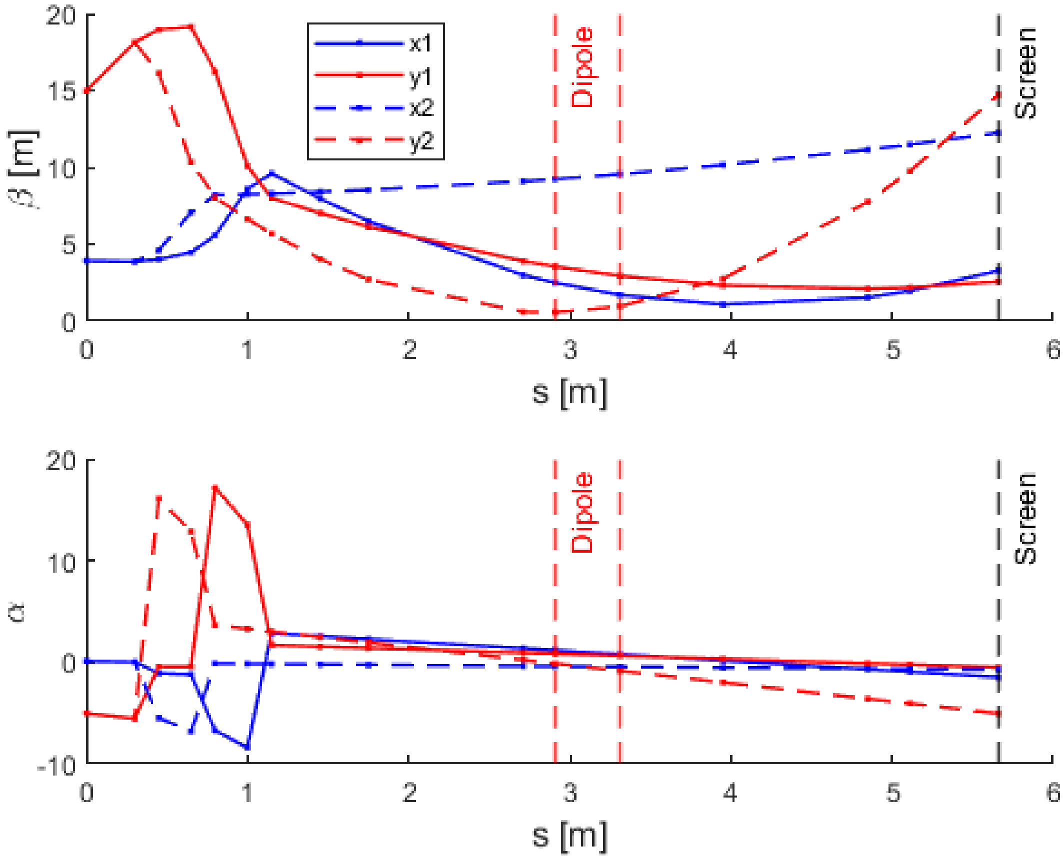


**Figure 4.20:** Twiss parameters evolution of the driver beam in the middle-energy diagnostics beamline, up to the screen on the straight section, for last quadrupole focusing in $x$-plane (1) and $y$-plane (2).

| Parameters | Driver ($x$) | Witness ($x$) | Driver ($y$) | Witness ($y$) |
|---|---|---|---|---|
| $\beta_x$ $[m]$ | 2.1 | 2.0 | 11.6 | 38.4 |
| $\beta_y$ $[m]$ | 2.2 | 5.7 | 10.5 | 37.2 |
| $\alpha_x$ | -1.02 | 0.54 | -0.66 | -3.91 |
| $\alpha_y$ | -0.26 | -2.99 | -4.2 | -12.86 |

**Table 4.17:** Driver and witness Twiss parameters at the screen, after the driver-optimized matching, for two conditions: ($x$) last quadrupole focusing in $x$ and ($y$) last quadrupole focusing in $y$.

For resolution-oriented studies, it is considered a witness-optimized optics. This configuration reduces the witness $\beta$ (and spot) at the screen, enabling the intended diagnostic performance, at the cost of a larger driver spot. The corresponding Twiss evolution and screen parameters are shown in Fig. 4.21 and Table 4.18.

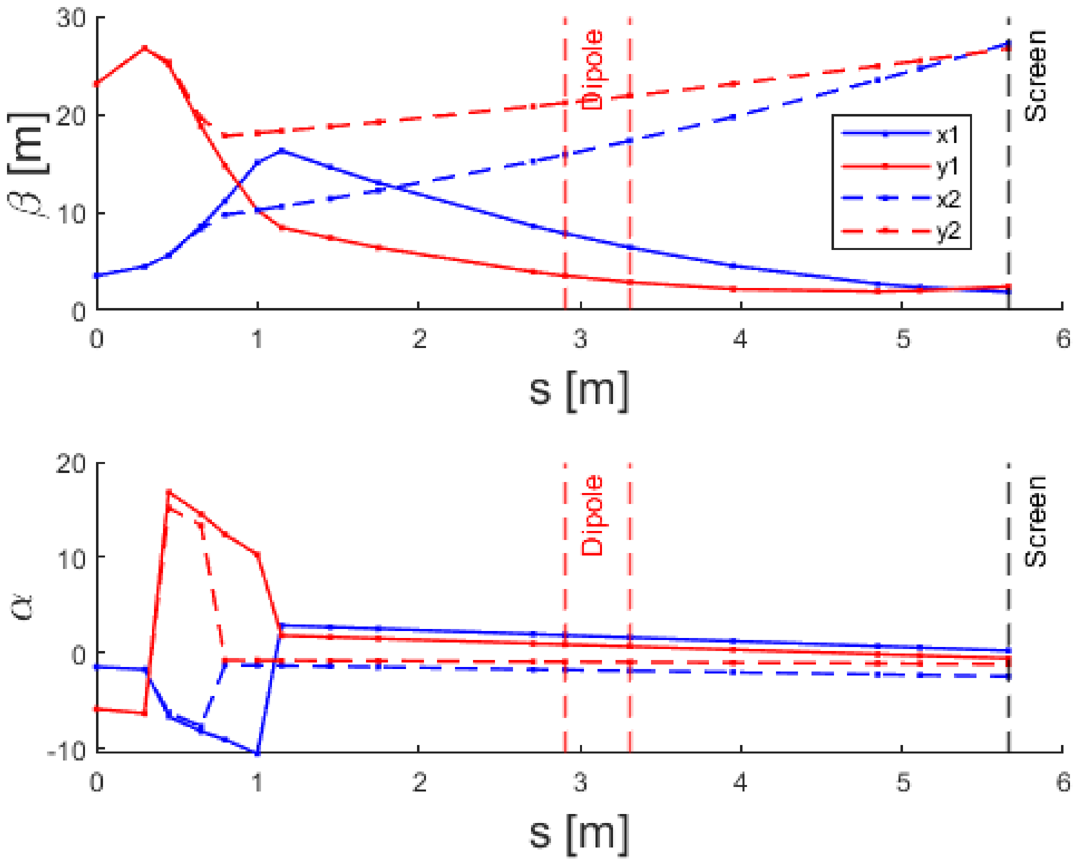


**Figure 4.21:** Twiss parameters evolution of the witness beam in the mid-energy diagnostics beamline, up to the screen on the straight section, for last quadrupole focusing in $x$-plane (1) and $y$-plane (2).

| **Parameters** | **Driver** $(x)$ | **Witness** $(x)$ | **Driver** $(y)$ | **Witness** $(y)$ |
|---|---|---|---|---|
| $\beta_x$ $[m]$ | 2.1 | 2.2 | 6.0 | 25.0 |
| $\beta_y$ $[m]$ | 9.3 | 2.0 | 37.0 | 25.6 |
| $\alpha_x$ | -0.98 | 0.55 | -0.38 | -2.29 |
| $\alpha_y$ | -0.55 | -0.28 | -3.50 | -1.08 |

**Table 4.18:** Driver and witness Twiss parameters at the screen, after the witness-optimized matching, for two conditions: $(x)$ last quadrupole focusing in $x$ and $(y)$ last quadrupole focusing in $y$.

### 4.5.4 Emittance measurement simulation

**Nominal bunch at 400 MeV** The emittance measurement at 400 MeV was performed using the quadrupole scan method, following the same procedure described for the low-energy case. Both witness and driver beams are simulated, and the beam size evolution as a function of the quadrupole strength was fitted to extract the normalized emittances.

The reconstructed values for the witness and driver bunch are summarized in Table 4.19.In both cases, the $x$-plane reconstruction yields errors below 8%, while the $y$-plane is affected by larger uncertainties, especially for the witness beam. In Fig. 4.22 are shown the quadrupole scan curves for the $x$-plane measurement of the witness emittance.

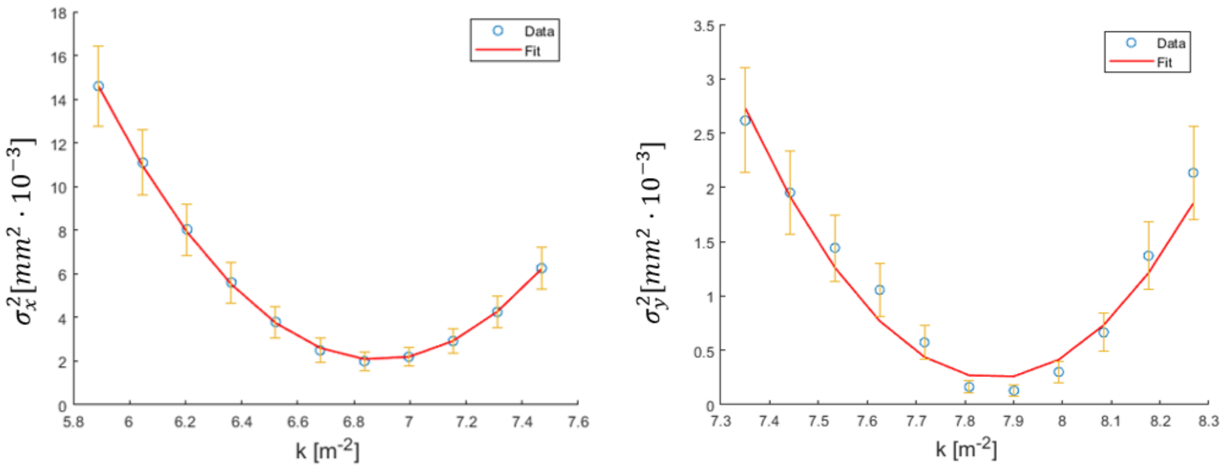


**Figure 4.22:** Virtual measurement of the transverse beam size as a function of the normalized quadrupole strength $k$ for the witness beam in the $x$-plane (left) and $y$-plane (right), at the mid-energy diagnostics beamline.

| **Parameters** | **Witness** | | **Driver** | |
|---|---|---|---|---|
| | $x$ | $y$ | $x$ | $y$ |
| Input $\varepsilon_n$ $[\mu m]$ | 1.40 | 0.68 | 1.65 | 0.74 |
| Reconstructed $\varepsilon_n$ $[\mu m]$ | 1.42 | 0.64 | 1.65 | 0.74 |
| Error $[\mu m]$ | 0.1 | 0.08 | 0.1 | 0.09 |
| Rel. Error [%] | 7.7 | 12.1 | 8.0 | 11.8 |

**Table 4.19:** Input and reconstructed emittances at 400 MeV for the witness and driver beams in both transverse planes.

**Resolution determination** The measurement resolution was further evaluated by repeating the simulation with Gaussian beams of progressively smaller emittance. The results, summarized in Table 4.20, show that the reconstructed emittance closely follows the input values down to about 0.2 $\mu m$ in the $x$-plane. In the $y$-plane larger deviations from the input value are obtained; however, they remain below 10% so that the effective resolution is consistent with the 0.2 $\mu m$ limit in the $x$-plane. Below this value, the measurement is not considered reliable, resulting in an effective resolution in both planes of approximately 0.2 $\mu m$.

| Plane | Input $\varepsilon_n$ [$\mu m$] | Reconstructed $\varepsilon_n$ [$\mu m$] | Error [$\mu m$] | Rel. error [%] | Difference [%] |
|---|---|---|---|---|---|
| $x$ | 0.50 | 0.49 | 0.03 | 5.7 | 2.6 |
| $x$ | 0.40 | 0.39 | 0.02 | 6.2 | 3.0 |
| $x$ | 0.30 | 0.29 | 0.02 | 6.7 | 3.0 |
| $x$ | 0.20 | 0.19 | 0.01 | 7.4 | 3.3 |
| $y$ | 0.50 | 0.54 | 0.04 | 6.6 | 8.9 |
| $y$ | 0.40 | 0.44 | 0.03 | 6.9 | 8.9 |
| $y$ | 0.30 | 0.33 | 0.02 | 7.6 | 8.8 |
| $y$ | 0.20 | 0.22 | 0.02 | 8.3 | 8.7 |

**Table 4.20:** Resolution study of the emittance measurement at 400 MeV. Input beams of decreasing emittance were simulated, and reconstructed values are shown with their absolute, relative, and differential errors.

**Screen resolution influence on emittance measurement** To assess the influence of the imaging system on the emittance measurement, a dedicated scan was performed by varying the screen resolution while keeping all other parameters fixed. The results are summarized in Table 4.21, and show how the uncertainties on the emittance corresponding to the resolution limit increase. As the reference case is considered the $y$-plane, giving a worse resolution with respect to x, and the results show the limit increases, providing comparable results for emittances up to 0.4 $\mu m$ at 7 $\mu m$ of screen resolution.

| **Parameter** | 3.5 [$\mu m$] | 5.2 [$\mu m$] | 7.0 [$\mu m$] |
|---|---|---|---|
| Reconstructed $\varepsilon_{n,y}$ [$\mu m$] | 0.2 | 0.3 | 0.4 |
| Rel. Error [%] | 8.3 | 9.2 | 9.8 |
| Deviation from input [%] | 8.7 | 8.0 | 8.0 |

**Table 4.21:** Emittance resolution scan as a function of the screen resolution at the mid-energy beamline. The reconstructed emittance is taken as the effective measurement resolution; the corresponding relative error and deviation from the input value are also reported.

### 4.5.5 Spectrometer simulation

The mid-energy diagnostics spectrometer is designed to measure the beam energy and energy spread in the 400–750 MeV range. It consists of a 40 cm-long dipole magnet with a nominal deflection angle of 22 degrees. In this section, the measurement parameters for different dipole-screen distances and different screen resolutions are evaluated, as described in section 4.4.6. The spectrometer line extends for approximately 3 m, terminating at the beam dump. Simulations were performed by varying the screen position from 0.5 m to 2 m downstream of the dipole exit, considering a reference distance of 1.5 m.

Figs. 4.23 and 4.24 show the simulated images and energy profiles of the two bunches on the dispersive screen (1.5 m screen distance, 3.5 $\mu m$ of screen resolution). The main parameters of the measurement are reported in Table 4.22.

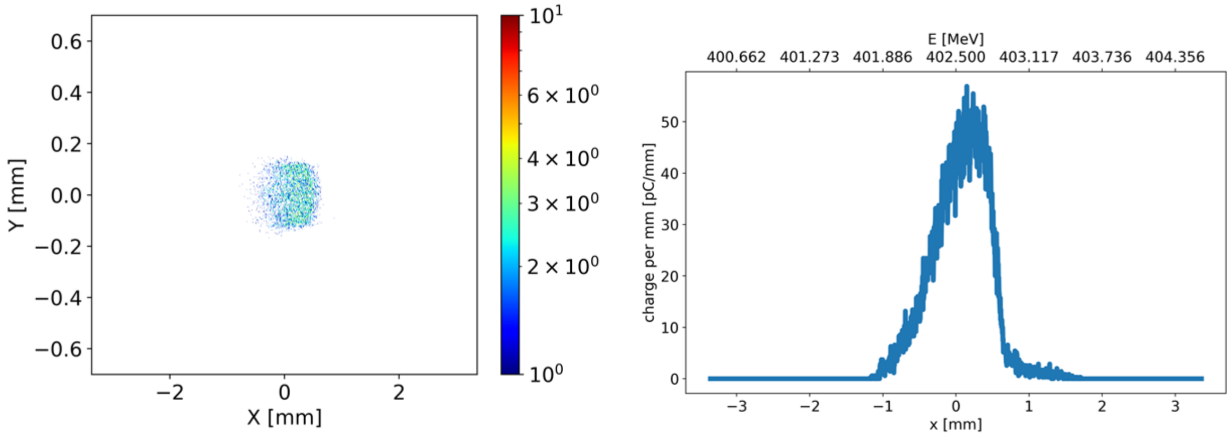


**Figure 4.23:** Witness signal acquired at the mid-energy spectrometer screen (left) and the corresponding energy profile (right), taken at the reference distance of 1.5 m from the dipole, and a screen resolution of 3.5 $\mu m$.

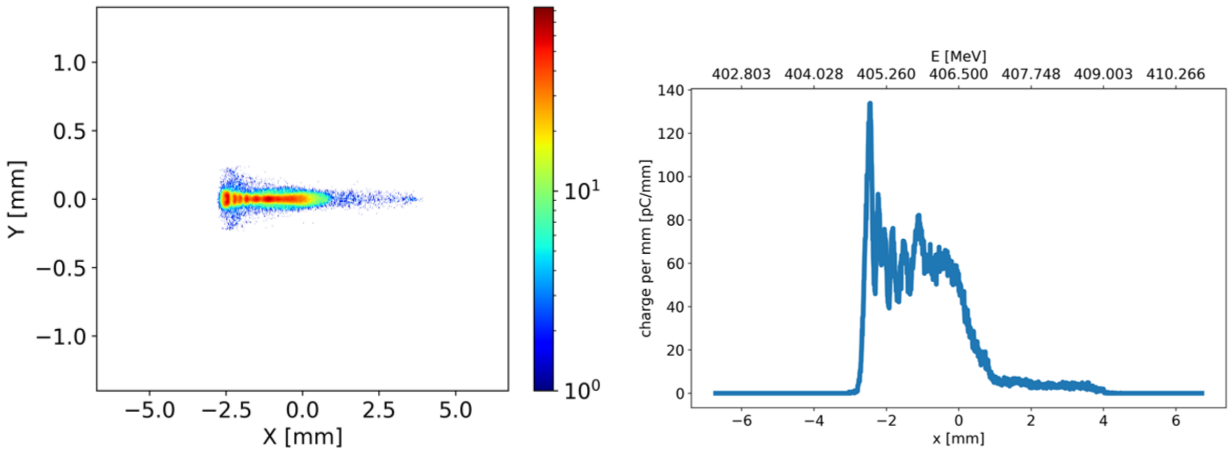


**Figure 4.24:** Driver signal acquired at the mid-energy spectrometer screen (left) and the corresponding energy profile (right), taken at the reference distance of 1.5 m from the dipole, and a screen resolution of 3.5 $\mu m$.

| Parameter | Witness | Driver | Unit |
|---|---|---|---|
| $E_{\text{mean}}$ | 402.5 | 405.9 | MeV |
| $\sigma_E$ | 236.6 | 762.4 | keV |
| $E_{\text{FWHM}}$ | 1427.3 | 2732.1 | keV |

**Table 4.22:** Summary of the spectrometer measurement results for the driver and witness bunches at the mid-energy diagnostics station. $E_{\text{mean}}$ is the average beam energy, $\sigma_E$ the RMS energy spread, and $E_{\text{FWHM}}$ the full width at half maximum of the energy distribution.

In Fig. 4.25, the driver and witness beams are visible in the same screen acquisition, confirming that the spectrometer provides sufficient resolution to separate the two bunches.

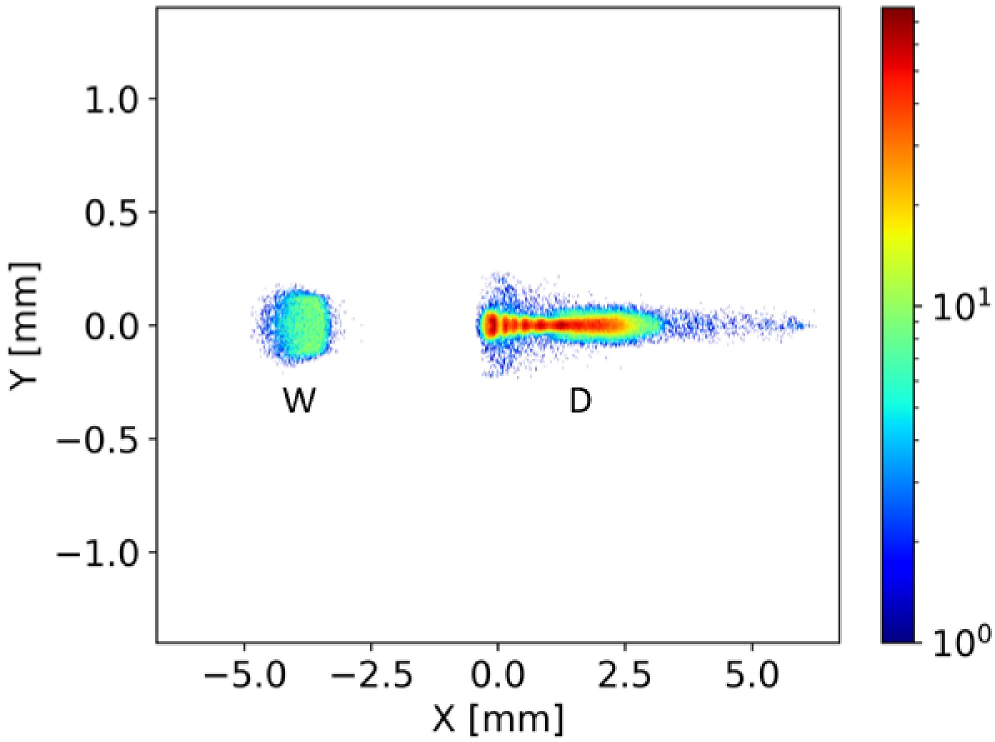


**Figure 4.25:** Mid-energy driver (D) and witness (W) bunches observed in the same spectrometer screen image, demonstrating the system's capability to resolve both beams, considering a screen at 1.5 m from the dipole with a resolution of 3.5 $\mu m$.

**Effect of synchrotron radiation** For the mid-energy spectrometer, the effect of synchrotron radiation is accounted for in the simulations. Table 4.23 reports the variations in the reconstructed parameters with and without SR, along with the differences between the reconstructed and initial mean energies and between the reconstructed and initial RMS energy spreads.

| Parameter | SR | NO SR |
|---|---|---|
| $E_{\text{mean}}$ [MeV] | 402.54 | 402.61 |
| $\sigma_E$ [keV] | 236.6 | 253.3 |
| $E_{\text{FWHM}}$ [keV] | 1427.3 | 1379.6 |
| $(E_{\text{mean}_{\text{input}}} - E_{\text{mean}_{\text{screen}}})$ [keV] | -79.9 | -15.1 |
| $(\sigma_{E_{\text{input}}} - \sigma_{E_{\text{screen}}})$ [keV] | -9.2 | 7.58 |

**Table 4.23:** Summary of the synchrotron radiation influence in the spectrometer measurement for the witness bunch at the mid-energy diagnostics station (screen distance 1.5 m, screen resolution 3.5 $\mu m$).

**Screen position determination** The energy resolution was evaluated as a function of the screen position along the spectrometer line, considering the witness beam as a reference. For each configuration, the differences between the simulated parameters (average and RMS energy) before the dipole and at the screen, the minimum and maximum energy bin sizes, and the retrieved RMS energy of the bunch were computed. The results are summarized in Table 4.24.

| **Parameter** | **0.5 m** | **1 m** | **1.5 m** | **2 m** |
|---|---|---|---|---|
| $(E_{\text{mean}_{\text{input}}} - E_{\text{mean}_{\text{screen}}})$ [keV] | -19.2 | -62.2 | -79.9 | -95.6 |
| $(\sigma_{E_{\text{input}}} - \sigma_{E_{\text{screen}}})$ [keV] | -38.4 | -20.1 | -9.2 | -2.5 |
| Min $E_{bin}$ [keV] | 5.09 | 3.01 | 2.13 | 1.65 |
| Max $E_{bin}$ [keV] | 5.35 | 3.10 | 2.18 | 1.68 |
| $\sigma_E$ [keV] | 207.4 | 225.6 | 236.6 | 243.3 |

**Table 4.24:** Simulated energy measurement parameters at the mid-energy spectrometer for different dipole-screen distance. All values are expressed in [keV].

The reference screen position at 1.5 m was selected as it provides a sufficient energy resolution while accurately reproducing the expected energy profile of the bunch.

**Effect of the Screen Resolution** The impact of the screen resolution was assessed by varying the effective pixel size on the dispersive axis to 3.5 $\mu m$, 5.25 $\mu m$, and 7 $\mu m$, corresponding to magnification settings of $M = \{1.0, 1.5, 2.0\}$, respectively. For each configuration, the same figures of merit used in the screen-distance scan are computed: the difference between the reconstructed values before and after the dipole, minimum and maximum bin width values along the energy axis, and the retrieved RMS energy spread of the bunch. The results are summarized in Table 4.25.

| **Parameter** | **3.5** $\mu m$ | **5.25** $\mu m$ | **7** $\mu m$ |
|---|---|---|---|
| $(E_{\text{mean}_{\text{input}}} - E_{\text{mean}_{\text{screen}}})$ [keV] | -79.9 | -79.9 | -79.9 |
| $(\sigma_{E_{\text{input}}} - \sigma_{E_{\text{screen}}})$ [keV] | -9.2 | -9.2 | -9.2 |
| Min $E_{bin}$ [keV] | 2.13 | 3.18 | 4.22 |
| Max $E_{bin}$ [keV] | 2.18 | 3.28 | 4.40 |
| $\sigma_E$ [keV] | 236.6 | 236.6 | 236.6 |

**Table 4.25:** Simulated energy measurement parameters at the mid-energy spectrometer for different screen resolutions (effective pixel sizes). All values are expressed in [keV].

Within the explored range, increasing the effective pixel size (i.e., coarser screen resolution) enlarges the energy-bin width as expected, yet the reconstructed mean energy and RMS energy spread remain essentially unaffected by the screen resolution (even for the coarsest setting), accurately reproducing the expected energy profile.

## 4.6 High-Energy beamline

The high-energy diagnostics are positioned downstream of the separation chicane, in the post-plasma acceleration section, and just upstream of the undulator modules, as shown in Figure 4.26. At this stage, the beam energy can reach 1 GeV, imposing stringent requirements on measurement resolution. For this reason, a long TDS capable of operating at high RF power is employed. After exiting the plasma, the beam consists of the driver, which is largely depleted due to energy transfer, and the witness, which has retained most of the energy. The beams are first transported through the capture section, a FODO lattice composed of 13 permanent quadrupoles with gradients up to 500 T/m, alternating between focusing and defocusing. This lattice is designed to properly match the witness beam to the subsequent section of the machine, namely the separation chicane. In the chicane, the driver and witness beams are separated due to their significant energy difference. A collimator positioned in the dispersive region of the chicane removes the driver, while the witness continues towards the high-energy diagnostics and, eventually, the undulator modules.

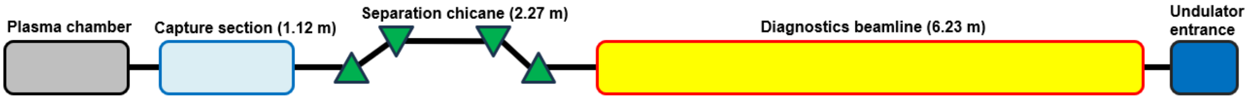


**Figure 4.26:** Layout of the beamline between the plasma chamber and the undulator entrance, highlighting the capture, separation, and diagnostics sections of the beamline.

### 4.6.1 Beamline layout

The station includes four electromagnetic quadrupoles for beam matching and focusing, each 0.2 m in magnetic length and spaced 0.2 m apart. A 0.96 m PolariX TDS enables the required resolution in bunch length measurements. A dipole spectrometer with a magnetic length of 0.6 m provides energy measurements on the dispersive screen, located 2.27 m after the magnet. A screen is placed at 3.07 m from the TDS on the straight section of the accelerator and is used for emittance and bunch length measurements. Additionally, screens are placed after each undulator module, enabling better resolution and greater flexibility in beam matching if necessary, as the distance traveled by the bunch varies. The straight section of the described layout is depicted in Fig. 4.27. The PolariX TDS will be powered by a dedicated X-band klystron, providing a maximum available integrated voltage of 56 MV.

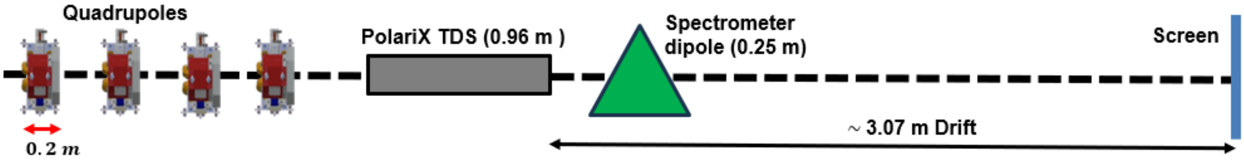


**Figure 4.27:** Layout of the high-energy diagnostic station (1 GeV). This section features four quadrupoles, a 96 cm PolariX TDS, a 0.6 m dipole, and a downstream screen at 3.07 m from the TDS.

### 4.6.2 Simulated Beam Parameters

At high energy, the diagnostics section characterizes the witness bunch after driver–witness separation. The beam exits the plasma with an average energy close to 1 GeV. At the capture section entrance, the witness has a charge of $\sim$ 30 pC, a bunch length of $\sim$ 22 fs, a normalized emittance close to $\sim 1\ \mu m$, and 1.06% of energy spread. The longitudinal phase space and current profile at this stage are shown in Fig. 4.28.

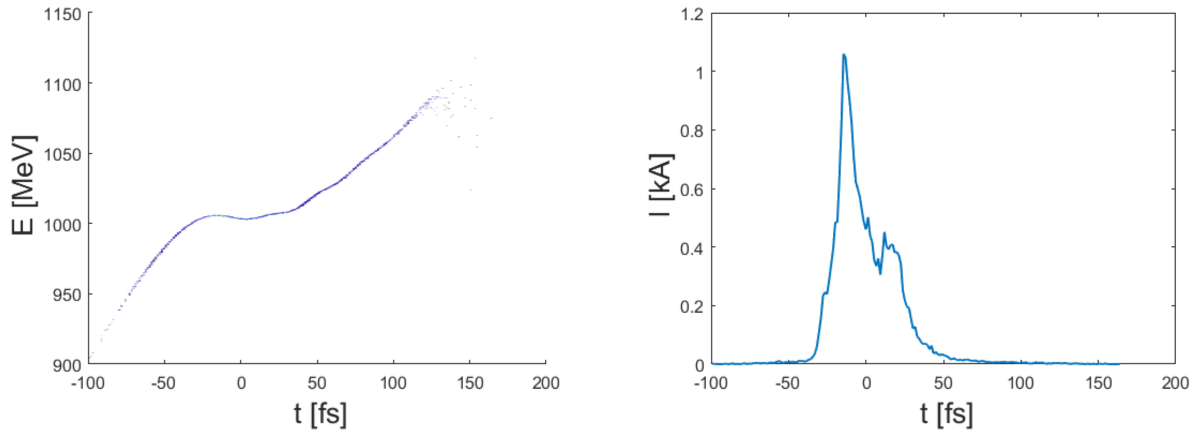


**Figure 4.28:** Longitudinal phase space (left) and corresponding current profiles (right) of the witness beam at the plasma exit (1 GeV), as provided by the input macroparticle distribution in ELEGANT.

After the separation chicane, the driver is removed and the witness beam is transported to the high-energy diagnostics. At this point, the bunch exhibits a reduced charge of about $\sim$24 pC due to losses in the transport beamline, a shorter bunch length of $\sim$15 fs, a slightly higher emittance of $\sim 1.2\ \mu m$, and a significantly lower energy spread (0.09%), while the average energy remains around 1 GeV. The transverse beam size increases as a result of the optics of the transport line, reaching $\sigma_x \simeq 157\ \mu m$ and $\sigma_y \simeq 105\ \mu m$ at the entrance of the diagnostics. The corresponding longitudinal phase space and current profile are shown in Fig. 4.29.

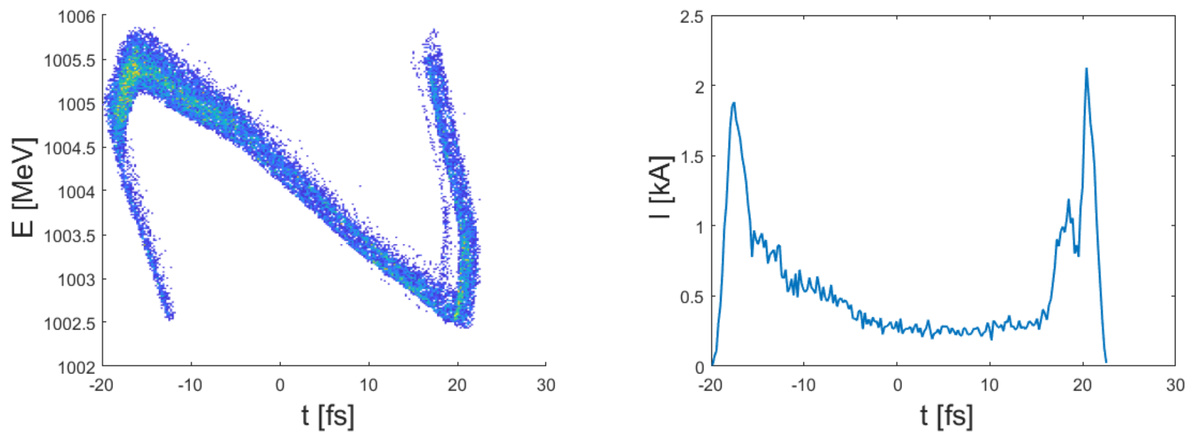


**Figure 4.29:** Longitudinal phase space (left) and corresponding current profiles (right) of the transported witness beam at the high-energy (1 GeV) diagnostics beamline.

The witness parameters after the plasma exit and at the diagnostics beamline entrance are reported in Table 4.26.

| **Parameters** | **Witness** (Plasma Exit) | **Witness Core** (Diagnostics beamline) |
|---|---|---|
| Charge $[pC]$ | 30 | 23.68 |
| Mean Energy $[MeV]$ | 1005.7 | 1004.34 |
| Energy Spread [%] | 1.06 | 0.09 |
| RMS Bunch length $[fs]$ | 21.98 | 14.72 |
| RMS Bunch length $[\mu m]$ | 6.59 | 4.41 |
| $\varepsilon_{n_x}$ $[\mu m]$ | 0.92 | 1.25 |
| $\varepsilon_{n_y}$ $[\mu m]$ | 1.01 | 1.15 |
| $\beta_x$ $[m]$ | 0.0025 | 38.84 |
| $\beta_y$ $[m]$ | 0.0025 | 18.81 |
| $\alpha_x$ | 0.11 | 11.21 |
| $\alpha_y$ | 0.14 | $-24.35$ |

**Table 4.26:** Witness parameters of the working point at the high-energy (1 GeV) plasma exit and diagnostics station.

### 4.6.3 Initial beam shot-to-shot fluctuations

Since the high-energy beamline is designed to measure beams accelerated by plasma, it is essential to evaluate the acceleration's effect on beam stability. Shot-to-shot fluctuations in the output beam parameters, such as energy, emittance, and transverse size, can occur as a consequence of the intrinsic jitter of the plasma source and the upstream beamline. These fluctuations, in turn, can affect the performance and accuracy of the downstream diagnostics, making it essential to quantify their typical amplitude.

Table 4.27 summarizes the average beam parameters used in the present analysis, together with their standard deviations, which indicate the natural variability of the beam over a dataset consisting of 45 different input macroparticle distributions. The reported standard deviations do not represent measurement uncertainties but rather the shot-to-shot spread of the beam properties, and thus give a measure of the stability of the accelerated bunches delivered by the plasma source.

| **Quantity** | **Mean Value** | **Std** |
|---|---|---|
| $\beta_x$ [m] | 5.0 | 0.5 |
| $\beta_y$ [m] | 6.8 | 0.6 |
| $\alpha_x$ | 1.9 | 0.4 |
| $\alpha_y$ | -6.8 | 0.4 |
| $\varepsilon_{n_x}$ $[\mu m]$ | 0.85 | 0.02 |
| $\varepsilon_{n_y}$ $[\mu m]$ | 0.65 | 0.01 |
| $\sigma_t$ [fs] | 15.7 | 0.1 |
| $E$ [MeV] | 1005 | 3 |
| $E_{\text{spread}}$ [MeV] | 1.4 | 0.1 |

**Table 4.27:** Statistical summary of the bunch parameters used for the jitter studies at high-energy.

### 4.6.4 Beamline matching

At high energy, the matching procedure was applied only to the witness beam, since the driver is no longer present after its removal in the separation chicane. The objective was to ensure a stable transport to the diagnostics station. For this purpose, the first section of the beamline includes a series of permanent quadrupoles to capture and focus the witness beam. At the same time, the separation chicane effectively removes the driver without affecting the transport of the witness. In Fig. 4.30, the Twiss parameters obtained by the transport in the capture and separation section are shown, up to the entrance of the high-energy diagnostics line.

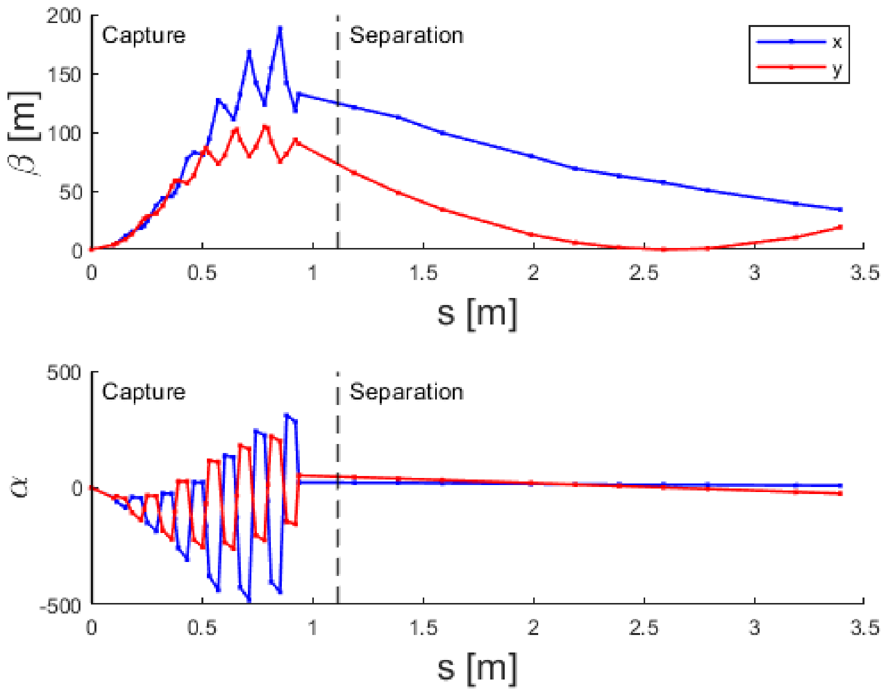


**Figure 4.30:** Twiss parameters evolution of the witness beam along the capture and separation sections, up to the diagnostics beamline entrance.

A baseline matching was performed by tuning the quadrupole strengths to obtain a symmetric configuration, with both $\beta_x$ and $\beta_y$ minimized at the screen position. In practice, the configuration was optimized by adjusting the last quadrupole magnet before the diagnostics station. Two cases are possible: a focusing configuration in the horizontal or vertical plane, depending on the measurement to be performed. For instance, when measuring the horizontal emittance, it is convenient to operate with the last quadrupole as focusing in the $x$-plane, providing a waist in $x$ at the screen. Conversely, for vertical emittance measurements, the last quadrupole can be tuned to focus in the $y$-plane.
The following results are presented for the focusing configuration in the horizontal plane ($k > 0$), corresponding to the setup used for the emittance and bunch length measurements described in the subsequent sections. Figure 4.31 shows the matched $\beta$-functions at the screen position, which are reported in Table 4.28.

| Parameters | Diagnostics Entrance | Screen |
|---|---|---|
| $\beta_x$ $[m]$ | 38.84 | 1.16 |
| $\beta_y$ $[m]$ | 18.81 | 0.72 |
| $\alpha_x$ | 11.21 | $-0.37$ |
| $\alpha_y$ | $-24.35$ | 0.55 |

**Table 4.28:** Twiss parameters at the high-energy diagnostics beamline entrance and at the screen, after the matching to the measurement screen.

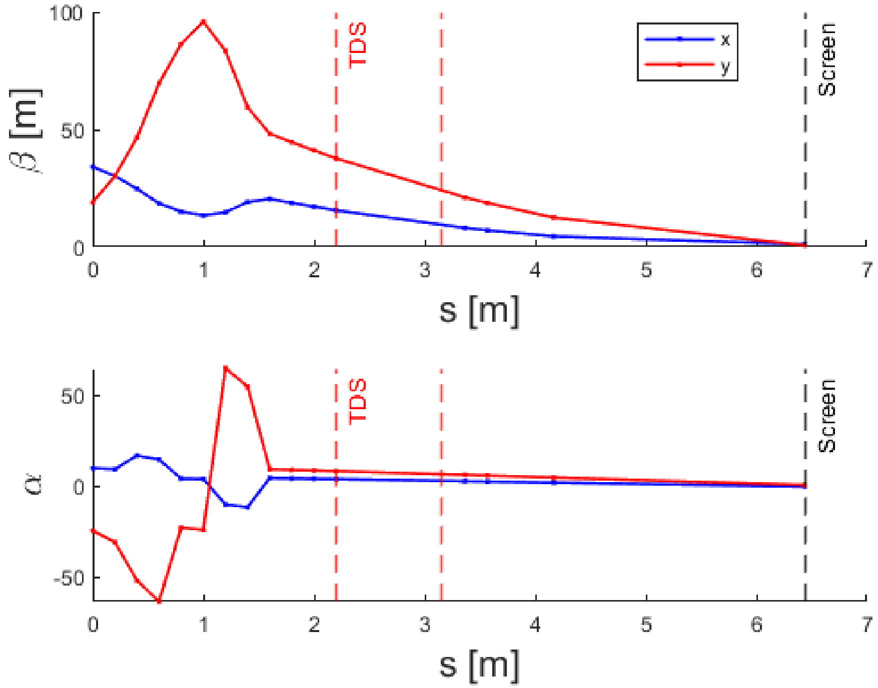


**Figure 4.31:** Twiss parameters evolution of the witness beam in the diagnostics beamline, up to the screen on the straight section, for last quadrupole focusing in $x$-plane.

### 4.6.5 Emittance measurement simulation

**1 GeV nominal bunch** The emittance measurement at 1 GeV was performed using the quadrupole scan method, following the same procedure as for the low- and middle-energy cases. Since the driver beam has already been removed in the separation chicane, the simulations have been done only for the witness beam.

The reconstructed values for the witness bunch are summarized in Table 4.29. In both cases, the reconstruction yields errors below 8%, in both transverse planes. In Fig. 4.32, the quadrupole scan curves for measuring the bunch emittance in $x$ and $y$ are shown.

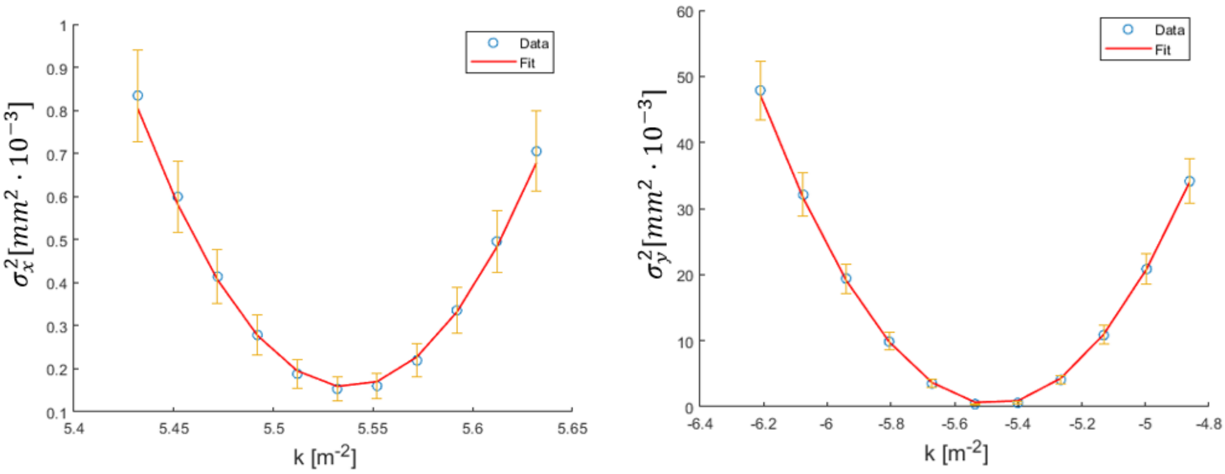


**Figure 4.32:** Virtual measurement of the transverse beam size as a function of the normalized quadrupole strength $k$ for the witness beam in the $x$-plane (left) and $y$-plane (right), at the high-energy diagnostics beamline.

| Parameters | Witness | |
|---|---|---|
| | $x$ | $y$ |
| Input $\varepsilon_n$ [$\mu m$] | 1.2 | 1.2 |
| Reconstructed $\varepsilon_n$ [$\mu m$] | 1.2 | 1.2 |
| Error [$\mu m$] | 0.1 | 0.1 |
| Rel. Error [%] | 8.3 | 8.3 |

**Table 4.29:** Input and reconstructed emittances at 1 GeV for the witness beam in both transverse planes.

**Resolution determination** The resolution of the emittance measurement at 1 GeV was evaluated through dedicated simulations using ideal Gaussian beams with progressively smaller input emittances. For each case, the quadrupole scan analysis was repeated following the same procedure described above, and the reconstructed emittance was compared to the nominal input value. The results in both planes, summarized in Table 4.30, show that the relative and differential errors exceed 12% for input emittances lower than 0.3 $\mu m$. Below this value, the accuracy of the reconstruction degrades significantly, indicating that the effective resolution of the diagnostic is on the order of 0.3 $\mu m$ in both transverse planes.

| Plane | Input $\varepsilon_n$ [$\mu m$] | Reconstructed [$\mu m$] | Error [$\mu m$] | Rel. Error [%] | Diff [%] |
|---|---|---|---|---|---|
| $x$ | 0.60 | 0.57 | 0.05 | 8.5 | 5.0 |
| $x$ | 0.50 | 0.47 | 0.05 | 9.4 | 5.6 |
| $x$ | 0.40 | 0.38 | 0.04 | 10.7 | 6.1 |
| $x$ | 0.30 | 0.28 | 0.03 | 12.7 | 7.3 |
| $x$ | 0.20 | 0.18 | 0.03 | 16.8 | 10.8 |
| $y$ | 0.60 | 0.64 | 0.04 | 6.0 | 6.8 |
| $y$ | 0.50 | 0.53 | 0.04 | 7.1 | 6.8 |
| $y$ | 0.40 | 0.43 | 0.04 | 9.4 | 6.9 |
| $y$ | 0.30 | 0.32 | 0.04 | 12.8 | 7.2 |
| $y$ | 0.20 | 0.21 | 0.04 | 18.1 | 6.9 |

**Table 4.30:** Resolution study of the emittance measurement at 1 GeV. Input beams of decreasing emittance were simulated, and reconstructed values are shown with their absolute, relative, and differential errors.

**Screen resolution influence on emittance measurement** To assess the influence of the imaging system on the emittance measurement, a dedicated scan was performed by varying the screen resolution while keeping all other parameters fixed. The results are summarized in Table 4.31, and show how the uncertainties on the emittance measurement in the $x$-plane increase, with a resolution limit up to 0.4 $\mu m$ at 7 $\mu m$ of screen resolution.

| **Parameter** | 3.5 [$\mu m$] | 5.2 [$\mu m$] | 7.0 [$\mu m$] |
|---|---|---|---|
| Resolution $\varepsilon_{n,x}$ [$\mu m$] | 0.3 | 0.3 | 0.4 |
| Rel. Error [%] | 12.7 | 14.6 | 16.5 |
| Deviation from input [%] | 7.3 | 8.7 | 8.4 |

**Table 4.31:** Emittance resolution scan as a function of the screen resolution at the high-energy beamline. The reconstructed emittance is taken as the effective measurement resolution; the corresponding relative error and deviation from the input value are also reported.

**Impact of jitter on the emittance measurement** At 1 GeV, the beam originates from plasma acceleration, which inherently introduces shot-to-shot fluctuations. These fluctuations affect not only the beam energy and bunch length, but also the normalized emittance and the initial Twiss parameters. To quantify their impact, a set of representative statistics for the main beam parameters was first collected, reporting the median values and the corresponding spread across the acquired shots, and performing emittance measurements for each shot. This spread is used as an estimate of the uncertainty due to plasma-induced jitter.

The emittance measurement was then performed with a fixed set of quadrupole strengths, chosen to match the optics to the average Twiss parameters at the diagnostic line entrance. This corresponds to the operational scenario in which a reference optics is defined and used for all incoming beams, despite their individual fluctuations. As a consequence, the measured beam size as a function of quadrupole strength does not collapse onto a single parabola, but rather results in a band. For each quadrupole setting, the beam size distribution reflects the shot-to-shot variations in the beam size. A "central" parabola is obtained, while the boundaries of the size distribution define a "lower" and "upper" parabola, respectively. These curves are shown in Fig. 4.33, and directly illustrate the influence of jitter on the quadrupole scan measurement.

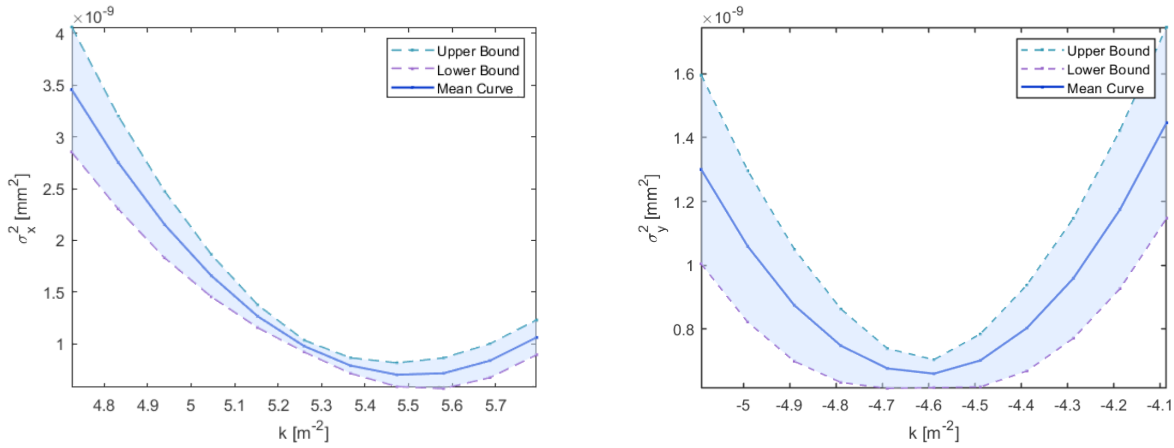


**Figure 4.33:** Quadrupole scan for the witness beam in the x- (left) and $y$-plane (right), at the high-energy diagnostics beamline, including the shot-to-shot fluctuations derived from plasma acceleration, defined by the "lower" and "upper" parabolas.

From this analysis, the reconstructed emittance is reported together with its statistical spread, which accounts for shot-to-shot fluctuations in the acceleration process. This spread quantifies the operational precision of the measurement under realistic conditions, and should be distinguished from the intrinsic instrumental resolution, which is determined from dedicated simulations with ideal Gaussian beams of decreasing emittance. In practice, the total uncertainty on a single-shot measurement can be approximated by the quadratic combination of these two contributions, as $\sigma^2_{\text{tot}} \simeq R^2_{\text{inst}} + S^2_{\text{op}}$. Due to jitter, the effective resolution threshold is reached at higher emittance values than in the ideal case, since the additional fluctuations broaden the measured parabolas and increase the relative error in the fit. When averaging over multiple shots, the operational component scales as $S_{\text{op}}/\sqrt{N}$, thereby improving overall precision without altering the instrumental floor. The measured emittance in both the horizontal and vertical planes exhibits a fluctuation of approximately $\sim 0.27\ \mu m$, attributed to beam instabilities. This leads to a degraded effective resolution of $\varepsilon_{res} = 0.4\ \mu m$ for the measurements performed at this diagnostics beamline. The corresponding values are summarized in Table 4.32.

| **Parameter** | **Value** | |
|---|---|---|
| | **x** | **y** |
| Input [$\mu m$] | 0.85 | 0.65 |
| Measured [$\mu m$] | 0.87 | 0.63 |
| Standard Deviation [$\mu m$] | 0.27 | 0.26 |
| Instrumental Resolution [$\mu m$] | 0.3 | |
| Effective Resolution [$\mu m$] | 0.4 | |

**Table 4.32:** In the Table are reported the emittances and corresponding spread evaluated from the jitter studies at the high-energy beamline, together with the instrumental and effective emittance resolution.

### 4.6.6 Spectrometer simulation

The energy measurement at the high-energy diagnostics station is performed with a magnetic spectrometer optimized for GeV energies. The spectrometer consists of a 60 cm-long dipole magnet providing a nominal deflection angle of 22 degrees.

The analysis is performed with the same methodology described in section 4.4.6. Only the witness bunch was included, since the driver beam has already been removed from the beamline. In Fig. 4.34, the simulated images and energy profiles of the bunch on the dispersive screen (1.5 m screen distance, 3.5 $\mu m$ of screen resolution) are shown. The main parameters of the measurement are reported in Table 4.33.

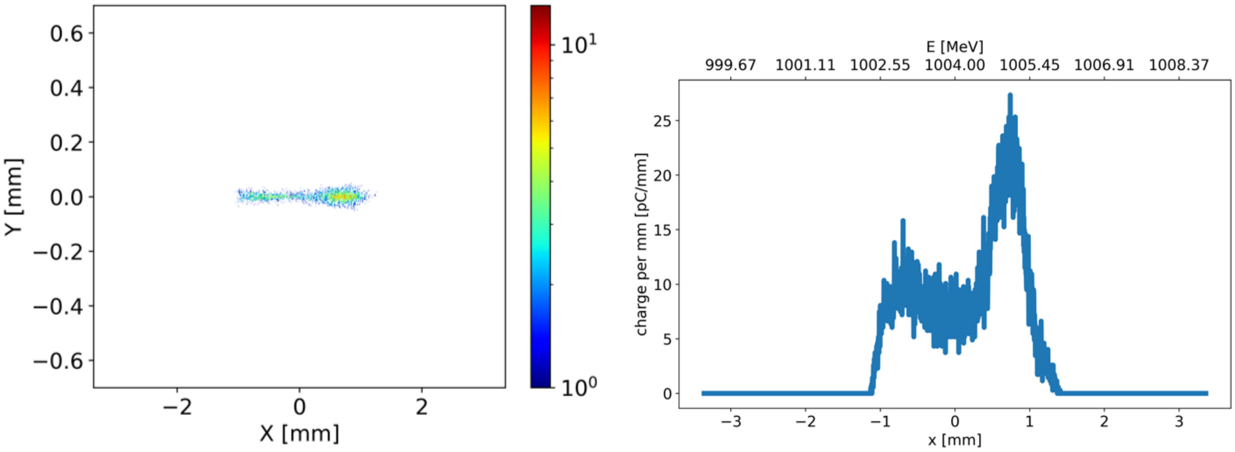


**Figure 4.34:** Witness signal acquired at the high-energy spectrometer screen (left) and the corresponding energy profile (right), taken at the reference distance of 1.5 m from the dipole, and a screen resolution of 3.5 $\mu m$.

| Parameter | Witness | Unit |
|---|---|---|
| $E_{\text{mean}}$ | 1004.3 | MeV |
| $\sigma_E$ | 923.7 | keV |
| $E_{\text{FWHM}}$ | 3543.7 | keV |

**Table 4.33:** Summary of the spectrometer measurement results for the witness bunch at the high-energy diagnostics station. $E_{\text{mean}}$ is the average beam energy, $\sigma_E$ the RMS energy spread, and $E_{\text{FWHM}}$ the full width at half maximum of the energy distribution.

**Effect of synchrotron radiation** For the high-energy spectrometer, the effect of synchrotron radiation is accounted for in the simulations. Table 4.34 reports the variations in the reconstructed parameters with and without SR, along with the differences between the reconstructed and initial mean energies and between the reconstructed and initial RMS energy spreads.

| Parameter | SR | NO SR |
|---|---|---|
| $E_{\text{mean}}$ [MeV] | 1004.30 | 1004.36 |
| $\sigma_E$ [keV] | 923.7 | 904.0 |
| $E_{\text{FWHM}}$ [keV] | 3543.7 | 3360.5 |
| $(E_{\text{mean}_{\text{input}}} - E_{\text{mean}_{\text{screen}}})$ [keV] | -63.1 | -6.2 |
| $(\sigma_{E_{\text{input}}} - \sigma_{E_{\text{screen}}})$ [keV] | -1.51 | -2.20 |

**Table 4.34:** Summary of the synchrotron radiation influence in the spectrometer measurement for the witness bunch at the high-energy diagnostics station (screen distance 1.5 m, screen resolution 3.5 $\mu m$).

**Screen position determination** The energy resolution was evaluated as a function of the screen position along the spectrometer line. For each configuration, the differences between the simulated parameters (average and RMS energy) before the dipole and at the screen, the minimum and maximum energy bin sizes, and the retrieved RMS energy of the bunch were computed. The results are summarized in Table 4.35.

| **Parameter** | **0.5 m** | **1 m** | **1.5 m** | **2 m** |
|---|---|---|---|---|
| $(E_{\text{mean}_{\text{input}}} - E_{\text{mean}_{\text{screen}}})$ [keV] | -71.8 | -65.8 | -63.1 | -61.6 |
| $(\sigma_{E_{\text{input}}} - \sigma_{E_{\text{screen}}})$ [keV] | -2.9 | -5.1 | -1.5 | 1.7 |
| Min $E_{bin}$ [keV] | 11.14 | 6.93 | 5.02 | 3.94 |
| Max $E_{bin}$ [keV] | 11.64 | 7.11 | 5.12 | 4.00 |
| $\sigma_E$ [keV] | 922.3 | 920.2 | 923.7 | 926.9 |

**Table 4.35:** Simulated energy measurement parameters at the high-energy spectrometer for different dipole-screen distances. All values are expressed in [keV].

The reference screen position at 1.5 m was selected as it provides a sufficient energy resolution while accurately reproducing the expected energy profile of the bunch.

**Effect of the Screen Resolution** The impact of the screen resolution was assessed by varying the effective pixel size on the dispersive axis to 3.5 $\mu m$, 5.25 $\mu m$, and 7 $\mu m$, corresponding to magnification settings of $M = \{1.0, 1.5, 2.0\}$, respectively. For each configuration, the same figures of merit used in the screen-distance scan are computed: the difference between the reconstructed values before and after the dipole, minimum and maximum bin width values along the energy axis, and the retrieved RMS energy spread of the bunch. The results are summarized in Table 4.36.

| **Parameter** | **3.5** $\mu m$ | **5.25** $\mu m$ | **7** $\mu m$ |
|---|---|---|---|
| $(E_{\text{mean}_{\text{input}}} - E_{\text{mean}_{\text{screen}}})$ [keV] | -63.1 | -63.1 | -63.1 |
| $(\sigma_{E_{\text{input}}} - \sigma_{E_{\text{screen}}})$ [keV] | -1.5 | -1.5 | -1.5 |
| Min $E_{bin}$ [keV] | 5.02 | 7.50 | 9.95 |
| Max $E_{bin}$ [keV] | 5.12 | 7.72 | 10.35 |
| $\sigma_E$ [keV] | 923.7 | 923.7 | 923.7 |

**Table 4.36:** Simulated energy measurement parameters at the high-energy spectrometer for different screen resolutions (effective pixel sizes). All values are expressed in [keV].

Within the explored range, increasing the effective pixel size (i.e., coarser screen resolution) enlarges the energy-bin width as expected, yet the reconstructed mean energy and RMS energy spread remain essentially unaffected by the screen resolution (even for the coarsest setting), accurately reproducing the expected energy profile.

### 4.6.7 Bunch length measurement simulation

**Longitudinal resolution** The bunch length measurement at the high-energy beamline was performed using the 96 cm PolariX TDS, operated in both vertical and horizontal streaking modes. To estimate the achievable system resolution, a maximum deflecting voltage of $V_{\text{max}} = 56$ MV was considered, in accordance with the RF limits of the structure. The unstreaked beam size at the measurement screen was $\sigma_{\text{off}} = 15$ $\mu$m in both transverse planes, with shot-to-shot fluctuations of approximately 10%. Table 4.37 summarizes the main parameters used for the resolution calculation. The target resolution was set to 0.5 $\mu$m in both planes as for the 118 MeV case.

| Parameter | Nominal |
|---|---|
| Beam energy [GeV] | 1 |
| Max Deflecting voltage [MV] | 56 |
| TDS Length [m] | 0.96 |
| Distance TDS-Screen [m] | 3.07 |
| $\sigma_{off}$ $[\mu m]$ | 15 |
| Max resolution [fs] | 1 |

**Table 4.37:** Beam and TDS parameters adopted for the longitudinal resolution evaluation at the high-energy section.

Fig. 4.35 shows the estimated longitudinal resolution as a function of the deflecting voltage for the given beam parameters. The dashed line represents the target resolution for each beam configuration, while the shaded upper and lower bounds correspond to a ±10% variation of the unstreaked beam size at the measurement screen.

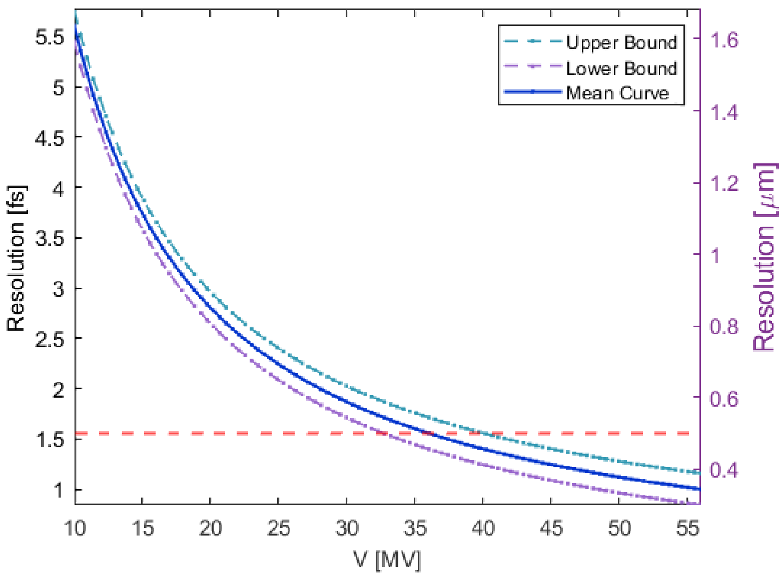


**Figure 4.35:** Estimated longitudinal resolution at the high-energy diagnostic beamline as a function of the deflecting voltage, up to the maximum achievable value of 56 MV, for nominal 1 GeV beam configuration. The solid curve indicates the mean estimated resolution, with upper and lower boundaries obtained by considering a ±10% variation of the unstreaked beam size at the measurement screen. The dashed horizontal lines represent the target resolutions of 0.5 $\mu$m.

**TDS Calibration** For calibration, the structure was operated at $V = 50$ MV, and the RF phase was scanned around the zero-crossing. The calibration curve is shown in Fig. 4.36, from which the calibration factor, shear parameter, and final longitudinal resolution were extracted, as summarized in Table 4.38.

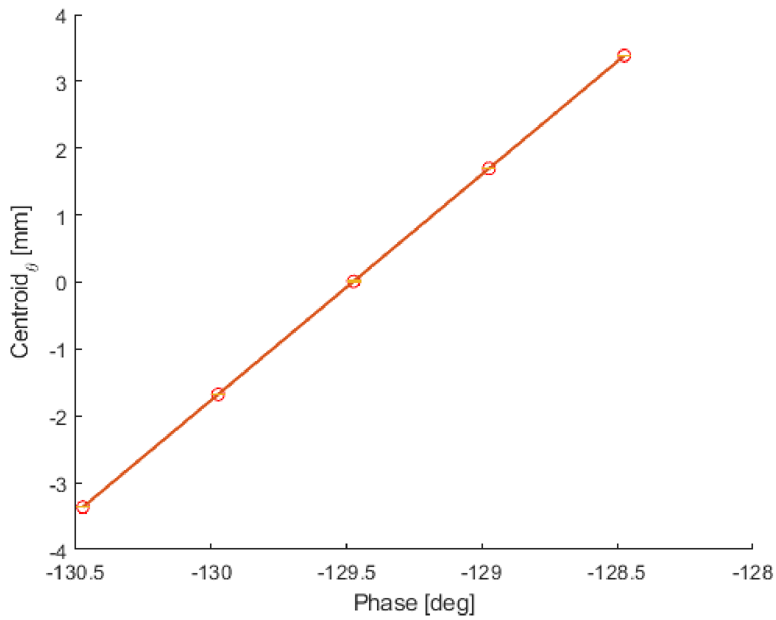


**Figure 4.36:** Calibration curve obtained by varying the RF phase of the vertically deflecting cavity around the zero-crossing. The linear fit provides the calibration coefficient and the integrated deflecting voltage.

| **Parameter** | **x Streaking** | **y Streaking** |
|---|---|---|
| $\sigma_{off}$ [$\mu m$] | $28 \pm 6$ | $15 \pm 5$ |
| V [MV] | $48.9 \pm 0.7$ | $51.4 \pm 0.5$ |
| Calibration [$\mu m$/fs] | $13.9 \pm 0.4$ | $14.6 \pm 0.8$ |
| Screen Calibration [fs/pixel] | $\sim 0.25$ | $\sim 0.24$ |
| Shear Parameter [$\mu m/\mu m$] | $46.2 \pm 0.3$ | $48.6 \pm 0.4$ |
| Resolution [fs] | $2.0 \pm 0.4$ | $1.0 \pm 0.2$ |

**Table 4.38:** TDS Calibration results for the high-energy beamline. The reported uncertainty corresponds to the propagated error from the linear fit parameters.

**Measurement results** In Fig. 4.37 are shown the simulated beam images obtained at the measurement screen for the two streaking configurations, while Fig. 4.38 reports the corresponding reconstructed current profile, showing that the temporal reconstruction correctly matches the input macroparticle distribution.

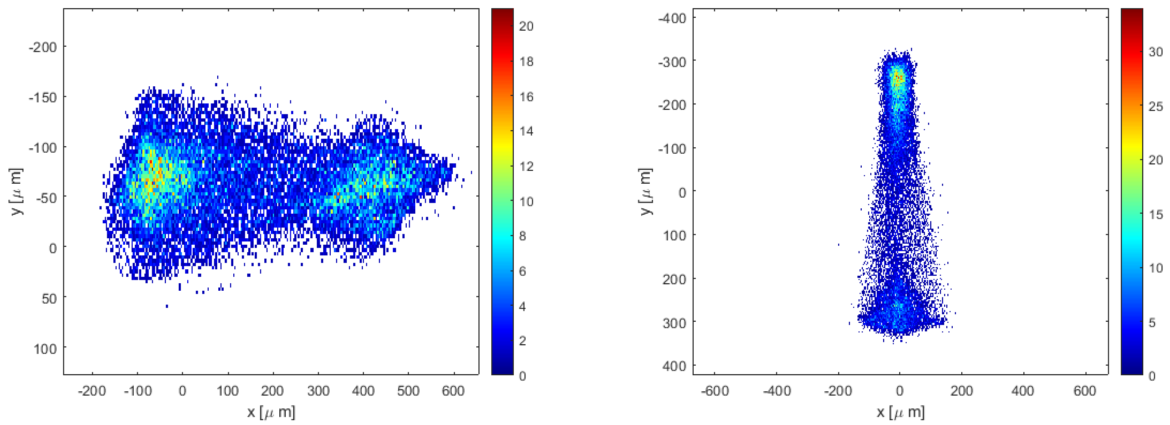


**Figure 4.37:** Simulated beam images at the measurement screen for the horizontal (left) and vertical (right) streaking configurations, obtained with the high-energy PolariX TDS at 50 MV integrated voltage.

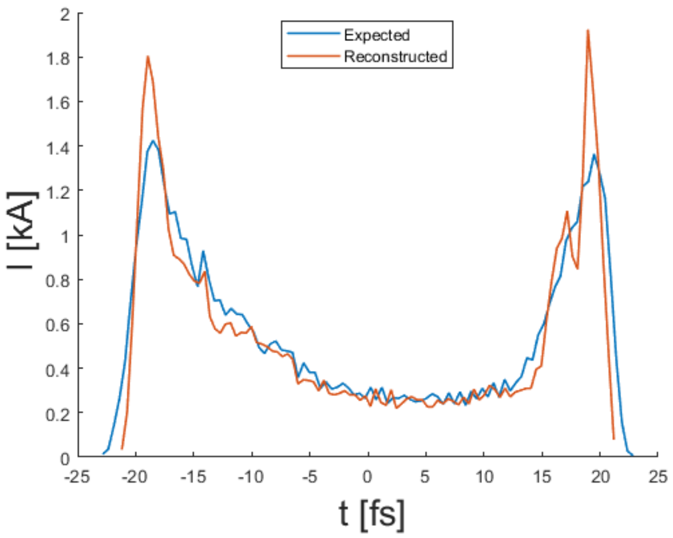


**Figure 4.38:** Reconstructed temporal profiles of the bunch from the vertical streaking configurations. The measurement yields consistent results for bunch length and profile shape.

In Table 4.39 are summarized the results for the bunch length measurements. Both streaking configurations yield consistent values of the bunch length, confirming the reliability of the measurement and the accuracy of the calibration procedure. With these simulated parameters and resolution, the reconstructed bunch length corresponds to $\sigma_t = 14.9 \pm 0.6$ fs, with a relative deviation of $\sim 1.4\%$ from the input value.

| **Parameter** | **x Streaking** | **y Streaking** |
|---|---|---|
| $\sigma_{t_{\text{expected}}}$ [fs] | $\sim 14.7$ | |
| $\sigma_t$ [fs] | $15.0 \pm 0.9$ | $14.8 \pm 0.9$ |
| $\sigma_{t_{\text{mean}}}$ [fs] | $14.9 \pm 0.6$ | |
| Rel. Error [%] | $\sim 4.0$ | |
| $\lvert\sigma_{t_{\text{mean}}} - \sigma_{t_{\text{expected}}}\rvert$ [%] | $\sim$1.4 | |

**Table 4.39:** Summary of the bunch length measurement results for both streaking directions at the high-energy beamline. The mean bunch length is obtained as the weighted average of the two measurements.

Table 4.40 shows how the result of the bunch length measurement varies as a function of the screen resolution, i.e., of the effective pixel size. As expected, the relative error increases for lower screen resolutions; however, it remains below 10% even for the worst resolution considered, confirming the robustness of the measurement.

| **Screen Res.** | 3.5 $\mu m$ | 5.25 $\mu m$ | 7 $\mu m$ |
|---|---|---|---|
| Pixel Calibration [fs/pixel] | 0.24 | 0.36 | 0.48 |
| $\sigma_t$ [fs] | 14.9 | 14.9 | 14.9 |
| Err. $\sigma_t$ [fs] | 0.6 | 1.1 | 1.3 |
| Rel. Error [%] | $\sim 4.0$ | $\sim 7.5$ | $\sim 8.6$ |
| $\lvert\sigma_{t_{\text{mean}}} - \sigma_{t_{\text{expected}}}\rvert$ [%] | $\sim 1.4$ | $\sim 1.4$ | $\sim 1.4$ |

**Table 4.40:** Summary of the bunch length measurement with respect to the screen resolution at the high-energy beamline.

## 4.7 EOS: Complementary longitudinal jitter measurement

Longitudinal beam diagnostics based on radio-frequency devices, such as TDS, provide precise measurements of the bunch temporal profile. However, these measurements are intrinsically multi-shot, and although the technique offers high resolution, it does not allow for the retrieval of single-shot information, which is essential for investigating shot-to-shot jitter in the beam temporal profile and its effect on the acceleration process. Moreover, since the driver–witness separation is on the order of $\approx$ ps, the two beams cannot be simultaneously imaged on the screen within the same acquisition window. As a result, their relative distance cannot be effectively measured. In the context of plasma acceleration, the witness beam experiences a different accelerating field depending on its phase within the plasma wave, and variations in the driver–witness separation directly translate into fluctuations in the final beam energy. Characterizing this temporal jitter on a shot-to-shot basis is therefore fundamental to evaluating the stability of plasma acceleration.
For this reason, a complementary single-shot diagnostic technique, known as electro-optic sampling (EOS), is employed. The EOS method relies on the interaction between the transient electric field of the relativistic electron bunch and a birefringent electro-optic crystal probed by a synchronized laser pulse. The electric field induces a transient birefringence in the crystal, imprinting the temporal profile of the bunch field onto the intensity (or polarization) profile of the laser pulse. In this way, the longitudinal profile of the bunch can be reconstructed in a single shot with a temporal resolution of approximately $\sim$ fs at the bunch leading edge and a global resolution of a few tens of femtoseconds. Unlike the TDS-based analysis, the EOS measurements presented here were carried out experimentally at the SPARC_LAB facility, without the need for numerical simulations [50]. This section describes the experimental measurement and results obtained from this single-shot diagnostic study at the existing EOS station at the SPARC accelerator.

### 4.7.1 Velocity bunching and RF-timing jitter

The bunch compression technique determines the observed timing jitter by means of a velocity bunching mechanism based on a longitudinal phase-space rotation induced by an initial velocity difference between the head and the tail of the electron bunch. The beam is injected into the RF cavity at the zero-crossing phase, as shown in Fig. 4.39, with a velocity smaller than the phase velocity of the RF travelling wave and an initial velocity chirp, where the head has a higher velocity than the tail. As a result, the bunch slips back in phase toward a higher accelerating field: the head experiences a weaker field compared to the tail, leading to simultaneous compression and energy chirping of the bunch [49, 51].
The velocity bunching process couples the longitudinal position of the bunch to the timing stability of the RF system, making the beam dynamics sensitive to arrival time jitter (ATJ). The ATJ is mainly determined by two contributions: variations in the laser arrival time at the photocathode and instabilities in the RF system timing. Other effects, such as fluctuations in the magnetic fields or RF amplitude, are negligible. The primary sources of timing jitter are therefore the photocathode laser and the two S-band klystrons, K1 and K2. K1 feeds the RF gun and the third accelerating section (S3), whereas K2 powers the first two sections (S1 and S2), with S1 operated for beam compression.

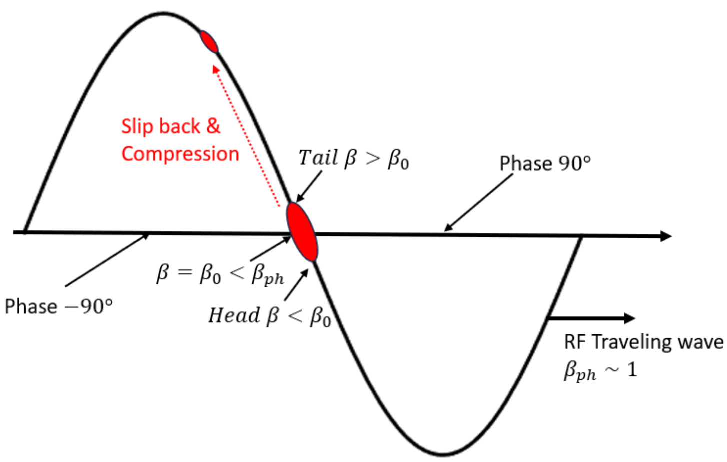


**Figure 4.39:** Velocity bunching principle: since the bunch velocity is smaller than the wave's phase velocity and there is a velocity chirp, it will slip in phase and be compressed [51].

The total beam arrival time variation at the linac exit can be expressed as:

$$\Delta t \simeq \sum_{i=1}^{3} c_i \, \Delta t_i \ , \tag{4.8}$$

where $i = 1$ refers to the laser photocathode, $i = 2$ to klystron K1, and $i = 3$ to klystron K2. Among these, the coefficient $c_3$ associated with the S1 field contribution is the dominant term, as it strongly affects the bunch compression process and thus the overall timing stability.
The arrival time jitter in the relative position between the driver and witness bunches translates into fluctuations in the witness energy during plasma acceleration. The driver excites a wakefield whose slope depends on the plasma density; therefore, as the witness oscillates in position along the wakefield due to timing jitter, it experiences different accelerating gradients and consequently varying energy gains from shot to shot [52].

### 4.7.2 Experimental setup

The beamline at the SPARC_LAB test facility is shown in Fig. 4.40. Two electron bunches of different charges, referred to as driver and witness, are generated using the laser-comb technique at the SPARC photo-injector, and the same technique will be employed at the EuPRAXIA@SPARC_LAB facility [53]. The injector consists of an RF gun that accelerates the beam to approximately 5 MeV, followed by three S-band accelerating sections, with the first (S1) acting as a velocity buncher for beam compression. Since compression occurs at low energy, a solenoid surrounding the gun provides emittance compensation, thereby preventing emittance growth due to space-charge effects.
The witness beam is subsequently accelerated by a plasma accelerator module consisting of a three cm-long and one mm-diameter discharge capillary filled with hydrogen. Within this capillary, the driver bunch excites a plasma wakefield that accelerates the witness bunch. The measured plasma density ranges from $n_e \sim 10^{15}$ to $10^{16}$ cm$^{-3}$ [54].

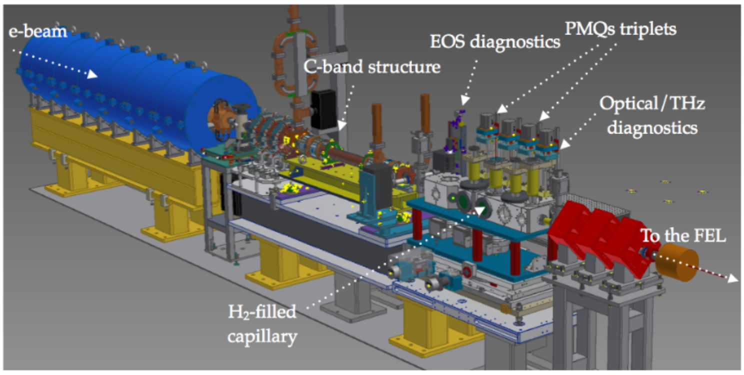


**Figure 4.40:** Layout of the SPARC linear accelerator at the SPARC_LAB test facility, highlighting the plasma module and EOS position in the beamline [50].

The diagnostic system includes an existing electro-optic sampling (EOS) station located upstream of the plasma accelerator and a magnetic spectrometer downstream of the plasma module. This configuration enables a complete longitudinal characterization of the beam. The spectrometer image is acquired using two Ce:YAG (Cerium-Doped Yttrium Aluminium Garnet) scintillator screens. A synchronized laser pulse stabilizes the plasma discharge; therefore, the observed timing jitter between the driver and witness bunches is mainly attributed to RF system instabilities.

**Electro-Optic Sampling (EOS)** The electro-optic sampling (EOS) working principle relies on the Coulomb field of the relativistic bunch, which induces a transient birefringence in an electro-optic crystal (The crystal used in this experiment is zinc telluride) [55]. A slowly varying external electric field $E_{\text{ext}}(t)$ (with a frequency in the THz region) induces a time-dependent change in the refractive indices of the crystal. This modulation can be detected using a linearly polarized laser pulse that crosses the crystal. The induced birefringence introduces a phase delay $\Gamma(t)$ between the horizontal and vertical components of the laser field, proportional to the beam's electric field. The detected laser intensity is given by:

$$I_{\text{det}} = I_{\text{laser}}^2 \sin^2 \Gamma(t) \ , \tag{4.9}$$

where the phase delay is expressed as:

$$\Gamma(t) = \frac{\pi d}{\lambda} n_0^3 r_{41} E_{\text{ext}}(t) \ , \tag{4.10}$$

with $E_{\text{ext}}(t)$ the external field generated by the beam, $r_{41}$ the non-linear electro-optic coefficient, $\lambda$ the laser wavelength, $d$ the crystal thickness, and $n_0$ the unperturbed refractive index of the crystal. The EOS chamber is located at the entrance of the plasma interaction chamber. In this experiment, the EOS was implemented in the spatial decoding configuration, where the laser crosses the ZnTe crystal at an angle of $\theta = 30°$ with respect to the beam propagation axis, as shown in Fig. 4.41. The passing electron bunch induces an external electric field that locally alters the crystal's refractive index. Different spatial points across the transverse laser profile traverse the crystal at different times, experiencing the field at successive instants. As a result, each position on the laser front encodes a distinct temporal slice of the bunch field [56].

The temporal coordinate $t$ is related to the transverse spatial coordinate $x$ of the laser pulse through:

$$t = \frac{x}{c} \tan\theta \ , \tag{4.11}$$

allowing the temporal profile of the bunch field to be reconstructed from the spatial modulation of the transmitted probe beam intensity.

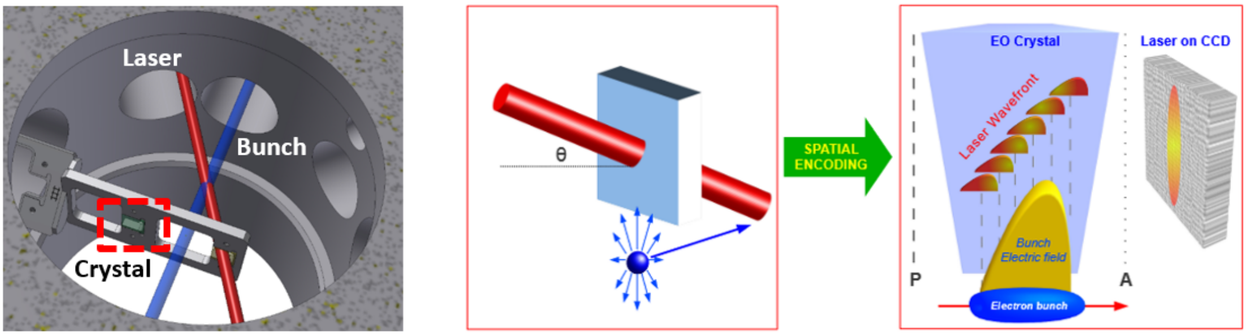


**Figure 4.41:** Layout of EOS chamber before the plasma module (left) and Working principle of the EOS spatial decoding configuration (right). The laser pulse crosses the crystal at an angle $\theta = 30°$; thus, different points on the pulse front interact with the bunch field at different times and acquire distinct polarizations. From the recorded laser profile, the longitudinal distribution of the electron bunch can be reconstructed [55].

### 4.7.3 Measurement and Analysis Results

The measurements of the witness energy were performed with the magnetic spectrometer downstream of the plasma accelerator. At the same time, the relative distance between the bunches was measured with the EOS station upstream of the plasma module. The corresponding recorded images are shown in Fig. 4.42, where each signal results from the superposition of all acquired shots.

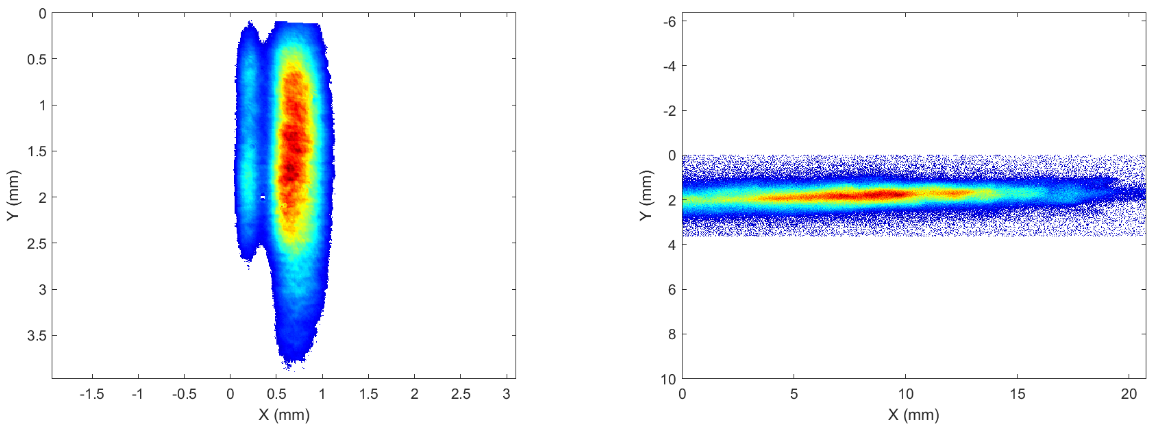


**Figure 4.42:** Driver-witness signal acquired with the EOS diagnostic (left) and energy measurement of the witness beam at the spectrometer screen (right). The image is obtained by summing the signal from all acquired frames.

The driver and witness beam charges were $Q_D = (200 \pm 5)$ pC and $Q_W = (20 \pm 3)$ pC, respectively. After the linac, the witness beam energy was approximately $E \simeq 87$ MeV with an energy spread of $\Delta E \simeq 0.45$ MeV.
Two measurement datasets were acquired, each consisting of 400 consecutive shots. After plasma acceleration, the average witness energy increased to $E_{\text{mean}} \approx 92$ MeV, corresponding to an acceleration of about $\Delta E = 5$ MeV. The average separation between the driver and witness bunches was measured as $\Delta t = (1.03 \pm 0.06)$ ps for the first dataset and $\Delta t = (1.20 \pm 0.10)$ ps for the second one. A clear linear correlation was observed between the measured driver–witness separation jitter and the corresponding witness energy jitter, as shown in Fig. 4.43. The slope of the correlation was $m_{\text{fit}} = (10 \pm 1)$ keV/fs for the first dataset and $(8.2 \pm 0.6)$ keV/fs for the second. The smaller slope in the second case is attributed to a lower plasma density, which reduces the wakefield gradient. The effect of jitter on the plasma acceleration is therefore significant, given the high accelerating field achieved in the plasma module [57]. The results are summarized in Table 4.41.

| **Parameter** | **1st Dataset** | **2nd Dataset** | **Unit** |
|---|---|---|---|
| $E_{\text{mean}}$ | $92.3 \pm 0.4$ | $92.1 \pm 0.4$ | MeV |
| $E_{\text{spread}}$ | $0.4 \pm 0.1$ | $0.5 \pm 0.1$ | MeV |
| $\Delta t$ | $1.03 \pm 0.06$ | $1.20 \pm 0.10$ | ps |
| $m_{\text{fit}}$ | $10 \pm 1$ | $8.2 \pm 0.6$ | keV/fs |

**Table 4.41:** Summary of the EOS and spectrometer measurement results for the two datasets. $E_{\text{mean}}$ is the witness mean energy, $E_{\text{spread}}$ the energy spread, $\Delta t$ the average bunch separation, and $m_{\text{fit}}$ the slope of the linear correlation between the jitter in distance and the energy.

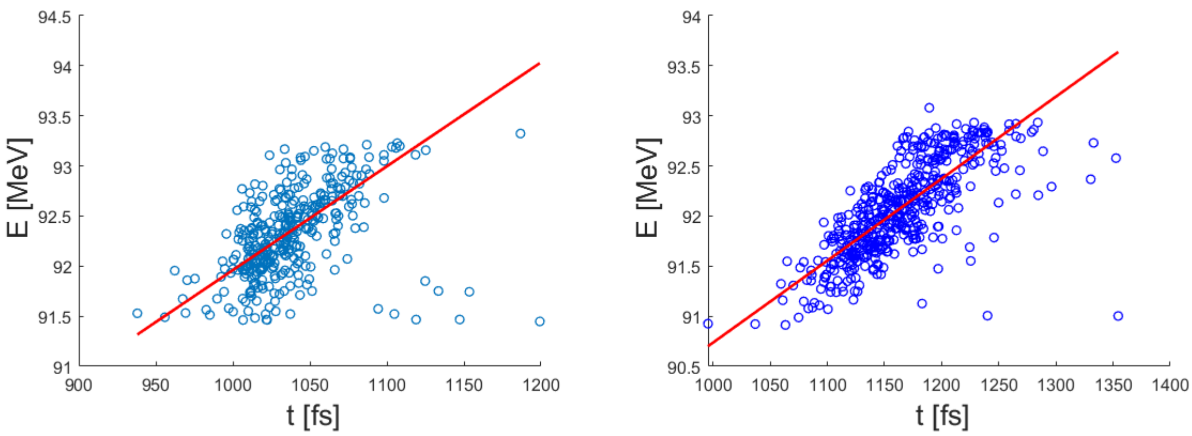


**Figure 4.43:** Measured correlation between the driver–witness distance and the witness energy after plasma acceleration for the first Dataset (left) and second Dataset (right). The linear fit has slope respectively $m = (10 \pm 1)$ keV/fs and $m = (8.2 \pm 0.6)$ keV/fs.

## 4.8 Tomographic reconstruction for EuPRAXIA@SPARC_LAB

The PolariX TDS, owing to its variable polarization capability, can operate not only as a conventional TDS but also as a tomographic diagnostic for reconstructing the three-dimensional (3D) charge distribution of the electron bunch. By rotating the polarization of the deflecting field, the bunch can be projected along different transverse directions, providing a set of streaked images corresponding to multiple projection angles. These projections are then combined using a tomographic reconstruction algorithm, which enables the retrieval of the 3D and, subsequently, the 5D phase-space distribution of the beam. A detailed description of the reconstruction procedure and its 5D extension is presented in the following chapter (see Chapter 5). In this section, the application of 3D tomography at the high-energy beamline is given, and the feasibility study of 5D tomography is presented.

### 4.8.1 3D reconstruction

In the present study, this method has been applied to the witness bunch at the high-energy beamline (1 GeV). The deflecting voltage was set to approximately 50 MV, yielding a longitudinal calibration factor of about 14.9 fs/$\mu m$, corresponding to 0.23 fs/pixel at a screen resolution of 3.5 $\mu m$. Ten different polarization angles were used to acquire the input projections for the tomographic reconstruction. The beam optics were matched to yield symmetric transverse beam sizes at the measurement screen, ensuring a uniform temporal resolution across all polarization angles, albeit at the expense of a degraded overall resolution, requiring the measurement to be performed at the far-distant screen (∼8.38 m from the TDS). This limit on achievable resolution imposes a consistent constraint on the application of tomography at low energy, so only the high-energy case is presented in this chapter. Considering a slice resolution of $\sim$ 2.1 fs, for a total of 22 slices, the 2D longitudinal–transverse projections from the reconstructed 3D distribution are shown in Fig. 4.44.

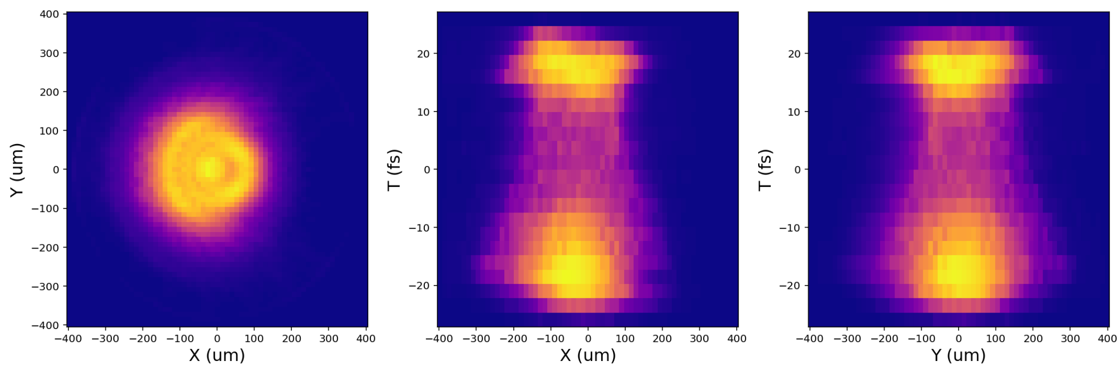


**Figure 4.44:** Reconstructed 2D projections at the high-energy beamline: transverse $(x, y)$ distribution (left), longitudinal $(x, t)$ projection (center), and longitudinal $(y, t)$ projection (right). Each image is obtained by integrating the reconstructed 3D distribution $I(t, x, y)$ along the corresponding axis [58].

From the reconstructed distribution, the temporal profile and the transverse beam sizes as functions of the longitudinal coordinate can be retrieved, as shown in Fig. 4.45.

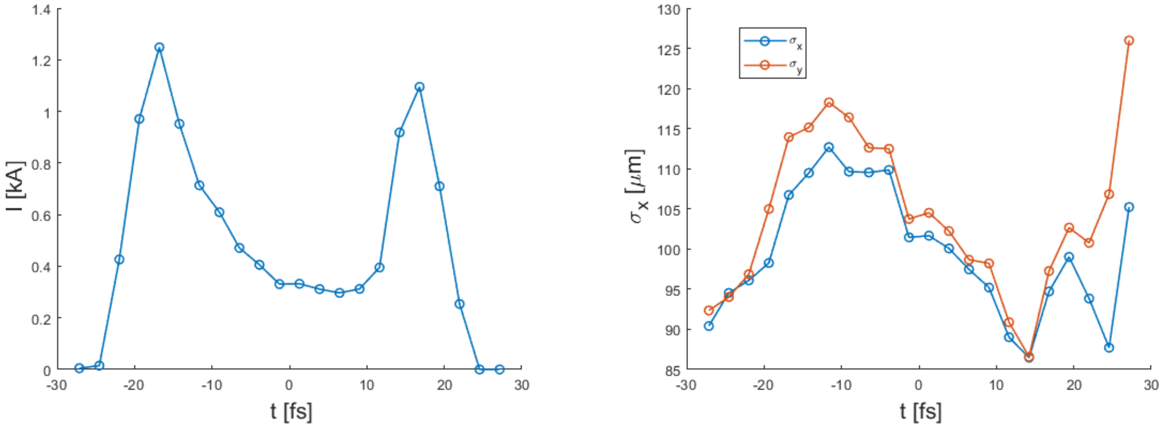


**Figure 4.45:** Time-dependent evolution of the current (left) and horizontal-vertical transverse beam sizes (right) obtained from the 3D reconstruction. Each point corresponds to a single temporal slice of the reconstructed 3D distribution.

The main reconstructed parameters are summarized in Table 4.42, including the longitudinal bunch length (both rms and full width), and the transverse rms sizes $\sigma_x$ and $\sigma_y$ at the reconstruction point corresponding to the TDS location. The relative difference between the reconstructed and the expected bunch length is approximately 6%. This value is larger than the 1.4% reported in Table 4.39, mainly due to the reduced temporal resolution associated with the larger streaked beam size. The 3D SART reconstruction algorithm used in this work is based on a code developed by D. Marx, as described in Ref. [58].

| **Quantity** | **Reconstructed** | **Expected** | Diff. [%] |
|---|---|---|---|
| $\sigma_x$ [$\mu$m] | $104 \pm 4$ | 106 | $\sim 2$ |
| $\sigma_y$ [$\mu$m] | $101 \pm 4$ | 103 | $\sim 2$ |
| $\sigma_t^{\text{rec}}$ [fs] | $16 \pm 2$ | 14.7 | $\sim 6$ |
| $\text{FWHM}_t^{\text{rec}}$ [fs] | $38 \pm 2$ | 40 | $\sim 5$ |

**Table 4.42:** Reconstructed beam parameters at the high-energy beamline, reporting the expected and reconstructed RMS transverse sizes $\sigma_x$, $\sigma_y$, bunch length $\sigma_t$ and $FWHM_t$, with respective standard deviations and difference relative to the input.

### 4.8.2 Feasibility study of the 5D tomographic reconstruction

The next level of tomographic reconstruction achievable with the PolariX TDS is the five-dimensional (5D) reconstruction, which aims at retrieving the full phase-space distribution of the bunch, including the transverse phase planes $(x, x')$ and $(y, y')$ together with the longitudinal coordinate. While the detailed experimental implementation will be discussed in the following chapter, here is presented a preliminary feasibility study based on beamline simulations for the EuPRAXIA@SPARC_LAB high-energy diagnostics section.
The goal of this study is to verify whether the EuPRAXIA beamline layout can support the operational requirements of a 5D tomographic measurement. Two main constraints must be satisfied:

- The presence of a PolariX TDS capable of variable polarization streaking
- The availability of a quadrupole section that allows performing a transverse phase-advance scan.

The first condition is already fulfilled by design, as the TDS system is integrated in the diagnostic beamline. The second condition, however, depends on the magnetic lattice's flexibility and the available drift length between the TDS and the observation screen. In the current EuPRAXIA beamline configuration, the dispersive screen is located approximately 3.27 m downstream of the TDS, at the entrance to the undulator section. This distance limits the achievable transverse phase advance, making it impossible to find suitable quadrupole settings for all desired combinations of $\mu_x$ and $\mu_y$. To overcome this limitation, an alternative screen position has been considered downstream of the undulators, extending the total beamline length to ~8.38 m. This modification enables a complete scan of the phase advance, with solutions found for ten steps in both the horizontal and vertical planes. The corresponding sets of phase advances, together with the matched Twiss parameters $\beta$ and $\alpha$, are shown in Fig. 4.46.

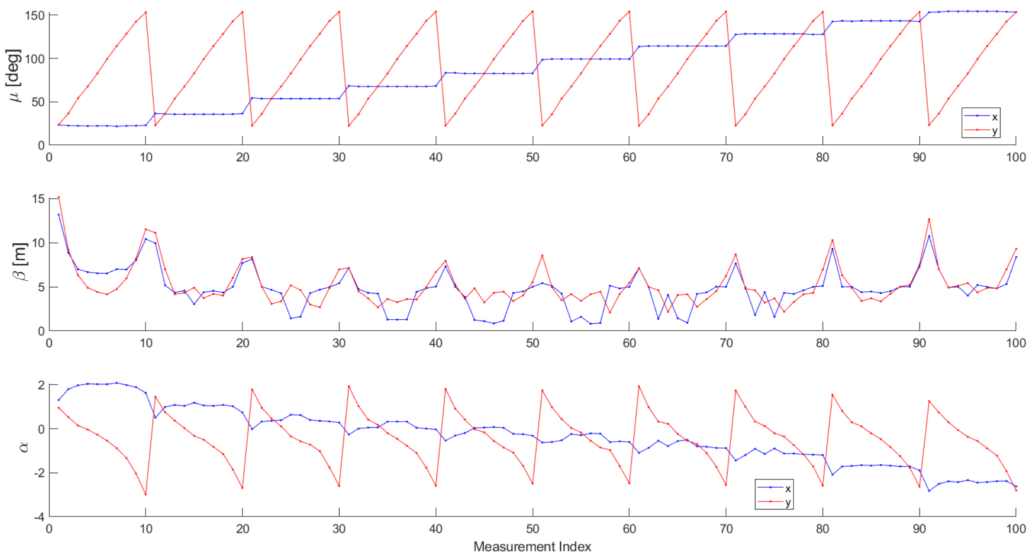


**Figure 4.46:** Optimized phase advance combination and Twiss parameters at the screen, for the horizontal (blue) and vertical transverse plane, at the high-energy beamline.

During the optimization, the $\alpha$ functions were kept as close to zero as possible to minimize beam rotation at the reconstruction point, while maintaining the $\beta$ functions below 10 m for both planes. The scan successfully covered a wide range of transverse phase advances, as shown in Fig. 4.46, while maintaining stable optical functions at the screen. The representative 1D scan reported in Table 4.43 illustrates how the Twiss parameters evolve when varying $\mu_y$ at fixed $\mu_x$.

| Index | $\mu_x$ [deg] | $\mu_y$ [deg] | $\beta_x$ [m] | $\beta_y$ [m] | $\alpha_x$ | $\alpha_y$ |
|---|---|---|---|---|---|---|
| 1 | 18.9 | 19.6 | 13.2 | 15.2 | 1.3 | 1.0 |
| 2 | 19.1 | 31.2 | 8.9 | 9.2 | 1.8 | 0.5 |
| 3 | 19.4 | 47.4 | 7.0 | 6.3 | 2.0 | 0.1 |
| 4 | 19.3 | 60.6 | 6.7 | 4.9 | 2.0 | -0.04 |
| 5 | 19.5 | 75.1 | 6.5 | 4.4 | 2.0 | -0.3 |
| 6 | 19.5 | 92.0 | 6.5 | 4.2 | 2.0 | -0.5 |
| 7 | 18.8 | 106.9 | 7.0 | 4.7 | 2.1 | -0.9 |
| 8 | 19.4 | 121.0 | 7.0 | 6.0 | 2.0 | -1.3 |
| 9 | 19.2 | 136.1 | 8.0 | 8.2 | 1.9 | -2.0 |
| 10 | 19.0 | 147.7 | 10.4 | 11.5 | 1.6 | -3.0 |

**Table 4.43:** Representative 1D scan (varying $\mu_y$, fixed $\mu_x$). Screen optics per setting.

The global statistics of the full $10 \times 10$ scan, summarized in Table 5.3, confirm this overall stability. Both $\beta_x$ and $\beta_y$ show average values close to 5 m, with standard deviations of only a few meters. More than 70% of the settings satisfy the target condition $|\beta - 5| \leq 10\%$, ensuring homogeneous phase-space coverage for the tomographic reconstruction. Similarly, the $\alpha$ functions remain small, with the majority of cases fulfilling $|\alpha| \leq 2$. These results demonstrate that the optics optimization provided a robust parameter space, suitable for the experimental requirements of the 5D reconstruction.

| | **Mean** | **Std** | **Min** | **Max** | **In-band** [%] |
|---|---|---|---|---|---|
| $\beta_x$ [m] | 4.8 | 2.3 | 0.8 | 13.2 | 75% ($|\beta_x - 5| \leq 10\%$) |
| $\beta_y$ [m] | 5.2 | 2.3 | 2.1 | 15.2 | 73% ($|\beta_y - 5| \leq 10\%$) |
| $\alpha_x$ | $-0.3$ | 1.2 | $-2.8$ | 2.1 | 85% ($|\alpha_x| \leq 2$) |
| $\alpha_y$ | $-0.4$ | 1.2 | $-3.0$ | 1.9 | 89% ($|\alpha_y| \leq 2$) |

**Table 4.44:** Summary statistics of the Twiss parameters at the screen over the $10 \times 10$ scan.

The presented studies in this section assess the feasibility of applying the 5D tomographic reconstruction at the high-energy beamline, showing the capability of performing the necessary quadrupole scan in both transverse planes—i.e., a phase-advance scan between the reconstruction point and the measurement screen—while preserving the stability of the beam parameters throughout the scan. Although the tomographic reconstruction itself is not implemented in this section, the present simulations establish that the EuPRAXIA high-energy diagnostic beamline fulfills both the lattice and resolution requirements for a future 5D reconstruction. The experimental verification of this methodology will be discussed in chapter 5.

## 4.9 Diagnostics simulations summary

This section summarizes the simulation results of virtual measurements at the three different diagnostics beamlines along the machine, aimed at evaluating the resolution and measurement limits.

- Downstream of the photoinjector, after the laser heater, at beam energy $E = 118\,\text{MeV}$.
- After the first X-band accelerating structure and the bunch compressor, at $E = 400\,\text{MeV}$.
- Downstream of the plasma module, just before the entrance to the undulator, at $E = 1\,\text{GeV}$.

In Table 4.45 are reported the beam parameters at each diagnostics beamline.

| **Parameter** | **Low-Energy** | | **Mid-Energy** | | **High-Energy** |
|---|---|---|---|---|---|
| | **Witness** | **Driver** | **Witness** | **Driver** | **Witness** |
| $E_{\text{Nom.}}$ [MeV] | 118 | 119 | 403 | 404 | 1000 |
| Charge [pC] | 30 | 200 | 30 | 200 | 30 |
| $\varepsilon_N$ [$\mu m$] | 0.7 | 1.5 | 0.7 | 1.5 | 1.2 |
| $\sigma_t$ [fs] | 17 | 193 | 28 | 97 | 15 |
| $E_{\text{spread}}$ [%] | 0.1 | 0.7 | 0.1 | 0.2 | 0.1 |

**Table 4.45:** Nominal Beam Parameters at the Diagnostic Stations.

The emittance resolution has been determined by simulating measurements using the quadrupole scan technique for different emittance values and screen resolutions. In Table 4.46, the resolution results for the reference screen resolution of 3.5 $\mu m/pixel$ are reported.

| **Parameter** | **Low-Energy** | **Mid-Energy** | **High-Energy** |
|---|---|---|---|
| Energy [MeV] | 118 | 400 | 1000 |
| Distance Quad.-Screen [m] | 4.05 | 4.11 | 4.84 |
| Resolution [$\mu m$] | 0.3 | 0.2 | 0.4 |

**Table 4.46:** Parameters of the emittance simulation results at the diagnostics station at low-, middle-, and high-energy.

The longitudinal bunch properties will be characterized using the PolariX TDS, which is installed at both the low-energy (60 cm long) and high-energy (96 cm long) beamlines. The diagnostics simulations have been developed and optimized to achieve a nominal resolution of approximately $\sim 1$ fs, in line with the beamline layout and the RF system's constraints on the maximum gradient achievable in the cavity. The parameters and results from the temporal profile measurements are presented in Table 4.47, for the reference case of the witness beam.

| **Parameter** | **Low-Energy** | **High-Energy** |
|---|---|---|
| Energy $[MeV]$ | 118 | 1000 |
| Drift TDS-Screen $[m]$ | 3.35 | 3.07 |
| TDS Length $[m]$ | 0.60 | 0.96 |
| Max Voltage $[MV]$ | 23 | 56 |
| Max Resolution $[fs]$ | 1.1 | 0.9 |
| Calibration [fs/pixel] | $\sim 0.07$ | $\sim 0.24$ |
| $\sigma_t$ [fs] | $16 \pm 1$ | $14.9 \pm 0.6$ |

**Table 4.47:** Parameters of TDS Measurements at the low-energy and high-energy diagnostics stations.

Finally, the energy measurement results at the spectrometers are reported in Table 4.48, for the reference case of the witness beam. These results take into account the effects of synchrotron radiation for the different energies, at the reference screen resolution of 3.5 $\mu m$.

| **Parameter** | **Low-Energy** | **Mid-Energy** | **High-Energy** |
|---|---|---|---|
| Mean $E_{bin}$ width [keV/pixel] | 0.66 | 2.16 | 5.07 |
| Mean Energy [MeV] | 118.2 | 402.5 | 1004.3 |
| RMS [keV] | 156.0 | 236.6 | 923.7 |

**Table 4.48:** Parameters of energy measurements for the witness beam at the different energy spectrometers.

The results presented in this chapter demonstrate that the diagnostic measurements foreseen for the SPARC_LAB operations are consistent with the expected beam parameters. The implemented diagnostic system effectively characterizes the electron beams produced in the facility. Moreover, the possibility of applying tomographic reconstruction techniques to the high-energy diagnostics section has been successfully verified, and their experimental implementation will be discussed in the following chapter. Overall, the obtained results confirm the reliability of the proposed diagnostic layout and its suitability for future experimental campaigns.

# Chapter 5

# Experimental activities with the PolariX TDS at SwissFEL

This chapter presents the experimental campaign conducted for the tomographic reconstruction of the three- and five-dimensional phase space at the SwissFEL facility at the PSI center. The objective is to describe the setup, the adopted methodology, and the main results obtained with the PolariX transverse deflection structure. The PolariX TDS opens new possibilities in beam diagnostics, providing enhanced resolution and reliability in the characterization of the electron bunch, with achievable temporal resolutions below the fs level [59].
Building on the unique features of the PolariX TDS, which allows for variable streaking direction, both three-dimensional and subsequently five-dimensional tomographic reconstructions have been successfully demonstrated, confirming its potential as an advanced diagnostic tool. Tomographic methods have been increasingly applied in accelerator physics to overcome the limitations of conventional diagnostics, extending the reconstruction of the beam distribution beyond 2D projections. In particular, these methods were initially developed for the reconstruction of the three-dimensional phase space, with early experimental demonstrations reported in Refs. [58, 60, 61]. They were subsequently further developed and systematically applied in experimental studies at the DESY center in Hamburg, establishing a robust framework for multidimensional phase-space reconstruction. More recently, the extension to five-dimensional phase-space reconstruction has been experimentally demonstrated, revealing correlations between transverse phase spaces and time that were previously inaccessible [9, 10].
The experimental campaign was the result of a collaboration between DESY, PSI, and INFN–LNF groups, each with distinct interests. At PSI and DESY, the primary goal was to establish 5D phase-space reconstruction at SwissFEL and to assess its potential as a routine diagnostic tool. The INFN–LNF group, on the other hand, was motivated by the prospect of applying the PolariX TDS and tomographic techniques in another facility, in view of their forthcoming implementation at the EuPRAXIA@SPARC_LAB accelerator. The contributions of the different institutes were complementary: DESY provided expertise in tomographic reconstruction algorithms and data analysis, while PSI was primarily responsible for the operation of the PolariX TDS and the experimental activities at SwissFEL. The INFN–LNF contribution was integrated across both experimental and analysis aspects within the collaboration. In this framework, a comprehensive understanding of the particle beam distribution, including temporal resolution and phase-space correlations, was consid-

ered essential. These requirements could be met thanks to the fs-level temporal resolution provided by the PolariX TDS and the advanced analysis enabled by 5D tomography. The overall aim of the campaign was therefore to evaluate and benchmark the 5D reconstruction technique on realistic electron beams at the Athos beamline of SwissFEL, demonstrating both the femtosecond resolution and the reliability of such diagnostics.

The chapter is organized as follows. Section 5.1 describes the experimental setup at the Athos diagnostic beamline of SwissFEL, providing an overview of the facility and of the instrumentation employed. Section 5.2 outlines the methodology for the 3D and 5D reconstructions, with a focus on the procedure adopted to retrieve high-dimensional phase-space distributions from the PolariX TDS measurements. Section 5.3 presents the beam-dynamics simulations performed to define the optics settings required for the measurements. Section 5.4 reports the results of the deflector calibration and the corresponding longitudinal resolution obtained. Section 5.5 presents the results of the 3D tomographic reconstruction, while Section 5.6 reports the outcomes of the 5D tomography analysis. Finally, in Section 5.7, the summary and conclusion of the presented experiment are reported.

## 5.1 Experimental setup - ATHOS beamline at SwissFEL

### 5.1.1 SwissFEL facility

SwissFEL is the X-ray free-electron laser facility at the Paul Scherrer Institute (PSI) in Villigen, Switzerland. It is based on a superconducting linac capable of delivering high-brightness electron beams with an energy up to 6 GeV, operating at a 100 Hz repetition rate. The machine hosts two undulator beamlines, Aramis and Athos, which cover the hard and soft X-ray regimes, respectively. SwissFEL has been designed to provide extremely short photon pulses with high peak brightness and full transverse coherence, serving a wide user community across physics, chemistry, biology, and materials science. In addition to user operation, SwissFEL serves as a testbed for advanced accelerator concepts and novel beam diagnostic techniques, thanks to its flexible layout and state-of-the-art instrumentation [62].
The SwissFEL layout is reported in Fig. 5.1, and consists of a high-brightness gun, coupled with a laser heater and a booster, three linear accelerating sections, and two magnetic compression stages. This main beamline is capable of producing electron beams with energies ranging from 2.1 GeV to 5.8 GeV, feeding two undulator beamlines, one in the soft x-rays, ATHOS (0.65-5 nm), and the second one in the hard x-rays, ARAMIS (0.1-0.7 nm) [63].

### 5.1.2 Athos beamline

The Athos branch of SwissFEL is dedicated to producing soft X-rays with energies ranging from approximately 250 eV to 2 keV. The corresponding electron beam energy at the undulator entrance ranges from 2.6 GeV to 3.4 GeV. Athos is designed to provide advanced operation modes, such as two-color lasing, the generation of attosecond pulse trains, and tailored polarization states, which place stringent demands on the quality and stability of the driving electron beam. To achieve these modes, Athos is equipped with a dedicated diagnostics section upstream of the undulators, including beam position monitors, screens, spectrometers, and a high-resolution longitudinal phase-

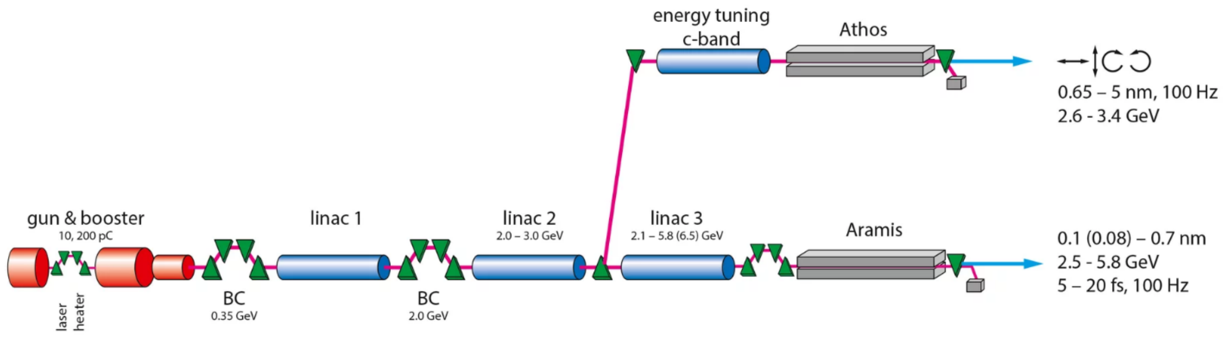


**Figure 5.1:** Illustration of the SwissFEL layout, highlighting the acceleration and bunch compression stages, and the two x-ray beamlines [62].

space diagnostics station. This flexibility makes Athos not only a unique user facility but also an ideal environment for experimental campaigns aimed at testing advanced diagnostics, such as the PolariX TDS, and demonstrating 3D and 5D phase-space reconstructions.

The electron bunch from ATHOS has a charge in the range 10 to 200 pC, a duration of 15 to 30 fs rms, and a normalized emittance of a few hundred nm. It comprises 16 undulator modules, each measuring 2 m in length and having a period of 38 mm, resulting in a maximum deflection parameter K of 3.8. Two magnetic chicanes between the undulator modules also allow the application of a delay to the electron beam [64].

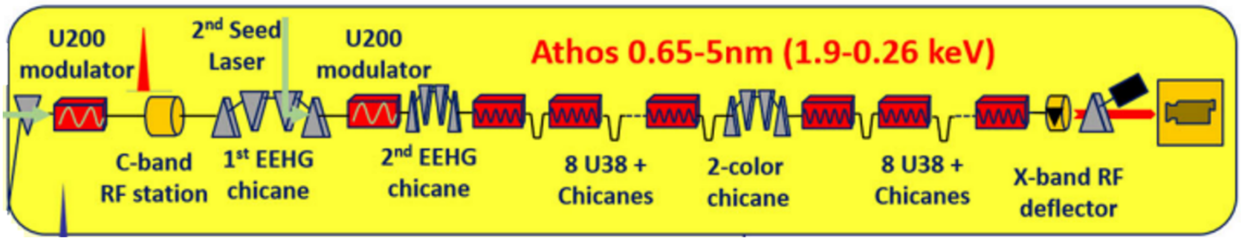


**Figure 5.2:** Illustration of the ATHOS layout, highlighting the acceleration and bunch compression stages, and the two x-ray beamlines [64].

### 5.1.3 Diagnostics beamline at Athos SwissFEL

The post-undulators diagnostics section of the Athos beamline, used for the present measurements, consists of a set of electromagnetic quadrupoles, two transverse deflecting structures (TDS), an RF phase shift system, and a downstream screen station. The beamline layout is shown in Fig. 5.3.

Six quadrupoles are located downstream of the undulator line, providing the required optics matching to the screen stations and to the TDS section. The quadrupole gradient at the nominal beam energy of 3.4 GeV corresponds to a normalized strength $k$ ranging between $-4.5$ and $+4.5$ m$^{-2}$, which translates into magnetic gradients up to approximately 50 T/m.

The core of the diagnostic section is composed of two PolariX TDS units, each approximately 1.2 m in length (corresponding to roughly 120 cells, with a cell length of 8.3 mm). Each structure features couplers approximately 0.16 m in length, resulting in an active length of nearly 1.0 m. A dedicated high-power klystron powers the structures through an RF distribution and control system.

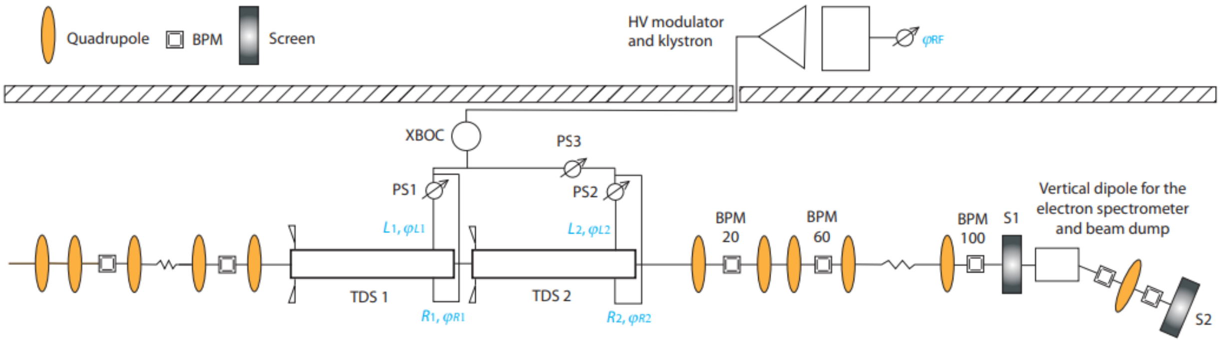


**Figure 5.3:** Diagnostics beamline at Athos SwissFEL, in which are shown the quadrupole elements used for matching to the TDS and screen, the two PolariX TDS with their RF feeding system, and the screen downstream the beamline [59].

Furthermore, a system of three phase shifters allows for the selection of the streaking direction in the TDSs. Downstream of the TDS section, an additional set of five quadrupoles is installed. These magnets are typically employed for slice emittance measurements or for beam studies in combination with the deflectors when the setup is not operated in the 5D phase-space reconstruction mode. In the present configuration, they were kept switched off. This choice is motivated by the fact that operating them would introduce transverse coupling effects: when a beam is streaked in the vertical or horizontal plane, the particles acquire an offset from the quadrupole axis. A quadrupole acting on an off-axis beam imparts kicks in both transverse planes, thereby distorting the reconstructed phase space. Keeping these quadrupoles off avoids such artificial cross-plane correlations.
Finally, a screen station is located approximately 11 m downstream of the deflectors. This station, described in detail in Section 5.1.5, provides the transverse images used for the temporal and phase-space measurements.

### 5.1.4 PolariX TDS system

Two PolariX TDs are installed in the diagnostics beamline, whose parameters are listed in Table 5.1. A dedicated klystron provides the necessary input power, supported by an X-band open-barrel cavity for RF pulse compression and the RF power distribution line feeding the cavities. A picture of the system highlighting the main components is shown in Fig. 5.4.

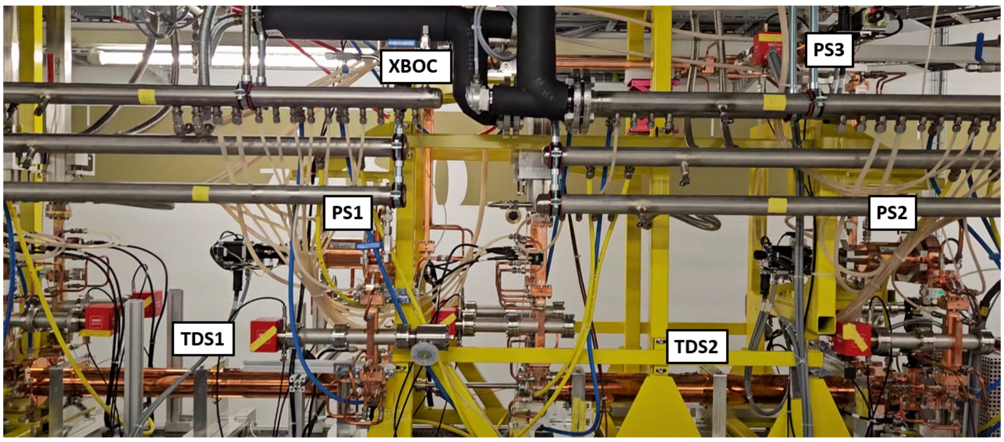


**Figure 5.4:** Picture of the PolariX RF system, including the two TDS, the phase shifters, and the XBOC.

| **TDS parameters** | **Value** | **Unit** |
|---|---|---|
| Frequency | 11,995.2 | MHz |
| Phase advance/cell | 120 | ° |
| Iris radius | 4 | mm |
| Iris thickness | 2.6 | mm |
| Group velocity | -2.666 | $\%c$ |
| Quality factor $Q$ | 6490 | |
| Shunt impedance | 50 | MΩ/m |
| Number of cells | 120 | – |
| Filling time | 129.5 | ns |
| Total length | 1160 | mm |
| Power-to-voltage | 6.1 | $\text{MV}/(\text{MW})^{1/2}$ |
| **2 × TDS + BOC** | **Value** | **Unit** |
| Power-to-voltage | 16.08 | $\text{MV}/(\text{MW})^{1/2}$ |
| Maximum voltage | 90 | MV |

**Table 5.1:** Main RF parameters of the PolariX TDS and the BOC power distribution system.

To provide flexible streaking conditions and to compensate for residual phase errors between the two cavities, a dedicated system of three phase shifters (PS) is installed along the RF distribution line. PS1 controls the phase of the first cavity, PS2 the phase of the second cavity, and PS3 regulates the relative phase difference between the two. The latter is essential to correct the transverse kicks in the plane orthogonal to the streaking, which was observed from the system at the zero crossing phase, which is by definition the phase at which there is no transverse displacement of the bunch centroid. Each PolariX cavity is fed by two input branches that excite the counter-rotating circular modes with defined amplitudes, and the transverse field on axis is the superposition of these two modes. When the amplitudes are balanced and the relative phase is set appropriately, the resulting field is linearly polarized, with a polarization angle that depends on the relative phase between the two branches. Any amplitude imbalance or phase error produces an elliptical polarization, introducing a finite field component in the plane orthogonal to the intended streaking direction and thus a residual orthogonal kick. In a system of two TDSs, the residual kick can also emerge from an incorrect combination of the three phase shifters' phases. By tuning the PS3, these effects can be minimized, ensuring that the streaking is purely aligned with the intended transverse axis.

### 5.1.5 Image acquisition system

The beam images were acquired using a scintillating screen coupled to a CCD camera system. The screen was made of Ce:Yag (Cerium doped yttrium aluminium garnet crystal), with a thickness of 50 $\mu m$, typically used in accelerator operations. The optical system is developed following a Scheimpflug geometry to minimize the effect of COTR generated from microbunching that may be present in the electron bunch [65], shown in Fig. 5.5.
The optical system is shown in Fig. 5.6, and consists of a Nikon 200 mm f/4 ED-IF Micro lens with an effective magnification of 1:1, which projected the screen image onto the camera sensor [66]. The scintillating screen is in a vacuum, tilted 15 deg, and the lens is 250 mm from the screen. A motorized stage for the lens and camera system allows for regulation of the optical path, thereby adjusting the system focus on the screen.

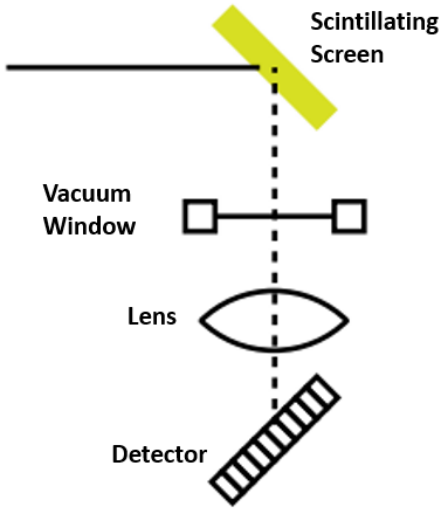


**Figure 5.5:** Illustration of the optical arrangement following the Scheimpflug principle. The scintillating screen is tilted with respect to the optical axis to minimize background and geometrical constraints. According to the Scheimpflug condition, the planes of the screen, the lens, and the detector intersect along a common line, ensuring that the image of the tilted screen remains in focus across its entire surface[65].

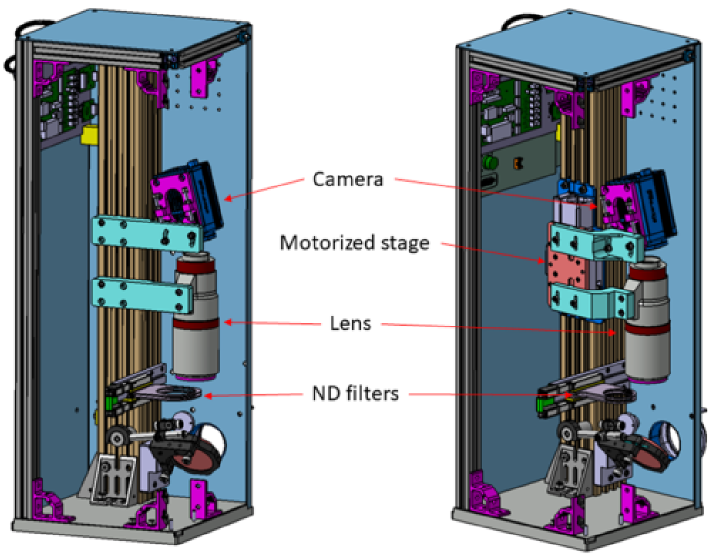


**Figure 5.6:** Layout of the optical system designed for the measurement screen, consisting of filters, a lens, a motorized stage, and the camera [66].

The camera is a **"pco.edge 5.5 DS CLHS sCMOS"**, with a pixel pitch of 6.5 $\mu m$ and a maximum dynamic range of 30000:1, as shown in Fig. 5.7. The camera operates in 16-bit mode and has a resolution of 2560×2160 pixels. The sensor type is "sCMOS" with an interframe time of 100 ns [67].


**Figure 5.7:** Photograph of the CCD camera used for the diagnostics. The camera features a pixel pitch of 6.5 $\mu m$, a resolution of [2560×2160] pixels, and a dynamic range of 30000:1 [67].

The scintillating light has a wavelength range of 500 nm to 700 nm, with a maximum at 550 nm. The design maintains a constant camera gain to maximize the signal-to-noise ratio of the camera electronics. The acquisition settings were optimized to balance resolution and signal-to-noise ratio, with typical exposure times of 9.7 ms and a region-of-interest (ROI) to limit readout to the active beam area.
This acquisition chain defined the effective spatial resolution of the system, combining the intrinsic pixel size, optical point-spread function, and scintillator blur, resulting in a calibration of $\sim$ 6.66 $\mu m$/pixel for the horizontal axis and $\sim$ 6.52 $\mu m$/pixel for the vertical one.

## 5.2 Phase space reconstruction methodology

The Phase Space reconstruction is based on combining two scans: the streaking-angle scan with the Polarix TDS (necessary for the 3D reconstruction) and the phase-advance scan in both transverse planes.

### 5.2.1 Three-dimensional reconstruction

The 3D reconstruction is based on the Polarix TDS, operated at different streaking angles spanning 180° [58, 68, 69]. Each angle provides a projection of the electron bunch's temporal profile along a different axis in the transverse plane. The images are acquired for each streaking angle, in this case, operating with a total of 10 different polarizations. In each image, the temporal profile is discretized into slices, where each slice $t$ corresponds to a one-dimensional projection $D_t(\theta)$ at a specific streaking angle, as shown in Fig. 5.8. Each set of one-dimensional projections, called a sinogram, serves as input to the tomographic algorithm.

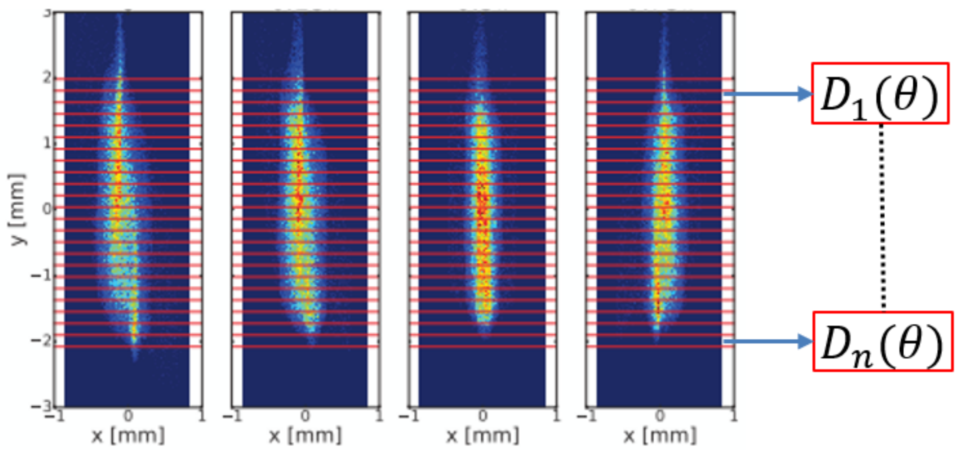


**Figure 5.8:** Each image, rotated by the streaking angle, is divided into temporal slices indicated by the (red lines), which are then considered as 1D projections $D_i(\theta)$ for the tomographic reconstruction algorithm [68].

The reconstruction algorithm employed is the Simultaneous Algebraic Reconstruction Technique (SART). This iterative method updates the intensity assigned to each grid element of the reconstructed distribution based on the discrepancy between the measured and the calculated projections. In matrix form, each projection can be written as: $P_t(\theta) = M_\theta \cdot I_t(x, y)$.
Where $P_t(\theta)$ is the measured projection at the streaking angle $\theta$, and $M_\theta$ is the corresponding projection matrix, and $I_t(x, y)$, is the discretized distribution to be reconstructed. At each iteration is defined the difference between the measured projections $D_t(\theta)$ and reconstructed $P_t(\theta)$:

$$r(\theta) = D_t(\theta) - P_t(\theta) \ , \tag{5.1}$$

The reconstruction distribution $I_t(x, y)$ is updated at each iteration by correcting the discrepancy between the measured and the calculated projections. The update rule can be written as:

$$I_t(x, y)^{(k+1)} = I_t(x, y)^{(k)} + \lambda\, M_\theta^T W \left(D_t(\theta) - P_t(\theta)\right) \ , \tag{5.2}$$

where $M_\theta^T$ is the transpose of the projection matrix, $W$ is a normalization factor accounting for the weight of each grid element in the projection, and $\lambda$ is a relaxation parameter controlling the convergence rate. SART is particularly suitable for cases where only a limited number of projections is available, as it provides stable results and mitigates artifacts compared to simple back-projection [70].
For each slice, a tomographic reconstruction of the transverse distribution is performed, and the collection of all slices is stacked together to form the 3D distribution $f(x, y, t)$, as shown in Fig. 5.9 [58]. This reconstruction is applied to each transverse phase-advance combination to perform full 5D tomography.

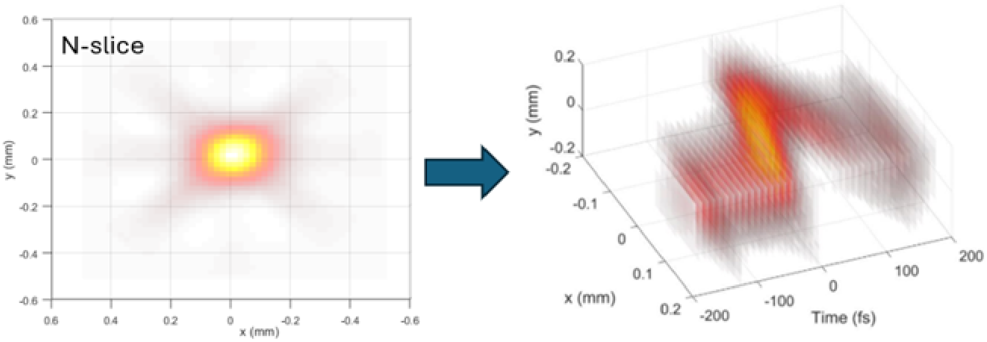


**Figure 5.9:** Reconstructed 2D intensity for the N-temporal slice in the transverse plane (left). The stacking of all slices along the longitudinal coordinate finally yields the three-dimensional distribution $f(x, y, t)$ (right) [58].

### 5.2.2 Four- and five-dimensional reconstruction

To extend the reconstruction to the transverse phase space, quadrupole scans are performed to vary the phase advance between the reconstruction point and the screen. Varying the quadrupole strength corresponds to a rotation in the normalized transverse phase space, so that the measured 2D images can be interpreted as projections of the higher-dimensional distribution $f(x, x', y, y')$.

$$I(x, y) = \iint f_{4D}(x, x', y, y')\, dx'\, dy' \ , \tag{5.3}$$

where the integration is carried out over the angular coordinates. A phase advance of $\theta_x = 90°$ in the horizontal plane can be described as a rotation of the transverse vector $(x, x')$:

$$\begin{pmatrix} x_1 \\ x_1' \end{pmatrix} = \begin{pmatrix} \cos\theta_x & \sin\theta_x \\ -\sin\theta_x & \cos\theta_x \end{pmatrix} \begin{pmatrix} x \\ x' \end{pmatrix} . \tag{5.4}$$

The corresponding rotated distribution $I(x_1, y)$ represents the projection $P_{y,\theta_x}(x_1)$ of the horizontal phase space along the angle $\theta_x$. The tomographic reconstruction is then carried out using the SART algorithm [71].

The reconstruction is performed for one transverse dimension at a time: first, from $I_y(x, \theta_x)$ the distribution $f(x, x', y)$ is obtained by keeping $y$ fixed. The same procedure is applied to the vertical coordinate to recover the full four-dimensional distribution $f_t(x, x', y, y')$. Treating each longitudinal slice independently and stacking the results finally yields the complete five-dimensional distribution $f(x, x', y, y', t)$, providing a comprehensive description of the bunch phase space [9, 30, 72, 73].

### 5.2.3 Experimental strategy and measurement conditions

The experimental campaign was designed to benchmark the diagnostic system's performance under defined operating conditions. The transverse deflecting structure was operated with an input power of 28 MW from the klystron, corresponding to a total deflecting voltage of approximately 70 MV, while the beam had an energy set to 3.4 GeV and a charge of 200 pC.

Two datasets were collected under different experimental conditions to test the robustness of the measurement procedure:

- **Dataset 1:** acquired in high-compression conditions, leading to a short beam ($\sigma_t \sim 20fs$) with the presence of horizontal-temporal correlations, due to non-linear effects in the compression stage.
- **Dataset 2:** acquired in moderate-compression conditions, leading to a longer beam ($\sigma_t \sim 40fs$) to relax the compression and reduce the observed correlations.

The comparison between the two datasets allows us to assess the reliability of the diagnostics procedure for resolving the different conditions and to validate the reconstruction procedure under various scenarios. This experiment enables the application of the reconstruction methodology to optimize bunch conditions at SwissFEL further. The measurement strategy adopted for the 5D reconstruction combined a quadrupole scan with a streaking-polarization scan provided by the PolariX TDS. Before data acquisition, high-power tests were performed to ensure the structure's stable operation up to about 70 MV, with a low risk of breakdown during the measurements. The three RF phase shifters were tuned to minimize residual transverse kicks and to select the desired polarization angle. The streaking direction was varied from 0° to 162° in steps of 18°, thus covering ten distinct orientations. The beam optics were then optimized using single-particle simulations of the transfer line, yielding quadrupole settings that achieved the required phase advance combinations at the screen. A total of 100 configurations were selected, corresponding to $(\mu_x, \mu_y)$ spanning from about 96° to 236°. These settings, described in Section 5.3, ensured both the necessary phase-space coverage and the stability of the optical functions at the observation point. For each optics configuration, images of the beam were recorded at all ten streaking directions. The effective streaking angle was subsequently determined by tracking the centroid shift in the transverse plane as the RF reference phase was varied. This allowed to verify the agreement between nominal and realized streaking orientations. Calibration measurements were performed at each polarization to determine the corresponding calibration factor and the longitudinal resolution. For each point, both streaked and unstreaked images were acquired, the latter serving as a reference for the system's intrinsic resolution. The acquired images underwent a standard pre-processing chain (background subtraction, rotation to the streaking axis, centering), as detailed in Appendix A.3.5. After this step, tomographic reconstructions were performed: first in 3D for each quadrupole setting, and subsequently combined to yield the full 4D and 5D phase-space reconstructions.

## 5.3 Beam optics simulations

**Normalized trace space and phase-advance rotation** For tomographic reconstruction, a quadrupole scan is performed to achieve controlled rotations of the transverse trace spaces between a reconstruction point (upstream of the TDS) and the observation screen. In normalized Courant–Snyder coordinates:

$$X \equiv \frac{x}{\sqrt{\beta_x}}, \qquad X' \equiv \alpha_x \frac{x}{\sqrt{\beta_x}} + \sqrt{\beta_x}\, x', \tag{5.5}$$

(and analogously for $(Y, Y')$), the linear transport between two locations acts as a pure rotation by the phase advance $\mu_x$ (and $\mu_y$ in the vertical plane):

$$\begin{pmatrix} X_1 \\ X_1' \end{pmatrix} = \begin{pmatrix} \cos\mu_x & \sin\mu_x \\ -\sin\mu_x & \cos\mu_x \end{pmatrix} \begin{pmatrix} X_0 \\ X_0' \end{pmatrix}, \qquad \begin{pmatrix} Y_1 \\ Y_1' \end{pmatrix} = \begin{pmatrix} \cos\mu_y & \sin\mu_y \\ -\sin\mu_y & \cos\mu_y \end{pmatrix} \begin{pmatrix} Y_0 \\ Y_0' \end{pmatrix} \tag{5.6}$$

This property motivates the optical design: by varying $\mu_x$ and $\mu_y$, each point in the scan corresponds to a set of evenly distributed projections of the higher–dimensional distribution [74].

**Quadrupole scan settings** For the scan are determined a set of quadrupole strengths $\{k_i\}^6$ (six quadrupoles upstream to the TDS) that produce the desired phase advances $(\mu_x, \mu_y)$ from the reconstruction point to the screen, while keeping the observation optics at the screen nearly invariant to avoid spurious changes in magnification. These optics settings are obtained with single–particle tracking simulation and built–in optimization in ELEGANT. For each target pair $(\mu_x^{(l)}, \mu_y^{(m)})$, the simulation determines the corresponding quadrupole strength combination. The lattice implemented in the simulations is shown in Fig. 5.10.

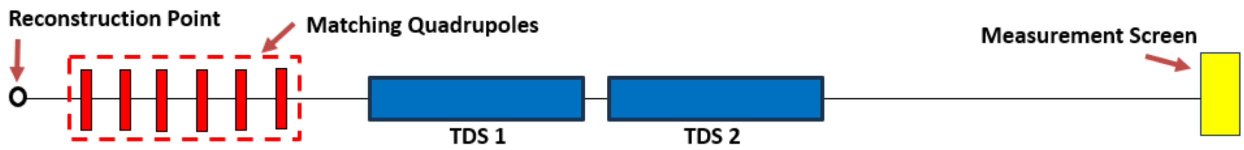


**Figure 5.10:** Diagnostics lattice implemented in the simulations, with highlighted the reconstruction point, matching quadrupoles, TDSs and measurement screen.

To cover all the projections range, is defined a $10 \times 10$ grid of phase advances, $\{\mu_x^{(l)}\}^{10}$ and $\{\mu_y^{(m)}\}^{10}$, uniformly spanning a projection range of 180 deg, yielding 100 optics settings, from 96 to 236 deg. Across the grid, the twiss parameters are also enforced at the screen to specific values: (i) $\beta_{x,y}$ tightly clustered around 20 m, and (ii) $\alpha_{x,y} \approx 0$, so that the beam is more collimated at the screen, and the longitudinal resolution is more stable around the same value during the measurement. Small residual variations in $\beta$ and $\alpha$ are acceptable and have a negligible impact on reconstruction quality.

**Beam optics simulation results** For documentation and reproducibility, for each of the 100 settings, are reported:

- the achieved $(\mu_x, \mu_y)$,
- $\beta_{x,y}, \alpha_{x,y}$ at the screen,
- the corresponding quadrupole set $\{k_i\}$ within hardware limits.

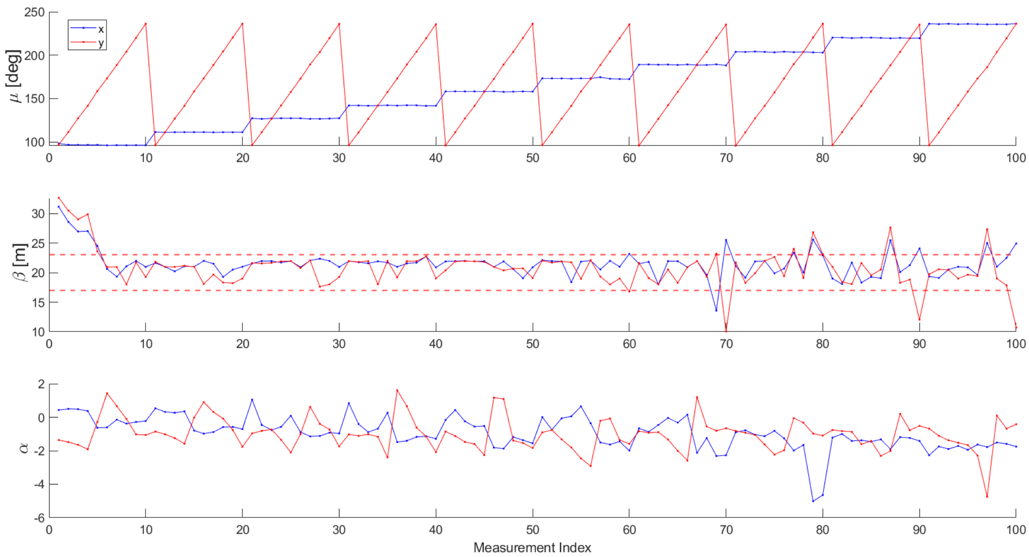


**Figure 5.11:** Optimized phase advance combination and Twiss parameters at the screen, for the horizontal (blue) and vertical transverse plane.

The scan successfully covered a wide range of transverse phase advances, as shown in Fig. 5.11, while maintaining stable optical functions at the screen. The representative 1D scan reported in Table 5.2 illustrates how the Twiss parameters evolve when varying $\mu_y$ at fixed $\mu_x$. In this case, $\beta_{x,y}$ remains within a narrow band around 20 m, with only a few points approaching more extreme values. The corresponding $\alpha_{x,y}$ oscillate around small negative values, occasionally crossing zero, but never reaching large deviations.

| Index | $\mu_x$ [deg] | $\mu_y$ [deg] | $\beta_x$ [m] | $\beta_y$ [m] | $\alpha_x$ | $\alpha_y$ |
|---|---|---|---|---|---|---|
| 1 | 98.3 | 97.0 | 31.2 | 32.7 | 0.4 | −1.4 |
| 2 | 96.8 | 111.4 | 28.6 | 30.5 | 0.5 | −1.5 |
| 3 | 96.7 | 127.4 | 27.0 | 29.0 | 0.5 | −1.7 |
| 4 | 96.7 | 141.6 | 27.0 | 29.9 | 0.4 | −1.9 |
| 5 | 96.7 | 158.7 | 24.5 | 23.5 | −0.6 | −0.3 |
| 6 | 96.2 | 173.3 | 20.6 | 20.9 | −0.6 | 1.4 |
| 7 | 96.4 | 188.7 | 19.3 | 21.0 | −0.1 | 0.7 |
| 8 | 96.3 | 204.1 | 21.1 | 18.0 | −0.4 | −0.1 |
| 9 | 96.4 | 220.1 | 22.0 | 21.8 | −0.3 | −1.0 |
| 10 | 96.3 | 236.3 | 21.0 | 19.3 | −0.2 | −1.1 |

**Table 5.2:** Representative 1D scan (varying $\mu_y$, fixed $\mu_x$). Screen optics per setting.

The global statistics of the full $10 \times 10$ scan, summarized in Table 5.3, confirm this overall stability. Both $\beta_x$ and $\beta_y$ show average values close to 20 m, with standard deviations of only a few meters. More than 85% of the settings satisfy the target condition $|\beta - 20| \leq 10\%$, ensuring homogeneous phase-space coverage for the tomographic reconstruction. Similarly, the $\alpha$ functions remain small, with the majority of cases fulfilling $|\alpha| \leq 2$. These results demonstrate that the optics optimization provided a robust parameter space, suitable for the experimental requirements of the 5D reconstruction.

| | Mean | Std | Min | Max | In-band [%] |
|---|---|---|---|---|---|
| $\beta_x$ [m] | 21.6 | 2.2 | 13.6 | 31.2 | 89% ($\lvert\beta_x - 20\rvert \leq 10\%$) |
| $\beta_y$ [m] | 20.7 | 3.3 | 10.0 | 32.7 | 89% ($\lvert\beta_y - 20\rvert \leq 10\%$) |
| $\alpha_x$ | $-0.93$ | 0.96 | 1.0 | $-5.0$ | 94% ($\lvert\alpha_x\rvert \leq 2$) |
| $\alpha_y$ | $-0.99$ | 0.98 | 1.6 | $-4.7$ | 87% ($\lvert\alpha_y\rvert \leq 2$) |

**Table 5.3:** Summary statistics of the twiss parameters at the screen over the $10 \times 10$ scan.

## 5.4 Deflector calibration and resolution

The streaking direction provided by the PolariX TDS was varied from 0° to 162° in steps of 18°, resulting in a total of ten polarization settings. For each polarization, a dedicated scan was performed by varying the RF phase around the zero-crossing, acquiring about 100 images per setting, to calculate the calibration factor converting the transverse distribution to the longitudinal one. From these images, the beam centroid positions in $x$ and $y$ were extracted as a function of RF phase.

**Variable polarization of the TDS** From the calibration data, images are acquired at the 10 different polarizations to verify the effective streaking angle imparted from the TDS. The images taken for each streaking angle are shown in Fig. 5.12.

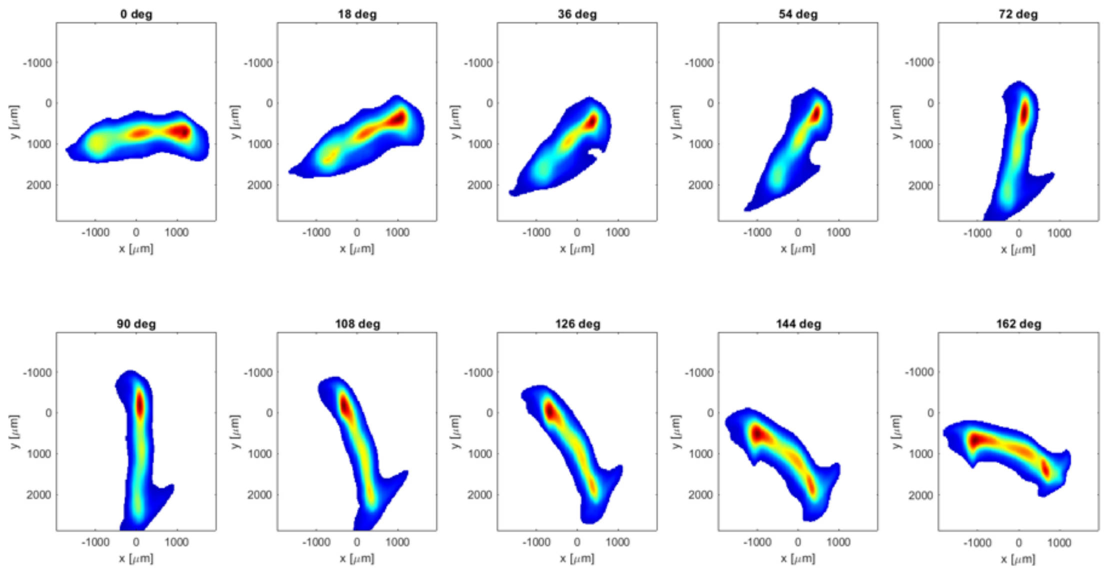


**Figure 5.12:** Beam images acquired at the zero-crossing of the RF phase for the ten polarization settings between 0° and 162°.

The centroid shifts allowed the determination of the effective streaking angle via:

$$\theta_{\text{eff}} = \arctan\left(\frac{C_y}{C_x}\right), \tag{5.7}$$

This provides a direct measure of the streaking orientation independently of possible intrinsic tilts in the beam distribution. This method ensures that the projection of transverse-longitudinal correlations in the beam itself does not bias the measured streaking angle.

The effective streaking angles extracted from the centroid analysis are summarized in Table 5.4, where they are compared with the nominal polarization settings. The agreement with the set polarization within a few degrees confirms the reliability of the phase-shifter tuning procedure.

| Polarization [deg] | Measured angle [deg] |
|---|---|
| 0 | $2.3 \pm 0.3$ |
| 18 | $19.6 \pm 0.3$ |
| 36 | $37.9 \pm 0.2$ |
| 54 | $56.6 \pm 0.5$ |
| 72 | $74.7 \pm 0.5$ |
| 90 | $92.9 \pm 0.2$ |
| 108 | $111.4 \pm 0.4$ |
| 126 | $130.1 \pm 0.2$ |
| 144 | $148.2 \pm 0.3$ |
| 162 | $165.2 \pm 0.5$ |

**Table 5.4:** Set polarization angles and corresponding measured streaking angles of the PolariX TDS.

**Calibration results** The PolariX TDS was calibrated by measuring the beam centroid offset as a function of RF phase around the zero-crossing. The dependence follows a sinusoidal trend, which can be linearized for small phases in the vicinity of the zero field. The slope of the linear fit provides the calibration coefficient $C$, also known as the shear parameter $S$, in normalized units.

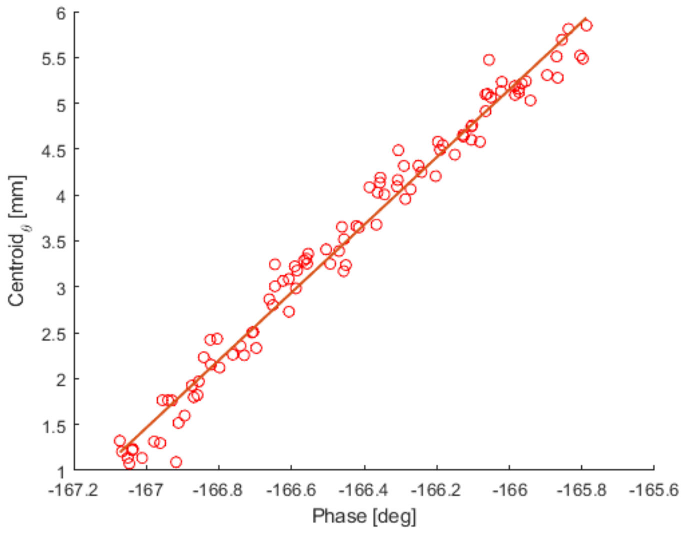


**Figure 5.13:** Linear fit of the measured bunch centroid offset with respect to the RF phase, for 0° polarization of the first dataset, yielding a factor $C = 15.9\ \mu m/\mu m$.

As representative examples, Fig. 5.13 shows the calibration fits obtained at polarization angles of 0° for the first dataset. The same procedure was applied to all streaking directions, and the extracted calibration factors are summarized in Table 5.5, where both $C$ and $S$ are reported for the two acquired datasets. The corresponding values as a function of the streaking angle are shown in Fig. 5.14.

Finally, Table 5.6 reports the global statistics of the calibration factor $C$, including mean, standard deviation, and minimum and maximum values. Because quadrupoles are not used after the TDSs,

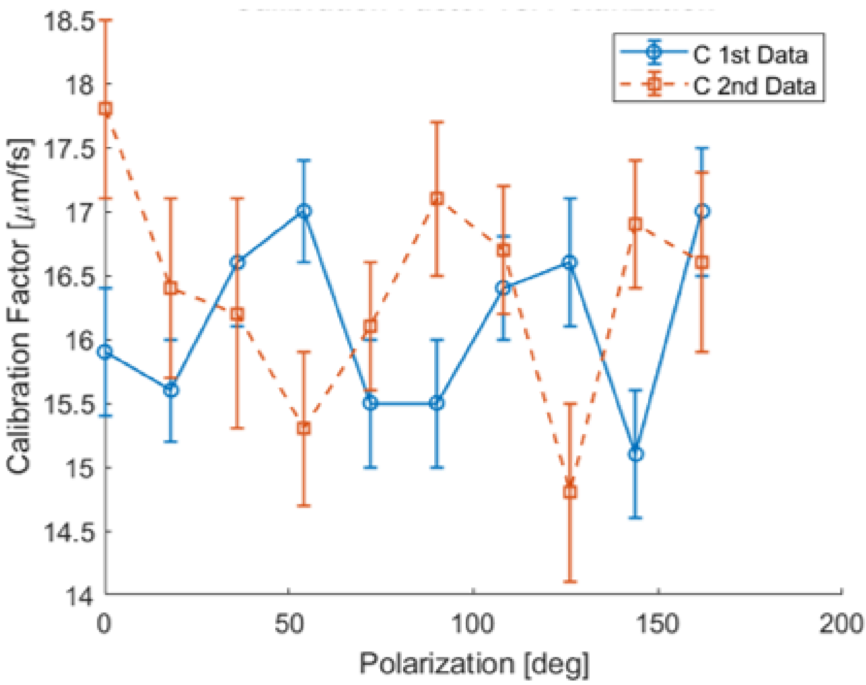


**Figure 5.14:** Measured Calibration factors for all the polarization angles, reported for dataset 1 and dataset 2.

| | Dataset 1 | | Dataset 2 | |
|---|---|---|---|---|
| **Polarization [deg]** | $C_1$ [$\mu m$/fs] | $S_1$ [$\mu m/\mu m$] | $C_2$ [$\mu$m/fs] | $S_2$ [$\mu m/\mu m$] |
| 0 | $15.9 \pm 0.5$ | $53 \pm 2$ | $17.8 \pm 0.7$ | $60 \pm 2$ |
| 18 | $15.6 \pm 0.4$ | $52 \pm 1$ | $17.4 \pm 0.7$ | $58 \pm 2$ |
| 36 | $16.6 \pm 0.5$ | $55 \pm 2$ | $16.2 \pm 0.9$ | $54 \pm 3$ |
| 54 | $17.0 \pm 0.4$ | $57 \pm 1$ | $15.3 \pm 0.6$ | $51 \pm 2$ |
| 72 | $15.5 \pm 0.5$ | $52 \pm 2$ | $16.1 \pm 0.5$ | $54 \pm 2$ |
| 90 | $15.5 \pm 0.5$ | $52 \pm 2$ | $17.1 \pm 0.6$ | $57 \pm 2$ |
| 108 | $16.4 \pm 0.4$ | $55 \pm 1$ | $16.7 \pm 0.5$ | $56 \pm 2$ |
| 126 | $16.6 \pm 0.5$ | $55 \pm 2$ | $14.8 \pm 0.7$ | $49 \pm 2$ |
| 144 | $15.1 \pm 0.5$ | $51 \pm 2$ | $16.9 \pm 0.5$ | $56 \pm 2$ |
| 162 | $17.0 \pm 0.5$ | $57 \pm 2$ | $16.6 \pm 0.7$ | $56 \pm 2$ |

**Table 5.5:** Calibration results for all streaking directions. For each polarization angle, the calibration coefficient $C$ and the shear parameter $S$ are reported for the two datasets (DS1 and DS2).

the calibration factor is expected to be the same for all polarizations and optics, since $C$ depends only on the deflecting structure parameters and the beam energy and transport, which remained unchanged during the measurement.

| **Quantity** | $C_1$ [$\mu$m/fs] | $C_2$ [$\mu$m/fs] |
|---|---|---|
| Mean | 16.1 | 16.5 |
| Std | 0.7 | 0.9 |
| Min | 15.1 | 14.8 |
| Max | 17.0 | 17.8 |
| Rel. var. [%] | 4.2 | 5.6 |

**Table 5.6:** Global statistics of the calibration coefficient $C$ over all streaking directions for the two datasets (Dataset 1).

### 5.4.1 Longitudinal Resolution

Once the calibration coefficient has been determined, the next step is to calculate the longitudinal resolution of the measurement. The longitudinal resolution is defined as:

$$R_t = \frac{\sigma_{\text{off}}}{C}, \tag{5.8}$$

where $\sigma_{\text{off}}$ is the unstreaked beam size along the direction of the streaking, and $C$ is the corresponding calibration coefficient. The unstreaked beam size is evaluated by calculating the beam size projected along the streaking axis. In this way, for example, at 0° the resolution is determined by the horizontal beam size, while at 90° it is determined by the vertical beam size.
Two levels of analysis are presented. In the first case, for each polarization angle, the resolution is averaged across all optical settings, yielding 10 values per dataset. These values are shown in Fig. 5.15 and summarized in 5.7, together with the standard deviation of the resolution distribution across the 100 optics at each polarization.

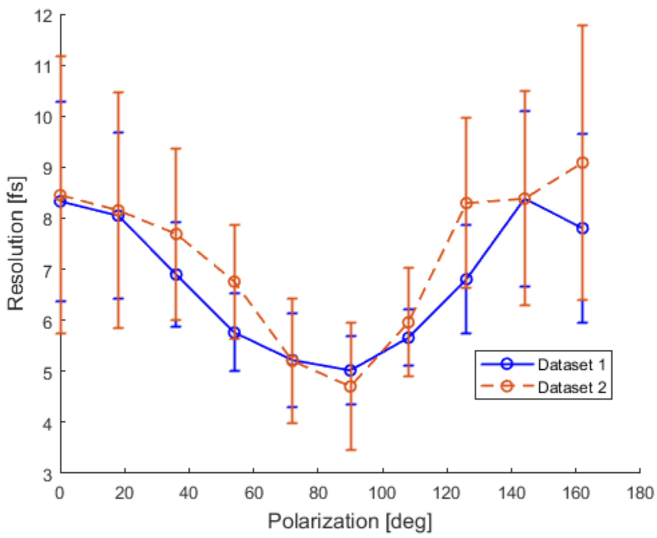


**Figure 5.15:** Measured longitudinal resolution for all the polarization angles, averaged over all optics settings, reported for dataset 1 and dataset 2.

| | Dataset 1 | | Dataset 2 | |
|---|---|---|---|---|
| **Polarization [deg]** | $\bar{R}_1$ [fs] | $\sigma_{R_1}$ [fs] | $\bar{R}_2$ [fs] | $\sigma_{R_2}$ [fs] |
| 0 | 8.3 | 1.9 | 8.5 | 2.7 |
| 18 | 8.0 | 1.6 | 8.2 | 2.3 |
| 36 | 6.9 | 1.0 | 7.7 | 1.7 |
| 54 | 5.8 | 0.8 | 6.8 | 1.1 |
| 72 | 5.2 | 0.9 | 5.2 | 1.2 |
| 90 | 5.0 | 0.7 | 4.7 | 1.3 |
| 108 | 5.7 | 0.6 | 5.9 | 1.1 |
| 126 | 6.8 | 1.1 | 8.3 | 1.7 |
| 144 | 8.4 | 1.7 | 8.4 | 2.1 |
| 162 | 7.8 | 1.8 | 9.1 | 2.7 |

**Table 5.7:** Average longitudinal resolution for each polarization angle (datasets 1 and 2).

In the second case, a global statistic is extracted by considering all the determined resolutions, as shown in Fig. 5.16 and reported in 5.8. This Table includes minimum, maximum, mean, standard deviation, and relative variation for both datasets.

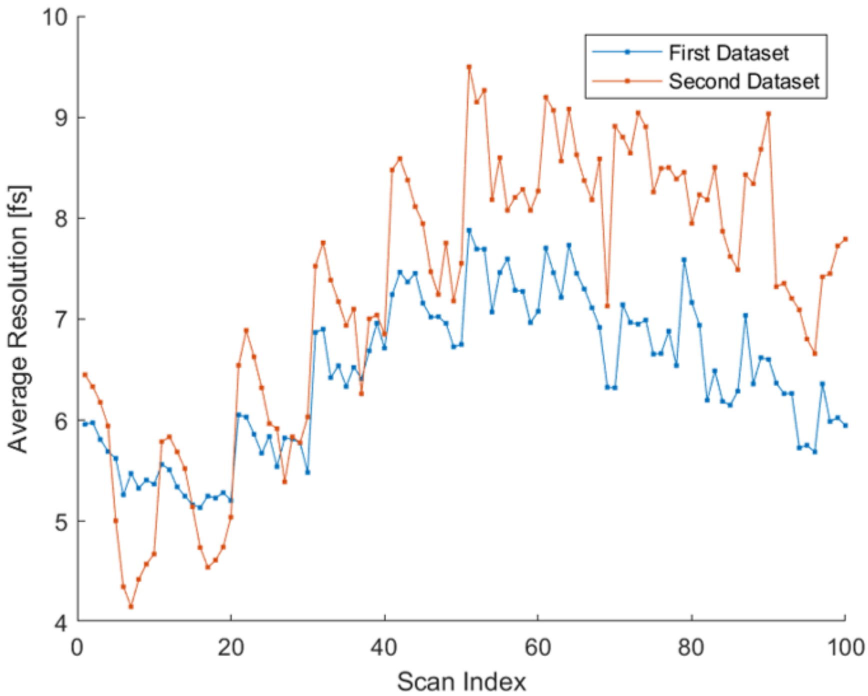


**Figure 5.16:** Average measured resolution over the 10 projections for all the optics settings, reported for dataset 1 and dataset 2.

| **Quantity** | $R_1$ [fs] | $R_2$ [fs] |
|---|---|---|
| Mean | 6.8 | 7.3 |
| Std | 1.8 | 2.4 |
| Min | 3.6 | 3.0 |
| Max | 11.7 | 12.4 |
| Rel. var. [%] | 26.6 | 32.7 |

**Table 5.8:** Statistical summary of all resolutions (datasets 1 and 2).

The results show that the longitudinal resolution varies significantly with the streaking direction and the optical configuration. The lowest and highest values provide the theoretical limits of the diagnostic system. However, while the worst-resolution limit limits the measurement, the reconstruction technique allows us to exploit information from higher-resolution points, enabling these features to be reconstructed in the final longitudinal phase space. For this reason, the effective resolution can be reasonably represented by the mean value, as it reflects the overall performance of the diagnostic setup.

**Measured bunch length** From the measurement of the calibration factor and the unstreaked beam size, the bunch length for the two datasets was derived from the corresponding streaked beam size, and the results are summarized in Table 5.9. The measured bunch length is $\sigma_t = 19.6 \pm 0.6$ fs for dataset 1, and $\sigma_t = 39 \pm 3$ fs for dataset 2.

| Quantity | Dataset 1 | | Dataset 2 | |
|---|---|---|---|---|
| | $x$ | $y$ | $x$ | $y$ |
| $\sigma_t$ [fs] | 18.9 | 20.2 | 42 | 37 |
| Std $\sigma_t$ [fs] | 0.7 | 0.9 | 3 | 2 |
| $\bar{\sigma}_t$ [fs] | 19.6 | | 39 | |
| $\Delta\ \sigma_t$ [fs] | 0.6 | | 3 | |

**Table 5.9:** Summary of the measured bunch length for the two datasets, reporting the measurement obtained from horizontal ($x$) and vertical ($y$) polarization, with respective standard deviations. The average value from the two polarizations is the measured bunch length.

## 5.5 3D Reconstruction and data analysis

In this section, the tomographic reconstruction of the 3D charge distribution is presented for datasets 1 and 2. The reconstruction algorithm employed is the *Simultaneous Algebraic Reconstruction Technique* (SART), which reconstructs the two-dimensional distribution $I_t(x, y)$ independently for each temporal slice of the bunch. The reconstruction is based on ten streaked projections acquired at different polarization angles between 0° and 180°, for a given temporal slice width $\Delta t_{\text{slice}}$. The 3D SART reconstruction algorithm used in this work is based on a code developed by D. Marx, as described in Ref. [58].

### 5.5.1 Dataset 1 - 3D reconstruction results

For the reference case, corresponding to a transverse phase advance of $\mu_x, \mu_y = 96$ deg, the reconstruction was performed using a slice width comparable to the temporal resolution of the measurement, i.e. $\sim 4.4$ fs

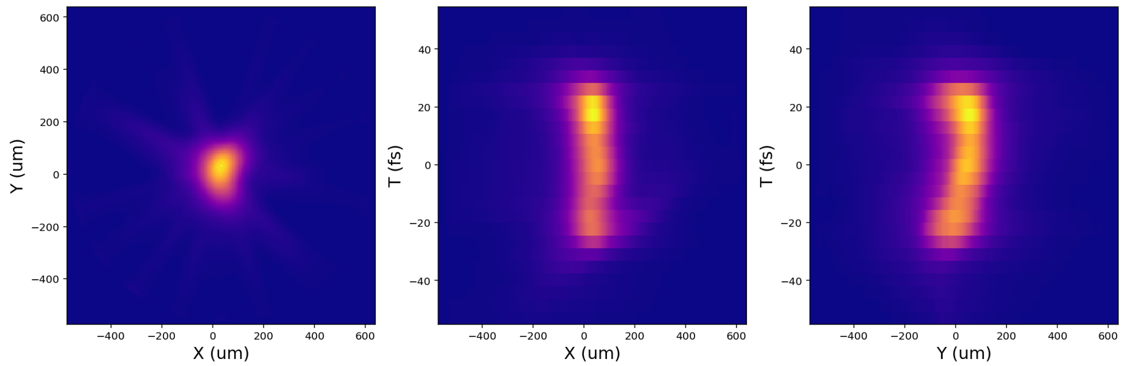


**Figure 5.17:** Reconstructed 2D projections: transverse $(x, y)$ distribution (left), longitudinal $(x, t)$ projection (center), and longitudinal $(y, t)$ projection (right). Each image is obtained by integrating the reconstructed 3D distribution $I(t, x, y)$ along the corresponding axis (Dataset 1).

Fig. 5.17 shows the reconstructed 2D projections $(x, y)$, $(x, t)$, and $(y, t)$ obtained by integrating the 3D distribution along the corresponding axes. These projections represent, respectively, the transverse image of the bunch and the two time-resolved streaked images in the horizontal and vertical planes. From these projections, the main beam parameters were extracted, namely $\sigma_x$, $\sigma_y$, and the reconstructed bunch length $\sigma_t$ and $\text{FWHM}_t$. The corresponding values are summarized in Table 5.10.

| Quantity | Value |
|---|---|
| $\sigma_x$ [$\mu$m] | 137 ± 7 |
| $\sigma_y$ [$\mu$m] | 135 ± 7 |
| $\sigma_t^{\mathrm{rec}}$ [fs] | 20 ± 4 |
| $\mathrm{FWHM}_t^{\mathrm{rec}}$ [fs] | 48 ± 4 |

**Table 5.10:** Reconstructed beam parameters for Dataset 1, reporting the RMS transverse sizes $\sigma_x$, $\sigma_y$, and the reconstructed bunch length $\sigma_t$ and $\mathrm{FWHM}_t$, with respective standard deviations.

The temporal profile reconstructed from the 3D tomographic data is shown in Fig. 5.18, together with the measured profiles obtained from the two reference projections at 0 deg and 90 deg. The visible differences between the reconstructed profile and the one measured at 90 deg are because the 3D reconstruction combines information from all ten projections, so that each temporal feature is weighted by its consistency across multiple viewing angles. Structures observed in most projections are therefore enhanced, while localized components visible in only one projection tend to be suppressed. This explains why complementary diagnostics, such as the quadrupole scan, remain essential for obtaining a complete description of the beam phase space, as they provide information on the second-order moments that are not directly accessible through the tomographic reconstruction alone.

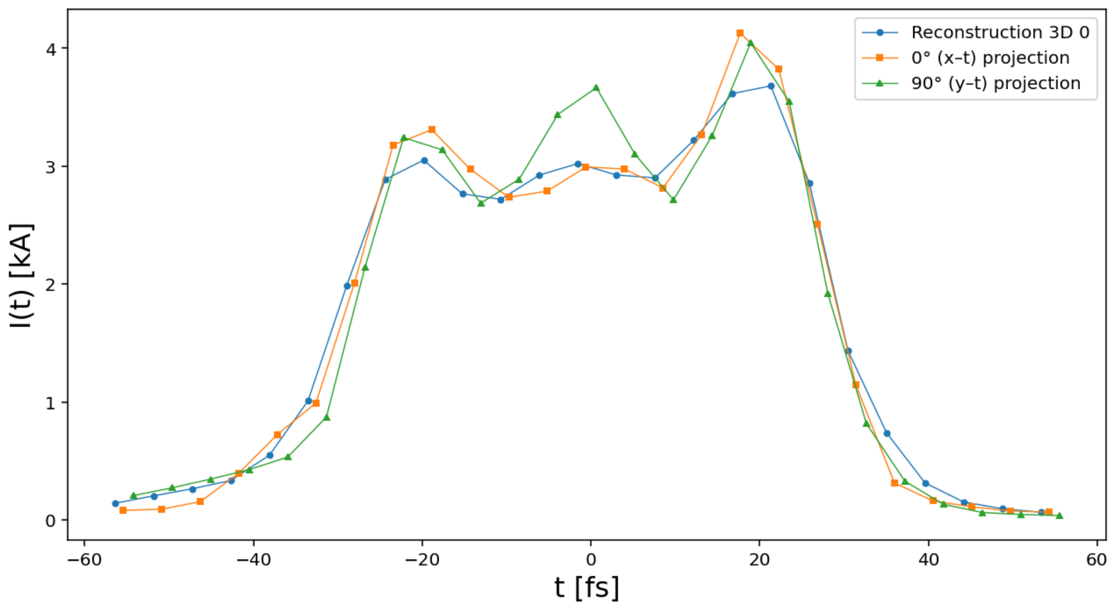


**Figure 5.18:** Reconstructed temporal profile from the 3D tomographic data (blue), compared with the profiles measured at 0 deg and 90 deg TDS polarization (orange and green lines). The reconstructed profile combines information from all ten projections, providing an averaged temporal distribution weighted over multiple viewing angles (Dataset 1).

This methodology also allows the reconstruction of the transverse distribution for each temporal slice. The evolution of the transverse beam sizes $\sigma_x(t)$ and $\sigma_y(t)$ along the bunch is shown in Figs. 5.19. Each curve shows the RMS width of the corresponding transverse projection at each temporal slice, illustrating the time-dependent focusing of the bunch.

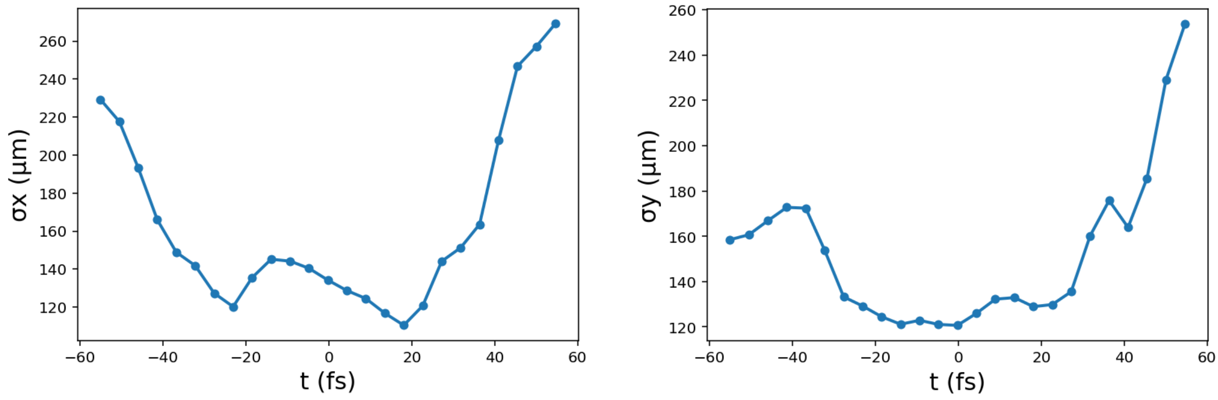


**Figure 5.19:** Time-dependent evolution of the horizontal (left) and vertical (right) transverse beam sizes obtained from the 3D reconstruction for Dataset 1. Each point corresponds to a single temporal slice of the reconstructed 3D distribution.

**Dependence on slice resolution** To quantify the reconstruction's dependence on the chosen slice dimension, which determines the effective reconstruction resolution, a dedicated scan was performed. The dataset was reconstructed multiple times using different slice widths $\Delta t_{\text{slice}}$, corresponding to different numbers of temporal slices $N_{\text{slice}}$. For each configuration, the full reconstruction workflow was repeated, yielding both the temporal profile and the time-dependent transverse sizes $\sigma_x(t)$ and $\sigma_y(t)$.

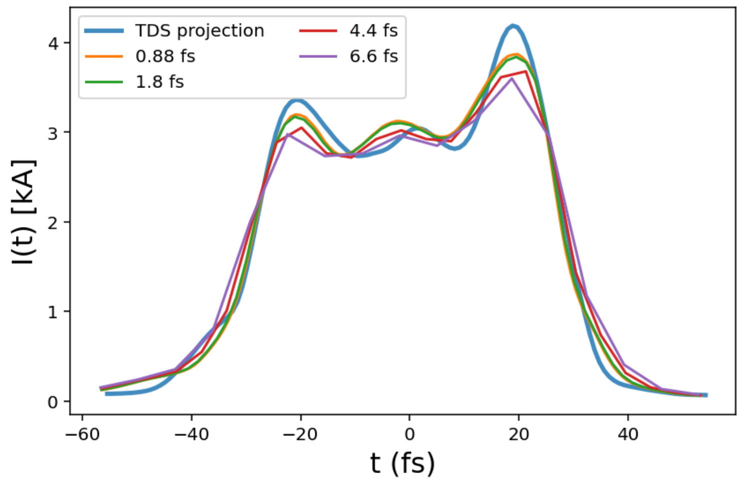


**Figure 5.20:** Reconstructed temporal profile from the 3D tomographic data (blue), compared with the obtained profiles for different slice widths (Dataset 1).

Figs. 5.20 and 5.21 show the superposition of the reconstructed temporal profiles and of the $\sigma_x(t)$ and $\sigma_y(t)$ curves for the various slice dimensions. Even when the slice duration is shorter than the intrinsic temporal resolution of the TDS measurement, the reconstruction rapidly converges to a stable result comparable to that obtained with longer slice durations. This demonstrates that the SART algorithm is robust to different temporal samplings and that the effective reconstruction resolution is primarily determined by the streaking system calibration rather than the chosen slice width.

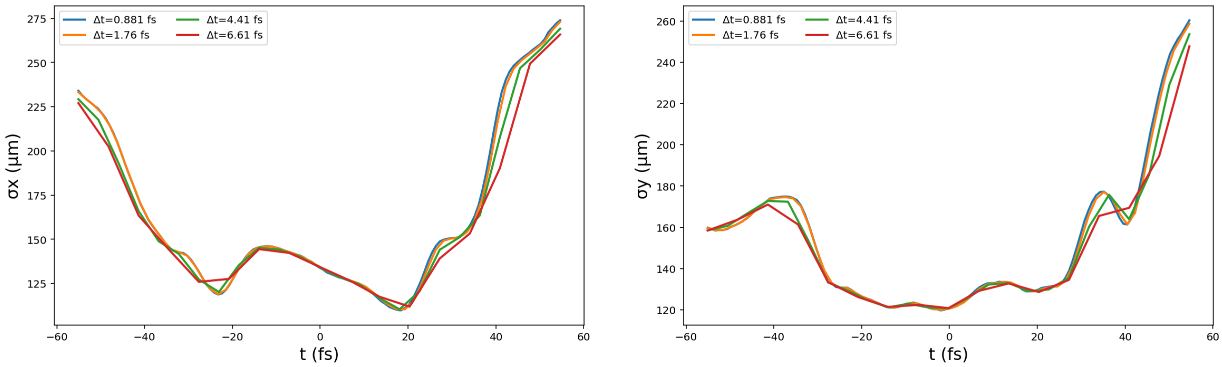


**Figure 5.21:** Time-dependent evolution of the horizontal (left) and vertical (right) transverse beam sizes obtained from the 3D reconstruction for Dataset 1, compared with the corresponding profiles reconstructed using different slice widths. The results show consistent trends, confirming the reconstruction's stability across different temporal slicing choices.

The quantitative results of the scan are reported in Table 5.11, which lists, for each configuration, the number of slices, the corresponding temporal width $\Delta t_{\text{slice}}$, the reconstructed bunch length $\sigma_t^{\text{rec}}$, and the relative deviation with respect to the value measured through the conventional TDS analysis.

| $N_{\text{slice}}$ | $\Delta t_{\text{slice}}$ [fs] | $\sigma_t^{\text{rec}}$ [fs] | $\Delta\sigma_t$ [%] |
|---|---|---|---|
| 125 | 0.88 | 19.82 | 0.56 |
| 63 | 1.76 | 19.93 | 1.13 |
| 25 | 4.41 | 20.38 | 3.38 |
| 17 | 6.61 | 20.74 | 5.13 |

**Table 5.11:** Results of the slice-resolution scan for Dataset 1, reporting the number of slices $N_{\text{slice}}$, the corresponding temporal width $\Delta t_{\text{slice}}$, the reconstructed bunch length $\sigma_t^{\text{rec}}$, and the relative deviation with respect to the TDS measurement.

The observed trend confirms that, for larger slice widths (and hence fewer slices), the reconstruction tends to slightly underestimate the bunch length due to reduced temporal sampling. As the number of slices increases, the reconstructed value of $\sigma_t$ progressively converges toward the expected measurement, demonstrating the consistency of the tomographic method across different discretizations.

### 5.5.2 Dataset 2 - 3D reconstruction results

For the reference case, corresponding to a transverse phase advance of $\mu_x, \mu_y = 96$ deg, the reconstruction was performed using a slice width comparable to the temporal resolution of the measurement, i.e. $\sim 7.2$ fs

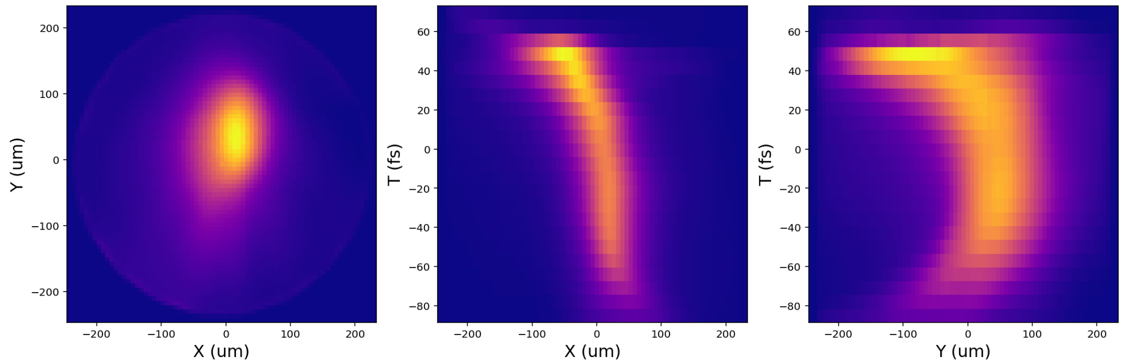


**Figure 5.22:** Reconstructed 2D projections: transverse $(x, y)$ distribution (left), longitudinal $(x, t)$ projection (center), and longitudinal $(y, t)$ projection (right). Each image is obtained by integrating the reconstructed 3D distribution $I(t, x, y)$ along the corresponding axis (Dataset 2).

Fig. 5.22 shows the reconstructed 2D projections $(x, y)$, $(x, t)$, and $(y, t)$ obtained by integrating the 3D distribution along the corresponding axes. From these projections, the extracted beam parameters are summarized in Table 5.12.
The temporal profile reconstructed from the 3D tomographic data is shown in Fig. 5.23, together with the measured profiles obtained from the two reference projections at 0 deg and 90 deg.

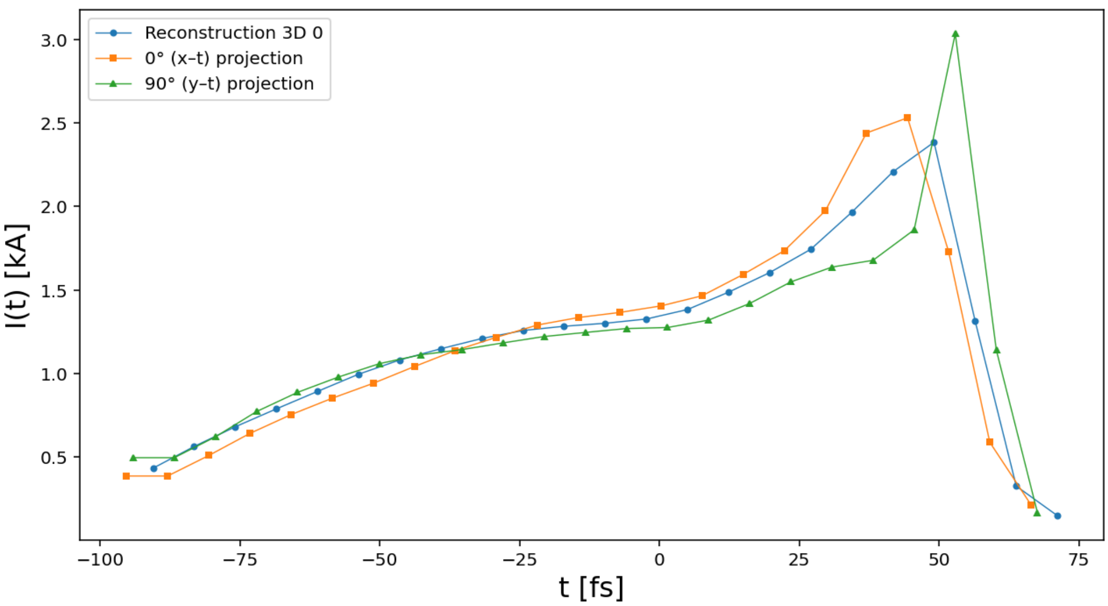


**Figure 5.23:** Reconstructed temporal profile from the 3D tomographic data (blue), compared with the profiles measured at 0 deg and 90 deg TDS polarization (orange and green lines). The reconstructed profile combines information from all ten projections, providing an averaged temporal distribution weighted over multiple viewing angles (Dataset 2).

| Quantity | Value |
|---|---|
| $\sigma_x$ [$\mu$m] | $70 \pm 7$ |
| $\sigma_y$ [$\mu$m] | $90 \pm 7$ |
| $\sigma_t^{\text{rec}}$ [fs] | $41 \pm 7$ |
| $\text{FWHM}_t^{\text{rec}}$ [fs] | $97 \pm 7$ |

**Table 5.12:** Reconstructed beam parameters for Dataset 2, reporting the RMS transverse sizes $\sigma_x$, $\sigma_y$, and the reconstructed bunch length $\sigma_t$ and $\text{FWHM}_t$, with respective standard deviations.

The evolution of the transverse beam sizes $\sigma_x(t)$ and $\sigma_y(t)$ along the bunch is shown in Fig. 5.24.

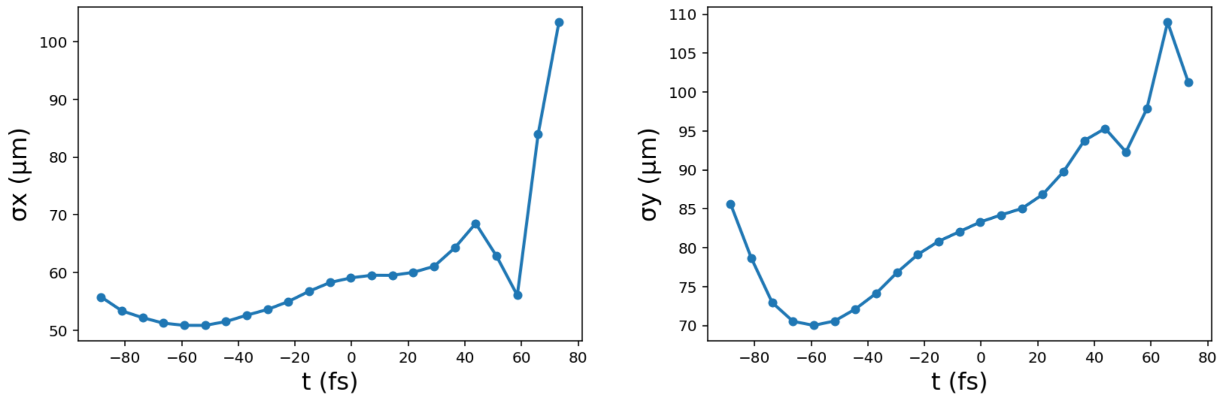


**Figure 5.24:** Time-dependent evolution of the horizontal (left) and vertical (right) transverse beam sizes obtained from the 3D reconstruction for Dataset 2. Each point corresponds to a single temporal slice of the reconstructed 3D distribution.

**Dependence on slice resolution** As for Dataset 1, Figs. 5.25 and 5.26 show the superposition of the reconstructed temporal profiles and of the $\sigma_x(t)$ and $\sigma_y(t)$ curves for the various slice dimensions. The quantitative results of the scan are reported in Table 5.13.

| $N_{\text{slice}}$ | $\Delta t_{\text{slice}}$ [fs] | $\sigma_t^{\text{rec}}$ [fs] | $\Delta\sigma_t$ [%] |
|---|---|---|---|
| 181 | 0.90 | 40.05 | 0.51 |
| 46 | 3.59 | 40.55 | 0.72 |
| 28 | 5.84 | 40.86 | 1.45 |
| 23 | 7.19 | 41.11 | 2.11 |

**Table 5.13:** Results of the slice-resolution scan for Dataset 2, reporting the number of slices $N_{\text{slice}}$, the corresponding temporal width $\Delta t_{\text{slice}}$, the reconstructed bunch length $\sigma_t^{\text{rec}}$, and the relative deviation with respect to the TDS measurement.

The observed trend confirms the same behavior seen in the reconstructed data of the first dataset, showing even smaller deviations from the measured bunch length. While the temporal profiles from all reconstructions converge to a nearly identical shape, the high-current peak exhibits slight variations in the $\sigma$-profile scan, reflecting the different effective resolutions associated with the various slice durations.

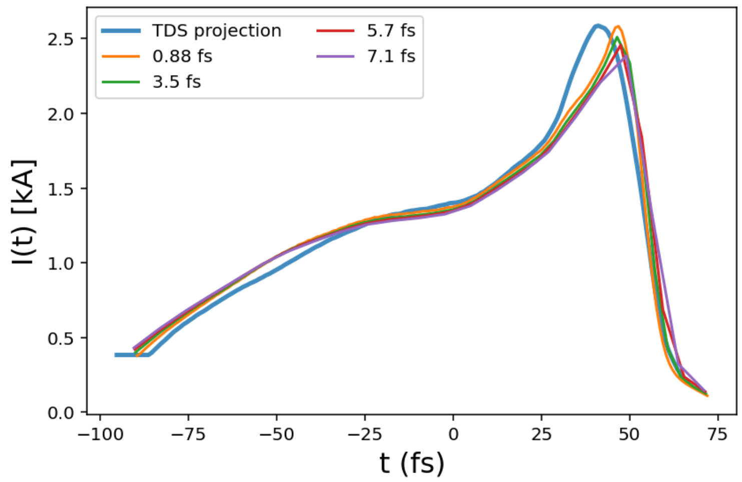


**Figure 5.25:** Reconstructed temporal profile from the 3D tomographic data (blue), compared with the obtained profiles for different slice widths (Dataset 2).

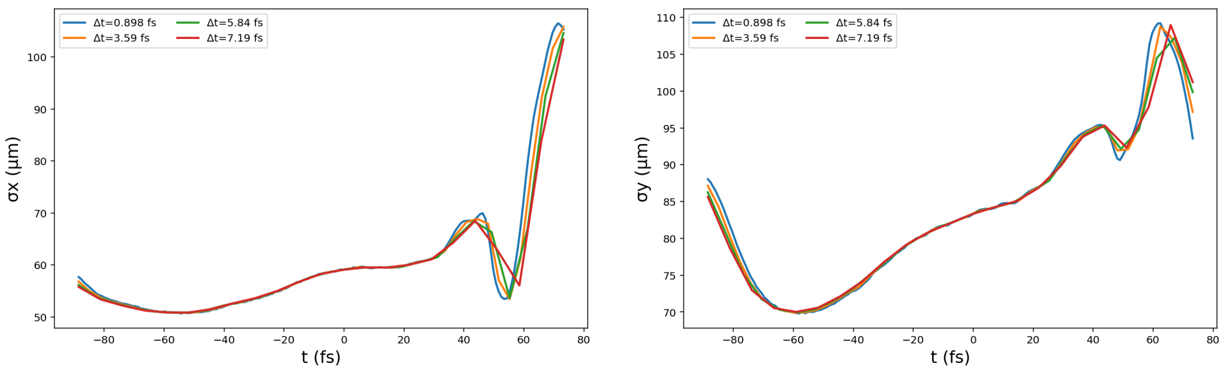


**Figure 5.26:** Time-dependent evolution of the horizontal (left) and vertical (right) transverse beam sizes obtained from the 3D reconstruction for Dataset 2, compared with the corresponding profiles reconstructed using different slice widths. The results exhibit consistent trends across all configurations, confirming the robustness of the reconstruction with respect to the choice of temporal slicing.

### 5.5.3 Summary of the 3D reconstruction

The tomographic 3D reconstruction was successfully performed for both datasets, corresponding to two different operating points of the compression stage. For each case, ten streaked projections acquired at different polarization angles were used as input to the SART algorithm, allowing the retrieval of the full three-dimensional charge distribution $I(t, x, y)$. The reconstruction was performed for all optics settings in both datasets. The resulting temporal profiles are compared in Fig. 5.27. As shown in the plots and summarized in Table 5.14, the reconstructed temporal parameters are consistent across all optics configurations, with values in good agreement with one another and with the expected bunch length.

| **Quantity** | **Dataset 1** | **Dataset 2** |
|---|---|---|
| Slice Resolution [fs] | 4.1 | 0.90 |
| $\sigma_t^{\mathrm{rec}}$ [fs] | 20.8 | 39 |
| Std $\sigma_t^{\mathrm{rec}}$ [fs] | 0.6 | 1 |
| $\mathrm{FWHM}_t^{\mathrm{rec}}$ [fs] | 49 | 90 |
| Std $\mathrm{FWHM}_t^{\mathrm{rec}}$ [fs] | 2 | 3 |

**Table 5.14:** Reconstructed temporal beam parameters for the two Datasets, obtained from the statistics of all the optics.

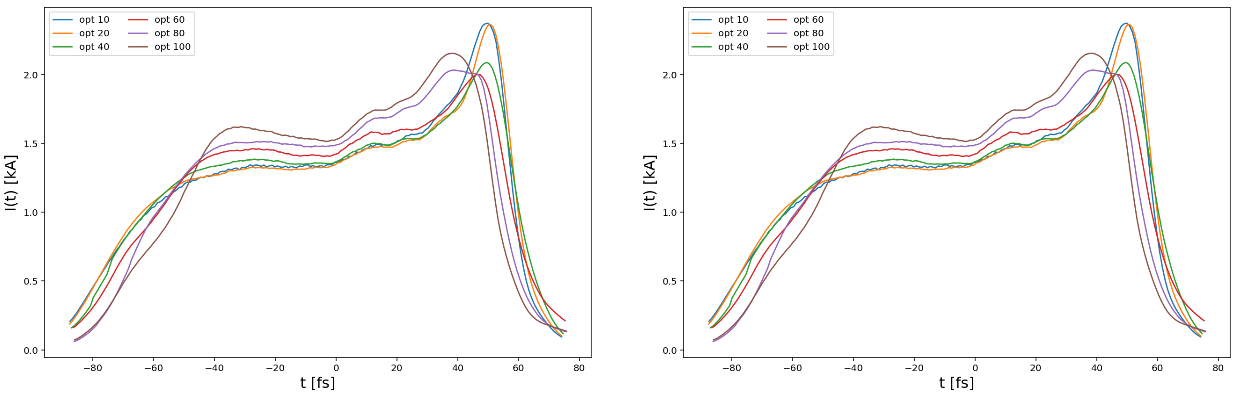


**Figure 5.27:** Reconstructed temporal profiles obtained from the 3D reconstruction across different optics settings for Dataset 1 (left) and Dataset 2 (right). The profiles reproduce the main features of the bunch temporal structure, showing consistent shapes and characteristic widths across all configurations.

The reconstruction has been repeated for multiple values of the slice duration $\Delta t_{\mathrm{slice}}$, showing that the resulting spatial and temporal profiles are stable and consistent across a wide range of temporal resolutions. The extracted bunch length $\sigma_t$ agrees with that obtained from direct TDS measurements, confirming the method's reliability.

The reconstructed temporal profiles show that the two datasets correspond to distinct compression regimes. In dataset 1, the bunch is found to be in an over-compression state, featuring a longer temporal profile and a more regular current distribution, indicating that the beam has passed beyond the point of maximum compression. Conversely, dataset 2 represents a less compressed configuration, with the current peak preceding a low-charge tail, with a single peak followed by a gradual charge decrease.

These results demonstrate that the 3D tomographic reconstruction provides an accurate representation of the longitudinal beam structure over different compression conditions.

## 5.6 5D Reconstruction analysis and results

In this section, the preliminary results of the tomographic reconstruction of the five-dimensional phase space are presented. The analysis is based on the two previously described experimental datasets. The 5D tomographic reconstruction results presented in this section, including the figures and tabulated data, were obtained within the collaboration, with the tomographic analysis and reconstruction procedures carried out by the DESY group responsible for this aspect of the work.

### 5.6.1 Dataset 1 - High compression

The first dataset corresponds to the high-bunch-compression case. The reconstructed bunch is extremely short, with an rms duration of approximately ∼19 fs and a full width at half maximum (FWHM) of about ∼ 56 fs.
A total of 25 longitudinal slices were used in the reconstruction, each with a temporal width of approximately 4.1 fs. The transverse phase space was discretized into 201 bins per plane, thereby defining the reconstruction's spatial resolution.
Fig. 5.28 shows the three-dimensional projection of the reconstructed five-dimensional distribution, obtained by integrating over the transverse momenta. This representation clearly highlights the short temporal length of the bunch.

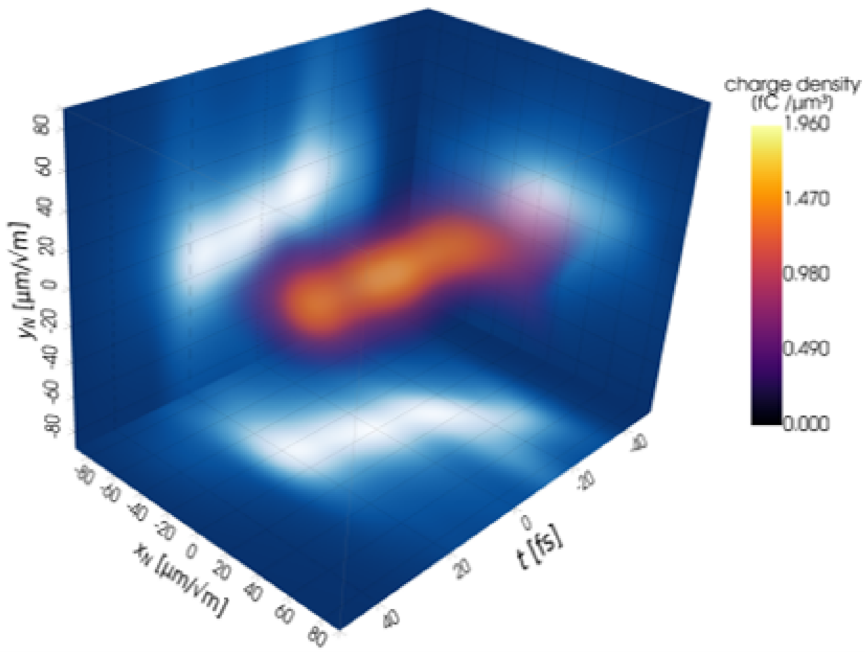


**Figure 5.28:** 3D charge density obtained from the 3D projection of the reconstructed 5D distribution, for the high-compression case (Dataset 1) [75].

From the five-dimensional reconstruction, the ten two-dimensional projections relating the normalized coordinates $(X, X', Y, Y')$ and the temporal one $t$ are also obtained, as reported in Fig. 5.29.

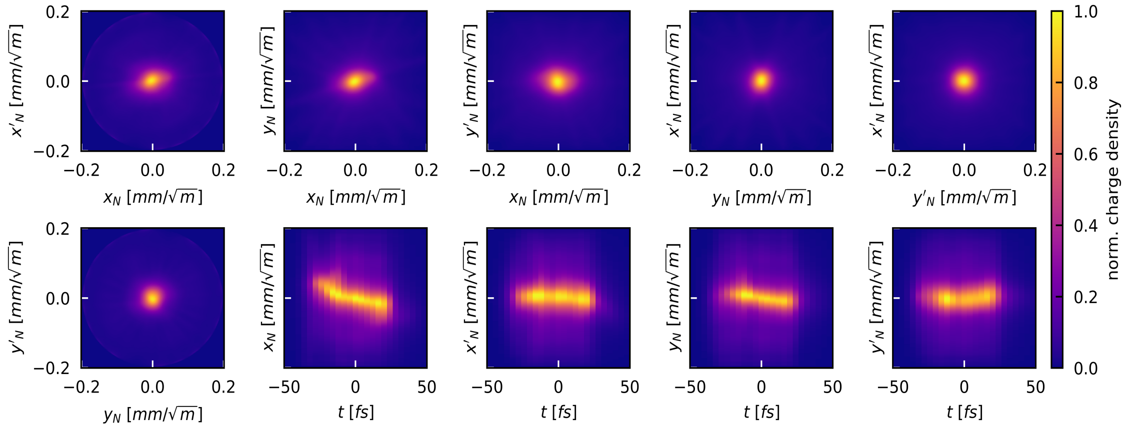


**Figure 5.29:** Ten 2D projections obtained from the reconstructed 5D distribution, for the high-compression case (Dataset 1) [75].

The most relevant reconstructed feature is the correlation between the horizontal position and time: the $x$–$t$ projection shows a clear tilt of the bunch. A smaller tilt is also evident in the $y$–$t$ plane, though less pronounced. In all the other phase-space planes, no significant correlations are observed.

The values reported in Table 5.15 were obtained from the 5D reconstruction, which allows calculating the linear correlations between the four transverse coordinates $(x, x', y, y')$ and the longitudinal coordinate $z$. These correlations quantify the coupling between the transverse and longitudinal dimensions of the phase space, and therefore quantify the observed beam tilt. The reported values correspond to the measured slopes of the linear correlations for this dataset.

| **Parameters** | **Unit** | **Value** |
|---|---|---|
| **Longitudinal** | | |
| $dx/ds$ | m/m | 7.92 |
| $dx'/ds$ | rad/m | -2.12 |
| $dy/ds$ | m/m | 3.98 |
| $dy'/ds$ | rad/m | 1.97 |
| **Transverse** | | |
| $dx'/dx$ | rad/m | -0.28 |
| $dy/dx$ | m/m | 0.45 |
| $dy'/dx$ | rad/m | 0.23 |
| $dy/dx'$ | m/rad | -1.11 |
| $dy'/dx'$ | rad/rad | -0.56 |
| $dy'/dy$ | rad/m | 0.52 |

**Table 5.15:** Reconstructed values of beam linear correlations with respect to the longitudinal and transverse coordinates, reported for Dataset 1.

Overall, dataset 1 demonstrates that the reconstruction procedure can capture both the ultra-short bunch duration and the phase-space correlations induced by the high-compression setting.

### 5.6.2 Dataset 2 - Moderate compression

The second dataset corresponds to moderate bunch compression, obtained by changing the compressor phase relative to the high-compression setting. In this configuration, the reconstructed bunch is longer, with an rms duration of approximately ∼40 fs and a full width at half maximum (FWHM) of about ∼ 108 fs.

A total of 29 longitudinal slices were used in the reconstruction, each with a temporal width of approximately 7.1 fs. The transverse phase space was discretized into 201 bins per plane, thereby defining the reconstruction's spatial resolution.

The three-dimensional projection of the five-dimensional distribution is reported in Fig. 5.30, which highlights the increased bunch length compared to dataset 1.

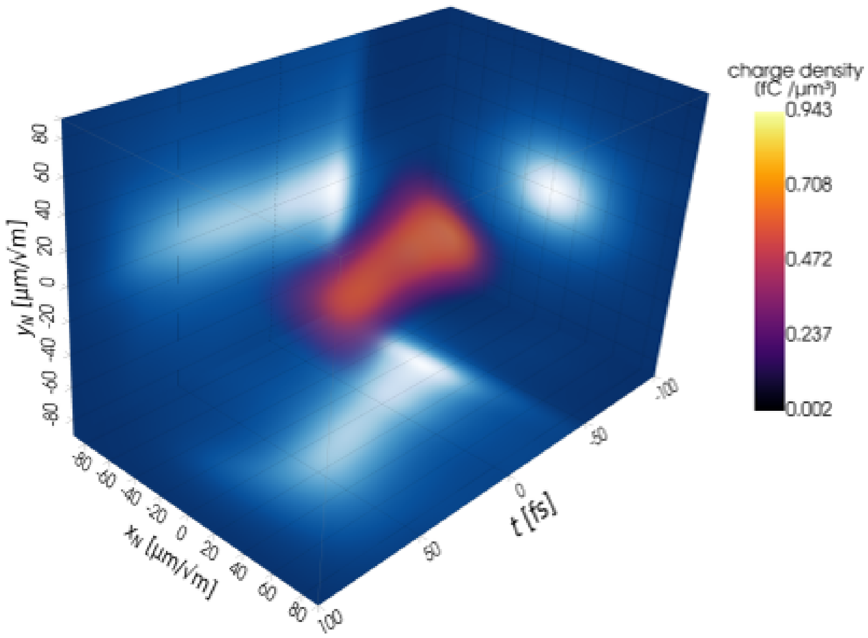


**Figure 5.30:** 3D charge density obtained from the 3D projection of the reconstructed 5D distribution, for the moderate-compression case (Dataset 2) [75].

The corresponding two-dimensional projections are shown in Fig. 5.31.

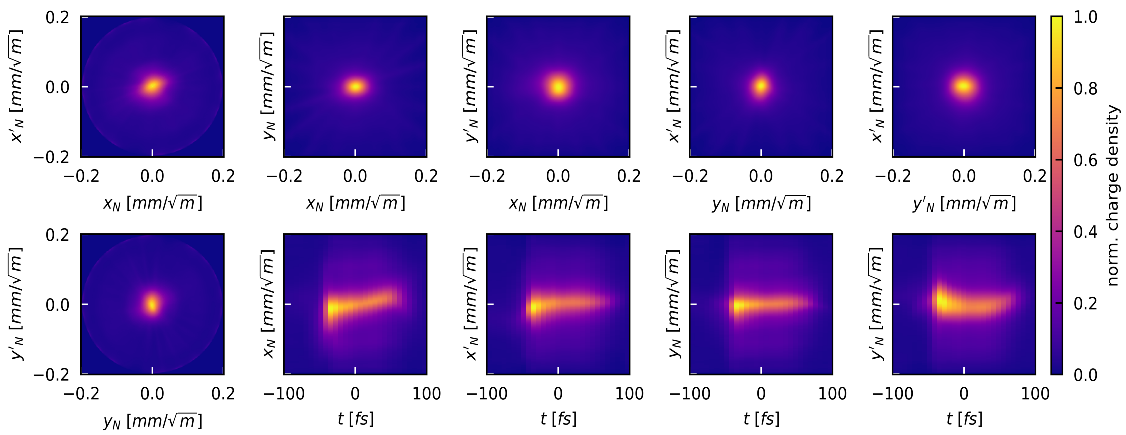


**Figure 5.31:** Ten 2D projections obtained from the reconstructed 5D distribution, for the moderate-compression case (Dataset 2) [75].

As for Dataset 1, Table 5.16 reports the linear correlations obtained from the 5D reconstruction for the second dataset. The comparison with dataset 1 shows a clear difference in the correlations: the tilt in the $x$–$t$ plane is strongly reduced, while in the $y$–$t$ plane it is practically absent. In all the other projections, no significant correlations are observed.

| **Parameters** | **Unit** | **Value** |
|---|---|---|
| **Longitudinal** | | |
| $dx/ds$ | m/m | -1.69 |
| $dx'/ds$ | rad/m | 0.12 |
| $dy/ds$ | m/m | -1.37 |
| $dy'/ds$ | rad/m | -0.65 |
| **Transverse** | | |
| $dx'/dx$ | rad/m | -0.27 |
| $dy/dx$ | m/m | -0.15 |
| $dy'/dx$ | rad/m | -0.07 |
| $dy/dx'$ | m/rad | 0.44 |
| $dy'/dx'$ | rad/rad | 0.19 |
| $dy'/dy$ | rad/m | 0.51 |

**Table 5.16:** Reconstructed values of beam linear correlations with respect to the longitudinal and transverse coordinates, reported for Dataset 2.

These results confirm that the five-dimensional reconstruction captures the expected change in the beam phase space as the compression strength is varied, demonstrating the diagnostic's sensitivity to different experimental conditions.

## 5.7 Summary and conclusion

This chapter reports the results of the experimental campaign conducted at the Athos beamline of SwissFEL, which aimed to apply the five-dimensional reconstruction technique to two datasets corresponding to realistic electron bunches produced by the accelerator. After describing in detail the reconstruction procedure and the experimental setup, the main results of the measurements are summarized here.

Concerning the measurement, two distinct experimental conditions were analyzed:

- **Dataset 1 (high-compression):** the bunch was extremely short, with an rms duration of $\sigma_t \sim 19$ fs. A clear tilt was observed in the $x$–$t$ projection, with a smaller correlation also visible in the $y$–$t$ projection. In the other phase-space plane, no significant correlations were observed.
- **Dataset 2 (moderate-compression):** the bunch was longer, with $\sigma_t \sim 40$ fs. Compared to dataset 1, the tilt in the $x$–$t$ plane was strongly reduced, while in the $y$–$t$ plane it was practically absent. Again, no correlations were observed in the remaining projections.

The reconstruction was based on a combination of 100 different beam-optics configurations and the ten polarization-streaking angles of the PolariX TDS. The calibration procedure was performed for each streaking configuration, with a mean calibration factor corresponding to $C_1 = 16.1 \pm 0.7\ \mu m/fs$

for the first dataset and to $C_2 = 16.2 \pm 0.5\ \mu m/fs\ \mu m/fs$ for the second one, with a corresponding variation with respect to the mean value, respectively of 4% and 5%, across all polarizations.

From the calibration, the diagnostic's longitudinal resolution was evaluated. For dataset 1, the effective resolution was found to be $R_1$ = 6.8 fs ± 1.8 fs, while for dataset 2 it was $R_2$ = 7.3 fs ± 2.4 fs. These values represent the average measurement resolution.

Successively, the 3D tomographic reconstruction was performed for both datasets, demonstrating the robustness of the method and its ability to reproduce the main spatial and temporal features of the beam across different compression regimes. The consistency of the reconstructed parameters with the reference TDS measurements confirms that the implemented SART-based workflow can reliably retrieve the bunch distribution. These results provide a solid experimental foundation for the subsequent 5D reconstruction, in which the complete phase-space correlations will be explored.

The values reported in Table 5.17 correspond to the reconstructed linear correlations between the transverse coordinates $(x, x', y, y')$ and the longitudinal coordinate $z$, as obtained from the 5D reconstruction. These correlations describe the beam's tilt and spatio-temporal coupling in the transverse planes. In particular, the $x$–$t$ plane represents the dominant contribution to the observed bunch tilt. The comparison between the two measurements shows that moving from the first to the second experimental configuration effectively reduced the tilt, as reflected in the smaller correlation coefficients reported in the Table.

| **Parameter** | **Unit** | **Measurement 1** | **Measurement 2** |
|---|---|---|---|
| $dx/dz$ | m | 7.92 | -1.69 |
| $dx'/dz$ | rad | -2.12 | 0.12 |
| $dy/dz$ | m | 3.98 | -1.37 |
| $dy'/dz$ | rad | 1.97 | -0.65 |

**Table 5.17:** Reconstructed values of beam correlations with respect to the longitudinal coordinate, reported for the two datasets. The units are meters for $x, y, z$ and radians for $x', y'$.

These results demonstrate that the five-dimensional reconstruction can resolve the main features of the longitudinal phase space across different operating conditions. The method has proven effective at capturing variations in bunch length and correlations induced by the compression settings; therefore, it can be considered a reliable diagnostic tool for characterizing realistic electron bunches.

In addition to the technical validation, this work also demonstrates the potential impact of the diagnostic for future applications at SwissFEL Athos. By providing direct access to high-dimensional phase-space characterization, the reconstruction technique can be used to optimize the machine setup and tailor the beam properties to specific experimental needs, opening new possibilities for advanced user experiments.

# Chapter 6

# Conclusion and Outlook

## 6.1 Conclusions

The research presented in this thesis focused on validating diagnostic techniques for high-brightness electron beams within the framework of the EuPRAXIA@SPARC_LAB project. These diagnostics are crucial for next-generation accelerators, which demand ultra-short, high-quality beams and require precise control over all beam parameters. The work is structured in three main parts, each addressing a specific aspect of the beam diagnostics chain, from simulation to experimental validation.

The first part of the thesis was dedicated to the study and numerical modeling of the PolariX X-band Transverse Deflection Structure (TDS), a key device for time-resolved measurements of the electron beam. This TDS allows variable polarization of the deflecting field, enabling multi-angle projections of the longitudinal phase space, which are fundamental for tomographic reconstruction techniques. Dedicated particle-tracking simulations were used to investigate the effects of realistic 3D field maps on beam dynamics and the differences in structures of different lengths. Field maps of a new 50-cell prototype structure were designed and characterized, optimized for operation at lower energies while preserving sufficient kick strength for femtosecond-scale resolution, with a focus on the impact of the structure couplers relative to those already implemented in other facilities.

The second part of the work focused on beam-dynamics simulations to validate the diagnostic performance along the EuPRAXIA beamline. Each diagnostic section — low-, medium-, and high-energy — was analyzed to estimate its resolution limits and assess the impact of key effects, such as space charge and shot-to-shot jitter. The low-energy section, equipped with the new PolariX TDS, was studied in detail to evaluate the effects of space charge on the longitudinal phase-space reconstruction. The medium-energy line, for which no deflector is foreseen, was modeled to benchmark the expected emittance and energy evolution using quadrupole- and dipole-based diagnostics. At high energy, the analysis included jitter simulations and feasibility studies for 5D tomographic reconstruction, revealing how plasma-induced fluctuations affect the effective measurement resolution.

The third part of the thesis presented the experimental activities carried out in collaboration with PSI and DESY centers, applying the 5D tomographic reconstruction technique to the high-brightness beams of the 3 GeV Athos branch at SwissFEL. The preparation of the experimental setup involved calibrating the RF deflecting cavity, characterizing the streaking strength, and performing beam-based measurements at multiple deflecting angles. A systematic study of the reconstruction parameters was performed, focusing on 3D reconstructions for different slice resolutions, showing that the effective longitudinal resolution depends on both the calibration factor and the discretization step of the temporal profile. Two working points were analyzed, corresponding to high and moderate compression. The results clearly demonstrated the ability of the diagnostic system to resolve the beam tilt in the $(x, t)$ plane induced by non-linear compression effects, and to track its reduction when the compression was relaxed. This confirmed the reliability of the 5D tomography as a powerful tool for bunch optimization and for the investigation of correlated effects in the longitudinal-transverse phase space.

In summary, this work established a complete and coherent framework that connects electromagnetic design, beam-dynamics modeling, and experimental reconstruction into a unified diagnostic methodology. The results demonstrate that PolariX-based diagnostics can provide high-resolution measurements across multiple energy ranges, supporting the commissioning and optimization of next-generation plasma-based accelerators.

## 6.2 Outlook

The results presented in this thesis were developed in the framework of the EuPRAXIA@SPARC_LAB project, which is currently entering its construction phase. The Technical Design Report (TDR) has defined the layout and operating parameters of the future facility, with commissioning planned for around 2030. Although the design is now consolidated, the development of each subsystem — including RF components, plasma sources, magnetic optics, and diagnostics — remains an active and dynamic process. Continuous progress in these areas is essential to ensure that the facility can fully exploit its potential as a next-generation accelerator.

In this context, the diagnostic systems will continue to evolve alongside the accelerator itself. Improvements in the beamline optics and magnet design, along with enhanced beam stability and reproducibility, will naturally translate into higher diagnostic precision. At the same time, new measurement strategies can be explored to extend the current diagnostic capabilities. The techniques presented in this work, based on RF deflectors and multi-angle tomographic reconstructions, demonstrate the versatility and potential of the PolariX TDS structure. Beyond enabling time-resolved measurements across different transverse planes with a single device, its continuously tunable streaking direction opens the way to a new class of high-dimensional beam characterization methods. Such flexibility makes the PolariX a unique platform for extending tomographic reconstruction to include energy correlations, ultimately paving the way for a more complete phase-space analysis.

A particularly promising direction for the future is the integration of machine-learning-based diagnostics. These algorithms can be trained using both simulated and experimental data to infer beam parameters without performing all the physical measurements. Once properly trained, they can predict quantities such as longitudinal phase-space correlations or emittance evolution with high accuracy and minimal acquisition time. However, these techniques are not intended to replace conventional diagnostics but to complement them. Their accuracy and stability depend critically on the quality of the measured data, making traditional diagnostics and tomographic methods indispensable for model training and benchmarking.

In summary, the work presented here provides a solid foundation for the continued development of advanced diagnostics for EuPRAXIA@SPARC_LAB. As the facility moves toward operation, both the hardware and the analysis techniques will continue to mature, driven by ongoing research and technological innovation. In this perspective, EuPRAXIA@SPARC_LAB provides not only a facility for user operations but also a versatile research environment where novel diagnostic concepts can be designed, tested, and benchmarked, ensuring that future developments in beam characterization can fully exploit the accelerator's capabilities. Each of these approaches will contribute to refining the accuracy and robustness of the overall diagnostic framework.

# Bibliography


[1] RW Assmann, MK Weikum, T Akhter, D Alesini, AS Alexandrova, MP Anania, NE Andreev, I Andriyash, M Artioli, A Aschikhin, et al. Eupraxia conceptual design report. *The European Physical Journal Special Topics*, 229(24):3675–4284, 2020.

[2] M Ferrario and R Assmann. Eupraxia and its italian construction site.

[3] Anna Giribono, A Bacci, E Chiadroni, A Cianchi, M Croia, M Ferrario, A Marocchino, V Petrillo, R Pompili, S Romeo, et al. Eupraxia@ sparc_lab: The high-brightness rf photo-injector layout proposal. *Nuclear Instruments and Methods in Physics Research Section A: Accelerators, Spectrometers, Detectors and Associated Equipment*, 909:282–285, 2018.

[4] B Serenellini, M Bellaveglia, F Cardelli, A Gallo, G Latini, L Piersanti, S Pioli, S Quaglia, M Scampati, G Scarselletta, et al. Upgrade of the sparc_lab llrf system and recent x-band activities in view of eupraxia@ sparc_lab project. *arXiv preprint arXiv:2310.17071*, 2023.

[5] Cristina Vaccarezza, D Alesini, A Bacci, A Cianchi, E Chiadroni, M Croia, M Diomede, M Ferrario, A Gallo, A Giribono, et al. Eupraxia@ sparc_lab: Beam dynamics studies for the x-band linac. *Nuclear Instruments and Methods in Physics Research Section A: Accelerators, Spectrometers, Detectors and Associated Equipment*, 909:314–317, 2018.

[6] P Craievich, J Alex, C Beard, HH Braun, M D'Amico, R Fortunati, R Ganter, Z Geng, R Kalt, T Kleeb, et al. Rf conditioning and first experiences with the polarix tds at psi. In *Proc. FEL*, 2022.

[7] Sonja Meike Jaster-Merz. *High-dimensional and ultra-sensitive diagnostics for electron beams.* PhD thesis, University of Hamburg, Hamburg, Germany, 2023.

[8] Daniel Marx. *Characterization of Ultrashort Electron Bunches at the SINBAD-ARES Linac.* PhD thesis, University of Hamburg, Hamburg, Germany, 2019.

[9] Sonja Jaster-Merz, RW Assmann, Reinhard Brinkmann, F Burkart, T Vinatier, et al. First studies of 5d phase-space tomography of electron beams at ares. *Proc. LINAC'22*, pages 247–251, 2022.

[10] S Jaster-Merz, RW Assmann, J Beinortaitė, J Björklund Svensson, R Brinkmann, F Burkart, P Craievich, H Dinter, P González Caminal, W Hillert, et al. Experimental demonstration of a tomographic five-dimensional phase-space reconstruction. *Physical Review Research*, 7(4):043211, 2025.

[11] David Alesini, Giampiero Di Pirro, Luca Ficcadenti, Andrea Mostacci, Luigi Palumbo, James Rosenzweig, and Cristina Vaccarezza. Rf deflector design and measurements for the longitudinal and transverse phase space characterization at sparc. *Nuclear Instruments and Methods in Physics Research Section A: Accelerators, Spectrometers, Detectors and Associated Equipment*, 568(2):488–502, 2006.

[12] Paul Emma, Josef Frisch, and Patrick Krejcik. A transverse rf deflecting structure for bunch length and phase space diagnostics. *LCLS Technical Note*, 12, 2000.

[13] R Akre, L Bentson, P Emma, and P Krejcik. A transverse rf deflecting structure for bunch length and phase space diagnostics. In *PACS2001. Proceedings of the 2001 Particle Accelerator Conference (Cat. No. 01CH37268)*, volume 3, pages 2353–2355. IEEE, 2001.

[14] G Berden, W Allan Gillespie, SP Jamison, E-A Knabbe, Allan M MacLeod, AFG Van Der Meer, PJ Phillips, H Schlarb, B Schmidt, P Schmüser, et al. Benchmarking of electro-optic monitors for femtosecond electron bunches. *Physical review letters*, 99(16):164801, 2007.

[15] B Steffen, V Arsov, G Berden, W Allan Gillespie, SP Jamison, Allan M MacLeod, AFG Van Der Meer, PJ Phillips, Holger Schlarb, Bernhard Schmidt, et al. Electro-optic time profile monitors for femtosecond electron bunches<? format?> at the soft x-ray free-electron laser flash. *Physical Review Special Topics—Accelerators and Beams*, 12(3):032802, 2009.

[16] G Berden, AFG Van Der Meer, SP Jamison, B Steffen, B Schmidt, P Schmüser, Allan M MacLeod, W Allan Gillespie, and PJ Phillips. Electro-optic techniques for longitudinal electron bunch diagnostics. In *30th International Free Electron Laser Conference*, pages 413–416, 2008.

[17] I Nozawa, K Kan, J Yang, A Ogata, T Kondoh, M Gohdo, K Norizawa, H Kobayashi, H Shibata, S Gonda, et al. Measurement of< 20 fs bunch length using coherent transition radiation. *Physical Review Special Topics-Accelerators and Beams*, 17(7):072803, 2014.

[18] Daniel Mihalcea, CL Bohn, U Happek, and P Piot. Longitudinal electron bunch diagnostics using coherent transition radiation. *Physical Review Special Topics—Accelerators and Beams*, 9(8):082801, 2006.

[19] C Thongbai, K Kusoljariyakul, S Rimjaem, MW Rhodes, J Saisut, P Thamboon, P Wichaisirimongkol, and T Vilaithong. Femtosecond electron bunches, source and characterization. *Nuclear Instruments and Methods in Physics Research Section A: Accelerators, Spectrometers, Detectors and Associated Equipment*, 587(1):130–135, 2008.

[20] Claudio Emma, A Edelen, MJ Hogan, B O'Shea, G White, and V Yakimenko. Machine learning-based longitudinal phase space prediction of particle accelerators. *Physical Review Accelerators and Beams*, 21(11):112802, 2018.

[21] Wolfgang Hillert. Transverse linear beam dynamics. *arXiv preprint arXiv:2107.02614*, 2021.

[22] Edmund JN Wilson. Transverse beam dynamics. 1985.

[23] Mauro Migliorati, A Bacci, C Benedetti, E Chiadroni, M Ferrario, Andrea Mostacci, Luigi Palumbo, AR Rossi, L Serafini, and Patrizio Antici. Intrinsic normalized emittance growth

in laser-driven electron accelerators. *Physical Review Special Topics—Accelerators and Beams*, 16(1):011302, 2013.

[24] Massimo Ferrario, Mauro Migliorati, and Luigi Palumbo. Space charge effects. *arXiv preprint arXiv:1601.05214*, 2016.

[25] Massimo Ferrario. Accelerator physics: basic principles on beam focusing and transport. In *Laser-Plasma Acceleration*, pages 41–63. IOS Press, 2012.

[26] Helmut Wiedemann. *Particle accelerator physics*. Springer Nature, 2015.

[27] Pasquale Arpaia, Roberto Corsini, Antonio Gilardi, Andrea Mostacci, Luca Sabato, and Kyrre N Sjobak. Enhancing particle bunch-length measurements based on radio frequency deflector by the use of focusing elements. *Scientific reports*, 10(1):11457, 2020.

[28] P González Caminal, F Christie, R D'Arcy, SM Jaster-Merz, R Assmann, F Burkart, B Conrad, H Dinter, M Foese, J Herrmann, et al. Beam-based commissioning of a novel x-band transverse deflection structure with variable polarization. *Physical Review Accelerators and Beams*, 27(3):032801, 2024.

[29] Alessandro Cianchi et al. Observations and diagnostics in high brightness beams. In *CERN YELLOW REPORTS. CONFERENCE PROCEEDINGS*, number November, pages 229–246. CERN, 2017.

[30] Sonja Jaster-Merz, RW Assmann, J Beinortaite, J Björklund Svensson, R Brinkmann, F Burkart, R D'Arcy, H Dinter, P Gonzalez Caminal, AL Kanekar, et al. 5d phase-space reconstruction of an electron beam. In *Proceedings of the 14th International Parcticle Accelerator Conference, IPAC2023, Venice, Italy (JACoW, Geneva, Switzerland, 2023)*, pages 1616–1619, 2023.

[31] Karl L Brown. A first-and second-order matrix theory for the design of beam transport systems and charged particle spectrometers. Technical report, SLAC National Accelerator Laboratory (SLAC), Menlo Park, CA (United States), 1967.

[32] E Kongmon, P Wongkummoon, and S Rimjaem. Simulations and measurements of the dipole magnet using in the 4-mev electron spectrometer. In *Journal of Physics: Conference Series*, volume 1144, page 012108. IOP Publishing, 2018.

[33] Eduard Prat, Philipp Dijkstal, Eugenio Ferrari, Alexander Malyzhenkov, and Sven Reiche. High-resolution dispersion-based measurement of the electron beam energy spread. *Physical Review Accelerators and Beams*, 23(9):090701, 2020.

[34] Sergey Tomin, Igor Zagorodnov, Winfried Decking, Nina Golubeva, and Matthias Scholz. Accurate measurement of uncorrelated energy spread in electron beam. *Physical Review Accelerators and Beams*, 24(6):064201, 2021.

[35] Michael Borland. Elegant: A flexible sdds-compliant code for accelerator simulation. Technical report, Argonne National Lab., IL (US), 2000.

[36] Klaus Flottmann, Steven Lidia, and Philippe Piot. Recent improvements to the astra particle tracking code. 2003.

[37] H Grote and F Schmidt. Mad-x-an upgrade from mad8. In *Proceedings of the 2003 Particle Accelerator Conference*, volume 5, pages 3497–3499. IEEE, 2003.

[38] Barbara Marchetti, Matthias Scholz, Riccardo Zennaro, Ingo Peperkorn, Eduard Prat, Markus Hüning, Tim Wilksen, Frauke Poblotzki, Joerg Herrmann, Bolko Beutner, et al. Jacow: X-band tds project. Technical report, 2017.

[39] Shyh-Yuan Lee. *Accelerator physics*. World Scientific Publishing Company, 2018.

[40] David Alesini. Linear particle accelerators. 2024.

[41] Paolo Craievich, Markus Bopp, H-H Braun, Alessandro Citterio, Renato Fortunati, Romain Ganter, T Kleeb, F Marcellini, Marco Pedrozzi, Eduard Prat, et al. Novel x-band transverse deflection structure with variable polarization. *Physical review accelerators and beams*, 23(11):112001, 2020.

[42] Alexej Grudiev. Design of compact high power rf components at x-band. Technical report, 2016.

[43] Paolo Craievich, M Bopp, H Braun, R Ganter, T Kleeb, M Pedrozzi, E Prat, S Reiche, R Zennaro, A Grudiev, et al. Status of the polarix-tds project. *Proc. IPAC'18*, pages 3808–3811, 2018.

[44] High Frequency Structure Simulator. Hfss, 2005.

[45] Fabio Villa, David Alesini, Maria P Anania, Marco Angelucci, Alberto Bacci, Antonella Balerna, Marco Bellaveglia, Angelo Biagioni, Bruno Buonuomo, Sergio Cantarella, et al. Eupraxia@ sparc_lab status update. In *X-Ray Free-Electron Lasers: Advances in Source Development and Instrumentation VI*, volume 12581, pages 92–101. SPIE, 2023.

[46] R Pompili, D Alesini, MP Anania, S Arjmand, M Behtouei, M Bellaveglia, A Biagioni, B Buonomo, F Cardelli, M Carpanese, et al. Free-electron lasing with compact beam-driven plasma wakefield accelerator. *Nature*, 605(7911):659–662, 2022.

[47] Antonella Balerna, Samanta Bartocci, Giovanni Batignani, Alessandro Cianchi, Enrica Chiadroni, Marcello Coreno, Antonio Cricenti, Sultan Dabagov, Andrea Di Cicco, Massimo Faiferri, et al. The potential of eupraxia@ sparc_lab for radiation based techniques. *Condensed Matter*, 4(1):30, 2019.

[48] Basler AG. ace 2 camera series. `https://www.baslerweb.com/en/cameras/ace2/`. Accessed: 2025-10-01.

[49] L Serafini and Massimo Ferrario. Velocity bunching in photo-injectors. In *AIP conference proceedings*, volume 581, pages 87–106. American Institute of Physics, 2001.

[50] Enrica Chiadroni, A Biagioni, D Alesini, MP Anania, M Bellaveglia, Fabrizio Bisesto, Emanuele Brentegani, Fabio Cardelli, Alessandro Cianchi, Gemma Costa, et al. Status of plasma-based experiments at the sparc_lab test facility. In *Proceedings of the IPAC2018—9th International Particle Accelerator Conference, Vancouver, BC, Canada*, volume 29, 2018.

[51] D Filippetto, D Alesini, M Bellaveglia, R Boni, M Boscolo, M Castellano, E Chiadroni, L Cultrera, G Di Pirro, M Ferrario, et al. Velocity bunching experiment at sparc. In *Proc. of the FEL 2009 conference, Liverpool, UK*, 2009.

[52] Riccardo Pompili, MP Anania, Marco Bellaveglia, Angelo Biagioni, G Castorina, E Chiadroni, A Cianchi, Michele Croia, D Di Giovenale, Massimo Ferrario, et al. Femtosecond timing-jitter between photo-cathode laser and ultra-short electron bunches by means of hybrid compression. *New Journal of Physics*, 18(8):083033, 2016.

[53] M Ferrario, D Alesini, A Bacci, M Bellaveglia, R Boni, M Boscolo, Paolo Calvani, M Castellano, E Chiadroni, A Cianchi, et al. Laser comb with velocity bunching: Preliminary results at sparc. *Nuclear Instruments and Methods in Physics Research Section A: Accelerators, Spectrometers, Detectors and Associated Equipment*, 637(1):S43–S46, 2011.

[54] A Biagioni, Maria Pia Anania, S Arjmand, E Behar, G Costa, Alessio Del Dotto, M Ferrario, M Galletti, V Lollo, D Pellegrini, et al. Gas-filled capillary-discharge stabilization for plasma-based accelerators by means of a laser pulse. *Plasma Physics and Controlled Fusion*, 63(11):115013, 2021.

[55] Riccardo Pompili. *Longitudinal diagnostics for comb-like electron beams by means of Electro-Optic Sampling.* PhD thesis, Università degli Studi di Roma Tor Vergata, SPARC_LAB, INFN-LNF, Frascati, Italy, 2013.

[56] SP Jamison, G Berden, Allan M MacLeod, DA Jaroszynski, B Redlich, AFG Van der Meer, and W Allan Gillespie. Electro-optic techniques for temporal profile characterisation of relativistic coulomb fields and coherent synchrotron radiation. *Nuclear Instruments and Methods in Physics Research Section A: Accelerators, Spectrometers, Detectors and Associated Equipment*, 557(1):305–308, 2006.

[57] Francesco Demurtas, MP Anania, A Biagioni, M Carillo, E Chiadroni, A Cianchi, G Costa, L Crincoli, A Del Dotto, M Del Giorno, et al. Experimental characterization of the timing-jitter effects on a beam-driven plasma wakefield accelerator. *IPAC...*, pages 553–556, 2024.

[58] Daniel Marx, Ralph Aßmann, Richard D'Arcy, and Barbara Marchetti. Simulations of 3d charge density measurements for commissioning of the polarix-tds. In *Journal of Physics: Conference Series*, volume 1067, page 072012. IOP Publishing, 2018.

[59] Eduard Prat, Zheqiao Geng, Christoph Kittel, Alexander Malyzhenkov, Fabio Marcellini, Sven Reiche, Thomas Schietinger, and Paolo Craievich. Attosecond time-resolved measurements of electron and photon beams with a variable polarization x-band radiofrequency deflector at an x-ray free-electron laser. *Advanced Photonics*, 7(2):026002–026002, 2025.

[60] Barbara Marchetti, Alexej Grudiev, Paolo Craievich, Ralph Assmann, H-H Braun, N Catalan Lasheras, Florian Christie, Richard D'Arcy, Renato Fortunati, Romain Ganter, et al. Experimental demonstration of novel beam characterization using a polarizable x-band transverse deflection structure. *Scientific reports*, 11(1):3560, 2021.

[61] Daniel Marx, Ralph Assmann, Paolo Craievich, Ulrich Dorda, Alexej Grudiev, and Barbara Marchetti. Longitudinal phase space reconstruction simulation studies using a novel x-band transverse deflecting structure at the sinbad facility at desy. *Nuclear Instruments and Methods in Physics Research Section A: Accelerators, Spectrometers, Detectors and Associated Equipment*, 909:374–378, 2018.

[62] Paul Scherrer Institute. Swissfel facility. `https://www.psi.ch/en/swissfel/facility`, 2025. Accessed: 8 October 2025.

[63] Christopher J Milne, Thomas Schietinger, Masamitsu Aiba, Arturo Alarcon, Jürgen Alex, Alexander Anghel, Vladimir Arsov, Carl Beard, Paul Beaud, Simona Bettoni, et al. Swissfel: the swiss x-ray free electron laser. *Applied Sciences*, 7(7):720, 2017.

[64] Eduard Prat, Andre Al Haddad, Christopher Arrell, Sven Augustin, Marco Boll, Christoph Bostedt, Marco Calvi, Adrian L Cavalieri, Paolo Craievich, Andreas Dax, et al. An x-ray free-electron laser with a highly configurable undulator and integrated chicanes for tailored pulse properties. *Nature communications*, 14(1):5069, 2023.

[65] Rasmus Ischebeck, Eduard Prat, Vincent Thominet, and Cigdem Ozkan Loch. Transverse profile imager for ultrabright electron beams. *Physical Review Special Topics—Accelerators and Beams*, 18(8):082802, 2015.

[66] Pavle Juranić and Eduard Prat. Testing high-resolution transverse profile monitors by measuring the dependence of the electron beam size on the beam energy at swissfel. *Review of Scientific Instruments*, 94(7), 2023.

[67] Excelitas Technologies. pco.edge 5.5 ds clhs scmos camera. `https://www.excelitas.com/product/pcoedge-55-ds-clhs-scmos-camera`. Accessed: 2025-09-29.

[68] Daniel Marx, Ralph Aßmann, Paolo Craievich, Ulrich Dorda, Alexej Grudiev, and Barbara Marchetti. Reconstruction of the 3d charge distribution of an electron bunch using a novel variable-polarization transverse deflecting structure (tds). In *Journal of Physics: Conference Series*, volume 874, page 012077. IOP Publishing, 2017.

[69] Daniel Marx, Ralph W Assmann, Paolo Craievich, Klaus Floettmann, Alexej Grudiev, and Barbara Marchetti. Simulation studies for characterizing ultrashort bunches using novel polarizable x-band transverse deflection structures. *Scientific reports*, 9(1):19912, 2019.

[70] A. H. Andersen and A. C. Kak. Simultaneous algebraic reconstruction technique (sart): A superior implementation of the art algorithm. *Ultrasonic Imaging*, 6(1):81–94, 1984.

[71] Anders H Andersen and Avinash C Kak. Simultaneous algebraic reconstruction technique (sart): a superior implementation of the art algorithm. *Ultrasonic imaging*, 6(1):81–94, 1984.

[72] Sonja Jaster-Merz, RW Assmann, Reinhard Brinkmann, Florian Burkart, Thomas Vinatier, et al. 5d tomography of electron bunches at ares. *Proc. IPAC'22*, pages 279–283, 2022.

[73] S Jaster-Merz, RW Assmann, R Brinkmann, F Burkart, W Hillert, M Stanitzki, and T Vinatier. 5d tomographic phase-space reconstruction of particle bunches. *Physical Review Accelerators and Beams*, 27(7):072801, 2024.

[74] KM Hock, MG Ibison, DJ Holder, A Wolski, and BD Muratori. Beam tomography in transverse normalised phase space. *Nuclear Instruments and Methods in Physics Research Section A: Accelerators, Spectrometers, Detectors and Associated Equipment*, 642(1):36–44, 2011.

[75] S. Jaster-Merz. Private communication, 2025.

[76] V Balandin, W Decking, and N Golubeva. Relations between projected emittances and eigen-emittances. *arXiv preprint arXiv:1305.1532*, 2013.

[77] Michael Röhrs, Christopher Gerth, Markus Hüning, and Holger Schlarb. Slice emittance measurements at flash. In *Proc. 10th Eur. Particle Accelerator Conference, Edinburgh, Scotland, UK*, page 77, 2006.

[78] BJ Holzer. Introduction to transverse beam dynamics. *arXiv preprint arXiv:1404.0923*, 2014.

# Appendix A

# Appendix

## A.1 Emittance: definitions, conventions, and use in this thesis

In beam dynamics, several emittance definitions are used depending on the context and on the level of coupling in the transverse planes. Unless otherwise stated, "emittance" refers to the *RMS geometric emittance* in a given transverse plane, with the *normalized emittance* defined as $\varepsilon_n = \beta\gamma\,\varepsilon$.

**Root-Mean-Squared Emittance** An ideal beam would occupy a well-defined ellipse in trace space, as individual particle trajectories are elliptical. However, real beams do not have sharp boundaries, making it necessary to define the occupied area statistically. This leads to the definition of RMS emittance:

$$\varepsilon_x = \sqrt{< x^2 >< x'^2 > - < xx' >^2} \tag{A.1}$$

This definition corresponds to the ellipse area that best approximates the beam distribution in the $(x, x')$ plane. It is the most commonly used measure of emittance in experiments, as it can be calculated directly from the beam's first and second statistical moments.

**Projected Emittance** The beam matrix in the 4D space is given by :

$$\Sigma_{4D} = \begin{pmatrix} \Sigma_{xx} & \Sigma_{xy} \\ \Sigma_{yx} & \Sigma_{yy} \end{pmatrix} \tag{A.2}$$

By taking the determinant of this matrix, the 4D rms emittance is defined as $\varepsilon_{4D} = |det(\Sigma_{4D})| = \varepsilon_1 \cdot \varepsilon_2$, where $\varepsilon_i$ are the 4D matrix eigenvalues, that are called intrinsic emittance. Similarly, the determinant of matrix $\Sigma_{xx}$ related to the 2D trace space defines the projected emittance. If the beam matrix is uncoupled, so that the correlation terms are zero, intrinsic and projected emittances coincide [76].

**Slice Emittance** In a Free-Electron Laser (FEL) facility, the efficiency and coherence of the emitted radiation depend on the local beam quality. These properties can vary along the bunch due to collective effects such as Coherent Synchrotron Radiation (CSR) and space-charge forces, which introduce a dependence on the beam's longitudinal distribution [77]. For this reason, it is common to analyze not only the projected (whole-bunch) emittance but also the emittance of longitudinal slices of the bunch. Each slice, defined as a longitudinal segment of the bunch, is characterized by its own emittance, providing a detailed map of the beam quality along the bunch.

## A.2 Twiss Parameters

In the trace space the single particle trajectory is described by the Courant-Snyder equation :

$$\gamma(s)x^2 + 2\alpha(s)xx' + \beta(s)x'^2 = \varepsilon \tag{A.3}$$

Since the emittance is an invariant of the motion, this equation is also an invariant and describes an ellipse in the $x, x'$ plane at fixed $s$. In this equation, are introduced the twiss parameters $\beta$, $\gamma$ and $\alpha$, which are related to each other from :

$$\alpha(s) = -\frac{\beta'(s)}{2} \tag{A.4}$$

$$\gamma(s) = \frac{1 + \alpha^2(s)}{\beta(s)} \tag{A.5}$$

As shown in figure A.1, the twiss parameters are related to the ellipse characteristics.

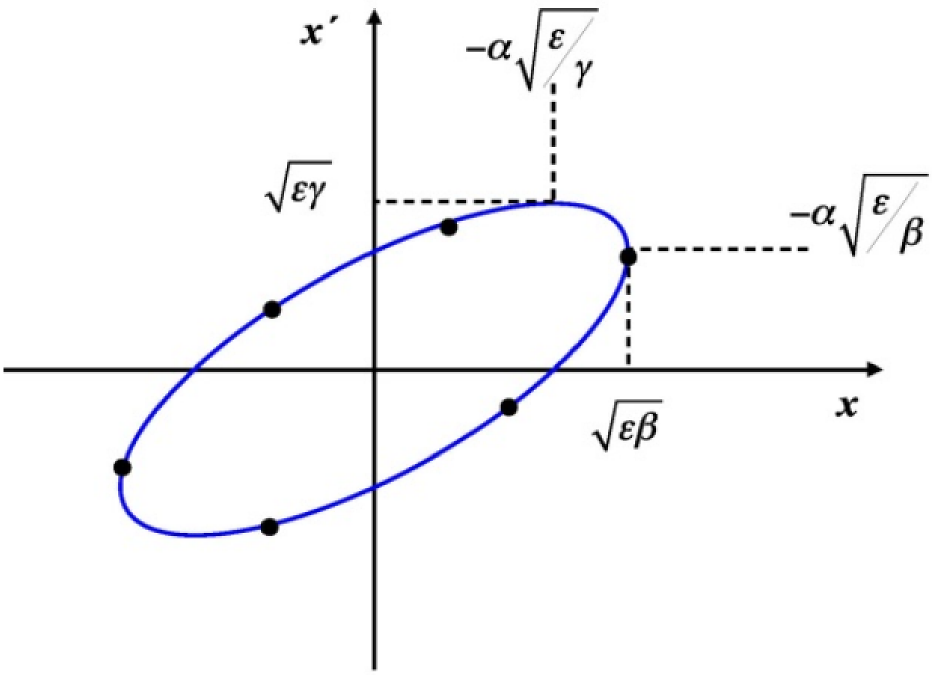


**Figure A.1:** Trace Space Ellipse of the particle trajectory, in which are highlighted the quantities related to the Twiss parameters [78].

When considering the entire ensemble of particles the beam matrix can be written in terms of the Twiss parameters, thus describing the beam at a fixed longitudinal position $s$.

$$\Sigma = \begin{pmatrix} < x^2 > & < xx' > \\ < xx' > & < x'^2 > \end{pmatrix} = \varepsilon_x \begin{pmatrix} \beta_x & -\alpha_x \\ -\alpha_x & \gamma_x \end{pmatrix} \tag{A.6}$$

Therefore, the Twiss parameters are linearly independent and related to the first and second order momentum of the particle distribution :

$$\beta_x = \frac{< x^2 >}{\varepsilon_x} \tag{A.7}$$

$$\alpha_x = -\frac{< xx' >}{\varepsilon_x} \tag{A.8}$$

$$\gamma_x = \frac{< x'^2 >}{\varepsilon_x} \tag{A.9}$$

- $\sqrt{\beta}$ represents the rms beam envelope per unit emittance
- $\sqrt{\gamma}$ represents the rms beam divergence per unit emittance
- $\sqrt{\alpha}$ is proportional to the correlation term and therefore to the derivative of the $\beta$ function

Their evolution through the accelerator from a point $s_0$ to $s_1$ is determined by applying the transfer matrix to the particle coordinates :

$$\vec{x}(s_1) = M_{s_1,s_2}\ \vec{x}(s_0) = \begin{pmatrix} C & S \\ C' & S' \end{pmatrix} \begin{pmatrix} x_0 \\ x'_0 \end{pmatrix} \tag{A.10}$$

Explicating the matrix elements leads to the expression of the initial coordinates in terms of the final ones:

$$x_0^2 = S'^2 x_1^2 - 2SS'x_1x'_1 + S^2x_1'^2 \tag{A.11}$$

$$x_0'^2 = C'^2 x_1^2 - 2CC'x_1x'_1 + C^2x_1'^2 \tag{A.12}$$

$$x_0x'_0 = -C'S'x_1^2 + (C'S + CS')x_1x'_1 - CSx_1'^2 \tag{A.13}$$

By definition of the Courant-Snyder invariant the same equation holds at the point $s_1$ and $s_0$ :

$$\gamma_1 x_1^2 + 2\alpha_1 x_1 x'_1 + \beta_1 x_1'^2 = \gamma_0 x_0^2 + 2\alpha_0 x_0 x'_0 + \beta_0 x_0'^2 \tag{A.14}$$

Substituting the equations A.11, A.12, A.13 in the expression A.14, allows to find the expression describing the evolution of the twiss parameters, which can be written as :

$$\begin{pmatrix} \beta \\ \alpha \\ \gamma \end{pmatrix}_{s_1} = \begin{pmatrix} C^2 & -2SC & S^2 \\ -CC' & S'C + SC' & -SS' \\ C'^2 & -2S'C' & S'^2 \end{pmatrix} \begin{pmatrix} \beta \\ \alpha \\ \gamma \end{pmatrix}_{s_0} \tag{A.15}$$

Through this matrix, the optical functions can be transformed depending on the lattice, and therefore their evolution after each element can be determined.

## A.3 Transfer matrix formalism

In the linearized equations of motion, the transverse dynamics is fully determined by the location of the beamline elements $s$, their magnetic characteristics $K(s)$ and the particle's momentum deviation $\frac{\Delta p}{p_0}$. For a single segment of the beamline in which the focusing function $K$ can be considered constant, an analytical solution for the particle motion can be obtained. Owing to the linearity of the equations of motion, the overall trajectory through the beamline can then be described as a sequential application of the individual solutions for each lattice element. The solution to the Hill's equation, by assuming that there is no coupling between the transverse planes, is given by a linear combination of harmonic functions:

$$x(s) = x_0 \cdot cos(\sqrt{K} \cdot s) + \frac{x'_0}{\sqrt{K}} \cdot sin(\sqrt{K} \cdot s) \tag{A.16}$$

$$x'(s) = -x_0\sqrt{K} \cdot sin(\sqrt{K} \cdot s) + x'_0 \cdot cos(\sqrt{K} \cdot s) \tag{A.17}$$

which can be described in a matrix form:

$$M_{x,y} = \begin{pmatrix} cos(\sqrt{K} \cdot s) & \frac{1}{\sqrt{K}} \cdot sin(\sqrt{K} \cdot s) \\ -\sqrt{K} \cdot sin(\sqrt{K} \cdot s) & cos(\sqrt{K} \cdot s) \end{pmatrix} \tag{A.18}$$

Each section can be described by a linear map, using the matrix formalism. The evolution of a particle from an initial position $s_0$ to a final position $s$, is then described by applying the related transfer matrix $M(s_0, s)$ to the particle's coordinates:

$$\begin{pmatrix} x_1 \\ x'_1 \\ y_1 \\ y'_1 \end{pmatrix} = M(s_0, s) \begin{pmatrix} x_0 \\ x'_0 \\ y_0 \\ y'_0 \end{pmatrix}$$

The transfer matrix $M(s_0, s)$ is determined by the product of the transfer matrix of the single beamline elements:

$$M(s_0, s) = \prod_i M_i \tag{A.19}$$

For simplicity in the next calculations, the matrix A.18 elements can be indicated as :

$$\begin{pmatrix} C & S \\ C' & S' \end{pmatrix} \tag{A.20}$$

where $C = cos(\sqrt{K}s)$ and $S = \frac{1}{\sqrt{K}}sin(\sqrt{K}s)$.

### A.3.1 Drift Space

In a drift space, $K(s) = 0$ and the equations of motion simplyfies to:

$$\begin{aligned} x''(s) &= 0 \\ y''(s) &= 0 \end{aligned} \tag{A.21}$$

The solution after a drift of length $l$ is then given by:

$$\begin{aligned} x(l) &= x_0 + lx'_0 \\ y(l) &= y_0 + ly'_0 \end{aligned} \tag{A.22}$$

And so the corresponding transfer matrix is given by:

$$M_D = \begin{pmatrix} 1 & l \\ 0 & 1 \end{pmatrix} \tag{A.23}$$

### A.3.2 Quadrupole

A quadrupole is a magnetic element used to focus charged particle beams. It generates a magnetic field with a linear gradient across the transverse plane, acting like a lens that focuses the beam in one plane while defocusing it in the orthogonal plane. A quadrupole magnet consists of four poles arranged symmetrically around the beam axis, producing a magnetic field given by:

$$\vec{B}(x, y) = g(x\hat{y} + y\hat{x}) \tag{A.24}$$

where $g$ is the quadrupole gradient, defined as $g = -\frac{\partial B_y}{\partial x} = -\frac{\partial B_x}{\partial y}$. The main parameters that define the quadrupole magnet in the lattice are the magnetic length $d$, defined as the distance over which the quadrupole gradient is uniform, and the quadrupole strength $k = \frac{g}{p/e}$, defined by normalizing the gradient by the particle momentum and charge.
In case of a quadrupole of length $d$ and strength $k$ the solution of the motion equation can be solved for $K(s) = \pm k$:

$$x(s) = x_0 \; cos(\sqrt{|k|}s) + \frac{x'_0}{\sqrt{|k|}} \; sin(\sqrt{|k|}s) \tag{A.25}$$

$$y(s) = y_0 \; cos(\sqrt{|k|}s) + \frac{y'_0}{\sqrt{|k|}} \; sin(\sqrt{|k|}s) \tag{A.26}$$

Therefore, the corresponding transfer matrix is given by:

$$M_{QF} = \begin{pmatrix} cos(\sqrt{k} \cdot d) & \frac{1}{\sqrt{k}} \cdot sin(\sqrt{k} \cdot d) \\ -\sqrt{k} \cdot sin(\sqrt{k} \cdot d) & cos(\sqrt{k} \cdot d) \end{pmatrix} \tag{A.27}$$

$$M_{QD} = \begin{pmatrix} cosh(\sqrt{k} \cdot d) & \frac{1}{\sqrt{k}} \cdot sinh(\sqrt{k} \cdot d) \\ -\sqrt{k} \cdot sinh(\sqrt{k} \cdot d) & cosh(\sqrt{k} \cdot d) \end{pmatrix} \tag{A.28}$$

respectively for the focusing and defocusing plane.
If the condition $kd << 1$ holds, the matrix can be written in the thin lens approximation, therefore becoming:

$$M_{QF,QD} = \begin{pmatrix} 1 & d \\ \mp\frac{1}{f} & 1 \end{pmatrix} \tag{A.29}$$

where $f = \frac{1}{kd}$ is the focal length of the quadrupole.
Since the quadrupole strength $k$ depends inversely on the particle momentum, particles with different energies experience different focusing strengths, leading to chromatic effects.

### A.3.3 Dispersion

To describe the beam dynamics of a real particle beam, in which the particles have different energies, the dispersive effect introduced by elements such as dipole magnets must be included. A reference particle is defined as the one following the design trajectory with nominal momentum $p_0$. Although the magnetic field $B$ is the same for all particles, those with different momenta experience different bending radii and thus follow slightly different paths compared to the reference particle. The dispersion function is defined as:

$$D(z) = \int_0^z k(\xi)[S(z)C(\xi) - C(z)S(\xi)]d\xi\,. \tag{A.30}$$

By using a perturbative approach, the particle deviation $u$ from the reference path can be written as $u = u_\beta + u_\delta$ where $u_\beta$ is the term from the non dispersive motion and $u_\delta$ is the term from the momentum deviation $\delta$ from the reference one. Therefore the transformation between two points $z$ and $z_0$ is given by:

$$\begin{pmatrix} u(z) \\ u'(z) \\ \delta \end{pmatrix} = M \begin{pmatrix} u_\beta(z_0) \\ u'_\beta(z_0) \\ \delta \end{pmatrix} + M \begin{pmatrix} u_\delta(z_0) \\ u'_\delta(z_0) \\ \delta \end{pmatrix}\,. \tag{A.31}$$

The displacement and slope of the particle with momentum error $\delta$ are then defined respectively as $u_\delta(z) = D(z)\delta$ and $u'_\delta(z) = D'(z)\delta$. Considering equation A.31 only for a dispersive element, the non-dispersive term can be neglected and the momentum error can be set to 1, so that the matrix equation is applied only to the dispersion function:

$$\begin{pmatrix} D(z) \\ D'(z) \\ 1 \end{pmatrix} = M \begin{pmatrix} D(z_0) \\ D'(z_0) \\ 1 \end{pmatrix}\,. \tag{A.32}$$

By applying the beam matrix for each dispersive element, is possible to calculate the dispersion function anywhere in the beamline. Finally the dispersion function is calculated with equation A.30 and A.18, considering $k = K = \frac{1}{\rho^2}$ :

$$D(z) = \rho[1 - cos(kz)] \tag{A.33}$$

$$D'(z) = sin(kz)\,. \tag{A.34}$$

Particles with momentum error $\delta$ will follow an equilibrium path given by $D(z)\delta$ [26].

### A.3.4 Dipole

A dipole is a magnetic element designed to deflect a charged particle generating a magnetic field perpendicular to the particle reference orbit. In case of horizontal bending the field is parallel to the vertical direction, and it is assumed to be described by a constant field $B_0$:

$$\vec{B}(x, y) = B_0 \cdot \hat{e}_y \tag{A.35}$$

The dipole strength $k_{dip}$ is defined by the orbit curvature radius $\rho$ and it is related to the magnetic field and particle momentum by the relation:

$$k_{dip} = \frac{1}{\rho} = \frac{q}{p}B_0 \tag{A.36}$$

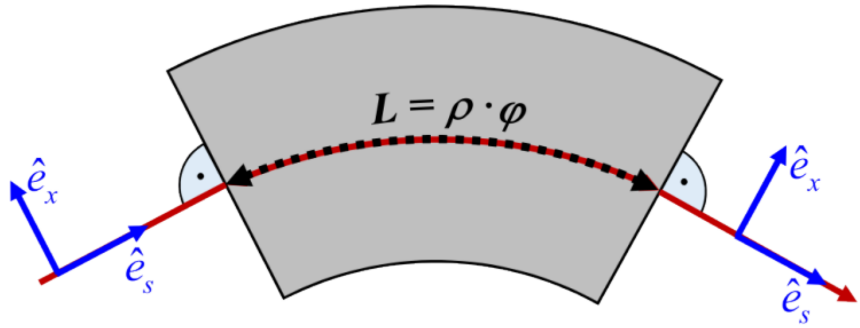


**Figure A.2:** Schematic of a sector dipole with constant magnetic field and with bending in the horizontal direction, in which are indicated the arc length $L$, the bending angle $\varphi$ and the curvature radius $\rho$ [21].

In this case a sector dipole for which the end faces are perpendicular to the reference orbit is considered, and the magnetic field is assumed to be constant inside the magnet and to drop to zero instantaneously outside, neglecting possible fringe fields. By doing these assumptions the curvature radius is constant between the two end faces. The product of the curvature radius and the bending angle defines the arc length $L$ of the magnet: $L = \rho \cdot \varphi$. In the equation of motion the magnetic term reduces to $K = \frac{1}{\rho^2}$ so that for the horizontal and vertical plane they become:

$$x''(s) + \frac{x}{\rho^2} = 0 \tag{A.37}$$

$$y''(s) = 0 \tag{A.38}$$

With solutions :

$$x(L) = x_0 cos(\varphi) + \frac{x'_0}{\rho} sin\varphi \tag{A.39}$$

$$y(L) = y_0 + Ly'_0 \tag{A.40}$$

Since the force acting in the perpendicular plane is zero, the motion in y is equivalent to a drift of length L. Therefore including also the dispersion term from A.30, in the bending plane the $3 \times 3$ matrix corresponding to the equation of motion solution is:

$$M_{dipole} = \begin{pmatrix} cos(\varphi) & \rho\ sin(\varphi) & \rho(1 - cos(\varphi)) \\ -\frac{1}{\rho}\ sin(\varphi) & cos(\varphi) & sin(\varphi) \\ 0 & 0 & 1 \end{pmatrix} \tag{A.41}$$

### A.3.5 Image preprocessing

For each dataset, five images were acquired for each combination of quadrupole setting and polarization, with a background acquisition, at a repetition rate of 1 Hz. The raw images acquired on the diagnostic screen require several pre-processing steps before being used as input for the tomographic algorithms. Each image is first corrected by subtracting the background and applying a Gaussian filter to reduce noise. The images are then rescaled to obtain square pixels and rotated according to the corresponding streaking angle. Streaking-axis calibration converts pixel coordinates to the longitudinal time axis. Since the measured calibration factors differ due to measurement fluctuations, the images are rescaled again to ensure consistent time/pixel calibration. Finally, the images are centered, and a region of interest (ROI) is defined to minimize artifacts during the reconstruction process. These steps are crucial for ensuring the consistency of the projection data and avoiding systematic errors in the subsequent tomographic reconstruction.

## List of publications

[1] Demurtas, F., et al. "Experimental characterization of the timing-jitter effects on a beam-driven plasma wakefield accelerator." IPAC... (2024): 553-556.

[2] Quartullo, D., et al. "DESIGN OF SPECTROMETER ENERGY MEASUREMENT SETUPS FOR THE FUTURE EUPRAXIA@ SPARC_LAB AND SSRIP LINACS."

[3] Curcio, Alessandro, et al. "Performance study on a soft X-ray betatron radiation source realized in the self-injection regime of laser-plasma wakefield acceleration." Applied Sciences 12.23 (2022): 12471.

[4] Curcio, Alessandro, et al. "Reconstruction of lateral coherence and 2D emittance in plasma betatron X-ray sources." Scientific Reports 14.1 (2024): 1719.

[5] Verra, L., et al. "Experimental observation of space-charge field screening of a relativistic particle bunch in plasma." Physical Review Letters 133.3 (2024): 035001.

[6] Verra, L., et al. "Effect of dielectric wakefields in a capillary discharge for plasma wakefield acceleration." Nuclear Instruments and Methods in Physics Research Section A: Accelerators, Spectrometers, Detectors and Associated Equipment 1072 (2025): 170157.

[7] Pompili, R., et al. "Recovery of hydrogen plasma at the sub-nanosecond timescale in a plasma-wakefield accelerator." Communications Physics 7.1 (2024): 241.

[8] Pompili, R., et al. "Guiding of charged particle beams in curved plasma-discharge capillaries." Physical Review Letters 132.21 (2024): 215001.

[9] Pompili, R., et al. "Acceleration and focusing of relativistic electron beams in a compact plasma device." Physical Review E 109.5 (2024): 055202.

# Acknowledgements

I would like to thank my supervisors, E. Chiadroni and A. Giribono, for their continuous guidance and support throughout the development of this work.

I would like to thank all members of the collaboration from DESY, PSI, and INFN-LNF who contributed to the experimental campaign and to the development of this work.

In particular, I would like to acknowledge S. Jaster-Merz for her significant contribution to the 5D tomographic reconstruction activities within the collaboration, including the analysis procedures and the results presented in this thesis. I further acknowledge her for providing the material used in Figures 5.28, 5.29, 5.30, and 5.31, as well as in Tables 5.15, 5.16, and 5.17, included in Chapter 5 of this manuscript. I would also like to acknowledge D. Marx for providing the reconstruction code used for the 3D tomographic analysis presented in this thesis.

I am also grateful to the PSI team, including P. Craievich, F. Marcellini, E. Prat, and P. Dijkstal, for their support in the preparation and operation of the PolariX transverse deflection structure, as well as for their contributions to beam dynamics studies, measurements, and data analysis. I further thank the other PSI collaborators involved in the experiment for their valuable support during the experimental campaign.

I also acknowledge D. Quartullo for his help on the diagnostics for EuPRAXIA and spectrometer systems, and R. Pompili for his support with the EOS diagnostics.